

Titre: Non-Linear Transmission Lines for Pulse Generation, Compression, Shaping, and Transmission for Ultrafast Electronics
Title:

Auteur: MuhibUr Rahman
Author:

Date: 2022

Type: Mémoire ou thèse / Dissertation or Thesis

Référence: Rahman, M.U. (2022). Non-Linear Transmission Lines for Pulse Generation, Compression, Shaping, and Transmission for Ultrafast Electronics [Thèse de doctorat, Polytechnique Montréal]. PolyPublie.
Citation: <https://publications.polymtl.ca/10713/>

 **Document en libre accès dans PolyPublie**
Open Access document in PolyPublie

URL de PolyPublie: <https://publications.polymtl.ca/10713/>
PolyPublie URL:

Directeurs de recherche: Ke Wu
Advisors:

Programme: Génie électrique
Program:

POLYTECHNIQUE MONTRÉAL

affiliée à l'Université de Montréal

**Non-linear transmission lines for pulse generation, compression, shaping, and
transmission for ultrafast electronics**

MUHIBUR RAHMAN

Département de génie électrique

Thèse présentée en vue de l'obtention du diplôme de *Philosophiæ Doctor*

Génie électrique

Décembre 2022

© Muhibur Rahman, 2022.

POLYTECHNIQUE MONTRÉAL

affiliée à l'Université de Montréal

Cette thèse intitulée :

Non-linear transmission lines for pulse generation, compression, shaping, and transmission for ultrafast electronics

présentée par **Muhibur RAHMAN**

en vue de l'obtention du diplôme de *Philosophiæ Doctor*

a été dûment acceptée par le jury d'examen constitué de :

Christian CARDINAL, présidente

Ke WU, membre et directeur de recherche

Halim BOUTAYEB, membre

Tayeb A. DENIDNI, membre externe

DEDICATION

To my beloved parents, brothers, and sisters

To my wife Munazza Amjad

ACKNOWLEDGEMENTS

I want to convey my sincere gratitude to my supervisor, Prof. Ke Wu, for giving me the chance to work with his research team at the Poly-GRAMES Research Center. Throughout my Ph.D. studies, his inspiring guidance and never-ending encouragement enabled me to progress and overcome each problem during my Ph.D. journey. Prof. Wu has also taught me how to think creatively and broadly, which is one of the most important qualities for becoming a competent independent researcher.

I would also like to express my gratitude to the president Prof. Christian Cardinal and other committee members Prof. Halim Boutayeb, and Prof. Tayeb A. Denidni for reviewing my thesis in their useful time and providing me with their valuable insights and comments.

I would also like to extend my gratitude to the technician and administrative team at Poly-GRAMES Research Center, especially Mr. Jean-Sébastien Décarie, Mr. Jules Gauthier, Mrs. Rachel Lortie, Dr. David Dousset, Mr. Maxime Thibault, Mr. Traian Antonescu, and Mrs. Brigitte.

I am very grateful to my colleagues in our research group for their friendship and help. I would like to thank Dr. Dongze Zheng, who sat behind my seat, and we have fruitful discussions every time. Thanks to Dr. Desong Wang for those valuable discussions with him regarding different ideas as well. I would also appreciate the discussions with other colleagues such as Chandan Roy, Amir Hossein Askarian, Dr. Xiaoqiang Gu, Dr. Intikhab Hussain, Ben You, Marzieh Mehri Dehnavi, etc. I would also like to thank my friends in Montreal who helped me to manage my Ph.D. life specifically Adnan Jafar, Saddam Hussain, Saqib, Mohsin Hassan, Sharjeel, etc. Additionally, I would like to thank Zeba Erum Jabeen Malik for motivating me and supporting me in my Ph.D. journey during my tough conditions.

Finally, I am thankful to my wife Munazza Amjad, my mother Izzat Begum, my father Aziz Ur Rahman, and my brothers and sisters for their endless love, encouragement, and unconditional support during my study. My parents have taught me how to be a good person while providing me with unwavering love and support throughout my entire life.

RÉSUMÉ

L'électronique ultrarapide se distingue dans les sciences et technologies émergentes axées sur les phénomènes ultrarapides, notamment à l'échelle de temps de la picoseconde et en dessous. Elle a un large éventail d'implications et d'applications dans de nombreux domaines tels que les sciences fondamentales, la détection et l'imagerie térahertz (THz), les mesures à haute fréquence, les communications à haute capacité, ainsi que la biologie et la médecine. Cela a attiré l'attention sur la question la plus critique, à savoir la génération, la compression, la mise en forme et la transmission d'impulsions électriques ultracourtes. En outre, dans les systèmes à bande ultralarge, y compris le système UWB, nous avons besoin d'un signal ultrarapide pour les applications de détection et d'imagerie, ainsi que pour les traitements médicaux avancés, notamment la détection du cancer du sein et des tumeurs, les mesures quantiques et les explorations géophysiques. Dans toutes ces applications, le défi et les limites sont la génération, la compression et la mise en forme des transitoires à grande vitesse, puis leur transmission correspondante.

La ligne de transmission non linéaire (NLTL) est généralement un réseau en échelle LC qui comprend des composants non linéaires chargés périodiquement, soit des inductances, soit des condensateurs. Elle peut être, par exemple, chargée périodiquement par des diodes varactor et Schottky polarisées en inverse. Le NLTL a déjà trouvé une large gamme d'applications dans les dispositifs et les systèmes, notamment le générateur de peignes, la réflectométrie dans le domaine temporel (TDR), le synthétiseur de fréquence, l'oscilloscope à échantillonnage à grande vitesse et le générateur de stimulus ou d'impulsions. NLTL a la capacité de générer des impulsions gaussiennes grâce au concept de soliton. Les solitons sont générés dans le NLTL lorsque la non-linéarité et la dispersion s'opposent exactement l'une à l'autre. Ce phénomène crée donc une opportunité pour les ingénieurs en micro-ondes d'aborder la non-linéarité de manière utile.

Ce travail présente des générateurs d'impulsions picosecondes propres pour l'électronique ultrarapide, l'électromagnétique biologique, la détection THz, l'exploration géophysique, le radar à pénétration de sol (GPR), le plasma à décharge, la détection des tumeurs du sein et les futurs oscilloscopes basés sur différentes classes de NLTL. De nouvelles classes de NLTL sont établies et la transformation des NLTL en un domaine magnétique est étudiée. À cet égard, une nouvelle

classe de NLTL a été développée, appelée ligne de transmission magnétique non linéaire (NLMTL).

Des générateurs d'impulsions basés sur la compression simultanée des temps de montée et de descente sont développés et les techniques de combinaison de transitoires électriques ultra-courts sont fournies. Une démonstration théorique est effectuée en transformant le concept de soliton et d'ondes de choc du domaine de l'hydrodynamique au domaine électrique correspondant. Enfin, la validation du concept est effectuée sur la base d'une expérimentation en temps réel et toutes ces contributions sont discutées dans le chapitre 3.

Une démonstration théorique et expérimentale complète pour l'analyse des NLMTLs prenant en compte les perturbations localisées qui apparaissent dans les matériaux ferrimagnétiques est également étudiée pour la première fois. Les NLMTL sont validés pour présenter la capacité de compression simultanée des temps de montée et de descente en raison de leur contrôle simultané de l'intensité du champ magnétique et de la tension de polarisation appliquée. Ces contributions sont bien articulées dans le chapitre 4.

Des impulsions ultracourtes sont générées à l'aide de diodes varactor empilées par cellule NLTL, où la capacité de compression est maximisée par l'obtention d'une impulsion gaussienne propre de près de 10,1 ps, avec une amélioration remarquable du comportement d'anneau, présentée au chapitre 5. Le schéma NLTL proposé découle d'une combinaison unique d'une diode varactor unique et d'une diode varactor empilée par cellule NLTL, qui est conçue pour exploiter un effet significatif de non-linéarité en relation avec la diode varactor. Cette technique génère un facteur de compression plus élevé dans les temps de montée et de descente des circuits NLTL par rapport aux diodes varactor simples par section NLTL. Ce schéma est validé pour fonctionner correctement dans une topologie NLTL à triple empilement en maximisant le facteur de compression.

De même, les NLTL gyromagnétiques et hybrides sont également étudiés pour la génération et la compression d'impulsions et sont discutés dans le chapitre 6. Une analyse théorique et de simulation complète est fournie et elle est finalement validée par l'expérimentation. En outre, la transformation des impulsions générées et compressées proposées est également effectuée et la dérivée supérieure des impulsions gaussiennes est développée sans affecter sa durée d'impulsion et son comportement d'anneau. La durée d'impulsion globale obtenue dans chaque scénario est bien

maintenue et elle est présentée au chapitre 7. De plus, le chapitre 8 traite des caractéristiques des impulsions rayonnées en analysant la transmission et la réception dans différentes combinaisons d'antennes à large bande et les modèles théoriques et analytiques correspondants sont fournis. Enfin, le chapitre 9 propose une conclusion générale et une discussion sur les travaux futurs.

ABSTRACT

Ultrafast electronics stands out in emerging ultrafast sciences and technologies, particularly on the picosecond phenomena-focused timescale and shorter. It has a wide range of implications and applications in many fields such as basic science, terahertz (THz) detection, imaging, sensing, high-frequency measurement, high-capability communications, as well as biology and medicine. This has drawn extensive attention to the most critical and foundational aspect in the field, that is, ultrashort electrical pulse generation, compression, shaping, and transmission. Also, in the development of well-publicized ultrabroadband (UWB) systems and technologies, we need an ultrafast signal for sensing, imaging, and communication applications, and advanced medical treatments including breast cancer detection and tumor detection, high-speed digital circuits and systems, quantum measurement, and geophysical explorations. In all these applications, the challenge and limitation are fundamentally related to the generation, compression, and shaping of high-speed transients and their corresponding transmission.

Nonlinear transmission line (NLTL) is generally an LC ladder network that comprises of periodically loaded nonlinear components in terms of either inductors or capacitors. It can be, for example, periodically loaded by reversely biased varactors and Schottky diodes. NLTL has already found a wide range of applications in devices and systems including comb generator, time domain reflectometry (TDR), frequency synthesizer, high-speed sampling oscilloscope, and stimulus or pulse generator. NLTL has the capability of generating Gaussian pulses through the concept of soliton. Solitons are generated in NLTL when the nonlinearity and dispersion effects exactly counteract with each other. So this phenomenon creates an opportunity for microwave engineers to tackle non-linearity in a useful way.

This work presents a series of picosecond pulse generators for ultra-fast electronics, biological electromagnetics, THz detection, geophysical exploration, ground penetrating radar (GPR), discharge plasma, breast tumor detection, and future oscilloscopes based on different classes of NLTLs. New classes of NLTLs are established and the transformation of NLTLs through the use of magnetic materials is investigated. In this regard, a new class of NLTLs is developed, termed as a non-linear magnetic transmission line (NLMTL).

Pulse generators based on simultaneous rise and fall time compression are developed and the techniques for the combination of ultrashort electrical transients are studied and discussed. Theoretical demonstration is conducted by transforming the concept of soliton and shock waves from the hydrodynamics domain to the corresponding electrical domain. Finally, the validation of the concept is performed based on real-time experiments and all these contributions are discussed in Chapter 3.

A complete theoretical and experimental demonstration for the analysis of NLMTLs considering the localized disturbances that arise within ferrimagnetic materials are studied for the first time. NLMTLs are validated, which present the capability of simultaneous rise and fall time compression due to their simultaneous control of magnetic field strength and applied biasing voltage. These contributions are well articulated in Chapter 4.

Chapter 5 presents the generation of ultrashort pulses using stacked varactor diodes per NLTL cell where the compression capability is maximized by achieving a clean Gaussian pulse of almost 10.1 ps with outstanding improvement in ringing behavior. The proposed NLTL scheme stems from a unique combination of a single varactor diode and stacked varactor diode per NLTL cell, which is designed to exploit a significant effect of non-linearity in connection with the varactor diode. This technique generates a higher compression factor in both rise and fall time of NLTL circuits in comparison to single varactor diodes per NLTL section. This scheme is validated to work well in a triple-stacked NLTL topology by maximizing the compression factor.

Similarly, gyromagnetic and hybrid NLTLs are also investigated for pulse generation and compression, which is discussed in Chapter 6. Complete theoretical and simulation analysis is provided and it is finally validated via experimentation. Furthermore, the transformation of the proposed generated and compressed pulses is also carried out and a higher derivative of the Gaussian pulses is developed without affecting its pulse duration and ringing behavior. The overall pulse duration achieved in each scenario is well maintained and it is described in Chapter 7. Additionally, Chapter 8 deals with the radiated pulse characteristics by analyzing the transmission and reception for different combinations of wideband antennas, and their corresponding theoretical and analytical models are also provided. Finally, Chapter 9 comes up with a general conclusion and discussion on future works.

TABLE OF CONTENTS

DEDICATION	III
ACKNOWLEDGEMENTS	IV
RÉSUMÉ.....	V
ABSTRACT	VIII
TABLE OF CONTENTS	X
LIST OF TABLES	XVI
LIST OF FIGURES.....	XVII
LIST OF SYMBOLS AND ABBREVIATIONS.....	XXVII
LIST OF APPENDICES	XXIX
CHAPTER 1 INTRODUCTION.....	1
1.1 Motivation and objectives	1
1.2 Outline and contributions of this thesis.....	3
CHAPTER 2 LITERATURE REVIEW.....	7
2.1 Definition of important pulse parameters.....	7
2.1.1 Pulse duration or pulse width.....	8
2.1.2 Full width half maximum (FWHM).....	8
2.1.3 Ringing level	8
2.1.4 Stretch ratio	8
2.2 Ultrafast ultra-broadband pulse definition	9
2.3 Various pulse generation, compression, and shaping techniques	11
2.3.1 Pulse generators using resonant tunneling diodes (RTDs).....	11
2.3.2 Pulse generators using schottky diode	12
2.3.3 Pulse generators using step recovery diode (SRD).....	13

2.3.4	Pulse generators using various SRDs topologies	14
2.3.5	Pulse generators using field effect transistors (FETs).....	15
2.3.6	Pulse generators using avalanche transistors	16
2.3.7	Pulse generators using NLTL.....	17
2.3.8	Pulse generators using gyromagnetic non-linear transmission lines (G-NLTLs).....	18
2.3.9	Pulse generators using dielectric non-linear transmission lines (D-NLTLs)	19
2.3.10	Pulse generators using delay lines.....	20
2.3.11	Pulse generators using micro-miniature mercury switches.....	21
2.3.12	Pulse generators using vacuum tube	22
2.3.13	Pulse generators using spark gaps.....	22
2.3.14	Pulse generators using Josephson junctions	23
CHAPTER 3 ARTICLE 1: A NONLINEAR TRANSMISSION APPROACH TO COMPRESSING RISE AND FALL TIME IN PICOSECOND PULSE GENERATION		25
3.1	Introduction	26
3.2	SRD pulse generating circuit.....	30
3.2.1	Equivalent circuit of SRD	30
3.2.2	SRD topology investigation for pulse sharpening.....	31
3.3	Theory of NLTL.....	33
3.3.1	NLTL solution utilizing kdv approach with experimental validation	33
3.3.2	NLTL rise time compression analysis.....	37
3.3.3	NLTL fall time compression analysis	39
3.4	Integrated ps pulse generators with rise time compression.....	42
3.4.1	SRD topology integration with linear NLTL	42
3.4.2	SRD topology integration with abrupt tapered NLTL	44

3.4.3	SRD topology integration with exponentially tapered NLTL.....	45
3.4.4	Fabrication and measurement setup	46
3.5	Integrated ps pulse generator with both rise and fall time compression	49
3.6	Comparison with recently proposed state of the art pulse generators.....	53
3.7	Conclusion.....	55
CHAPTER 4 ARTICLE 2: A NONLINEAR TRANSMISSION LINE TECHNIQUE FOR GENERATING EFFICIENT AND LOW-RINGING PICOSECOND PULSES FOR ULTRABROADBAND AND ULTRAFAST SYSTEMS		
		57
4.1	Introduction	58
4.2	Related work and background.....	59
4.3	Theory and analysis.....	62
4.3.1	Theory and analysis of NLTL with single varactor diode per section	62
4.3.2	Theory and analysis of NLTL with stacked varactor diode per section.....	64
4.4	Design of pulse generators with results and discussions.....	69
4.4.1	Integrated triple-stacked NLTL pulse generator based on rising time-compression .	70
4.4.2	Prototype and measurement of the proposed pulse generator based on rising time-compression.....	73
4.4.3	Simulation and measurement of integrated triple-stacked NLTL pulse generator based on fall time-compression.....	75
4.4.4	Frequency response of the proposed pulse generators	77
4.4.5	Reconfiguring the proposed pulse generators to higher derivatives including monocycle and doublet pulses.....	77
4.5	Comparison with state-of-the-art pulse generators published in literature	79
4.6	Conclusion.....	81

CHAPTER 5	ARTICLE 3: THEORETICAL AND EXPERIMENTAL ANALYSIS OF PULSE COMPRESSION CAPABILITY IN NON-LINEAR MAGNETIC TRANSMISSION LINE.....	82
5.1	Introduction	82
5.2	Theoretical development of NLMTLs	86
5.3	Design and modelling of NLMTLs	90
5.4	Results and discussions	93
5.4.1	NLMTL circuits and measurement setup	94
5.4.2	Experimental validation of NLMTL theory	96
5.4.3	NLMTL pulse compression capability	98
5.4.4	NLMTL pulse compression capability with arbitrary magnetization direction	103
5.5	Difference between NLGTL and NLMTL	104
5.6	Conclusion.....	106
CHAPTER 6	ARTICLE 4: THEORY AND PRACTICE OF PULSE COMPRESSION IN HYBRID AND GYROMAGNETIC NON-LINEAR TRANSMISSION LINES	107
6.1	Introduction	107
6.2	Theory and design of hybrid NLTL	111
6.3	Theory and design of gyromagnetic NLTL.....	116
6.4	Analysis of compression capability.....	120
6.4.1	Hybrid NLTL pulse compression capability and parametric analysis	120
6.4.2	Gyromagnetic NLTL pulse compression capability	123
6.5	Experimental demonstration	127
6.6	Difference between hybrid and gyromagnetic NLTLs	129
6.7	Conclusion.....	129

CHAPTER 7	ARTICLE 5: A RECONFIGURABLE PICOSECOND PULSE GENERATOR IN NON-LINEAR TRANSMISSION LINE FOR IMPULSE RADAR ULTRAWIDEBAND APPLICATIONS	131
7.1	Introduction	131
7.2	Design and configuration	132
7.3	Results and discussions	136
7.4	Prototype and measurements.....	137
7.5	Comparisons with the state of the art	138
7.6	Conclusion.....	138
CHAPTER 8	PICOSECOND PULSE GENERATION, SHAPING, TRANSMISSION, AND RECEPTION CHARACTERISTICS FOR WIRELESS SENSING APPLICATIONS.....	139
8.1	Introduction	139
8.2	Design and measurement of ultrashort reconfigurable pulse generator with multiple pulse shapes.....	142
8.3	Various wideband antennas with simulations and measurements	144
8.3.1	Vivaldi antenna	144
8.3.2	Antipodal Vivaldi antenna	146
8.3.3	Wideband slotted patch monopole antenna.....	148
8.3.4	Biconical antenna	150
8.3.5	Ridged horn antenna.....	151
8.4	Radiating pulse characteristics in different scenarios	152
8.4.1	Vivaldi —Vivaldi combination.....	153
8.4.2	Antipodal Vivaldi —Antipodal Vivaldi combination.....	154
8.4.3	Slotted monopole patch —Slotted monopole patch combination.....	155
8.4.4	Double ridged horn —Double ridged horn combination	155

8.4.5	Antipodal Vivaldi Antenna —Biconical Antenna combination	156
8.5	Experimental demonstrations	157
8.6	Received pulse analysis in terms of important pulse parameters	160
8.6.1	Stretch ratio (SR).....	161
8.6.2	System fidelity factor (SFF)	161
8.6.3	Ringling behavior	162
8.6.4	Figure of merit (FOM)	163
8.7	Conclusion.....	163
CHAPTER 9	GENERAL DISCUSSION.....	164
CHAPTER 10	CONCLUSION AND RECOMMENDATIONS.....	167
10.1	Conclusion.....	167
10.2	Recommendations	168
REFERENCES	170
APPENDICES	187

LIST OF TABLES

Table 2.1 Commercially developed vacuum pulse generators	22
Table 3.1 Overall summary of the developed ps pulse generators	49
Table 3.2 Comparison with ps generators in the literature [Proposed 1: four section linear NLTL integrated, Proposed 2: four section exponentially tapered NLTL integrated, Proposed 3: ten section linear NLTL integrated, Proposed 4: Two NLTL's integrated with SRD topology of opposite diode polarities] (N/R means not reported)	53
Table 4.1 Comparison of the proposed pulse generators with current states of the arts. (N/A means not applicable and N/R means not reported)	79
Table 5.1 Comparison between YIG and Nickel Ferrite	95
Table 5.2 Summary of performance behaviors of NLMTL in terms of different important parameters.....	102
Table 5.3 Summary of performance behaviors of NLMTL and NLGTL in terms of different important parameters	105
Table 6.1 Summary of a parametric study of hybrid NLTL.....	123
Table 6.2 Summary of a parametric study of gyromagnetic NLTL	126
Table 6.3 Summary and performances of hybrid and gyromagnetic NLTLS.....	129
Table 7.1 Comparison of the proposed reconfigurable ps pulse generator based on NLTL with other reported works recently published in the literature.	138
Table 8.1 Summary and relationship of transmitting and receiving antennas for different antenna combinations.....	157
Table 8.2 Stretch ratio for various angles at $\phi=0^\circ$ plane	161
Table 8.3 SFF is calculated from the corresponding measured transfer functions.....	162
Table 8.4 Detailed ringing level of received pulses in various scenarios.....	162
Table 8.5 FOM of received pulses in various scenarios	163

LIST OF FIGURES

Figure 2.1	Generational evolution of commercially developed pulse generators by different industrial organizations including Hewlett Packard, Colby, Tektronix, Tau Tron, BNC, Ana-Pico, etc	9
Figure 2.2	Transformation between time and frequency domain. (a) Conversion using FFT and IFFT. (b) Normalized pulse having pulse duration of almost 7 ps. (c) 7 ps normalized pulse in frequency domain	10
Figure 2.4	Pulse generators based on RTD. (a) Rise edge transients pulse generator using high-speed RTD presented in [11]. (b) Pulse generator using a combination of high-speed RTD presented in [12].....	12
Figure 2.5	Gaussian and monocycle pulse generator using Schottky diodes presented in [13] ...	13
Figure 2.6	Gaussian pulse generator using single SRD. (a) Shunt arrangement of SRD. (b) Series arrangement of SRD.....	14
Figure 2.7	Gaussian pulse generator using SRD in series with wave-shaping circuit [16].....	14
Figure 2.8	(a) Gaussian pulse generator using SRD topology presented in [17]; (b) Response of circuit topology from simulation.....	15
Figure 2.9	Block diagram of MESFET-based PG presented in [19].....	16
Figure 2.10	Block diagram of pulse generation technique presented in [22].....	17
Figure 2.11	Block diagram of pulse generation scheme presented in [23].....	17
Figure 2.12	Gyromagnetic NLTL used for pulse compression.....	18
Figure 2.13	Transmission line element-based model of a ferrite loaded gyromagnetic NLTL to be used for pulse compression	19
Figure 2.14	D-NLTL used for pulse generation	19
Figure 2.15	Output response from D-NLTL used for pulse generation [40]	20
Figure 2.16	Rectangular pulse generator by transforming rise edge transients presented in [42] .	20
Figure 2.17	Circuit diagram of the mercury switch-based pulse generator	21

Figure 2.18 Circuit diagram of dual spark gap pulse generator	23
Figure 2.19 Circuit diagram of Josephson junction as a pulse generator	24
Figure 3.1 Pulse producing circuit based on SRD with corresponding equivalent circuit and I-V characteristic curve. (a) SRD spice model generated in ADS; (b) Extracted SRD equivalent circuit model; (c) I-V characteristic and forward resistance changing curves of modeled SRD	31
Figure 3.2 SRD circuits in different arrangements. (a) shunt arrangement; (b) series arrangement; (c) mixed arrangement.....	32
Figure 3.3 Response of SRD based pulse generation schemes in series, shunt, and mixed topology configurations and impact of input voltage and inductance on pulse width and amplitude. (a) SRD circuit arrangement response in series, shunt, and mixed topology; (b) Zoomed in view of circuit response; (c) Varying input voltage with fixed inductance of 20 nH; (d) Varying inductance with a fixed voltage of 5 V	32
Figure 3.4 Section of dissipative capacitive NLTL with nonlinear capacitor and linear inductor	33
Figure 3.5 Fabricated six and ten-section NLTLs with corresponding response (biasing wires and connectors are not shown in the fabricated prototypes). (a) Six section NLTL prototype; (b) Response from theory and measurement for the developed six-section NLTL prototype; (c) Ten section NLTL prototype; (d) Response from theory and measurement for the developed ten section NLTL prototype	36
Figure 3.6 Six sections capacitive NLTL utilized for rise time compression. (a) Distributed design model; (b) Lumped design model	37
Figure 3.7 Rise time compression (T_r) of NLTL by varying voltage	39
Figure 3.8 Six sections capacitive NLTL utilized for fall time compression. (a) Distributed model; (b) Lumped model	40
Figure 3.9 Fall time compression of NLTL with step input	40
Figure 3.10 Fall time compression (T_f) of NLTL by varying voltage	41

Figure 3.11 Block diagram of SRD topology-based pulse generating circuit integrated with different NLTL topologies for generating different pulse schemes	42
Figure 3.12 Integration of four sections linear NLTL with SRD topology-based pulse generating circuit.....	43
Figure 3.13 Simulated result of linear NLTL integrated with SRD topology-based generator. (a) Four section NLTL; (b) Ten section NLTL	43
Figure 3.14 Integration of ten sections tapered NLTL with SRD topology-based pulse generating circuit.....	44
Figure 3.15 Simulated result of tapered NLTL integrated with SRD topology-based generator. (a) Four section tapered NLTL; (b) Four section exponentially tapered NLTL.....	45
Figure 3.16 Integration of four sections exponentially tapered NLTL with SRD topology-based pulse generating circuit	45
Figure 3.17 Fabricated pulse generators for rise time compression, the corresponding biasing wires are not displayed. (a) circuit 1: Four-sections linear NLTL integrated with SRD topology; (b) circuit 2: Four-sections exponentially tapered NLTL integrated with SRD topology; (c) circuit 3: Ten sections linear NLTL integrated with SRD topology	46
Figure 3.18 Experimental verification: the system is composed of a periodic signal generator, a dc power supply, an oscilloscope, and developed NLTL based ps pulse generators placed between universal test fixture for measurement.....	47
Figure 3.19 Simulated vs. measured results of ps pulse generators based on SRD topology with multi-section linear and tapered NLTL. (a) ps pulse generator with four sections linear case; (b) ps pulse generator with four-sections tapered case; (c) ps pulse generator with ten sections linear case	47
Figure 3.20 Pulse duration vs resistor (R_3) of the proposed ps generators in four sections exponentially tapered NLTL case	48
Figure 3.21 FWHM vs resistor (R_3) of the proposed ps generators in four sections exponentially tapered NLTL case	48

Figure 3.22 Integration of two NLTL circuits having opposite polarities with SRD topology-based pulse generating circuit with prototypes of all blocks, biasing wires, and connectors are not displayed. (a) circuit 1: ps pulse generator established on mixed SRD topology; (b) circuit 2: a circuit for rise time compression; (c) circuit 3: a circuit for fall time compression.....	50
Figure 3.23 Simulated result of rise and fall time circuitry integrated separately with SRD topology-based generating circuit.....	51
Figure 3.24 Simulated response of two NLTL circuits with opposite polarities integrated with SRD topology-based pulse generating circuit.....	52
Figure 3.25 Simulated vs. measured response of two NLTL circuits with opposite polarities integrated with SRD topology-based pulse generating circuit.....	53
Figure 4.1 Equivalent circuit of NLTL with single varactor diode per cell	62
Figure 4.2 Six section NLTL circuit for rising and fall time compression. (a) Rise time compression circuit; (b) Fall time compression circuit	64
Figure 4.3 Shortest possible rising and falling edge in six section NLTL utilizing single varactor diode per NLTL cell. (a) Rise time compression factor by changing voltage; (b) Fall time compression factor by changing voltage	64
Figure 4.4 Schematic circuit diagrams of NLTL utilizing: (a) Single varactor diode per NLTL cell; (b) Two stacked varactor diodes per NLTL cell; (c) Triple stacked varactor diodes per NLTL cell; (d) N-stacked varactor diodes connected in series per NLTL cell; (e) Generalized equivalent circuit for single and stacked varactor diodes per NLTL cell.....	67
Figure 4.5 Six section N-stacked NLTL (N=1,2,3) circuit for rising and fall time compression. (a) Rise time compression circuit having (N=1,2,3); (b) Fall time compression circuit ..	69
Figure 4.6 Response of corresponding rising and fall time compression circuits in six section stacked varactor diodes per NLTL cell. (a) Rise time compression factor; (b) Fall time compression factor	69
Figure 4.7 Block diagram of the overall scheme for developing pulse generators	70

Figure 4.8 Six section triple stacked NLTL circuit for rising time compression integrated with mixed SRD topology	71
Figure 4.9 Response of the circuit without the integration of triple stacked NLTL	72
Figure 4.10 Response of the circuit at Node A	72
Figure 4.11 Response of the circuit at Node B	72
Figure 4.12 Response of the circuit with the integration of triple stacked NLTL for rise time compression.....	72
Figure 4.13(a) Response of the proposed circuit with and without stacked NLTL along with input voltage. (b) Zoomed-in view output response with and without stacked NLTL	73
Figure 4.14 Block diagram of experimental setup of the proposed fabricated ps pulse generator based on rise time compression and triple stacked NLTL (The corresponding biasing wires are not indicated in the prototype)	74
Figure 4.15 Snapshot of experimental setup during measurement.....	74
Figure 4.16 Response from simulation and measurement of the proposed pulse generator based on rise time compression and triple stacked NLTL	74
Figure 4.17 Six section triple stacked NLTL circuit for fall time compression integrated with mixed SRD topology	75
Figure 4.18 Prototype and measured response. (a) Prototype photo of the circuit for corresponding fall time compression. (b) Response from simulation and measurement of the proposed pulse generator based on fall time compression and triple stacked NLTL	76
Figure 4.19 Computed and circuit simulated FWHM for parasitic and ideal cases	76
Figure 4.20 Power spectrum of the proposed pulse generator-based on fall time compression and triple stacked NLTL	77
Figure 4.21 Reconfigurable behavior between monocycle and gaussian pulse shapes based on six sections triple stacked NLTL circuit for rise time compression integrated with mixed SRD topology	78

Figure 4.22 Output response of the reconfigurable pulse generator based on triple stacked NLTL. (a) Gaussian pulse shape; (b) Monocycle pulse shape	78
Figure 5.1 Classification of NLTLs	85
Figure 5.2 Unit Section of NLMTLs	86
Figure 5.3 Geometry of NLMTLs magnetized in arbitrary angles H_θ and H_ϕ	87
Figure 5.4 NLMTL with six sections. (a) Distributed model of NLMTL configuration; (b) Equivalent circuit model of NLMTL configuration.....	91
Figure 5.5 Dispersion diagram of lumped NLMTL unit cell configuration	93
Figure 5.6 Characteristic impedance vs. frequency of lumped NLMTL unit cell configuration .	93
Figure 5.7 Calculated permeability components at 12 GHz. (a) Complex tensor dispersive permeability components of YIG and NF; (b) Complex tensor dissipative permeability components of YIG and NF	95
Figure 5.8 Output waveform of the implemented six-section NLMTL with $H_0=0.1T$ and data extracted from the theoretical approach (solid blue line), measurement result (dashed red line).....	96
Figure 5.9 Output waveform of the implemented ten-section NLMTL with $H_0=0.1T$ and data extracted from the theoretical approach (solid blue line), measurement result (dashed red line).....	97
Figure 5.10 Output waveform of the implemented ten-section NLMTL with $H_0=0.2T$ and data extracted from the theoretical approach (dotted red line), measurement result (solid blue line).....	97
Figure 5.11 Principle of pulse sharpening behavior in ferrite material. (a) Spin saturation front at $t=0$; (b) Spin saturation front at $t=T_1$; (c) Spin saturation front at $t=T_2$; (d) Spin saturation front at $t=T_R$	99
Figure 5.12 Measured output response of the ten-section NLMTL when $H_0=0.1T$	100
Figure 5.13 Measured output response of the ten-section NLMTL when $H_0=0.2T$	100

Figure 5.14 Measured output response of the ten-section NLMTL when $H_0=0.3T$	101
Figure 5.15 Measured output response of the ten-section NLMTL when $H_0=0.35T$	101
Figure 5.16 Comparison between important metrics of six-section NLMTL.....	102
Figure 5.17 Comparison between important metrics of ten-section NLMTL.....	103
Figure 5.18 Measured output response of the ten-section NLMTL by varying φ with fixed θ . (a) $\theta=0^\circ$ and $\varphi=45^\circ$; (b) $\theta=0^\circ$ and $\varphi=90^\circ$	104
Figure 5.19 Measured output response of the ten-section NLMTL by varying θ with fixed φ . (a) $\theta=45^\circ$ and $\varphi=0^\circ$; (b) $\theta=90^\circ$ and $\varphi=0^\circ$	104
Figure 6.1 Different types of NLTL utilized in literature for pulse generation and compression	110
Figure 6.2 Hybrid NLTL having (a) nonlinear capacitors configuration; (b) nonlinear inductors configuration	112
Figure 6.3 Response from theory and simulation for ten section hybrid NLTL	115
Figure 6.4 RF load resistance analysis. (a) load resistance analysis versus pulse amplitude in hybrid NLTL; (b) load resistance analysis versus FOM in hybrid NLTL	116
Figure 6.5 Gyromagnetic NLTL used for pulse compression	116
Figure 6.6 Transmission line element-based model of ferrite loaded gyromagnetic NLTL to be used for pulse compression	118
Figure 6.7 A typical unit section of a nonlinear gyromagnetic transmission line	118
Figure 6.8 Comparison of pulse width from theory and simulations	120
Figure 6.9 Circuit model of the designed hybrid NLTL.....	121
Figure 6.10 Varying the number of sections (n) of the designed hybrid NLTL and its corresponding effect on output pulse	121
Figure 6.11 Varying load resistance (R_L) of the designed hybrid NLTL and its corresponding effect on output pulse	122

Figure 6.12 Effect of input pulse variation on output response of the designed hybrid NLTL....	123
Figure 6.13 Varying the number of sections (n) of the designed gyromagnetic NLTL and its corresponding effect on output pulse	125
Figure 6.14 Variation of rise time with damping parameter of the gyromagnetic NLTL	125
Figure 6.15 Variation of rise time with an input voltage amplitude of the designed gyromagnetic NLTL.....	126
Figure 6.16 Variation of the rise time with saturation magnetization of the designed gyromagnetic NLTL.....	127
Figure 6.17 Block diagram of the measurement setup along with prototype	128
Figure 6.18 Snapshot of the experimental demonstration.....	128
Figure 6.19 Simulated vs. measured responses of ten section hybrid NLTL.....	128
Figure 6.20 Comparison of output response from theory, simulation, and measurements of ten section hybrid NLTL	128
Figure 7.1 Schematic of reconfigurable picosecond pulse generator.....	134
Figure 7.2 Simulation results of reconfigurable picosecond pulse generator based on NLTL. (a) Gaussian pulse shape without using NLTL in the circuit with PIN diode ON; (b) Gaussian pulse shape along with NLTL in the circuit with PIN diode ON; (c) Monocycle pulse shape with PIN diode OFF; (d) Controlled FWHM using fine-tuning resistor R_c	135
Figure 7.3 Controlled monocycle pulse duration using fine-tuning resistor R_c . (a) Pulse duration=100ps; (b) Pulse duration=90ps; (c) Pulse duration=8ps; (d) Pulse duration=70ps.....	135
Figure 7.4 Power spectrum of generated monocycle and gaussian pulses	137
Figure 7.5 Experimental setup and measured results. (a) Gaussian pulse shape; (b) Monocycle pulse shape; (c) Experimental setup with fabricated pulse generators; the related biasing wires are not shown	137

Figure 8.1	Complete system model for radiative pulse characteristics having all modules	142
Figure 8.2	Ultrashort picosecond pulse generator switching between Gaussian and monocycle pulse shape. (a) Schematic of the pulse generator; (b) Gaussian pulse shape; (c) Monocycle pulse shape; (b) Prototype of the pulse generator	143
Figure 8.3	(a) Prototype of the designed wideband Vivaldi antenna; (b) Simulated vs. measured reflection coefficient response of the designed wideband monopole antenna	145
Figure 8.4	Measured radiation pattern of the designed wideband Vivaldi antenna. (a) 4.5 GHz; (b) 8 GHz; (c) 14 GHz	146
Figure 8.5	Snapshot during radiation pattern measurement. (a) Vivaldi antenna; (b) Slotted patch monopole antenna.....	146
Figure 8.6	Prototype of the designed wideband antipodal Vivaldi antenna	147
Figure 8.7	Simulated vs. measured reflection coefficient response of the designed wide band antipodal vivaldi antenna.....	147
Figure 8.8	Measured radiation pattern of the designed antipodal Vivaldi antenna. (a) 4.5 GHz; (b) 8 GHz; (c) 14 GHz	148
Figure 8.9	Prototype of the designed wideband slotted patch monopole antenna.....	149
Figure 8.10	Simulated vs. measured reflection coefficient response of the designed wideband slotted patch monopole antenna	149
Figure 8.11	Measured radiation pattern of the designed wideband slotted patch monopole antenna. (a) 4.5 GHz; (b) 8 GHz; (c) 14 GHz.....	149
Figure 8.12	Design perspectives of bicone antenna	150
Figure 8.13	Simulated reflection coefficient of the designed bicone antenna.....	150
Figure 8.14	(a) Double ridged horn antenna; (b) S11 vs. frequency plot	151
Figure 8.15	Various fundamental pulse shapes. (a) Gaussian pulse shape (zeroth order); (b) monocycle pulse shape (Order 1); (c) Doublet pulse shape (Order 2).....	152
Figure 8.16	Block diagram of the overall system with all modules integrated	153

Figure 8.17 Received pulse at the output for the case where both Tx and Rx antennas are Vivaldi structure	154
Figure 8.18 Received pulse at the output for the case where both Tx and Rx antennas are antipodal Vivaldi structure	154
Figure 8.19 Received pulse at the output for the case where both Tx and Rx antennas are slotted patch structure	155
Figure 8.20 Received pulse at the output for the case where both Tx and Rx antennas are double ridged structure.....	155
Figure 8.21 Received pulse at the output for the case where Tx antenna is antipodal Vivaldi and Rx antenna is bicone.....	156
Figure 8.22 Complete measurement setup block diagram	158
Figure 8.23 Measured received pulse at the output for the case where both Tx and Rx antennas are Vivaldi structure	158
Figure 8.24 Measured received pulse at the output for the case where both Tx and Rx antennas are antipodal Vivaldi structure	159
Figure 8.25 Measured received pulse at the output for the case where both Tx and Rx antennas are slotted patch structure.....	160
Figure 8.26 Measured received pulse distortion at various angles between the Tx and Rx antennas for the case where both Tx and Rx antennas are a slotted patch structure.....	160

LIST OF SYMBOLS AND ABBREVIATIONS

AC	Alternating Current
ADS	Advanced Design System
AVV	Antipodal Vivaldi Antenna
AWG	Arbitrary Waveform Generator
BC	Biconical Antenna
BJT	Bipolar Junction Transistor
BST	Barium Strontium Titanate
DC	Direct Current
FET	Field Effect Transistor
FMR	Ferro-Magnetic Resonance
FOM	Figure Of Merit
FWHM	Full Width Half Maximum
GPR	Ground Penetrating Radar
IR-UWB	Impulse Radar Ultra-Wide Band
KDV	Korteweg-de-Vries
LL	Landau and Lifshitz
LLG	Landau and Lifshitz and Gilbert
MCLT	Minority Carrier Lifetime
MEMS	Micro-Electro-Mechanical-Systems
NF	Nickel Ferrite
NLCTL	Non-Linear Capacitive Transmission Line
NLDTL	Non-Linear Dielectric Transmission Line
NLETL	Non-Linear Electrical Transmission Line

NLGTL	Non-Linear Gyromagnetic Transmission Line
NLHTL	Non-Linear Hybrid Transmission Line
NLITL	Non-Linear Inductive Transmission Line
NLMTL	Non-Linear Magnetic Transmission Line
NLTL	Non-Linear Transmission Line
PG	Pulse Generator
PS	Picosecond
PSPL	Pico-Second Pulse Lab
RF	Radiofrequency
RTD	Resonant Tunneling Diode
SFF	System Fidelity Factor
SRD	Step Recovery Diode
SR	Stretch Ratio
TDR	Time Domain Reflectometry
TT	Transition Time
UWB	Ultra-Wide Band
VV	Vivaldi Antenna
YIG	Yttrium Iron Garnet

LIST OF APPENDICES

Appendix A LIST OF PUBLICATIONS & AWARDS187

CHAPTER 1 INTRODUCTION

1.1 Motivation and objectives

With the advent of microfabrication techniques and microsystem developments, the timescale of electronic devices and measurement systems are continuously shrinking for fast response and ultra broadband, which need an ultrashort pulse generator such that they meet a required range or other parametric measurement resolution in different applications such as target detection, vital signs monitoring, and radar communication applications. Interestingly, the chronological progress of pulsed-based time resolution or time response for electronics and instrumentations, for example, can be well reflected through the following observation. The early development of the 1950s were focused on 100ns intervals of time for electronic instrumentation, which was significantly improved to 10ns then in the 1960s. By the 1970s-1990s, it had progressed to temporal scales of 1ns. In the early 2000s, special efforts from different researchers and groups worldwide were directed towards the picosecond arena. This continued progress has been enabled by much improved high-speed electronics through the development of advanced diodes and transistors like Schottky diodes, step-recovery diodes, avalanche transistors, and resonant tunneling diodes in the picosecond domain. Of course, this advancement has been pushed forward by the development of high-speed interconnects and short electronic pulse systems. In any case, the fast electronics is currently being lagged far away behind the fast photonics in terms of time scale, which is now running in the attoseconds. This difference was even highlighted by the recent Nobel Prize Winning topic where a short pulse is first positively chirped (dispersed) in time, while passing through the diffraction gratings. It is amplified by as much as 11 orders of magnitude and then recompressed by passing through the other set of diffraction gratings, but negatively dispersive pair of gratings this time. The recompressed output pulse has now an energy of million times higher than the original counterpart with a pulse duration of 2ps [1, 2].

Also, UWB systems make use of short-range electromagnetic pulses for medical imaging, sensing, communication, military, and industrial applications. For example, a better range resolution is needed for high-accuracy sensing applications, which necessitates a short pulse-width [3]. The two most utilized pulses for radar applications including ground penetrating radar (GPR) and impulse-radar UWB are chirps and Gaussian pulses. Due to their simplicity and low cost for production,

Gaussian pulses have a wide range of applications, particularly in short ranges. Although it is simple to create Gaussian pulses, however, it is very challenging to achieve pulses that have a pulse duration in the picosecond range.

In this connection, researchers have paid much attention to the development of ultrafast pulse generators that are capable of creating attractive such features as shorter pulse duration, full width half maximum (FWHM), reduced ringing level, higher amplitude, and clean pulse shape [4]. In particular, different pulse generation techniques have been reported so far in the literature to tackle the challenge of shorter pulse duration along with reduced ringing capability [5-6]. It is very common in the literature to talk about Gaussian pulse generators. However, it is very well known that antenna neither transmits nor radiates the dc contents that are present in Gaussian pulses [7]. Hence, it is also very important to develop pulse generators that have the capability to generate higher order Gaussian pulse shapes including monocycle, doublet, and other Gaussian higher derivatives. As such, for a wireless pulse transmission, the monocycle pulse shape is the best choice as its spectrum have no dc contents [8]. In this case, the pulse generators developed so far may usually be classified into two different categories: (1) pulse generators having single pulse shape [9]; (2) pulse generators capable of transforming to multiple pulse shapes [10].

A non-linear transmission line (NLTL) is an important candidate for the generation and compression of ultrafast pulses. NLTL is a type of transmission line that comprises of lumped elements such as inductors and varactors which are periodically loaded into the host transmission line and can have the capability to generate solitons and shockwaves. Solitons are a unique class of pulse-shaped waves that propagate without changing their shape in nonlinear dispersive media. It is due to a balancing mechanism between nonlinearity and dispersion effects that ultimately generate a Gaussian pulse shape. In microwave electronics, NLTL works as a nonlinear dispersive medium that is responsible for the propagation of voltage solitons.

There is a huge number of applications of ultrashort pulses in everyday life that came across us everywhere. Among them, some of the well-known are UWB radars for human respiration through a wall, wireless vital signs monitoring, breast tumors detection, THz detection, medical imaging, heart beat monitoring, and GPR applications. All these applications need clean and ultrashort pulses having reduced levels of ringing, different pulse shapes for various applications, simultaneous rise and fall time compression, and reduced full width half maximum (FWHM). This

this research strives to bridge the gap in the utilization of ultrashort pulses in the microwave electronics by transforming the concept of solitons and shock waves to the electrical domain. This will be executed by providing innovative NLTL techniques along with introducing new classes of NLTL. The main contribution of this thesis can be summarized as:

- (a) **Pulse generation.** Various techniques are provided for pulse generation and exploring new NLTL topologies and pulse generation in the magnetic domain.
- (b) **Pulse compression.** The generated pulses are compressed by providing new innovative ideas based on NLTLs.
- (c) **Pulse shaping.** The transformation of Gaussian pulse shapes into other important pulse shapes are studied from application perspectives.
- (d) **Pulse transmission.** The radiated pulse characteristics are explored while transmitting various pulse shapes wirelessly via a practical antenna setup.

1.2 Outline and contributions of this thesis

This thesis is organized in the article-based format, containing six original journal papers:

Chapter 1: Introduction

This chapter presents a brief introduction and motivation of pulse generation, compression, shaping, and transmission. The development of electronically ultrashort pulse generators with reduced ringing is the primary goal of this Ph.D. thesis.

Chapter 2: Literature review

This chapter presents the historical overview of pulse generation, compression, and shaping techniques based on microwave electronics presented in the literature as well as available in the market. A detailed survey of the state-of-the-arts electronic pulse generation and compression schemes with focus on important pulse parameters including pulse duration, FWHM, ringing level, and pulse amplitude will be conducted. Electronically developed pulse generators having the

capability to adopt multiple pulse shapes will also be discussed in detail and their advantages and disadvantages will be highlighted. This chapter will give a clear picture of the previous research in the field and the research gaps present in the literature.

Chapter 3: Article 1: A nonlinear transmission approach to compressing rise and fall time in picosecond pulse generation

This chapter presents the generation and compression scheme of picosecond (ps) pulses based on both step recovery diode (SRD) topology and nonlinear transmission line (NLTL) scheme with a focus on simultaneous rise and fall time compression. Four different pulse generators are developed in which the first three are based on rise time compression and the fourth one is based on simultaneous rise and fall time compression. All these pulse generators are compared with the state of the arts in the literature where they utilize different techniques for sharpening and the superiority of the proposed designs are highlighted.

Chapter 4: Article 2: A Nonlinear Transmission Line Technique for Generating Efficient and Low-Ringing Picosecond Pulses for Ultrabroadband and Ultrafast Systems

This chapter presents an NLTL-based scheme to develop an efficient and low-ringing picosecond pulse generator for ultrabroadband and ultrafast system applications. The proposed NLTL scheme stems from a unique combination of a single varactor diode and stacked varactor diode per NLTL cell, which is designed to exploit a significant effect of nonlinearity in connection with the varactor diode. This technique generates a higher compression factor in both rise and fall time of NLTL circuits in comparison to single varactor diodes per NLTL section. Two pulse generators are then developed based on the proposed concept, where a mixed step recovery diode (SRD) topology is used for Gaussian pulse generation and integrated with a triple-stacked NLTL. Theoretical development and simulation of two triple-stacked NLTLs based on the rise and fall time-compression are provided, and final experimental prototypes for pulse generators are fabricated and measured. Finally, the reconfigurable capability of the pulse generators is also briefly explored, and it is shown that the proposed pulse generators can easily be reconfigured between Gaussian and monocycle pulse shapes.

Chapter 5: Article 3: Theoretical and experimental analysis of pulse compression capability in non-linear magnetic transmission line

This chapter presents a theoretical and experimental analysis of nonlinear magnetic transmission lines and demonstrates the phenomenon and capability of simultaneous rise and fall time compression. A theoretical approach is formulated in which a new version of the modified Korteweg-de Vries equation is developed utilizing the Gardner–Morikawa transformation, continuum limit approximation, Toda-lattice approximation, and Mei theory of Maxwellian circuits. The proposed theoretical foundation work is validated through experimental demonstration. The pulse compression capabilities of NLMTLs are also discussed in detail and the design strategy for magnetic pulse generators are carried out. Finally, the localized disturbance within ferrimagnetic materials is also studied, and its impact on the output waveforms is also discussed. This study can potentially open up a new and fruitful entry to explore magnetic materials and their impacts in the field of ultrafast electronics.

Chapter 6: Article 4: Theory and practice of pulse compression capabilities in hybrid and gyromagnetic NLTLs

This chapter provides a comprehensive analysis of pulse compression capability in hybrid and gyromagnetic NLTLs. Theoretical analysis in the hybrid and gyromagnetic NLTLs are derived and discussed in detail with the generation and sharpening aspects of leading and trailing pulse edges. The parameters responsible for pulse sharpening are examined and their corresponding pulse compression capability is modeled by providing the output waveform while varying these parameters. A holistic overview and mathematical development of hybrid and gyromagnetic NLTLs are also conducted, which are modeled and validated through an equivalent lumped element model. Important parameters such as saturation magnetization, gyromagnetic NLTL sections, and damping parameters are elaborated and their influences on pulse sharpening and compression capability are studied. Finally, the results achieved from hybrid and gyromagnetic NLTLs are briefly summarized, and their corresponding advantages and disadvantages are highlighted.

Chapter 7: Article 5: A Reconfigurable Picosecond Pulse Generator in Non-linear Transmission Line for Impulse Radar Ultrawideband Applications

This chapter proposes a reconfigurable picosecond (ps) pulse generator (PG) having Gaussian and monocycle pulse shapes for impulse radar ultrawideband (IR-UWB) applications. A mixed step recovery diode (SRD) topology is used in combination with NLTL and pulse-shaping circuit to realize the PG. The pulse-shaping network comprises an RC differentiator embedded with a single PIN diode to provide two different switchable states. This PG is capable of directly switching from a Gaussian to a monocycle pulse without resorting to the increase in pulse width twice of the original Gaussian pulse as deployed in the previous reconfigurable PGs.

Chapter 8: Picosecond Pulse Generation, Shaping, Transmission, and Reception Characteristics for Wireless Sensing Applications

This chapter proposes the transmission and reception of picosecond pulses by estimating antenna effects while considering the order of the pulse, ringing distortion, system fidelity factor, stretch ratio, and duration of the pulse. A systematic analysis is performed in such a way that first a Gaussian pulse is developed, which is adequately transformed to its derivative for wireless transmission. For transmission and reception, some wideband antennas of interest are explored and developed including Vivaldi, antipodal Vivaldi, slotted patch, bicone, and ridged horn antennas. An experimental demonstration is performed, and a complete system model is provided while presenting radiated pulse characteristics in different scenarios.

Chapter 9: General Discussion

This chapter will provide a general discussion of the proposed research outcomes in this thesis work.

Chapter 10: Conclusion and recommendations

This chapter summarizes the entire thesis research and highlights key research contributions in a compact manner. Additionally, some potential future extensions of this research work are described as part of this research endeavour.

CHAPTER 2 LITERATURE REVIEW

Picosecond pulses are required in many ultrabroadband and ultrafast applications, such as time-domain reflectometry, sampling oscilloscopes, frequency synthesizer, indoor geolocation, and ultra-wideband (UWB) communication applications. UWB technology has been a choice of preference for impulse radar developments in medical, industrial, and military domains [4]. For all these applications, the generation of clean ultra-short ps pulses is highly desirable along with higher rise or fall time-compression capability and proper pulse repetition factor (PRF). So, it is rather challenging to achieve a very efficient short pulse with a flexible compression capability along with an acceptable ringing behavior.

One of the most crucial parts of every wideband and ultrafast system is the pulse generator. The Gaussian, monocycle, doublet, and polycycle pulses are the most often realised pulses and each has its own benefits. However, due to their wide spectrum capabilities and more straightforward architecture realisation and design, the monocycle and gaussian forms are the most widely used shapes. Researchers have paid enough attention in this regard, to design ultrashort pulse generators that have the capability of shorter pulse duration and full width half maximum (FWHM), reduced ringing level, higher amplitude, and clean pulse shape [4]. The historical overview of the pulse generators developed commercially is shown in Figure 2.1.

This chapter will provide a detailed survey of the state of arts electronic pulse generation, compression, and shaping schemes with a focus on important pulse parameters including pulse duration, FWHM, ringing level, and pulse amplitude. Pulse generators having the capability to adopt multiple pulse shapes will also be discussed in detail and their advantages and disadvantages will be highlighted. The definition of ultrashort and ultrabroad-band pulse will also be provided. Finally, the application of the pulse generators in practical applications will also be discussed briefly. This chapter will give a clear picture of the previous research of pulse generators and its utilization in ultrafast systems and interconnects. First, the important pulse parameters will be discussed in detail that will be used in the overall thesis.

2.1 Definition of important pulse parameters

This section discusses some useful and important pulse parameter metrics including pulse duration, FWHM, ringing level, and stretch ratio that will be used throughout the thesis.

2.1.1 Pulse duration or pulse width

The time interval between a reference point on the leading edge of a pulse waveform and a reference point on the trailing edge of the same waveform. The two reference points are usually 95% of the steady-state amplitude of the waveform existing after the leading edge, measured with respect to the steady-state amplitude existing before the leading edge.

2.1.2 Full width half maximum (FWHM)

FWHM refers to the width of a pulse or spectrum curve measured between those points on the y-axis that are half the maximum amplitude. FWHM is a common form of measurement for pulse waveforms, and the spectral width of sources used for optical communications and pulse engineering in microwave electronics.

2.1.3 Ringing level

Ringing is the undesired ripples found along with the radiated signals. The detailed ringing level of the output pulse (R_l) can be given by the following equation.

$$R_l = 20 \log \frac{\text{Ringing amplitude}_{\text{peak-to-peak}}}{\text{Pulse amplitude}_{\text{peak-to-peak}}} \quad (2.1)$$

It is also termed as a detailed ringing level and one of the important metrics to judge the quality of the waveform. If the ringing level is lower than -10 dB, it can be easily retrieved on the receiver side, and we say that ringing is within an acceptable limit.

2.1.4 Stretch ratio

The temporal width of the transmitted pulses can be a significant factor in the design of a UWB transceiver. For signal $x(t)$, the normalized cumulative energy function of the signal is given as:

$$E_s(t) = \frac{\int_{-\infty}^t |x(t')|^2 dt'}{\int_{-\infty}^{\infty} |x(t')|^2 dt'} \quad (2.2)$$

The corresponding pulse width for 95% of the captured energy is utilized to calculate the stretch ratio by removing 5% of the energy on either side of the pulse. If $h(t)$ is the radiated electric field waveform and $G(t)$ is the input source, then the pulse stretch ratio (SR) can be defined as:

$$SR = \frac{E_h^{-1}(0.95) - E_h^{-1}(0.05)}{E_G^{-1}(0.95) - E_G^{-1}(0.05)} \quad (2.3)$$

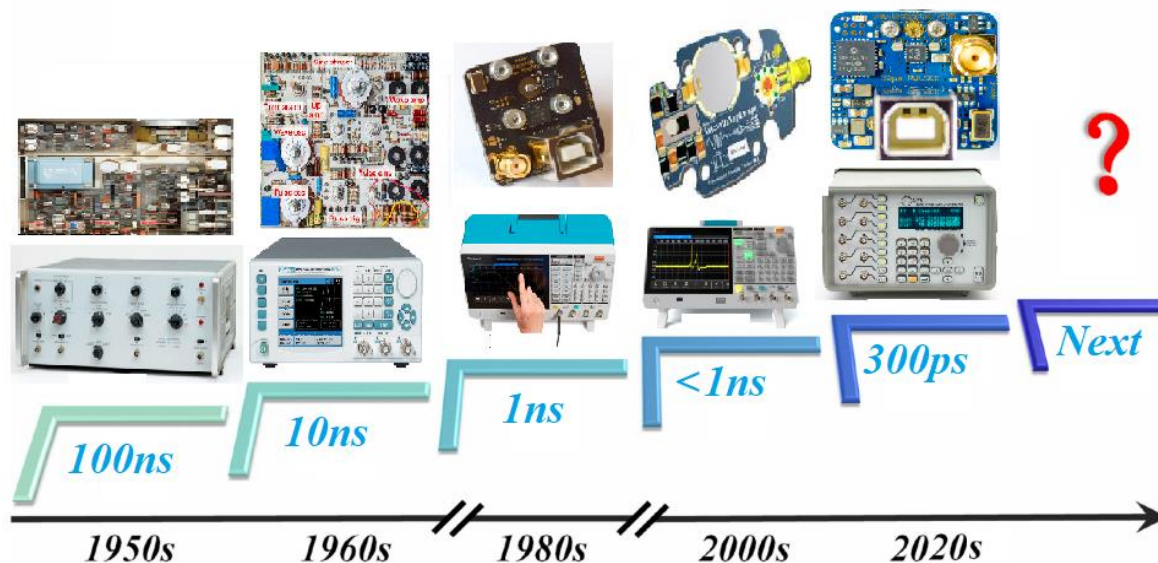


Figure 2.1 Generational evolution of commercially developed pulse generators by different industrial organizations including Hewlett Packard, Colby, Tektronix, Tau Tron, BNC, Ana-Pico, etc

2.2 Ultrafast ultra-broadband pulse definition

This thesis is completely based on observing the pulse in the time domain. However, it is also important to define the pulse in the frequency domain. This would show that how the pulse counterpart looks like in a different domain. In frequency domain, by the uncertainty Principle, a 1-ps pulse has bandwidth of 1/2 THz. As shown in Figure 2.2 (a), such a time domain signal can be transformed to the frequency domain by using the fast Fourier transform (FFT) technique. It can be converted back to the time domain by using an inverse fast Fourier transform (IFFT). To better understand this concept, we provide an example in both time and frequency domain as shown in

Figure 2.2 (b) and (c), respectively. It can be seen that a pulse having a pulse duration or width of almost 7 ps corresponds to 300 GHz in the frequency domain.

In the time domain, the higher-order derivatives of the Gaussian pulse are similar to the sinusoids modulated by a Gaussian pulse-shaped envelope. As the order of the derivative increases, the number of zero crossings in time also increases; more zero crossings in the same pulse width correspond to a higher “carrier” frequency sinusoid modulated by an equivalent Gaussian envelope. It means that taking the derivative will increase the center frequency of the pulse. These observations suggest considering higher-order derivatives of the Gaussian pulse as candidates for wideband pulse transmission and reception. It must also be noted that changing the pulse shape having the same pulse duration will not affect the bandwidth as explained from the analysis.

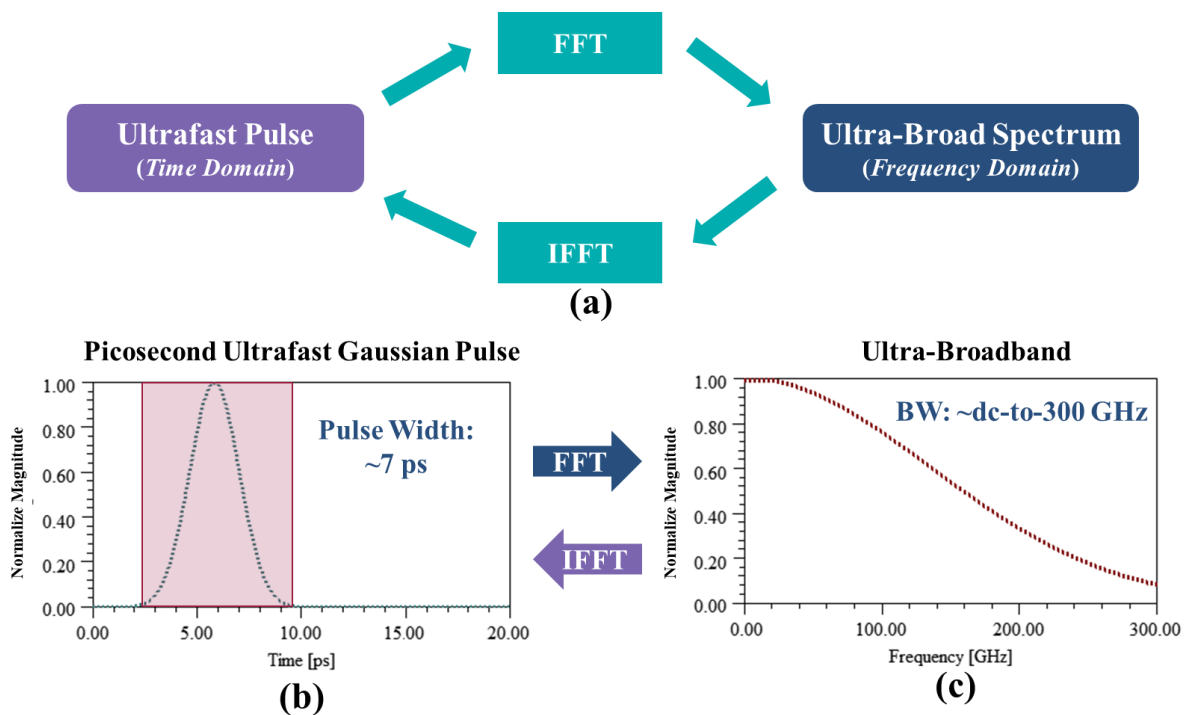


Figure 2.2 Transformation between time and frequency domain. (a) Conversion using FFT and IFFT. (b) Normalized pulse having pulse duration of almost 7 ps. (c) 7 ps normalized pulse in frequency domain

2.3 Various pulse generation, compression, and shaping techniques

Various techniques have been presented in the literature for the development of ultrashort pulse generation schemes. We will discuss each of them step by step with their corresponding design circuits along with the presented pulse parameters and targeted applications. A useful and efficient way for the comparison is provided after the discussion highlighting important pulse parameter metrics including pulse duration, FWHM, ringing level, and pulse amplitude.

2.3.1 Pulse generators using resonant tunneling diodes (RTDs)

The design procedure of a pulse generator using RTD was discussed in [11-12]. The circuit topology of [11] is shown in Figure 2.3 (a) which comprises of a source and high-speed RTD. This RTD is shunted to the ground across a 50-ohm matched transmission line. This technique is able to develop rise edge transients in the picosecond regime with a 15ps rise edge transient. However, this combination is not able to provide a complete Gaussian pulse or the derivative of a Gaussian pulse. This is due to the reason that single RTD can only be used for switching applications and for complete gaussian pulse generation we need a combination of RTD's.

Following the work of [11], an attempt was made to develop a sub-nanosecond pulse generator using RTD [12]. Here the authors utilized a pair of RTDs in cascade along with a PIN diode combination to develop a pulse generator having a pulse duration of 200-300ps with a pulse amplitude of 0.3-0.9V. The circuit diagram of this kind of pulse generator is summarized in Figure 2.3 (b).

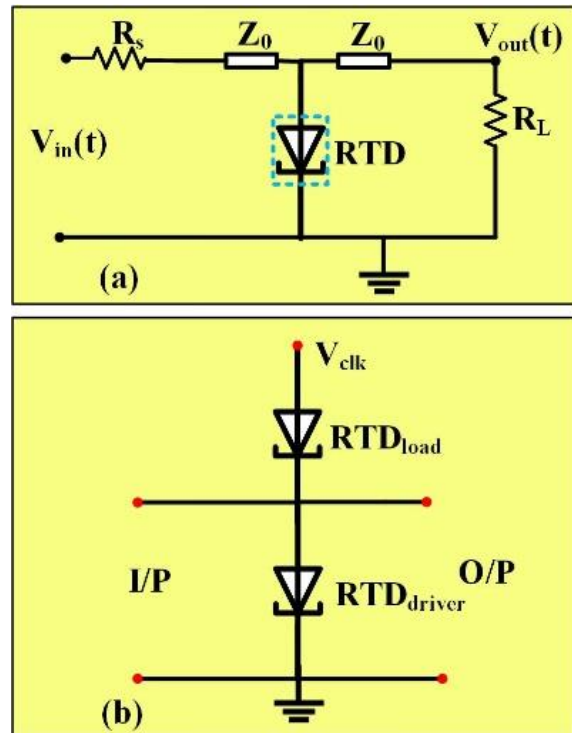


Figure 2.3 Pulse generators based on RTD. (a) Rise edge transients pulse generator using high-speed RTD presented in [11]. (b) Pulse generator using a combination of high-speed RTD presented in [12]

2.3.2 Pulse generators using schottky diode

Various techniques have been presented in the literature to develop gaussian pulse and transform it to corresponding monocycle pulse generators using a combination of schottky diodes. One state-of-the-art technique presented in [13] is illustrated in Figure 2.4, where a schottky diode is utilized with lumped elements and transmission lines to generate a gaussian and monocycle pulse generator. This pulse generator is based on rise time compression having a pulse duration of 1 ns, the amplitude of the pulse is between 1.8-1.85 V, and the detailed ringing level is -17.15 dB. The impedance matching is improved by placing an attenuator between an oscillator source and pulse generator that ultimately contributes to improve the ringing level. The working principle is that the reflection signal propagates back from the pulse generator to the stimulus source node and then returns. The amplitude of the pulse generator is attenuated at least twice while the incident stimulus

signal is attenuated once by the attenuator. A configuration like this provides a simple yet effective solution for improving circuit impedance matching and reducing signal reflections.

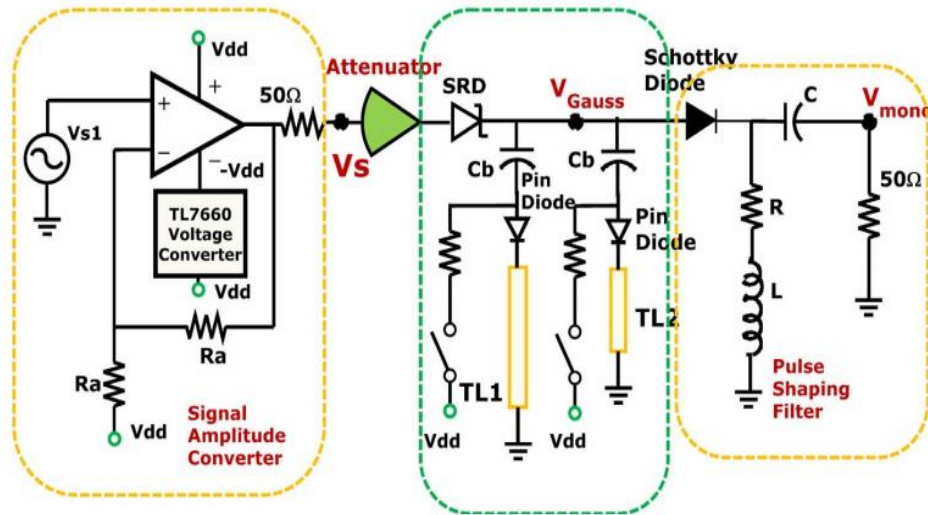


Figure 2.4 Gaussian and monocycle pulse generator using Schottky diodes presented in [13]

2.3.3 Pulse generators using step recovery diode (SRD)

SRD pulse generation is one of the well-known and useful methods. However, the main issue that arises due to the utilization of SRD is controlling ringing behavior which becomes challenging. SRD is used to create gaussian and monocycle pulses and one such method is described in [14] by the authors, who used a single SRD in a shunt to create a gaussian pulse. Similarly, a single SRD for pulse generation is reported in [15] while utilizing it in series. Figure 2.5 (a) and Figure 2.5 (b) show the single SRD arrangement for pulse generation in shunt and series, respectively.

Similarly, a single SRD was used in [16] for compressing a gaussian pulse, where a pulse duration of 150 ps was achieved with a reduced ringing level of -23.55 dB. The detailed circuit configuration of this work is shown in Figure 2.6.

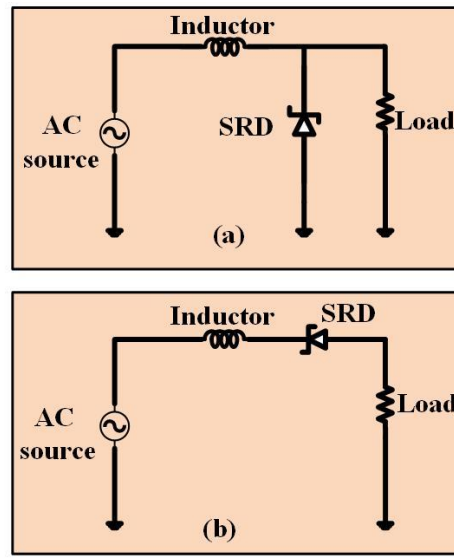


Figure 2.5 Gaussian pulse generator using single SRD. (a) Shunt arrangement of SRD. (b) Series arrangement of SRD

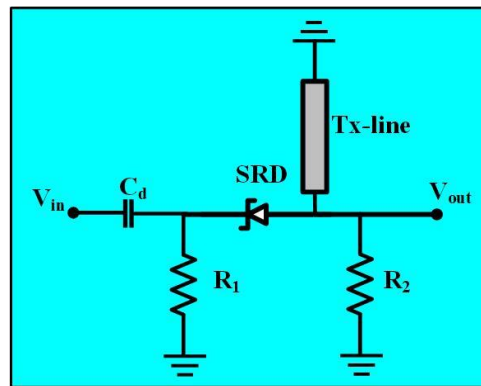


Figure 2.6 Gaussian pulse generator using SRD in series with wave-shaping circuit [16]

2.3.4 Pulse generators using various SRDs topologies

The performance of picosecond pulse generators is improved using a variety of SRD topologies, including compression factor and ringing reduction. In [17], the authors presented a picosecond pulse generator based on SRD topology as shown in Figure 2.7 (a) that has the capability to operate within the UWB spectrum in the frequency domain in connection with a pulse duration of 300 ps-1 ns in the time domain. The corresponding output response of the presented pulse generator is shown in Figure 2.7 (b).

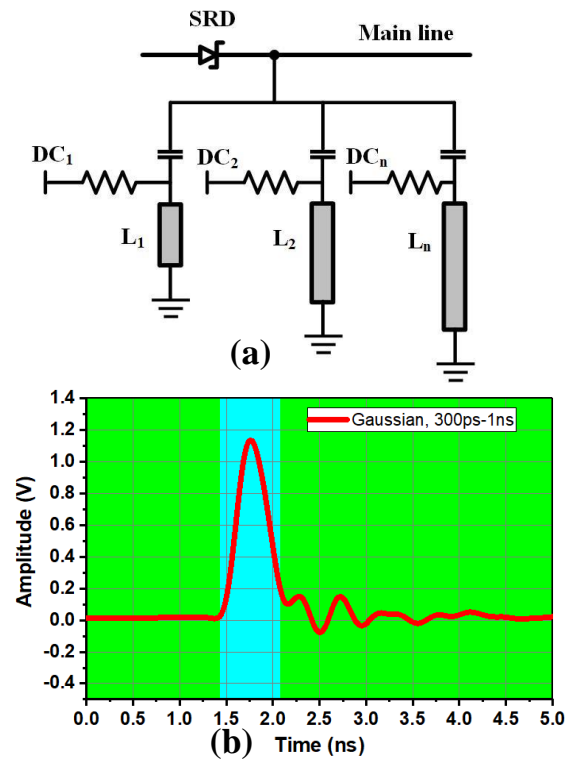


Figure 2.7 (a) Gaussian pulse generator using SRD topology presented in [17]; (b) Response of circuit topology from simulation

2.3.5 Pulse generators using field effect transistors (FETs)

A fully MESFET-based picosecond pulse transient techniques was investigated in [18] as shown in Figure 2.8. This circuit is made of main FET sampling gate, FET base pulse generator, FET-based test step generator, and a step sharpener. The connection of these blocks is shown in detail using Figure 2.8. This topology can achieve rise or fall edge transients that are almost 28 ps in the time domain whose corresponding frequency domain is equivalent to 12 GHz. This topology is specifically designed for high-speed electronics, and picosecond instrumentation.

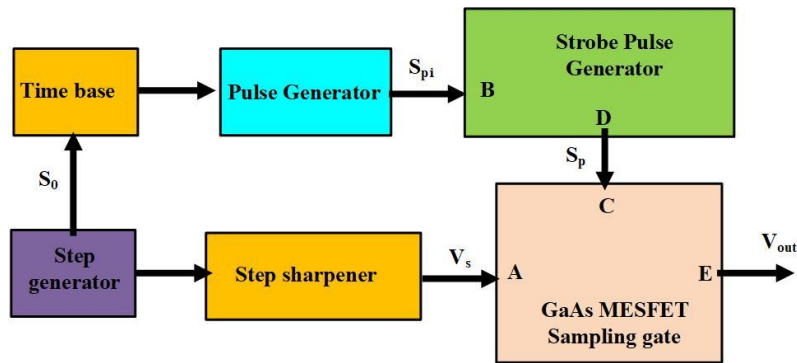


Figure 2.8 Block diagram of MESFET-based PG presented in [19]

2.3.6 Pulse generators using avalanche transistors

Avalanche transistors are widely used for generating picosecond transients due to their widespread application and having promising characteristics including tiny size, low intrinsic inductance, low jitter, high frequency, and high switching speed operation. Various topologies of avalanche transistors have been utilized in the published work to achieve sub-nanosecond transients or gaussian pulse generation. The most well known case in this regard is the utilization of the N-MARX parallel circuit presented in [19-21]. MARX-based connection of avalanche transistors have good performance, however, they suffer severely from ringing, which distorts the complete pulse shape. Also, it is noteworthy that due to the poor heat dissipation and slow charging speed of the avalanche transistors, it is very difficult to operate at a high frequency.

Following this work, authors in [22] developed a UWB pulse generator based on the avalanche effect of the avalanche transistor as shown in Figure 2.9. Their circuit is capable of generating a negative going gaussian pulse with a pulse amplitude of -11.2V having a pulse duration of almost 890ps from simulations. Also, a pulse generator is presented in [23] that can change the width continuously and also based on avalanche transistors as demonstrated in Figure 2.10.

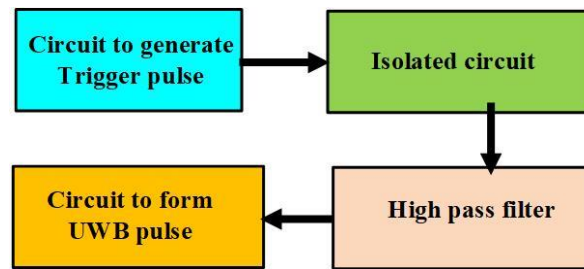


Figure 2.9 Block diagram of pulse generation technique presented in [22]

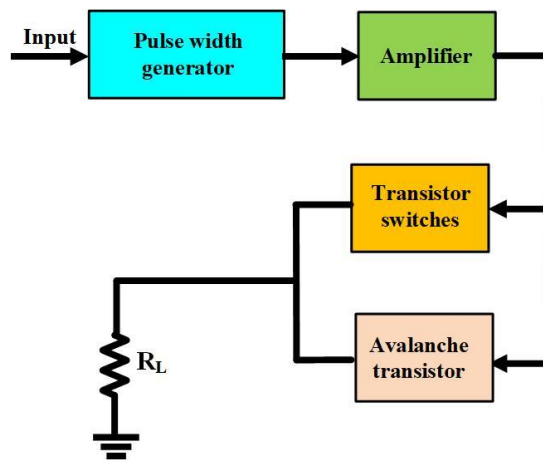


Figure 2.10 Block diagram of pulse generation scheme presented in [23]

2.3.7 Pulse generators using NLTL

NLTL is also considered as one of the prominent candidates for sub-nanosecond and picosecond pulse generation. They are further utilized in LSI chips and high-speed non-linear systems. If the inductor and capacitor in NLTL are a decreasing function of corresponding currents and voltages, the velocity of the wave traveling in NLTL will increase with their amplitude. This is an interesting property of NLTL where higher portion of the waveform moves quicker than the lower portion. This phenomenon of NLTL is applied in order to achieve pulse compression, harmonic generators, picosecond pulse generators, and picosecond shock wave generation [24-35]. It is very difficult to analyze the NLTL function and majority of them claim it from related physical point of view.

The harmonic balance technique is recognized to be a powerful technique for the solution of circuits including non-linear elements under a condition that the waveform does not include higher

harmonics. All the above techniques are valid for achieving pulse generators within sub-nanosecond regime along with dramatic ringing. Also, majority of the above techniques have discussed only gaussian pulse shape which is due to the case that NLTLs are capable of soliton generation. For compression we need NLTL shock wave solution in order to compress the rise and fall edge transients as much as possible.

2.3.8 Pulse generators using gyromagnetic non-linear transmission lines (G-NLTLs)

There also exists another class of magnetic NLTL termed as gyromagnetic NLTL that has been studied in [36] and can generate RF with high power. Here, magnetic elements are used to create the medium that separates the line conductor. Due to the magnetic moment created by damped gyromagnetic precession in ferromagnetic materials, this form of NLTL is employed as a small, solid-state RF source [37,38]. The amplitude and rising time of the output generated pulse are controlled by the applied in-pulse and externally applied bias magnetic field. The resulting rise time decrease is limited by the ferrite's switching properties, which are essentially the time needed to go from one state to another on the material B-H curve. [39]. The construction of G-NLTL for pulse compression capability is shown in Figure 2.11 while the corresponding transmission line element-based model of ten sections of G-NLTL is shown in Figure 2.12.

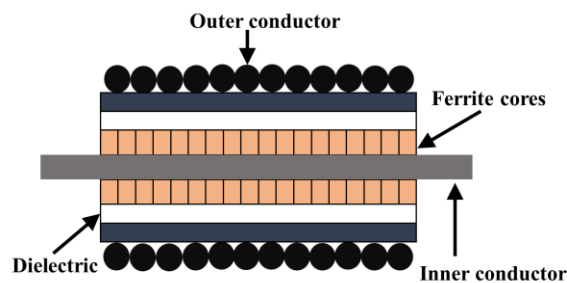


Figure 2.11 Gyromagnetic NLTL used for pulse compression

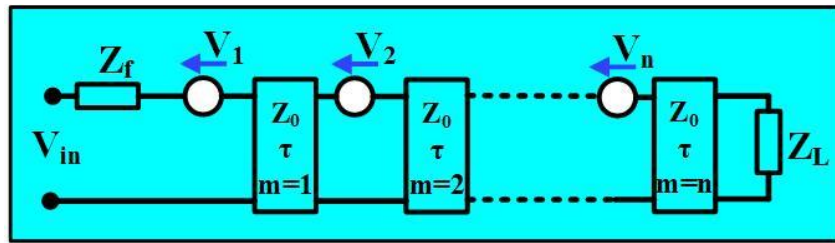


Figure 2.12 Transmission line element-based model of a ferrite loaded gyromagnetic NLTL to be used for pulse compression

2.3.9 Pulse generators using dielectric non-linear transmission lines (D-NLTLs)

A parallel plate design for an NLTL was created, as seen in Figure 2.13, which uses the periodic loading of the dielectric slab as a nonlinear medium and investigated in [40-41]. The output response of D-NLTL in [40] is shown in Figure 2.14. As can be seen from the output response that this type of structure is not a good candidate for pulse generation and compression. Because of dielectric losses, this type of NLTL suffers greatly from RF oscillations in the output waveforms, and due to it, researchers have not given any attention to such structures.

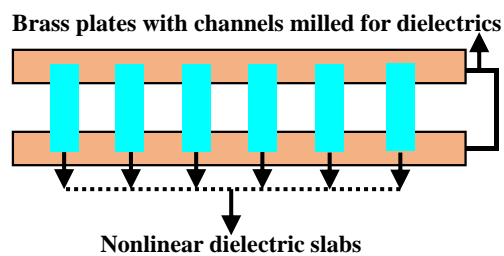


Figure 2.13 D-NLTL used for pulse generation

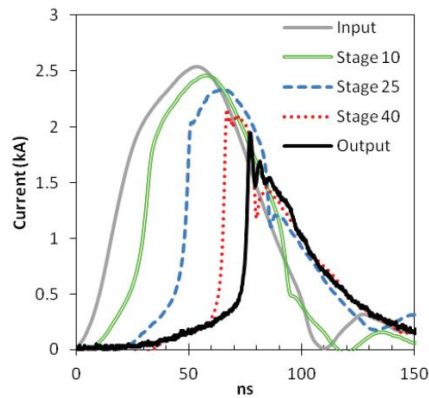


Figure 2.14 Output response from D-NLTL used for pulse generation [40]

2.3.10 Pulse generators using delay lines

Some researchers have also utilized delay lines for generating sub-nanosecond pulses. In [42], the authors used a microstrip delay line as shown in Figure 2.15 that can convert a step signal with 25 ps rise time to a regular pulse ranging from 50 ns to 500 ns. This technique was advantageous as previously enough work was done on rise and fall edge transients but there was no good technique to convert them into a regular pulse. This was the first attempt for conversion but as can be seen that pulse duration is highly increased while converting from edge transients to the regular pulse shape. Similarly, a tunable monocycle pulse generator was developed in [43] using a delay line that has the capability of generating a monocycle pulse shape having a pulse duration ranging from 400-850 ps with an output peak amplitude of 200-500 mV. Since this method was not further used by researchers due to the main reason in that this technique has very limited capability of pulse compression.

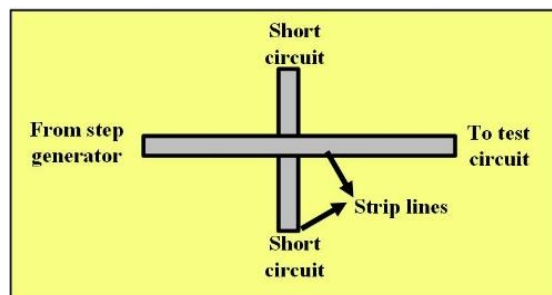


Figure 2.15 Rectangular pulse generator by transforming rise edge transients presented in [42]

2.3.11 Pulse generators using micro-miniature mercury switches

For many years, mechanical switch relays with mercury have been utilized to create sub-nanosecond pulses. It is simple to obtain pulses up to 1 kV with a rise time of 12 ns using ordinary relays. A typical setup entails either a capacitor bank that is connected to the output load using a relay-operated switch or a charged transmission line, as shown in Figure 2.16. The ‘Log Cell’ produced by the 5th Dimension, is the smallest and fastest mercury switch currently in use. In [44], the authors reported utilizing a Log-Cell to produce a 2V pulse with a 12 ps rise time. A 50V, 40 ps rise time pulse employing the Log Cell [45-46] has been created by NBS. Similar results have been attained by employees at EG&G and Los Alamos Scientific Labs. A typical rise time for traditional mercury-switch pulses is 1/2 ns.

The mercury-switch pulser provides a number of benefits. It is simple to construct, and the output waveform is predictably shaped. The amount of charge line cable utilized determines how long it will last. By adjusting the supply voltage, the amplitude is adjustable. For these good reasons, it has been used as a pulse-amplitude calibration source for many years. It has also been utilized as a spectrum amplitude calibration source for measurements of electromagnetic interference (EMI).

There are several drawbacks to the mercury switch as well. It will only function at low repetition rates, typically up to 100 Hz, though some switches have been driven at a mechanical resonant frequency to function at a few kHz. The mercury switch cannot be accurately activated by an external electrical trigger because it is a mechanical device. Moreover, the output pulse amplitude occasionally displays amplitude instabilities of 1 to 2 percent due to statistical changes in the contact surface at the instant of closure. Mercury switches also have a short lifespan and lose quality with time.

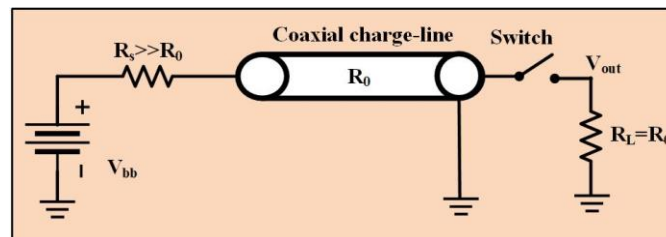


Figure 2.16 Circuit diagram of the mercury switch-based pulse generator

2.3.12 Pulse generators using vacuum tube

Vacuum tubes are employed in the development of pulse generators, mainly for high-voltage, high-current, and high-average power applications where suitable semiconductors are not readily available. Power levels between kilowatts and megawatts are often transmitted using high-power transmitting tubes. The rise time at these power levels ranges from tens of nanoseconds to microseconds. Some of the commercially available pulsers in this category are included in Table 2.1. The majority of these manufacturers also create transformers to offer outputs with either higher voltage or higher current.

The alpha model from power Spectra Inc. pulse generator offers remarkable performance specifications [60]. This generator has a figure of merit of 3.3 kV/nsec with an output of 5 kV into 50 ohms and a rise time of 1.5 ns. The model “125B” from E H int, which generates 10 V pulses with 200 ps rise time using a tiny microwave triode, is the fastest conventional vacuum-tube pulse generator as mentioned in Table 2.1.

Table 2.1 Commercially developed vacuum pulse generators

Manufacturer	Model	Peak power	Peak voltage	Transition time
Velonex	345	6kW	1kV	35ns
Cober	606	31kW	25kV	20ns
Cober	604	9kW	15kV	25ns
Power spectra	Alpha	500kW	5kV	15ns
E H int	125B	2W	10V	200ps
Velonex	350	26kW	21kV	30ns

2.3.13 Pulse generators using spark gaps

A spark gap is often utilized as the switching element to connect the charged transmission line or capacitor bank to the output load for higher-voltage applications than a mercury switch as shown in Figure 2.17. A free-running spark gap pulser needs a supply voltage greater than the gaps breakdown voltage. Through the charging resistor (R_c) the charge line steadily charges up. In a similar fashion to that of a mercury-switch pulser, it discharges into the load resistor (R_L) when the

charge-line voltage approaches the breakdown voltage, the gap arcs over and permits this discharge. A spark gap switching time might frequently be much less than 1 ns. The geometry, distance, and dielectric materials of the gap affect the actual gap-breakdown voltage.

A spark-gap pulse leading edge rise time can be further shortened by passing it through more spark gaps, as depicted in Figure 2.16. A compact, dual-gap pulser is capable of generating 2 kV pulses into 50 ohms with a rise time of under 200 ps. McDonald in [48] constructed a dual-gap pulser and got step-like pulses with a rise time of 300 ps and voltage up to 60 kV.

The spark gap has the benefit of consistently triggering. Either a powerful laser pulse or an electrical trigger introduced into the gap via a third electrode. Similar to mercury switches, spark gaps have the drawbacks of having a short life span and degrading with time.

The largest pulse generators, both in terms of output and size, utilize spark gaps. Massive machines developed by Maxwell Labs, Naval Research Lab, Sandia Labs, EG&G Bedford, Cornell, and Physics International create pulses with a rise time of tens of nanoseconds to micro-seconds that range from kV to MV and kA to MA. These generators are used for other applications as well such as to drive E-beam and ion beam accelerators and for lightning simulation.

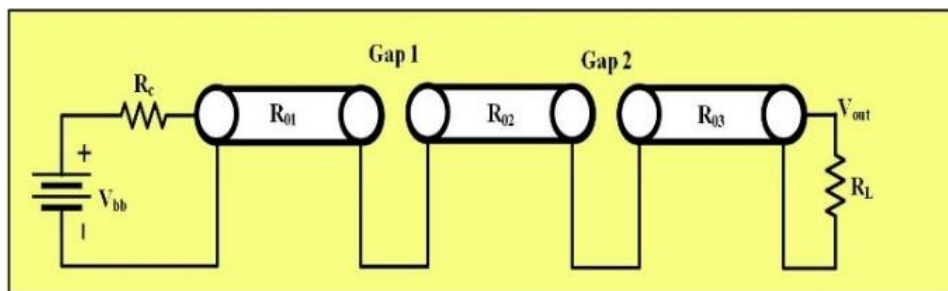


Figure 2.17 Circuit diagram of dual spark gap pulse generator

2.3.14 Pulse generators using josephson junctions

The area of superconducting cryo-electronics is at the other extreme from the massive spark-gap machines. A completely new area of incredibly quick, picosecond electronics has emerged as a result of the discovery of the superconducting Josephson junction. All of the work in this field to date has been completed in high-tech research labs. A Josephson junction can be switched in under

10 picoseconds, according to Hamilton at the National Bureau of Standards (now NIST) in Boulder, Colorado. According to theory in [49], switching transition times will be around 2 picoseconds. IBM has tried to use Josephson junctions to create a superconducting computer.

However, there are several significant drawbacks to extensive commercial applications with the Josephson junctions. First and foremost, its requirements are for a cryogenic, liquid-helium environment, and secondly, the extremely low, millivolt-level signals that are involved.

A Josephson junction is used in a picosecond pulse generator in [50] to create rise time transients of almost 7ps-9ps. An external load resistor is linked to the junction in the shunt by a balanced transmission line. The circuit diagram of the Josephson junction utilized in connection with the oscillator is shown in Figure 2.18.

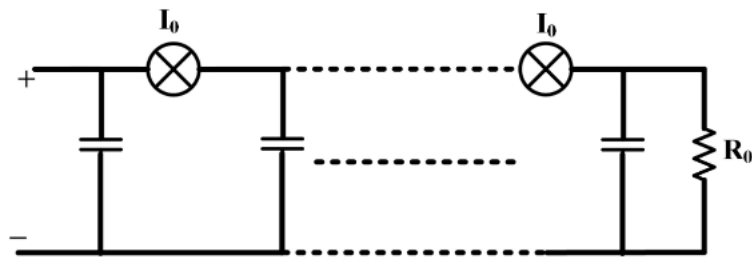


Figure 2.18 Circuit diagram of Josephson junction as a pulse generator

CHAPTER 3 ARTICLE 1: A NONLINEAR TRANSMISSION APPROACH TO COMPRESSING RISE AND FALL TIME IN PICOSECOND PULSE GENERATION

MuhibUr Rahman and Ke Wu

Published in the *IEEE Transactions on Instrumentation and Measurement*, vol. 70, pp. 1-13, 2021, Art no. 2004013. (Publication date: April 26, 2021)

This paper presents the generation scheme of picosecond (ps) pulses based on both step recovery diode (SRD) topology and nonlinear transmission line (NLTL) scheme with focus on simultaneous rise and fall time compression. First, the SRD topology is suggested and investigated for manifesting the capability of pulse compression. The SRD solution is then integrated with different NLTL schemes for alienating and achieving rise or fall time compression in the picosecond regime. It is observed that single NLTL integration only sharpens the rising or falling edge at the same time. To overcome this challenge, Two NLTL's having different diode polarities are then integrated with SRD topology-based picosecond pulse generator to compress rise and fall time simultaneously. Theory of NLTL is developed in each case and based on it the shortest rise and fall time is selected for the final design. Several parameters that are responsible for waveform distortion are also investigated in detail as well. Finally, we have fabricated four different pulse generators in which the first three only compress the rise time while the fourth one is responsible for both rise and fall time compression. The overall pulse duration for the first three generators falls within 80 ps to 95 ps having different ringing levels and they are based on rise time compression only. The pulse duration for the fourth pulse generator is almost 25 ps having a detailed ringing level of -14.24 dB and Full-Width Half Maximum (FWHM) of 10.1 ps based on both rise and fall time compression. Finally, all these pulse generators are compared with state of the arts in the literature where they utilize different techniques for sharpening and the superiority of our proposed designs is provided. These generators will find their key role and will be the best candidates for UWB radars for electromagnetic imaging and sensing applications, ultra-fast electronic techniques including edge sharpening, future oscilloscopes, comb, or pulse generators, and geophysical exploration.

3.1 Introduction

Nonlinear transmission line (NLTL) is generally an LC ladder network that comprises of a periodically loaded nonlinear components either inductors or capacitors. It can be, for example, periodically loaded by reversely biased varactor and Schottky diodes. NLTL has already found a wide range of device and system applications including comb generator, time domain reflectometry (TDR), frequency synthesizer, high-speed sampling oscilloscope, and stimulus or pulse generator [51, 52]. Among them, a clean picosecond pulse generator is very desirable in ultra-fast electronics, biological electromagnetics, geophysical exploration, discharge plasma, and future oscilloscopes. However, it is of critical importance to have such pulse generator having the capability of shortest rise/fall time. It is also vital that there is a control over rise and fall time compression instead of single edge control to achieve good compression factor.

Since it has been well known that fast electrical transitions can be generated by utilizing NLTL through the shockwave concept. These shockwaves were investigated and also implemented for either rise time or fall time compression, but not both at the same time [51, 52]. Instead of making use of the shockwave effect, some researchers also looked into soliton effects and attempted to compress fall time through such a technique as demonstrated in [53]. They achieved the generation of pulses with 5.5 ps FWHM (full-width half maximum) and 3.9 V output amplitude along with NLTL having 54 sections. Since the reported work is only based on simulation with huge number of NLTL sections which is not practical. Furthermore, caused by the huge number of varactor diodes, the reported pulse generator exhibits a significant amount of ringing with no rise time compression. Similarly, in [54], they also deployed the concept of soliton compression and developed a transmission line having the capability to compress the rise time unfortunately at the expense of a fall time expansion. They validated the scheme via simulations only that we can possibly achieve a good rise time compression factor by utilizing an inhomogeneous NLTL. Based on the above concepts, 130 GHz GaAs diode sampling head was developed in [55]. Nevertheless, the majority of the previously documented works have ushered in NLTL development with no detailed theoretical foundations.

In [56], authors tried to explain the fundamental physical properties of solitons in terms of the LC ladder network by demonstrating it mathematically and thus establishing analytical expressions.

They formulated a mathematical expression for the case of capacitive lines and observed its soliton phenomenon. Based on these formulations, authors in [57] developed an impulse-forming circuit which generates a fine impulse from corresponding step function utilizing NLTL with reduced ringing. Similarly, [58, 59] utilized the same capacitive mathematical formulation to delineate and develop a sub-nanosecond high voltage pulse generation. On the other hand, 480 fs fall time transient pulse was generated and demonstrated upon the integration of a delta doped Schottky diode NLTL in [60]. Since they achieved a well compressed fall time, the overall pulse compression was not appealing unfortunately because of the expansion of the rise time. Such a problem seriously disturbed the pulse shaping and the proposed technique failed to yield a fine and clean pulse. In [5], the picosecond pulse lab (PSPL) developed a comb generator with enhanced performance utilizing NLTL structures.

In [61], a CMOS-based monocycle pulse generation technique was reported utilizing 90 nm CMOS technology to achieve 380 ps pulse duration having 660 mV peak to peak voltage. However, the main design challenge including pulse compression was not presented and the parameters responsible for those aspects were also absent in the documented research. In [62], resonant tunneling diodes instead of varactor Schottky diodes were used, which claimed that short transition time can be obtained instead of utilizing switching circuits. An ultrashort electrical pulse based on photoconductive switches was reported in [63], whose duration is only constrained by the RC time constant of the photoconductive switch.

On the other hand, bipolar junction transistors (BJT) have also been used in different scenarios to generate ultrashort electrical pulses. One such technique was reported in [64], where the authors utilized BJT for achieving 90 ps to 800 ps pulse duration having a maximum voltage of almost 6 V. Similarly, field effect transistors (FET) have been also considered and investigated in different ways for ultrashort pulse generation. A two-stage FET based ps pulse sharpener was reported in [65] having 95 ps rise time pulse compression. Nevertheless, most of these reported works were concerned with the compression either in rise or fall time but not both at the same time. Hence, it is rather challenging to propose a circuitry that has the capability of handling both rise and fall time compressions so that a full control over pulse duration can be realized by managing rise and fall time simultaneously. A new distributed waveform generator was proposed in [66] which is basically the combination of single pulses to obtain a multicycle pulse. Also, different techniques

have been adopted to achieve monocycle pulses [67-69]. They are mainly based on the use of digital circuits and Gaussian filters. In this case, Gaussian filters are employed by cascading complex analog filters through analog/digital circuitry techniques.

A picosecond pulse generator utilizing a microstrip delay line was reported in [42], which demonstrated the capability of transforming a step input signal into its corresponding rectangular pulse having a pulse duration ranging within 50 to 500 ns. The artifacts identification and correction were performed in [70] that arise in magnetic waveforms and provide uncertainty that is associated with the procedure. Also in [71], they presented a low cost UWB pulse generator for utilization in an UWB indoor ranging system and geophysical exploration. A fully MESFET hybrid system was developed in [18] that includes a FET test step generator and a FET sampling pulse generator. The pulse generator used in this sampling setup has a rise time of 60 ps with the corresponding fall time of 70 ps. A detailed comparison of six low-cost pulse generator devices having sub-nanosecond transition time was investigated in [72]. Also, in [73] they utilized SRD topology integrated with tapered capacitive NLTL to achieve 80 ps pulse generator. Similarly, in [14] they also utilized SRD topology as a pulse generating circuit integrated with pulse shaper and developed ps pulse generator whose corresponding pulse width is 307 ps having amplitude of almost 1.88 V. In [85], they also tried to develop pulse generator based on single SRD integrated with NLTL and achieve 130 ps pulse generator having amplitude of 3.3 V. They used the rise time compression and there is no simultaneous fall time compression. This is due to the reason that they used a single polarity NLTL that can achieve the shortest rising edge using shock wave concept. Since all these pulse generators have different architectures including microstrip pulse shaper, SRD pulse generating circuit, transistors driven in the avalanche region, AHCMOS logic gates, ECL logic gates having first and second version, and upconverting mixer approach. Nevertheless, all the above techniques are used to realize sub-nanosecond pulse generators with integrated circuit implementation having an economy of scale and reduced power consumption. However, no information and techniques have been mentioned and reported for achieving simultaneous rise and fall time compression including pulse shape optimization, ringing reduction, and improving overall performance.

In this paper, we propose and present a class of ps pulse generators based on SRD (step recovery diode) topology integrated with different NLTL structural schemes. In this case, NLTL is responsible for rise or fall time compression through which we come up with the development of

four different pulse generators. These proposed pulse generators are studied, simulated, fabricated, and measured in this work. The first three are set only to compress the rise time while the fourth one is developed for both rise and fall time compression having independent biasing schemes for rise and fall time sharpening circuits. The overall pulse duration for the first three generators falls within 80 ps to 95 ps having different ringing levels. The pulse duration for the fourth pulse generator is almost 25 ps having a detailed ringing level of -14.25 dB and FWHM of 10.1 ps based on both rise and fall time compression. The theory of NLTL is derived in each case, thereby guiding the selection of the shortest rise and fall time for final designs. A number of critically important parameters are discussed in detail and the impact on possible waveform distortion is also examined.

This manuscript is an extension of [73] where the focus was pulse generation with reduced ringing based on different SRD topologies. They were theoretically investigated and a fine and clean ps based pulse generator was developed with reduced ringing level having rise time compression capability only. The main goal of the proposed manuscript is to provide a technique for simultaneous rise and fall time compression and develop a corresponding circuitry for it based on NLTL. Also, the integration aspects are investigated in detail and theoretical foundation of the proposed work is built to have shortest possible rise and fall time compression. Four different ps generators are validated in order to show that the proposed technique works well in different scenarios including rise time compression and simultaneous rise/fall time compression. Apart from the rise and fall time compression, the corresponding developed cascaded topology integration of NLTL's with opposite polarities provides an opportunity of generating negative pulses instead of positive counterparts without the use of any delay lines. Nevertheless, we have only investigated it only for positive going pulse generation in our experiment.

The remainder of this paper is arranged in the following manner. Section II provides the theoretical aspects of SRD pulse generation schemes, their equivalent models, and different topologies based on corresponding output waveforms, which is basically a short overview of the work performed in [73]. Section III deals with theoretical background developed for rise and fall time compression and a simple NLTL experiment is used to verify our proposed theory. Section IV presents the first three pulse generators proposed for showing the compression of rise time with corresponding circuits, simulated results, prototypes, measurement setup, and measured results. Section V is concerned with the fourth pulse generator successfully made for both rise and fall time compression

based on two NLTLs with different polarities having independent biasing circuits for rise and fall time edge sharpeners. Section VI compares the proposed solutions with the recent state of the arts in the field in terms of pulse duration, FWHM, ringing level, and rise/fall time compression capability, which is finally followed by the conclusion.

3.2 SRD pulse generating circuit

3.2.1 Equivalent circuit of SRD

SRDs are extensively utilized in frequency multipliers, comb generators, and wave formers due to its strong nonlinear behavior. It is seen that SRD circuit developed on idealized diode model comprising of two linear circuits have limited accuracy and good performance of the circuit can be achieved only using the experimental adjustments. Thus, for more accurate circuit designs, it is very important to have optimization and simulation of SRD circuits as commercial circuit simulators cannot provide such opportunity. SRD equivalent circuit model is developed based on analysis in [74] and then ADS spice model is designed as discussed in detail in [75]. The corresponding Spice ADS model, equivalent circuit model, and I-V characteristic curve are shown in Figure 3.1 (a)-(c), respectively. All these parameters along with SRD operation is explained in [74] and the corresponding equation is derived in [75], which is given as:

$$Q(V) = \begin{cases} C_r \times V_d & (V_d \leq 0) \\ \frac{C_f - C_r}{2V_j} \left(V_d + \frac{C_r V_j}{C_f - C_r} \right) - \frac{C_r^2}{2(C_f - C_r)} \times V_j & (0 < V_d < V_j) \\ C_f V_d - \frac{C_f - C_r}{2} V_j & (V \geq V_j) \end{cases} \quad (3.1)$$

where, C_r represents a small reverse bias capacitor, V_d corresponds to the diode terminal voltage, C_f characterizes maximum forward bias capacitance, V_j represents the barrier potential of the junction, and Q represents the corresponding charge stored in the diode.

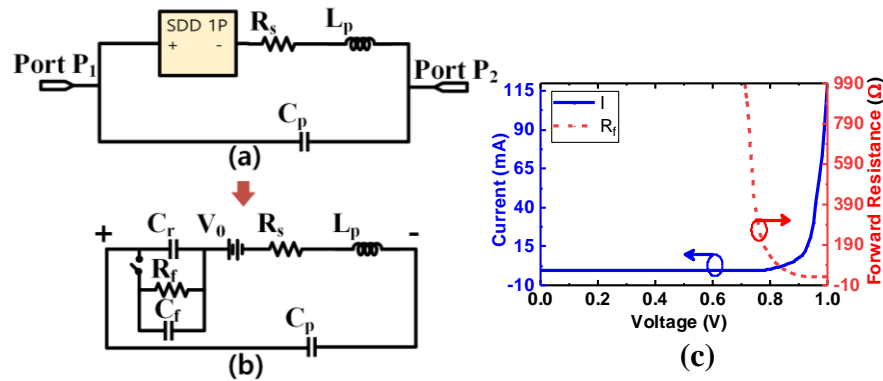


Figure 3.1 Pulse producing circuit based on SRD with corresponding equivalent circuit and I-V characteristic curve. (a) SRD spice model generated in ADS; (b) Extracted SRD equivalent circuit model; (c) I-V characteristic and forward resistance changing curves of modeled SRD

3.2.2 SRD topology investigation for pulse sharpening

Various SRD topological configurations are investigated in detail in [73] and it is shown that corresponding mixed SRD topology possesses greater sharpening capabilities as compared to shunt and series. These topologies are shown here in shunt, series, and mixed arrangement as Figure 3.2 (a)-(c) respectively. Their corresponding results are summarized in Figure 3.3 (a) and (b). To obtain optimal pulse shape, we need a proper adjustment of the parameters including input voltage and inductance. Simulations are performed in this connection and based on it the optimal values are selected for input voltage having a 10 MHz sinusoidal wave as an input excitation source. The impact of inductance and input voltage on corresponding pulse amplitude and duration is shown in Figure 3.3 (c)-(d), respectively. It is clear that the inductor has a little impact on pulse duration while adjusting pulse amplitude having the selected optimal value of 20 nH. It is also evident that increasing input voltage generates a higher pulse amplitude with a narrower width. A minimum input voltage of 3V is required to obtain a proper response from the circuit; however, beyond 6V of input voltage, the pulse duration does not change substantially. If higher pulse amplitude is required, the input voltage should be increased where the diode breakdown voltage is a limiting factor. Based on the analysis from Figure 3.3 (c)-(d), the selected input voltage is 5 V while the inductance is chosen as 20 nH.

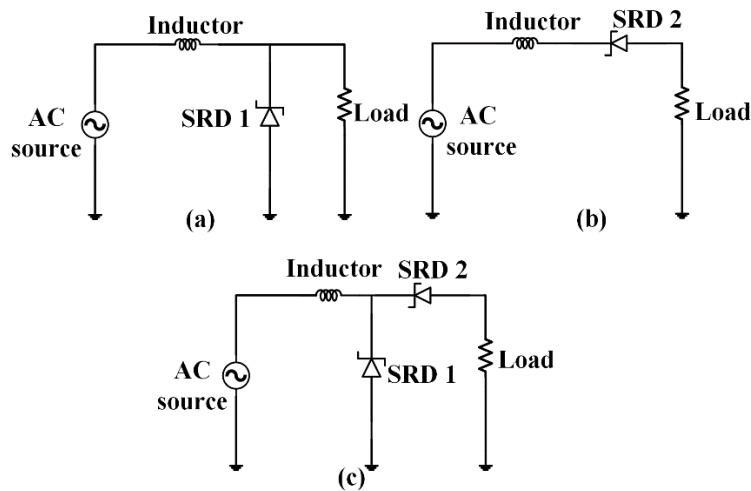


Figure 3.2 SRD circuits in different arrangements. (a) shunt arrangement; (b) series arrangement; (c) mixed arrangement

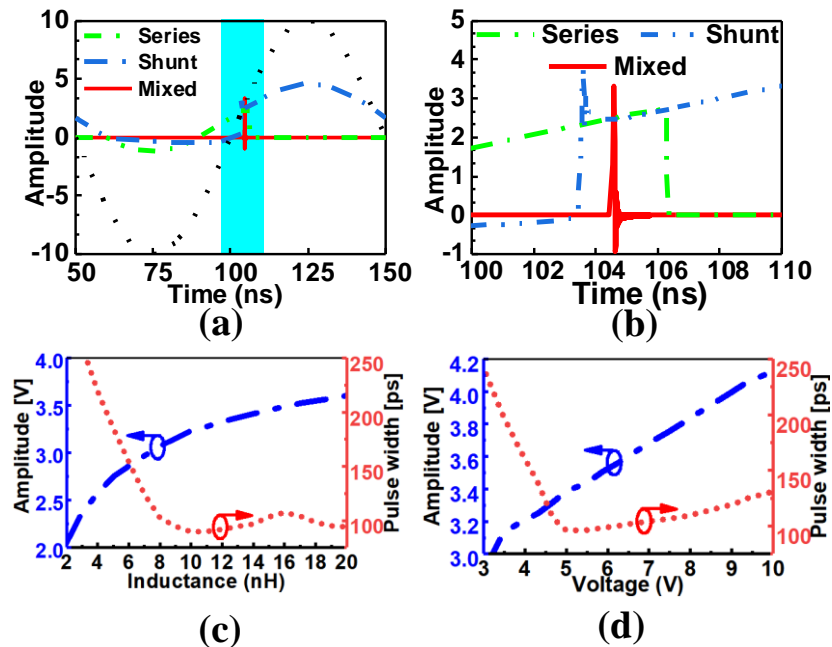


Figure 3.3 Response of SRD based pulse generation schemes in series, shunt, and mixed topology configurations and impact of input voltage and inductance on pulse width and amplitude. (a) SRD circuit arrangement response in series, shunt, and mixed topology; (b) Zoomed in view of circuit response; (c) Varying input voltage with fixed inductance of 20 nH; (d) Varying inductance with a fixed voltage of 5 V

3.3 Theory of NLTL

3.3.1 NLTL solution utilizing kdV approach with experimental validation

In this section, we begin with the analysis of NLTL in detail, which is utilized in this work for pulse generation. Theoretical foundation of this work is based on nonlinear lattice and soliton theory which is first proposed in mathematical form in [76] and then correspondingly modified and evaluated in hydrodynamic domain in [77] as now celebrated as Korteweg-de-Vries (KdV) equation. First, an NLTL solution is developed, which is verified and validated via a simple experiment.

Consider a section of dissipative NLTL that is comprised of voltage-dependent capacitance $C(V)$, linear inductance L , resistance R , and conductance G as shown in Figure 3.4.

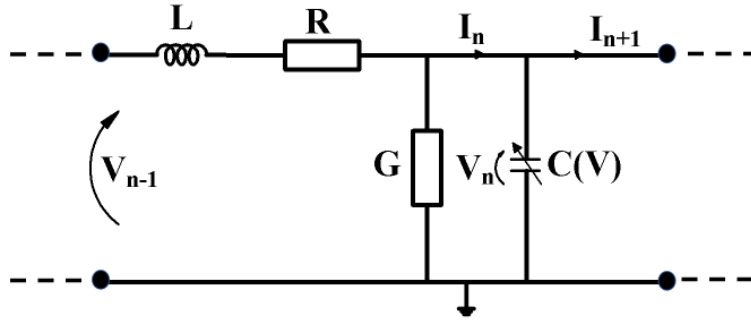


Figure 3.4 Section of dissipative capacitive NLTL with nonlinear capacitor and linear inductor

The nonlinear capacitors are usually made of a series of reverse-biased schottky diodes in capacitive NLTL. The corresponding differential-difference equations of the network is given as:

$$L \frac{\partial}{\partial t} I_n(t) + R I_n = V_{n-1}(t) - V_n(t) \quad (3.2a)$$

$$\frac{\partial}{\partial t} Q_n(t) + G V_n = I_n(t) - I_{n+1}(t) \quad (3.2b)$$

where $I_n(t)$ signifies the a.c. current flowing through the nonlinear inductor and $V_n(t)$ represents the a.c. voltage across the nonlinear capacitance. The differential charge $Q_n(t)$ stored in the nth nonlinear capacitor is given by [78]

$$Q_n(t) = \int_{V_0}^{V_0 + V_n} C(V) dV \quad (3.3)$$

where V_0 represents the capacitor's biasing voltage. The voltage dependency of the capacitance is discussed in much more detail in [79] and can be given in final form as:

$$C(V) = \frac{Q_0}{F_0 - V_0 + V} \quad (3.4)$$

In equation 3.4, the parameters that characterize the corresponding nonlinear capacitor are F_0 , and Q_0 . After eliminating I_n from equations (3.2a) and (3.2b), we get:

$$LQ_0 \frac{\partial^2}{\partial t^2} \ln \left[1 + \frac{V_n}{F_0} \right] = V_{n+1} + V_{n-1} - 2V_n \quad (3.5)$$

Now, this system corresponds to a one-dimensional lattice, termed as Toda lattice, which is a complete integrable soliton system whose initial value problem can be easily solved using an inverse scattering approach. By relating V_n and y_n to each other using equation (3.6) and other parameters using equation (3.7) as:

$$\ln \left[1 + \frac{V_n}{F_0} \right] = -b(y_n - y_{n-1}) \quad (3.6)$$

$$LQ_0/F_0 = m/ab \quad (3.7)$$

equation (3.5) now becomes:

$$m \frac{\partial^2}{\partial t^2} y_n = a \left\{ \exp[-b(y_n - y_{n-1})] - \exp[-b(y_{n+1} - y_n)] \right\} \quad (3.8)$$

This new equation represents a mechanical one-dimensional system having equal masses, associated by nonlinear springs, with the nearest interaction potential between neighbours, which is calculated as follows:

$$\phi = \frac{a}{b} \exp[-b(y_n - y_{n+1}) + a(y_n - y_{n+1})] \quad (3.9)$$

where y_n represents the displacement from the equilibrium position of the n th particle. The corresponding first and second terms denote the repulsive and attractive forces, respectively. This system was first modeled to observe the nonlinear behavior in the crystal lattice to visualize the thermal expansion under excitation, the finiteness of thermal conduction, and the energy partitioning between different vibration modes. The corresponding simplest single soliton solution of equation (3.8) is given as:

$$\exp[-b(y_n - y_{n+1})] - 1 = \beta^2 \operatorname{sech}(\mu n \pm \beta t) \quad (3.10)$$

where, $\beta = \sqrt{(ab/m)} \sinh \mu$ and using the corresponding transmission line analogy, we get:

$$V_n(t) = F_0 \Omega^2 \operatorname{sech}^2(\Omega v_0 t - Pn) \quad (3.11)$$

where, $\Omega = \sinh P$, and $v_0 = \{LC(V_0)\}^{-1/2}$ in which P is a finite real constant that determines the amplitude of the lattice soliton having the normalized soliton velocity given as: $v_0 = \Omega/P = (\sinh P)/P$ which increases with corresponding increase in the amplitude of soliton represented by Ω^2 as represented in equation (3.11).

For long wavelength, approximating V_{n+1} , and V_{n-1} can be made by the following truncated series.

$$V_{n\pm 1} \approx V_n \pm \left[\frac{\partial}{\partial n} V_n \right] + \frac{1}{2} \left[\frac{\partial^2}{\partial n^2} V_n \right] \pm \frac{1}{6} \left[\frac{\partial^3}{\partial n^3} V_n \right] + \frac{1}{24} \left[\frac{\partial^4}{\partial n^4} V_n \right] \quad (3.12)$$

Using the perturbation reduction technique with corresponding scaling and Gardner Morikawa transformation [80] to achieve the KdV equation. $x = \varepsilon^{1/2}(n - v_0 t)$, $\tau = \varepsilon^{3/4} v_0 t / 24$, and $V = -\varepsilon F_0 u / 2$. The lowest non-trivial terms generate the KdV equation as follows

$$u_\tau + 6uu_x + u_{xxx} = 0 \quad (3.13)$$

This is the case where nonlinearity of varactors exactly counteracts the dispersion generated by the periodic loading. Due to this counteracting effect, solitons are generated and propagate along the line and can be given:

$$V(t, n) = \Omega^2 \operatorname{sech}^2 \left[\Omega \omega_B \left(t - \frac{P}{\Omega \omega_B} n \right) \right] \quad (3.14)$$

where amplitudes Ω^2 and P are associated with the relation presented above $\Omega = \sinh P$, ω_B is the Bragg cut-off frequency of NLTL, and n represents the n th section of NLTL. The Bragg cut-off frequency of NLTL is inversely related to the length of the transmission line segment and difficult to accurately write analytically. The FWHM and detailed ringing level of the pulse generated here can be given by the following relations.

$$t_{FWHM} = \frac{1.76}{\Omega \omega_B} \quad (3.15)$$

$$R_r = 20 \log \frac{\text{Peak to peak ringing amplitude}}{\text{Peak to peak pulse amplitude}} \quad (3.16)$$

A simple experiment is performed to show the validity of our analytical procedure. To this end, a six and ten section NLTL prototypes with fixed inductors and varying voltage-dependent capacitors are fabricated and measured. The experimental setup comprising of a periodic signal generator, DC power supply, an oscilloscope, and developed NLTL prototypes shown in Figure 3.5 (a) and (c), for six and ten section NLTL, respectively. The corresponding response from the developed theory correlated with the measured response are shown in Figure 3.5 (b) and (d), for six and ten section NLTL, respectively. It is observed that results predicted by the theory developed here matches well with measured counterparts having an amplitude of 3.4V, FWHM of 2.3 ns, and the ringing of almost -38.7 dB in six section NLTL case, which validates our solution and can be used for capacitive NLTL circuitry with different NLTL sections.

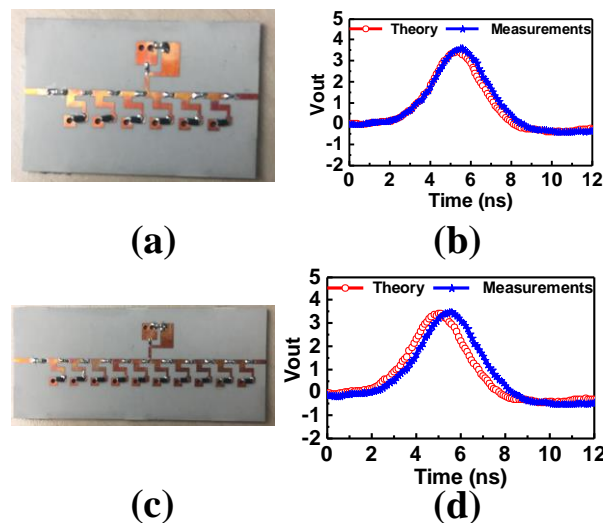


Figure 3.5 Fabricated six and ten-section NLTLs with corresponding response (biasing wires and connectors are not shown in the fabricated prototypes). (a) Six section NLTL prototype; (b) Response from theory and measurement for the developed six-section NLTL prototype; (c) Ten section NLTL prototype; (d) Response from theory and measurement for the developed ten section NLTL prototype

3.3.2 NLTL rise time compression analysis

The objective of this section is to provide a comprehensive analysis of rise time compression capability in NLTL with corresponding distributed and equivalent lumped model. Consider an NLTL as in Figure 3.6 with the distributed model as Figure 3.6 (a) and the corresponding equivalent lumped model as Figure 3.6 (b), where the proposed rise time compression circuit is biased by DC source and triggered by the input voltage (V_i) having current limiter (R), RF choke (L), the DC input blocking capacitor (C), distributed capacitance of microstrip line (C_0), fixed inductances (L_1 - L_6), junction capacitance (C_m), and parasitic series resistance of the varactor diode (R_m).

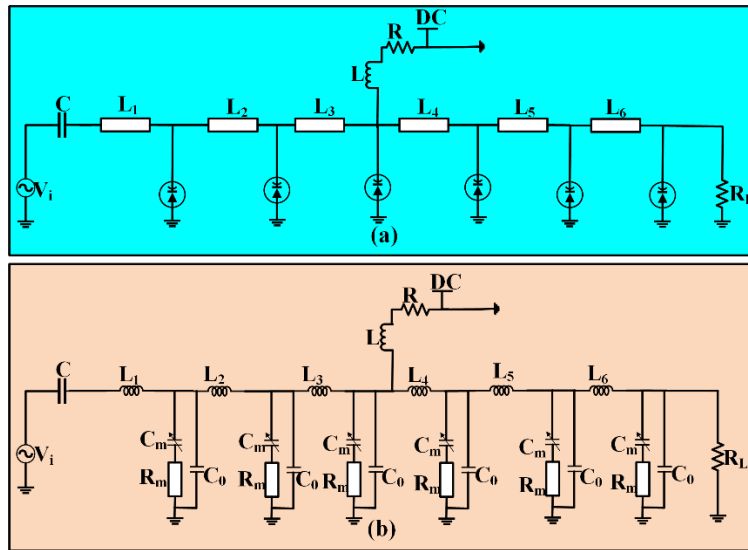


Figure 3.6 Six sections capacitive NLTL utilized for rise time compression. (a) Distributed design model; (b) Lumped design model

The corresponding cut-off frequency of the designed model in Figure 3.6 (b) is represented as:

$$\omega_{per} = \frac{2}{L_0 [C_m(V) + C_0]} \quad (3.17)$$

It is well known that the upper bound of NLTL operating frequency is dependent on cut-off frequency of the varactor diode. Considering $R_m=0$, then the corresponding voltage of the subsequent node is given as:

$$V_0(t) = V_m [t - T(V)] \quad (3.18)$$

where $T(V) = \sqrt{L_0(C_0 + C_m(V))}$. It shows that NLTL delay arises due to varactor diode junction capacitance with corresponding equation as:

$$C_m(V) = \frac{C_{j0}}{\left(1 + \frac{V}{V_b}\right)^k} \quad (3.19)$$

where C_{j0} represents the zero-bias capacitance, V represents voltages that reverse biases the varactor diode, k is the grading coefficient, and V_b signifies the barrier potential of the varactor diode junction. The corresponding delay for NLTL having two different voltage levels V_H and V_L such that ($V_H > V_L$), is expressed as:

$$\Delta T = T(V_L) - T(V_H) = \sqrt{L_0[C_m(V_L) + C_0]} - \sqrt{L_0[C_m(V_H) + C_0]} \quad (3.20)$$

The corresponding phase velocity, in this case, can be given by

$$v_p = \frac{1}{\sqrt{LC(V)}} \quad (3.21)$$

The pulse leading edge propagates at a velocity written by

$$v_p(0) \approx \frac{1}{\sqrt{LC(0)}} \quad (3.22)$$

The crest of the pulse will now travel with velocity as:

$$v_p(V_{\max}) \approx \frac{1}{\sqrt{LC(V_{\max})}} \quad (3.23)$$

The crest captures up the leading edge after passing through N sections of lumped elements line, where

$$N = \frac{v_p(V_{\max})v_p(0)\Delta t}{v_p(V_{\max}) - v_p(0)} \quad (3.24)$$

where Δt represents the initial rising time of the pulse. The velocities are characterized in terms of sections per second. When the input rise time is varied, we can obtain 10% to 90% rise time data by observing the output pulse. Eventually, the shortest rise time can be predicted and is given as:

$$t_{rise,min} \approx \frac{\pi}{4} \sqrt{LC(V_{max})} \quad (3.25)$$

It is clear from equation (3.21) that if the nonlinear capacitor decreases with voltage, the corresponding propagation velocity along the line will increase. Now it means that by increasing the voltage we can ultimately achieve a pulse having the shortest rise time as evidenced from equation (3.25) and validated via the NLTL circuit as shown in Figure 3.6 for different voltage values with corresponding output response as displayed in Figure 3.7. It can be depicted that a shortest possible rise time that can be achieved from circuit in Figure 3.6 having six section NLTL is almost 6.4 ps. The rise time compression factor calculated in this case is 4.18.

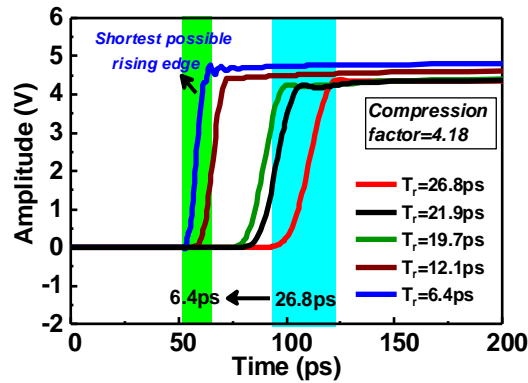


Figure 3.7 Rise time compression (T_r) of NLTL by varying voltage

3.3.3 NLTL fall time compression analysis

Here we will briefly investigate in detail about the falling time compression capability in NLTL with corresponding distributed and equivalent lumped models. Let us consider an NLTL as in Figure 3.8 with the distributed model as Figure 3.8 (a) and the corresponding equivalent lumped model as Figure 3.8 (b). This circuit is biased like Figure 3.6 with DC source and triggered by the input voltage (V_i) having current limiter (R), RF choke (L), and DC input blocking capacitor (C). Now assuming $R_m=0$, the n th diode voltage is given as:

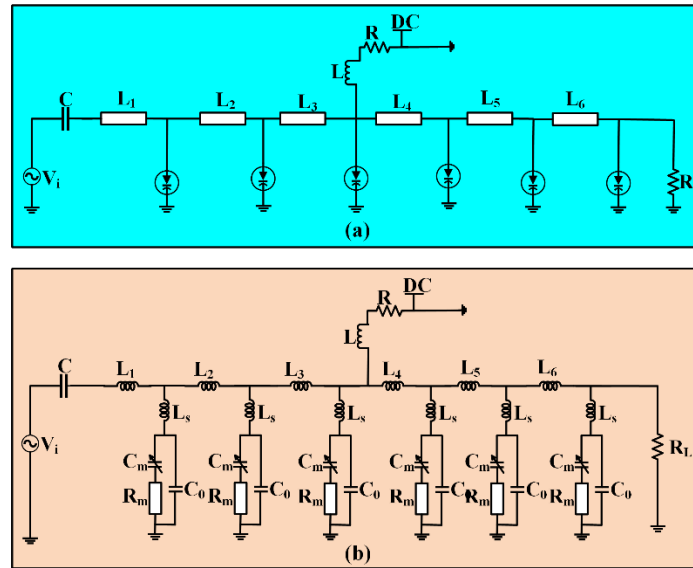


Figure 3.8 Six sections capacitive NLTL utilized for fall time compression. (a) Distributed model; (b) Lumped model

$$V_n(t) = V_m[t - nT(V)] \quad (3.26)$$

where $T(V) = \sqrt{L_0(C_r(V))}$, having $C_r(V) = C_0 + C_m(V)$ which signifies the overall capacitance at each NLTL section. When the propagation delay $T(V)$ is varied, it results in a sharpening of the negative-going waveform. As can be seen from Figure 3.9 that an input pulse $V_i(t)$ having a step falling function with initial voltage V_h and final voltage V_l with corresponding input fall time $T_{f,in}$, which linearly decrease after propagating along the n th NLTL sections and is represented as $T_{f,n}$, given by

$$T_{f,n} = T_{f,in} - n\Delta T = T_{f,in} - n[T(V_h) - T(V_l)] \quad (3.27)$$

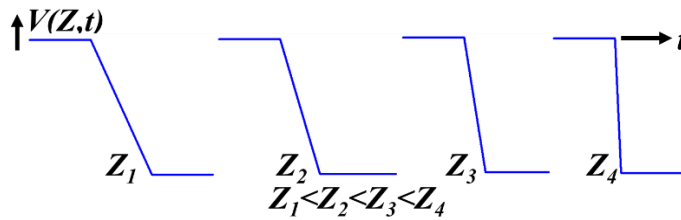


Figure 3.9 Fall time compression of NLTL with step input

where ΔT represents the compression in falling time at each NLTL segment. Through a sufficient number of sections of NLTL, the voltage $V_n(t)$ will become discontinuous as can be seen in Figure 3.9, and which is termed as shockwave propagation having the shortest possible fall time. These shockwave propagation properties can be calculated using large signal diode capacitance C_{ls} given as:

$$C_{ls}(V_l, V_h) = \frac{1}{V_h - V_l} \int_{V_l}^{V_h} C_m(V) dV \quad (3.28)$$

After the shockwave generation, their delay at each NLTL section is given as:

$$T_{ls}(V_l, V_h) = \sqrt{L_\tau (C_{ls}(V_l, V_h) + C_l)} \quad (3.29)$$

The minimum compressed fall time $T_{f,min}$ for these waves can be achieved when the diode cut-off frequency dominates ($\omega_d < \omega_{per}$) and can be written as:

$$T_{f,min}(10\% - 90\%) = \frac{8.8}{\omega_d(0)} \frac{1}{\sqrt{1 - v/\phi} - 1} \quad (3.30)$$

Given a diode utilized with $\phi = 0.4 \text{ V}$ and $\omega_d(0)/2\pi = 1 \text{ THz}$ then from equation (3.30), it can be predicted that 2.74 ps fall time can be achieved for the 6 V step input function. Figure 3.10 shows the simulation of a shockwave formation over the six sections NLTL as designed in Figure 3.8. It can be seen that almost 7.2 ps output fall time is achieved with an input fall time of 50 ps within acceptable ringing level range. The fall time compression factor calculated in this case is 4.06.

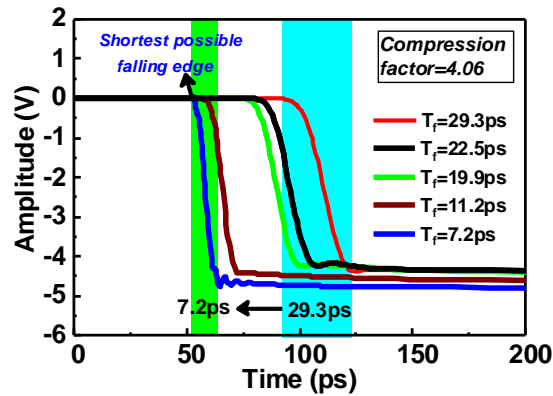


Figure 3.10 Fall time compression (T_f) of NLTL by varying voltage

3.4 Integrated ps pulse generators with rise time compression

The SRD configuration [73] discussed in section II is integrated with different NLTL topologies for generating different pulse schemes as illustrated as a block diagram in Figure 3.11. The SRD topology-based pulse generating circuit includes input voltage (V_i), DC source having current limiter (R_2), bypass capacitor (C_2), RF choke (L_2), DC blocking capacitor (C_1), with R_3 for controlling the pulse width, and L_1 for controlling the adjustment of the pulse position as shown in Figure 3.12. The optimized parameter values are $R_2=50 \Omega$, $R_3=4.6 \text{ K}\Omega$, $L_1=20 \text{ nH}$, a supply voltage of 5V, and SRD diodes having a model from the MAVR-0447 series. After this network arrangement, there is an NLTL topology which may be either linear, abrupt tapered, and exponential tapered NLTLs for only rise or fall time compression and cascaded NLTLs configuration for simultaneous rise/fall time compression with independent biasing circuits. All these NLTLs are discussed in detail in the coming sections with corresponding results.

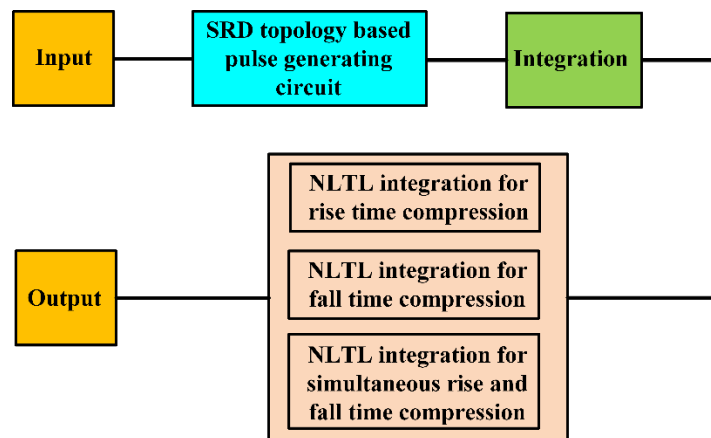


Figure 3.11 Block diagram of SRD topology-based pulse generating circuit integrated with different NLTL topologies for generating different pulse schemes

3.4.1 SRD topology integration with linear NLTL

SRD topology is integrated with linear NLTL sections. It must be noted that by linear NLTL we mean that we have still non-linear components in the circuit including varactor diodes, however the length and width of the line between adjacent sections is same as can be seen from Figure 3.12. The proposed circuit is shown in Figure 3.12 with corresponding values mentioned in the previous section. Since the nominal length, in this case, is the same between adjacent NLTL sections and

represented by L as shown in Figure 3.12. Figure 3.13 (a) and (b) show the simulated result of four and ten sections linear NLTL integrated with SRD topology-based generator, respectively. It is seen that increasing the number of NLTL section improves the ringing level. However, the size of circuit is going to increase. It is observed that pulse generator, in this case, has a main pulse duration width of almost 95 ps, amplitude of 3.95V, FWHM of 34 ps having a detailed ringing level of -19.36 dB in the four sections linear NLTL case. By increasing the number of NLTL sections from four to ten, it is seen that the ringing level is improved from -19.36 dB to -22.48 dB.

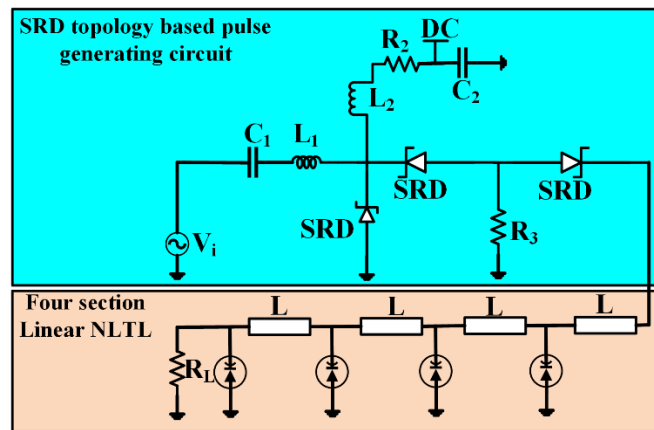


Figure 3.12 Integration of four sections linear NLTL with SRD topology-based pulse generating circuit

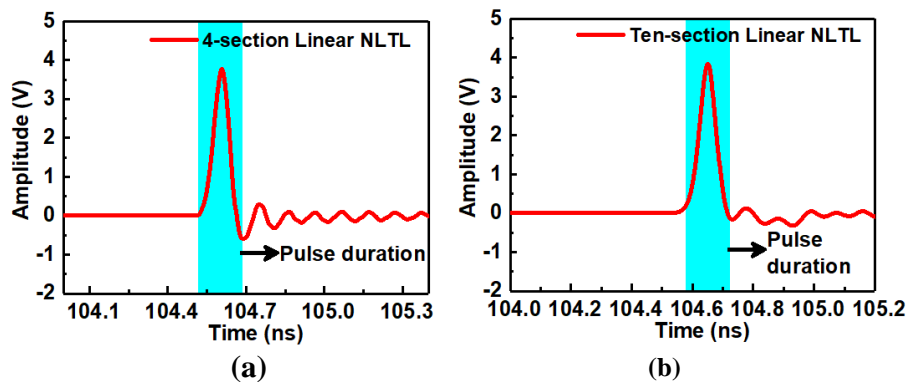


Figure 3.13 Simulated result of linear NLTL integrated with SRD topology-based generator. (a) Four section NLTL; (b) Ten section NLTL

3.4.2 SRD topology integration with abrupt tapered NLTL

Now, the SRD topology is integrated with ten sections abruptly tapered NLTL and the proposed circuit is shown in Figure 3.14. In this case, the tapered NLTL is designed by first calculating the length of transmission line between varactors by relation $L_n = d.k^n$, where d represents the nominal length of NLTL, k stands for the tapering factor, and n signifies the n th section, which is selected to be 10 in the present case. The designed ten section abrupt tapered NLTL based on the above relation and integrated with SRD topology is shown in Figure 3.14, featured by a corresponding simulated response in Figure 3.15 (a). The ringing level is substantially enhanced by integrating the abrupt tapered NLTL sections. A very clean pulse waveform is generated having corresponding width of almost 80 ps, amplitude of 3.90 V, and FWHM of 26 ps. The detailed ringing level is improved from -19.36 dB to -32.9 dB in this case by utilizing an abrupt tapering technique and increasing NLTL sections.

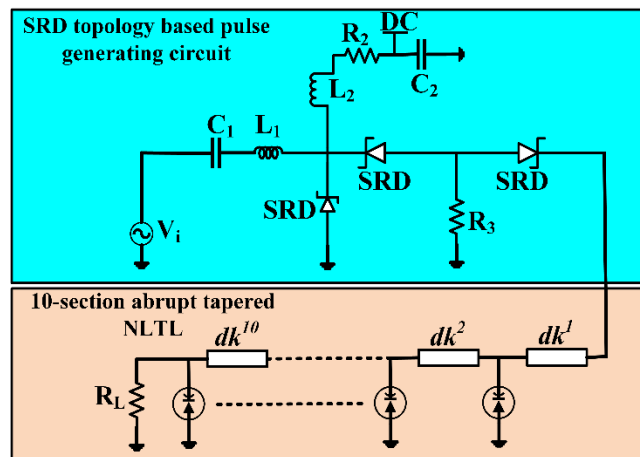


Figure 3.14 Integration of ten sections tapered NLTL with SRD topology-based pulse generating circuit

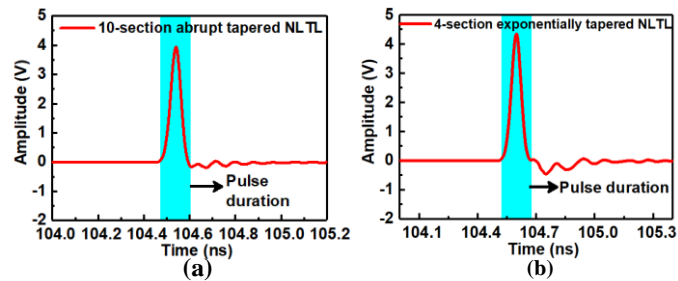


Figure 3.15 Simulated result of tapered NLTL integrated with SRD topology-based generator. (a) Four section tapered NLTL; (b) Four section exponentially tapered NLTL

3.4.3 SRD topology integration with exponentially tapered NLTL

In this section, the SRD topology is integrated with four sections exponentially tapered NLTL and the proposed circuit is shown in Figure 3.16. The exponentially tapered NLTL is designed in this case by first calculating the length of transmission line between varactors by relation $L_n = d.e^n$, where d represents the nominal length, and n indicates the n th section of NLTL, and the tapering factor is modified to be the exponential tapering factor such that $k=e$. The designed four-section exponentially tapered NLTL based on the above relation and integrated with SRD topology as shown in Figure 3.16 with a corresponding simulated response in Figure 3.15 (b). The ringing level is found to be considerably enhanced as compared to the linear NLTL topology nevertheless compared to the tapered case it is almost the same. The pulse generator developed in this case retains a pulse width of almost 80 ps, the amplitude of 4.1 V, and FWHM of almost 24 ps. The detailed ringing level calculated here is almost -30.4 dB.

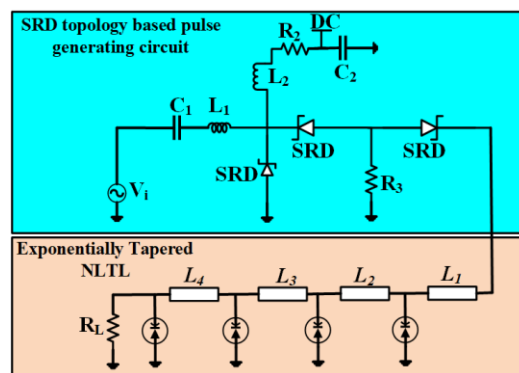


Figure 3.16 Integration of four sections exponentially tapered NLTL with SRD topology-based pulse generating circuit

3.4.4 Fabrication and measurement setup

We have fabricated the four sections linear NLTL, the four sections exponentially tapered NLTL, and the ten sections linear NLTL for validation purpose as shown in Figure 3.17 (a-c), respectively. The circuits of the mentioned ps pulse generators are developed by utilizing RogerR04350 with dielectric constant of 3.5, and the microstrip line of 50Ω .

To validate the analysis and design, the experimental setup arranged in this work is comprised of a periodic signal generator, a DC power supply, an oscilloscope, and developed NLTL based ps pulse generators. 14-bit AWG Keysight M8190A is used for generating 10 MHz sine wave as an input signal for the designed circuit boards, output pulse is observed utilizing an oscilloscope as demonstrated in Fig 3.18. Note that a DC voltage source is employed to control the DC bias of the varactors. The measured results correlated with simulated counterparts are shown in Figure 3.19, which shows a good agreement. The simulated vs. measured results in each case are shown in Fig 3.19 (a-c) and it can be seen that there is a slightly undesired delay which is attributed to RF cables utilized in the experimental measurements. The slight variation in pulse width observed is possibly caused by the limitations in the modeling of SRD diodes, parasitic effects related to soldering, and thermal behavior.

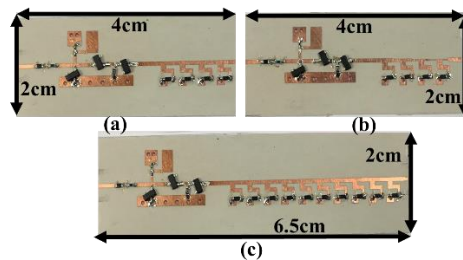


Figure 3.17 Fabricated pulse generators for rise time compression, the corresponding biasing wires are not displayed. (a) circuit 1: Four-sections linear NLTL integrated with SRD topology; (b) circuit 2: Four-sections exponentially tapered NLTL integrated with SRD topology; (c) circuit 3: Ten sections linear NLTL integrated with SRD topology

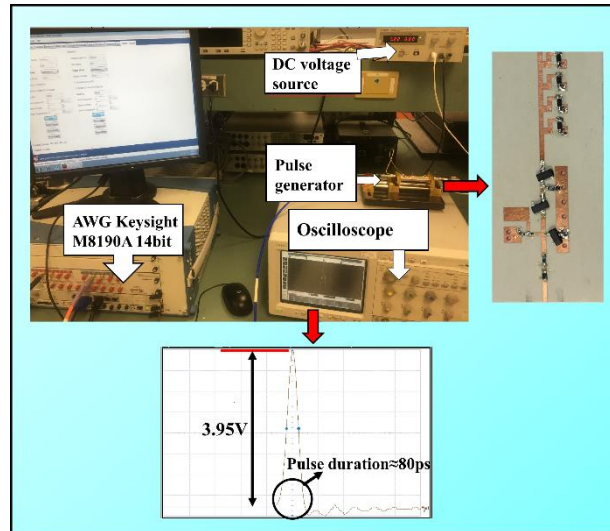


Figure 3.18 Experimental verification: the system is composed of a periodic signal generator, a dc power supply, an oscilloscope, and developed NLTL based ps pulse generators placed between universal test fixture for measurement

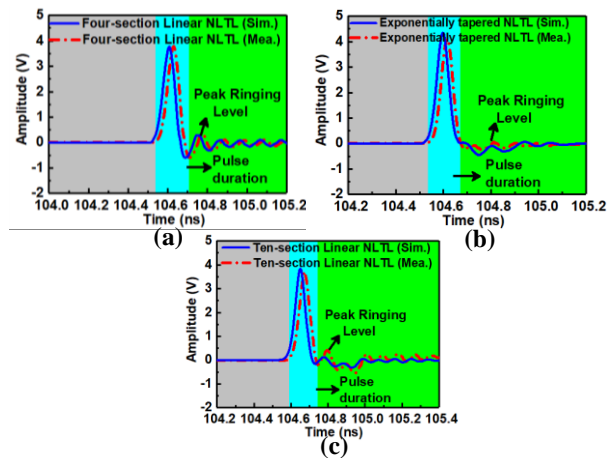


Figure 3.19 Simulated vs. measured results of ps pulse generators based on SRD topology with multi-section linear and tapered NLTL. (a) ps pulse generator with four sections linear case; (b) ps pulse generator with four-sections tapered case; (c) ps pulse generator with ten sections linear case

The critical parameters of all these circuits are R_3 which is responsible for pulse width control with corresponding value selected for shortest compression capability. The pulse can also be adjusted to a desired value by varying parameter L_1 .

The corresponding R_3 vs. related compression in pulse width is demonstrated in Figure 3.20 with proper comparison with ideal and package inductances and capacitances from SRD. Figure 3.21 illustrates the FWHM compression vs. parameter R_3 along with ideal and package inductances and capacitances. R_3 is optimized and selected based on the information in these plots and the measurement is performed at two different values of 3 K Ω and 4.6 K Ω respectively shown in Figure 3.20 and Figure 3.21 as well. The overall summary of these ps pulse generators are provided in Table 3.1.

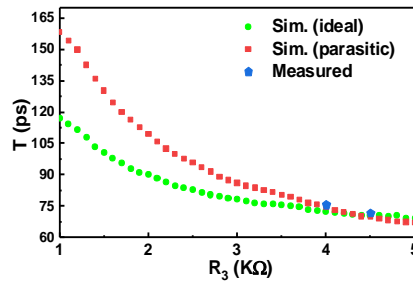


Figure 3.20 Pulse duration vs resistor (R_3) of the proposed ps generators in four sections exponentially tapered NLTL case

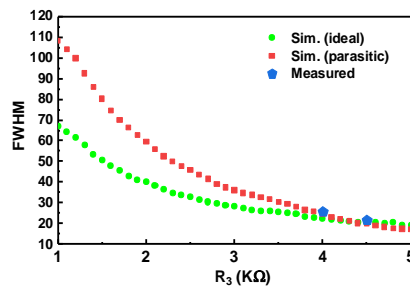


Figure 3.21 FWHM vs resistor (R_3) of the proposed ps generators in four sections exponentially tapered NLTL case

Table 3.1 Overall summary of the developed ps pulse generators

ps generators	Amp. (V)	Pulse width (ps)	Ringing (dB)	FWHM (ps)
Linear four sections	3.95	95	-19.36	34
Exponentially tapered four sections	4.1V	80	-30.4	24
Abrupt tapered ten sections	3.90	80	-32.9	24
Linear ten sections	3.92	95	-22.48	34

3.5 Integrated ps pulse generator with both rise and fall time compression

In the previous section, we have presented pulse generators that exhibit the only capability of rise time compression. Here we propose and develop a new topology that has the capability of both rise and fall time compression simultaneously by utilizing two NLTL circuits based on the section III analysis to obtain the possible shortest rise and fall time. The SRD based generator is first integrated with both these topologies along NLTL that are responsible for it. To better understand the proposed scenario, we divide our whole circuit into three blocks as can be described in Figure 3.22 including (a), (b), and (c). Block (a) involves the SRD topology-based pulse generator that has been designed and discussed in section II. Block (b) presents the six section NLTL that is responsible for rise time compression based on section III (b). Block (c) again show off the six section NLTL that is designed for rise time compression based on section III (c). Since blocks (b) and (c) are comprised of the same sections having the opposite polarities of diodes for sharpening rise and falling edges with independent biasing circuits. By combining both these topologies and integrating into a cascade with the same sections of NLTL, we can achieve the shortest possible rise and fall time edge compression and ultimately with the shortest pulse duration. Equation (3.25) and (3.30) that has been derived in section III is responsible for achieving the shortest rise and fall time for block (b) and (c), respectively.

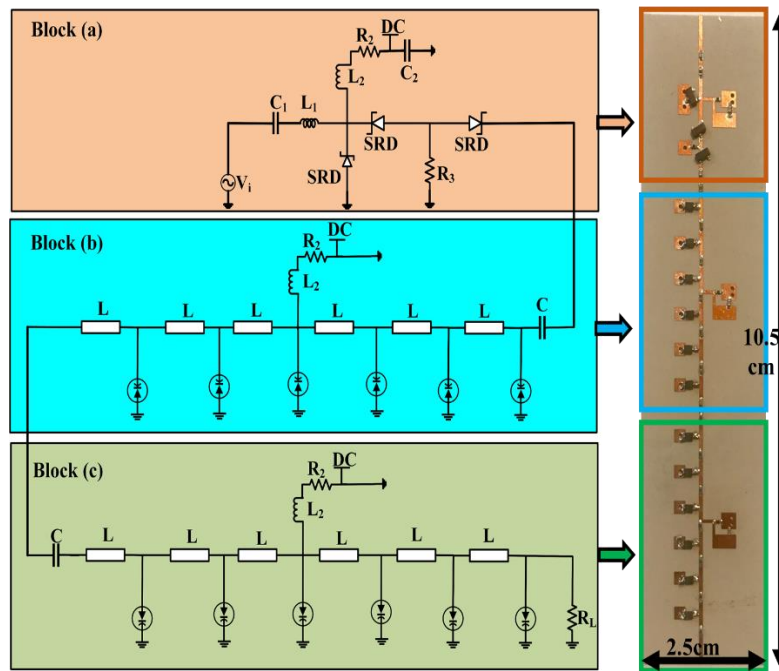


Figure 3.22 Integration of two NLTL circuits having opposite polarities with SRD topology-based pulse generating circuit with prototypes of all blocks, biasing wires, and connectors are not displayed. (a) circuit 1: ps pulse generator established on mixed SRD topology; (b) circuit 2: a circuit for rise time compression; (c) circuit 3: a circuit for fall time compression

Also, it is observed in section IV that a single NLTL approach can only either sharpen the rise or falling edge depending on the polarity of varactor diodes. To overwhelm such a hurdle, we have integrated two NLTLs in a cascade of the same sections with opposite polarities with independent biasing circuits to sharpen both edges of the generated pulse. Proper care should be taken so that both waveforms should overcome the misalignments to mitigate the undesired ringing in the pulse. If there is a small misalignment, there would be a considerable ringing and then distort the whole pulse. The whole concept is demonstrated in the circuit diagram in Figure 3.22 while the shortest rise and fall edge for the selected circuitry is shown in Figure 3.23 in our case.

Apart from the rise and fall time compression, this combination of NLTLs provides an opportunity of generating negative pulses instead of positive counterparts without the use of any delay lines. Since the polarity and pulse duration width can be controlled easily by the NLTL circuitry for both

blocks. Hence, if we generate signals from the block (b) and (c) such that block (c) signal lags block (b), instead of a positive waveform at the output, we will have a negative waveform. This promising feature can be easily implemented from the proposed circuitry and can be utilized for desired applications.

The simulated response of the two NLTL circuits with opposite polarities integrated with the SRD topology-based pulse generating circuit is shown in Figure 3.24. The proposed approach is first utilized in a separate block integrated with the SRD pulse generating circuit and the rise and fall time is managed properly to have a clean positive-going pulse as illustrated in Figure 3.23. These individual NLTL edge sharpeners are then combined and the resultant NLTL simulated waveform at the output is shown in Figure 3.24. It can be seen from Figure 3.24 that the shortest possible rise and fall time pulse generator is developed, having a pulse duration of almost 25 ps, amplitude of 3.65V, and FWHM of 10 ps from simulations. The detailed ringing level calculated here is -14.24 dB.

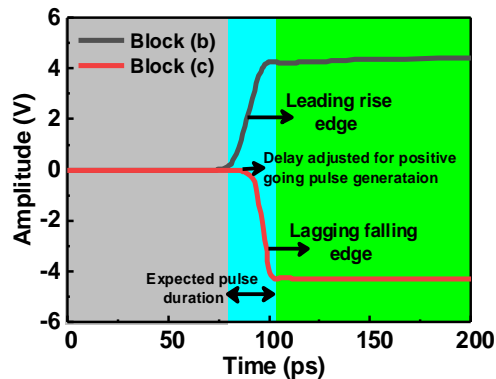


Figure 3.23 Simulated result of rise and fall time circuitry integrated separately with SRD topology-based generating circuit

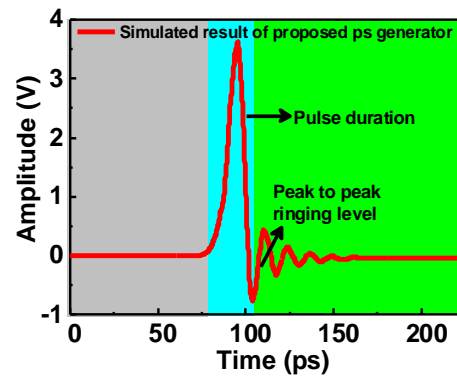


Figure 3.24 Simulated response of two NLTL circuits with opposite polarities integrated with SRD topology-based pulse generating circuit

The proposed ps generator featuring the rise and fall time compression is also fabricated and all the blocks including SRD topology-based pulse generating circuit, rise time, and fall time compression circuits are shown in Figure 3.22 (a-c) respectively. These circuits are also developed by utilizing Roger R04350. One obvious drawback with the presented ps pulse generator having simultaneous rise and fall time compression is the increased layout area that is $10.5\text{cm} \times 2.5\text{cm}$. However, this concept can be further extended and studied in the future for implementation in integrated circuits as well. Also, the layout area can be further decreased by proposing some possibly innovative biasing scheme and reducing it from three to a single biasing source.

To validate the measured results, the experimental setup is arranged as the previous experiments, which consists of a periodic signal generator, a DC power supply, an oscilloscope, and integrated circuitry. The input pulse is generated utilizing an arbitrary pulse generator and the waveform is monitored by an oscilloscope. Note that a DC voltage source is again employed to control the DC bias of the varactors. The measured response correlated with the simulated one is shown in Figure 3.25. The measured result shows a slight deviation from the simulated one and the ringing becomes more dominant in the measurement as can be seen in Figure 3.25. The output pulse achieved from the measurement has an overall pulse duration of 26.5 ps, the amplitude of 3.5 V, and FWHM of 10.8 ps. The detailed ringing level is slightly degraded as compared to the simulated result. However, the peak of the ringing is still eight times lower than the peak amplitude of the pulse, which is within acceptable range.

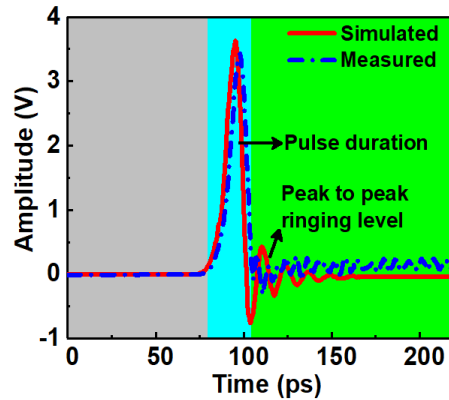


Figure 3.25 Simulated vs. measured response of two NLTL circuits with opposite polarities integrated with SRD topology-based pulse generating circuit

3.6 Comparison with recently proposed state of the art pulse generators

The proposed ps pulse generators are also compared with the recent state of the arts electronically developed pulse generation techniques. The proposed pulse generators are advantageous in terms of pulse duration, FWHM, ringing level, and specifically the rise and fall time compression capability. Table 3.2 gives a brief overview and a clear superiority of the proposed work reported in this paper. The ringing level in Table 3.2 is calculated based on equation (3.16).

Table 3.2 Comparison with ps generators in the literature [Proposed 1: four section linear NLTL integrated, Proposed 2: four section exponentially tapered NLTL integrated, Proposed 3: ten section linear NLTL integrated, Proposed 4: Two NLTL's integrated with SRD topology of opposite diode polarities] (N/R means not reported)

Year	Ref.	Technique implemented	Amp.	Pulse width	Ringing	FWHM	Compression (Rise/Fall)
			(V)	(ps)	(dB)	(ps)	
2020	[73]	SRD topology integrated with four section tapered NLTL	3.95	80	-32.7	26	Rise
2001	[81]	Combination of Schottky diodes, step recovery diode, and	0.7	350	-20.9	N/R	N/R

		charging and discharging circuit						
2002	[82]	Combination of Schottky diodes, step recovery diode, and RC high-pass filter	0.4	300	-17	120	Rise	
2005	[83]	Integration of clock driving circuit with pulse shaping circuit via delay line	0.2	600-780	-20	N/R	N/R	
2012	[13]	Combination of Schottky diodes, step recovery diode, and pulse shaping filter	1.8-1.85	1000	-17.15	>300	Rise	
2015	[14]	Step recovery diode topology	1.88	307	-22.5	110	N/R	
2006	[84]	Integration of clock driving circuit with pulse shaping circuit via SRD coupling	8	450	-11.2	160	N/R	
2016	[85]	Single step recovery diode integrated with NLTL	3.3	130	-22.1	N/R	Rise	
2014	[86]	Step recovery diode in series with Schottky diode	0.6-0.87	170-401	-22	N/R	Rise	
2004	[87]	PIN diodes and MESFETs	1.4-1.9	300-800	N/R	62	N/R	
2007	[12]	Resonant tunnelling diodes	0.3-0.9	100-120	N/R	35-40	N/R	
2008	[88]	NLTL shock wave concept	0.1-0.3	800	-12.4	N/R	Fall	
2012	[26]	NLTL soliton concept on standard 90 nm CMOS	0.8-1.2	75	N/R	14	Fall	
2018	[89]	Double-uniform Schottky diode NLTL on gallium arsenide	-8	N/R	6.02	N/R	Generating fall transients	
2020	[16]	Step recovery diode integrated with pulse shaping network	1.4	150	-11	N/R	N/R	
2019	[90]	Combination of Schottky diodes, sharp rise time pulse train	1.67	100	-14.6	153	Rise	

		generator, and pulse shaping network						
2021	Proposed (1)	Four section linear NLTL rise time pulse sharpener integrated with SRD topology	3.95	95	-19.36	34	Rise	
2021	Proposed (2)	Four section Exponentially tapered NLTL rise time pulse sharpener integrated with SRD topology	4.1	80	-32.9	24	Rise	
2021	Proposed (3)	Ten section linear NLTL rise time pulse sharpener integrated with SRD topology	3.92	95	-22.48	34	Rise	
2021	Proposed (4)	NLTL rise and fall time pulse sharpeners with independent biasing networks integrated with SRD topology	3.65	25	-14.24	10.1	Rise/Fall (Both)	

3.7 Conclusion

In this work, we proposed, studied, and demonstrated four different pulse generators in the picosecond regime based on SRD topology and its integration with different NLTL schemes. The first three generators can sharpen the rise time while the fourth one can simultaneously compress rise and fall time. The theoretical background is developed and explained for all the NLTL schemes, which have been explored in detail with distributed and lumped models. Critical parameters that affect the pulse duration and FWHM are analyzed in detail and the optimization scheme is provided as well. All these generators are fabricated and tested for validation purposes. Good agreements have been observed between simulated and measured responses. The proposed pulse generators are compared with the recent state-of-the-art pulse generators developed electronically and the superiority of our work is summarized in terms of pulse duration, FWHM, edge compression, output amplitude, detailed ringing level, and proposed technique. It is clear that

this technique can simultaneously compress the rise and fall time with the final proposed pulse generator having a pulse duration of 25 ps with FWHM of almost 10.1 ps which is very promising. It is believed that these fast-electronic pulse generators will find their applications in subsurface sensing, geophysical exploration, nondestructive examination, medical applications and will pave the way of ultrafast pulse generation in pulsed-wave interconnects and ultrafast electronics.

CHAPTER 4 ARTICLE 2: A NONLINEAR TRANSMISSION LINE TECHNIQUE FOR GENERATING EFFICIENT AND LOW-RINGING PICOSECOND PULSES FOR ULTRABROADBAND AND ULTRAFAST SYSTEMS

MuhibUr Rahman and Ke Wu

Published in the *IEEE Transactions on Instrumentation and Measurement*, vol. 71, pp. 1-11, 2022, Art no. 2005511. (Publication date: September 05, 2022)

This paper presents a nonlinear transmission line (NLTL)-based scheme to develop an efficient and low-ringing picosecond pulse generator for ultrabroadband and ultrafast system applications. The proposed NLTL scheme stems from a unique combination of single varactor diode and stacked varactor diode per NLTL cell, which is designed to exploit a significant effect of non-linearity in connection with the varactor diode. This technique generates a higher compression factor in both rise and fall time of NLTL circuits in comparison to single varactor diodes per NLTL section. This scheme is validated to work well in a triple-stacked NLTL topology by maximizing the compression factor. Two pulse generators are then developed based on the proposed concept, where a mixed SRD topology is used for gaussian pulse generation and integrated with a triple-stacked NLTL. This achieves shorter pulse durations and a higher compression capability. The use of NLTLs with triple-stacked varactor diodes in a cell is also explored theoretically and is shown to maximize the compression capability by effectively increasing the punch through, turn-on, and break down voltages. Theoretical development and simulation of two triple-stacked NLTLs based on the rise and fall time-compression are provided, and final experimental prototypes for pulse generators are fabricated and measured. It is found from measurements that the full-width half maximum (FWHM) of the rise time-compression-based pulse generator is almost 15.78ps with a ringing level of -11.29dB, while the FWHM of the fall time-compression-based pulse generator is almost 17ps with a ringing level of -8.43dB. Finally, these pulse generators are compared with the current states of the art in terms of the implemented scheme, pulse duration, FWHM, pulse shapes, and detailed ringing level. The reconfigurable capability of the pulse generators is also briefly explored, and it is shown that the proposed pulse generators can easily be reconfigured between gaussian and monocycle pulse shapes. The power spectrum of the proposed pulse generators is also

presented. It is found that they are well suitable for ultra-broadband and ultrafast systems, such as Impulse Radar Ultrawideband (IR-UWB) applications, due to higher pulse compression capability, ease of integration, flexible pulse tunability, and modification to higher order gaussian waveforms.

4.1 Introduction

A typical nonlinear transmission line (NLTL) is an LC ladder network that is loaded periodically with lumped inductors and reversely biased varactor diodes. Other NLTLs are also possible in the form of other periodically loaded nonlinear elements or completely distributed nonlinear media. NLTLs exhibit non-linearity due to the varactor diodes and dispersion due to the structural periodicity. Harmony between dispersion and non-linearity can be made through a soliton, which is a voltage travelling pulse. This phenomenon makes the NLTL one of the best candidates for pulse generation and compression in microwave systems and ultrafast electronics.

Picosecond (ps) pulses are required in many ultrabroadband and ultrafast applications, such as time-domain reflectometry, sampling oscilloscopes, frequency synthesizer, indoor geolocation, and ultra-wideband (UWB) communication applications. UWB technology has been a choice of preference for impulse radar developments in medical, industrial, and military domains [71]. For all these applications, the generation of clean ultra-short ps pulses is highly desirable along with higher rise or fall time-compression capability and proper pulse repetition factor (PRF). So, it is rather challenging to achieve a very efficient short pulse with a flexible compression capability along with an acceptable ringing behavior.

Gaussian and higher-order derivatives of Gaussian pulses are a variety of important types used in impulse radar-UWB or IR-UWB applications [52]. Such pulsed systems may also find emerging multifunctional wireless developments such as joint radar-communication platforms [91,92]. The impulse radar radiates impulse-like waveforms generally falling into the sub-nanosecond regime having broadband features. This waveform of broad bandwidth related to compressed ps pulses will yield higher resolution and data rate. This sort of waveform includes Gaussian pulses, Gaussian doublets, and higher-order Gaussian pulses [93]. The conventional approach to generating such pulses is to use non-linear devices with reference to a particular frequency source [42].

The pulse generator is one of the vital and important components of UWB communication systems [94]. Depending on specific applications, the transmitter must be capable of emitting a pulse that possesses the characteristics of shorter pulse width, higher amplitude, clean pulse shape, and low ringing level. In pulsed radar applications, radiated pulse shape from the antenna determines and identifies target response. However, a majority of antennas usually suffer from internal reflections. As such, a distorted pulse waveform is emitted, which needs a post-processing ringing mitigation technique. However, the post-processing ringing mitigation technique is complicated and impractical [95]. So, a pulse generator that yields efficient, low ringing, and minimally distorted pulse waveform is highly preferred to be deployed in UWB and ultrafast electronic systems.

4.2 Related work and background

Different types of pulse generators have been investigated and developed in the literature, based on the Schottky diode, tunneling diode, step recovery diode (SRD), field effect transistors, and avalanche transistors [12,13]. In [13], a low ringing pulse generator was proposed through a combination of Schottky diode and SRD with an RLC filter as a pulse shaping circuit. The pulse generator has an amplitude of almost 1.85V, pulse width of 1000ps, detailed ringing level of -17.15dB, and FWHM greater than 300ps. In [12], a pulse generator was devised on a resonant tunneling diode having an amplitude of 0.9V and a pulse width greater than 110ps. A pulse generator devised on the SRD combination and abrupt tapered NLTL was studied in [73], where the pulse width is almost 80ps with an improved ringing level. Also, in [96] they presented the generation of narrow pulses that is established on spectrum stitching method. The pulse width of the developed pulse generator falls between 2ns and 4ns, while the spectrum coverage is almost 500 MHz. Similarly, in [97] they proposed an arbitrary waveform generator based on static random access memory and having the capability of generating gaussian and square waveforms. Since the average power consumption of the presented waveform generator is much lower and can be efficiently used in multiresolution spectrum sensing applications.

In [98], they analyzed the avalanche transistors based on the sub-nanosecond pulse generation in corresponding 4×10 -stage Marx bank circuits. The circuit can generate rise time pulse compression of less than 4ns. Similarly, following the technique in [98], a high peak voltage picosecond pulse generator was designed in [99], having an FWHM of 660ps, rising edge of almost 160ps, and

amplitude of 5000V. Nevertheless, the majority of these pulse generators discussed above suffer from ringing problems and have the main drawback of a limited rise or fall time-compression along with complex topology. Hence, it is very important to develop a pulse generator that has flexible rise or fall time-compression capability by enhancing the non-linearity region.

It was previously explored in detail how the NLTL is capable of generating fast electrical transitions, including rising edge compression, falling edge compression, and overall pulse compression [4]. Since the NLTL is capable of generating soliton and shockwaves, the former is suitable for generating pulse and compression, while the latter is good for edge sharpening [57, 88]. However, there are certain techniques that use a combination of both concepts to create clean ps pulses [85]. A soliton-based pulse generator having a pulse amplitude of 1.2V and electrical transitions of almost 80ps was reported in [26] based on 90nm CMOS standard technology. Similarly, in [90], a combination of sharp rise time pulse train generator, Schottky diodes, and pulse shaping circuit was deployed in order to develop a pulse generator capable of producing a waveform having an amplitude of 1.67V and pulse width of 100ps.

The theoretical development of NLTL in terms of lattice solitons was first reported in [56], where the authors demonstrated and confirmed experimentally and mathematically the observation of Zabusky and Kruskal regarding solitons. The nonlinear soliton and lattice theory and its implementation on the NLTL was first presented in [76], where the authors arranged the NLTL relation to be equivalent to the Boussinesq equation and thus extracted the soliton equation. Based on the above concepts, the authors in [78] studied a model loaded with a periodic NLTL for the wave propagation of solitons. This model can generate solutions for capacitive NLTLs numerically. Similarly, an NLTL loaded with heterostructure barrier varactors was studied in [79], where the approximation and transformation of [80] were used to obtain an analytical expression that completely describes soliton waveforms.

Nevertheless, all the discussed structures and models have the limitation of the rising and fall time-compression due to the Bragg cut-off frequency. It is well understood that the upper bound of the NLTL is totally conditioned by the corresponding cutoff frequency of used varactor diodes. This phenomenon is usually termed as a transition limitation in the NLTL where the shortest rising and falling edges are obtained. Beyond this point, an increasing voltage will no longer further sharpen the edges, and a considerable ringing behavior will arise. So, it is highly desirable to develop a

technique through which the NLTL can meet the limitation raised in a single varactor per NLTL cell. Also, it is very demanding that the proposed pulse generators must have the flexibility to be easily reconfigured to higher-order Gaussian pulse shapes, which are necessary in different applications. So, it is preferable and advantageous that we have such pulse generators that can overcome the main hurdle of the transition limitation, which can be reconfigured to monocycle and doublet pulse shapes as well. This will indirectly meet the compression requirements for higher-order Gaussian pulse shapes and will simultaneously solve two important issues.

In this paper, we present an NLTL-based technique to develop a pulse generator that has the capability of eliminating the limitation of edge sharpening in a single varactor diode per NLTL cell. In this regard, we first devise and show an independent topology for rising and falling edge compression based on a single varactor diode per NLTL cell followed by our proposed stacked varactors diodes per NLTL cell. The proposed rising and falling edge circuits are then integrated with mixed SRD schemes to further compress waveforms. It is also shown that utilizing NLTLs with triple-stacked varactor diodes connected in series considerably enhances the compression capability by effectively increasing the punch through, turn-on, and break down voltages. Theoretical background of the stacked NLTL is presented in each scenario and the final designs for the developed pulse generators are measured. Then, we compare the proposed pulse generators with the state of the art to show the superiority of the proposed concept in terms of FWHM, pulse width, pulse amplitude, detailed ringing level, reconfigurability between pulse shapes, and implemented scheme. The power spectrum of the proposed pulse generators is also plotted, and it is shown to fit well within the IR-UWB spectrum. The proposed solutions is believed to pave the way towards the development of ultrafast electronics by resolving the major issues of compression limitation within NLTL structures, which is a promising candidate for IR-UWB and other fast pulses-related applications. This technique will be an important breakthrough in the evolution of ultrafast electronics, providing a path towards a frequency-engineered ultrashort pulse instrumentation for low-loss and low-dispersion transmission.

The remaining sections of this work are organized as follows. Section III presents a theoretical analysis of the NLTL structures with an emphasis on single varactor diode per NLTL cell and stacked varactor diodes per NLTL cell. Section IV provides the design guidelines of the proposed triple-stacked pulse generators. The former is based on the rise time-compression circuit integrated

with a mixed SRD topology, while the latter is based on fall time-compression circuit integrated with mixed SRD topology. Simulation, fabrication, and measurement setup of both pulse generators are also explained in this section, and the final results are presented. Modification of the proposed pulse generators and reconfigurability for higher-order Gaussian pulse shapes are also described with corresponding results. The power spectrum of the proposed pulse generators is also briefly discussed in this section. Section V discusses a comparison table that lists important pulse system parameters with the current state of the art and ends with a conclusion.

4.3 Theory and analysis

4.3.1 Theory and analysis of NLTL with single varactor diode per section

Consider Figure 4.1 where an NLTL is composed of inductors represented by L and non-linear capacitors represented by C . When the applied voltage increases, the corresponding differential capacitance represented by C would decrease. The n th section voltage denoted by V_n and its current denoted by I_n can be given by the following set of equations:

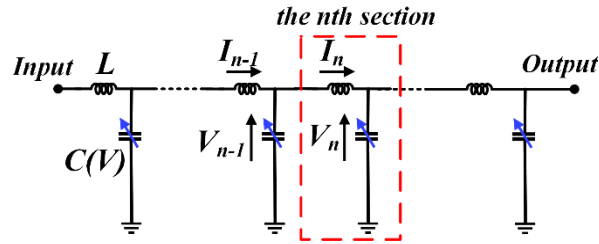


Figure 4.1 Equivalent circuit of NLTL with single varactor diode per cell

$$L \frac{dI_n}{dt} = V_{n-1} - V_n \quad (4.1)$$

$$\frac{dQ_n}{dt} = I_n - I_{n+1} \quad (4.2)$$

The differential charge Q_n can be given as:

$$Q_n = \int_0^{V_n} C(V) dV \quad (4.3)$$

The voltage dependency of the capacitor is described by:

$$C(V) = \frac{Q(V_0)}{F(V_0) - V_0 + V} \quad (4.4)$$

where V_0 represents the biasing voltage, and $F(V_0)$ and $Q(V_0)$ is the particular value of V_0 having the corresponding dimension of voltage and charge, respectively. By eliminating I_n from equation (4.1) and (4.2), we obtain:

$$LQ(V_0) \frac{d^2}{dt^2} \ln \left[1 + \frac{V_n}{F(V_0)} \right] = V_{n+1} + V_{n-1} - 2V_n \quad (4.5)$$

Now equation (5) is equivalent to a Toda lattice, which analytically has a corresponding soliton solution. The corresponding soliton solution is provided as [29]:

$$V_n = F(V_0) \sinh^2 k \operatorname{sech}^2 \left\{ kn - \frac{1}{\sqrt{LC(V_0)}} (\sinh k) t \right\} \quad (4.6)$$

Due to the counteracting effect of dispersion and non-linearity, the waves in NLTL change their shape to a more stable form temporally. As represented in equation (4.6), once a soliton or soliton array is produced in the NLTL, it will then propagate without changing its shape. The pulse width and amplitude of the corresponding soliton can be estimated by the values of inductors and characteristics of the non-linear capacitors.

Since it is well documented in [4] that the corresponding rising and fall time of the single varactor diode per NLTL cell topology is limited, and modeled through equation (4.7) and (4.8), respectively:

$$T_{rise, \min} \approx \frac{\pi}{4} \sqrt{LC(V_{\max})} \quad (4.7)$$

$$T_{fall, \min} = \frac{8.80}{\omega_d(0)} \frac{1}{\sqrt{1 - v/\phi} - 1} \quad (4.8)$$

where $T_{rise, \min}$ and $T_{fall, \min}$ represent the minimum compressed rising and fall time, respectively. Now, let's consider the distributed model of the six section NLTL circuit for the corresponding rising and fall time-compression as modelled in Figure 4.2 (a) and (b), respectively. These circuits are biased by a DC source having an input voltage of 10 MHz PRF represented as V_i , dc input blocking capacitor (C), current-limiter (R), RF-choke (L) with fixed inductances (L_1 - L_6). It is seen from simulations that by utilizing a single varactor diode per stage in the six section NLTL circuit, we have a rise time-compression factor of 4.18 and fall time-compression of 4.06, as shown in Figure 4.3 (a) and (b), respectively.

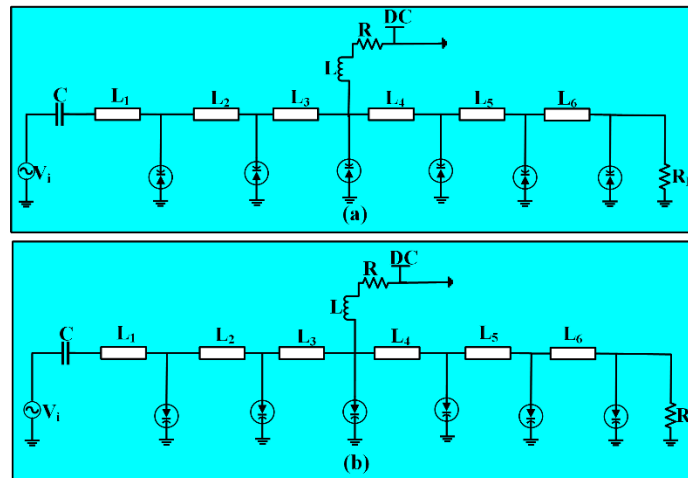


Figure 4.2 Six section NLTL circuit for rising and fall time compression. (a) Rise time compression circuit; (b) Fall time compression circuit

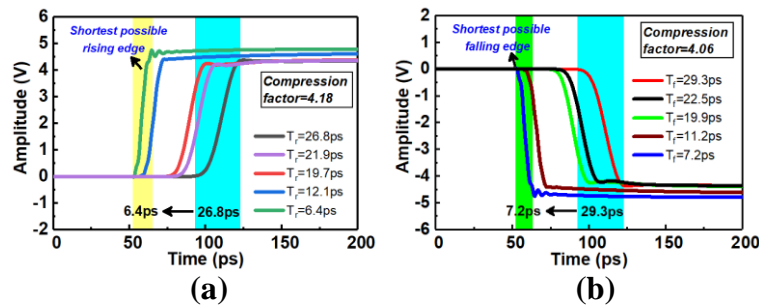


Figure 4.3 Shortest possible rising and falling edge in six section NLTL utilizing single varactor diode per NLTL cell. (a) Rise time compression factor by changing voltage; (b) Fall time compression factor by changing voltage

4.3.2 Theory and analysis of NLTL with stacked varactor diode per section

It is well known that when a hyper-abrupt varactor diode is used for its non-linear properties, it is ideally considered to operate over the maximum limit of the reverse bias voltage (punch-through voltage) and the maximum limit of the forward bias voltage (turn-on voltage). The voltage represented by $V_{deplete}$ is basically the punch-through voltage at which there is no additional decrease in corresponding varactor diode capacitance [100]. These constraints limit the rising and

fall time-compression in the NLTL, which uses a single varactor diode per NLTL cell or stage. So, any part of the waveform that exceeds the punch-through voltage of the corresponding diode in the NLTL cell will go through it without being functioned by the non-linearity of the diode, and thus there will be no more sharpening. The highest power transfer efficiency is utilized when the full non-linearity of the varactor diode is utilized in each stage, and thus we have the maximum sharpening. However, this sharpening is not enough for some applications, which fall beyond the capacity of a single varactor diode per NLTL cell. Hence, an NLTL is highly recommended where a greater range of non-linearity is utilized, and it is no longer dependent on a single varactor diode fabrication process.

To overcome this limitation, we propose the NLTL topology, both for rising and fall time-compression (depending on the polarity of varactor diode), that utilizes a different number of stacked varactor diodes per NLTL cell in order to increase the non-linearity region. Also, by utilizing stacked varactor diodes connected in series per NLTL cell, an effective depletion voltage of the corresponding cell will increase, i.e. (number of stacked varactor diodes per cell, $N=2,3,\dots$), and thus a greater portion of the non-linearity is utilized per NLTL cell. This combination gives a higher compression when compared to the single varactor diode per NLTL cell with corresponding shorter circuit dimensions. Additionally, the oscillatory tail that arises in the pulse compression process is significantly quenched, thus increasing the detailed ringing level of the pulse generator. It also provides higher flexibility and freedom to the designer in the customization and operation for a wide range of applications.

Consider Figure 3.4 (a)-(c) where single-, double-, and N-stacked varactor diodes are used per NLTL section, respectively. It is clear from Figure 3.4 (b) that the double-stacked NLTL section includes two varactor diodes (V_1 and V_2) per NLTL cell that are connected in series while interconnected with a transmission line. Similarly, the triple-stacked varactor diode includes three varactor diodes (V_1 , V_2 , and V_3) per NLTL section that are connected in series, as demonstrated in Figure 3.4 (c). Also, an N-stacked NLTL section contains N-varactor diodes (V_1 , V_2 , V_3 , ..., V_N) per NLTL cell that are connected in series while interconnected with a transmission line, as shown in Figure 3.4 (d). The generalized equivalent circuit for single and stacked varactor diodes per NLTL cell is modeled in Figure 3.4 (e), where L_i and C_i are the distributed inductance and capacitance of the line, respectively; L_s represents the inductance of the connections to the diodes;

$C_m(V)$ or C_{eq} is the capacitance of the varactor diodes that is voltage dependent; and R_s and R_{eq} are the parasitic series resistance of the varactor diodes in single and stacked scenarios, respectively. The varactor diodes ($V_1, V_2, V_3, \dots, V_N$) are the diodes that operate in the reverse bias in Figure 3.4 and thus produce voltage dependent relative capacitance, $C_m(V)$. This variation of the capacitance as a function of V is modelled as [100,101]:

$$C_m(V) = \frac{C_{j0}}{\left(1 + \frac{V}{V_b}\right)^k} \quad (4.9)$$

where C_{j0} is the junction capacitance at zero bias; V_b is the diode junction potential; V is the voltage that reversely biases the diode; and k represents the grading coefficient. In comparison to the unloaded transmission line, the capacitance of the corresponding varactor diode per NLTL cell is selected to be much larger in order to create a substantial non-linearity per stage.

The total capacitance of a cell when an N-stacked varactor diodes are associated in series per NLTL cell, as demonstrated in Figure 3.4 (d), is given as:

$$\frac{1}{C_m^{stack}(V)} = \sum_{i=1}^N \frac{1}{C_{m,i}(V)} \quad (4.10)$$

If all the N-varactor diodes are identical, then equation (4.10) will become:

$$C_m^{stack} = \frac{C_{j0}}{N \left(1 + \frac{V}{NV_b}\right)^k} \quad (4.11)$$

Also, the total series resistance will become:

$$R_s^{stack} = \sum_{i=1}^N R_{s,i} = NR_s \quad (4.12)$$

The overall capacitance of the stack will become:

$$C_{eq} = K_{eq}^{stack} C_{j0} \quad (4.13)$$

where,

$$K_{eq}^{stack} = \frac{V_b}{(V_2 - V_1)(1-k)} \left\{ \left[1 + \frac{V_1}{NV_b} \right]^{1-k} - \left[1 + \frac{V_2}{NV_b} \right]^{1-k} \right\} \quad (4.14)$$

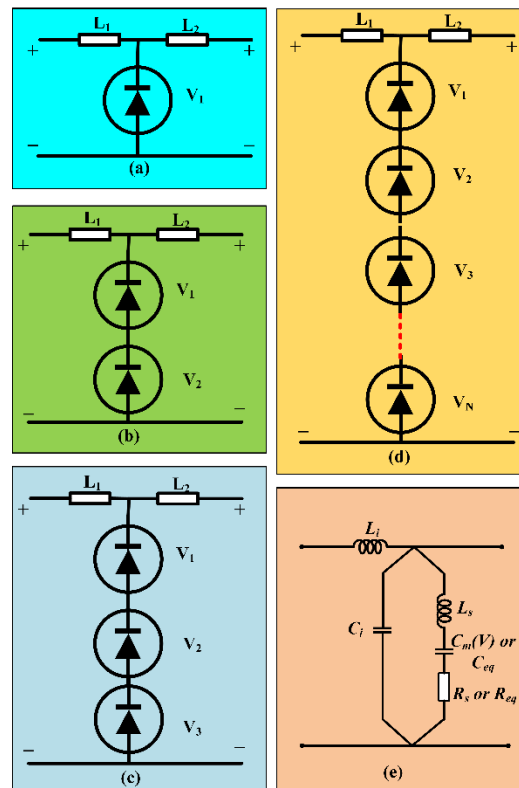


Figure 4.4 Schematic circuit diagrams of NLTL utilizing: (a) Single varactor diode per NLTL cell; (b) Two stacked varactor diodes per NLTL cell; (c) Triple stacked varactor diodes per NLTL cell; (d) N -stacked varactor diodes connected in series per NLTL cell; (e) Generalized equivalent circuit for single and stacked varactor diodes per NLTL cell

Now, consider the distributed model of the six-section-stacked NLTL circuit for the corresponding rising and fall time-compression as developed in Figure 3.5 (a) and (b), respectively. This NLTL circuit comprises of a single varactor diode per NLTL cell at the first two stages, double-stacked varactor diodes per NLTL cell at the next two stages, and triple-stacked varactor diodes per cell at the final two NLTL stages followed by the load resistance R_L . Such circuits are biased by a dc source, like in the previous section with input voltage (V_i), dc input blocking capacitor (C), current limiter (R), RF choke (L), and fixed inductances (L_1 - L_6). It is seen from Figure 3.6 (a) that by utilizing a triple-stacked varactor diodes topology per cell in the six section NLTL circuitry, we have a rise time-compression factor of 7.61, which was 4.18 in the single NLTL case. Similarly, by utilizing the stacked topology for fall time-compression, we have a compression factor of 6.91,

which was 4.06 in the single NLTL case. This clearly verifies our proposed concept, and how we enhanced the compression factor with the stacking concept. A varactor diode is ideally considered to work over a corresponding voltage range as:

$$\begin{aligned} |V_{\text{high}}| = |V_{\text{deplete}}| &\leq |V_{\text{bd}}| \\ 0 \leq |V_{\text{low}}| &< |V_{\text{on}}| \end{aligned} \quad (4.15)$$

where V_{low} and V_{high} are the low and high voltage points on an input waveform, respectively; V_{bd} is the breakdown voltage; and V_{on} is the turn-on voltage of the corresponding varactor diode. Equation (4.9) is valid within the limits of equation (4.15). Now, in case the varactor diodes become fully depleted, then we have ($C_m(V_{\text{deplete}}) = C_{\text{min}}$). By solving equation (4.9) for V_{deplete} , we will get the final relations as:

$$V_{\text{deplete}} = \left[\left(\frac{C_{\text{jo}}}{C_{\text{min}}} \right)^{1/k} - 1 \right] V_b \quad (4.16)$$

The parameters (C_{jo} , k , and $C_{\text{jo}}/C_{\text{min}}$) will be set by the varactor diode fabrication process. If $|V_{\text{bd}}| < |V_{\text{high}}|$ or $|V_{\text{on}}| < |V_{\text{low}}|$, the propagation pulse will be clipped by the varactor diode. Thus, we will have a limited pulse steepening capability. V_{bd} and V_{on} can be increased by using varactor diodes with larger barrier heights (V_b). However, a larger barrier height of the varactor diode possesses a limited range, where most V_{on} can only be increased up to 50%. So, the only solution is the series stacked varactor diodes that have no limited range, since both V_{bd} and V_{on} can be scaled with N for N -stacked case. This yields $V_{\text{bd}}' = NV_{\text{bd}}$ and $V_{\text{on}}' = NV_{\text{on}}$. So, it is concluded that using an N -stacked varactor diodes topology enhances the compression factor, since all NLTL cells give an effective punch-through, turn-on, and breakdown voltages, being N times better and greater than the utilization of a single varactor diode per NLTL cell.

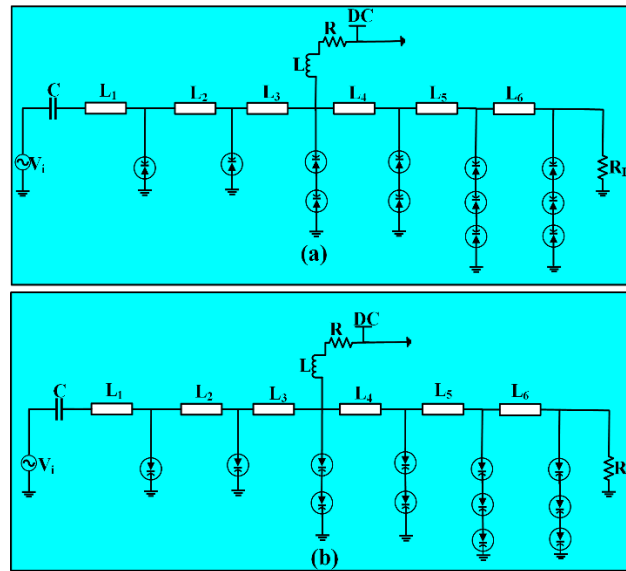


Figure 4.5 Six section N-stacked NLTL ($N=1,2,3$) circuit for rising and fall time compression. (a) Rise time compression circuit having ($N=1,2,3$); (b) Fall time compression circuit

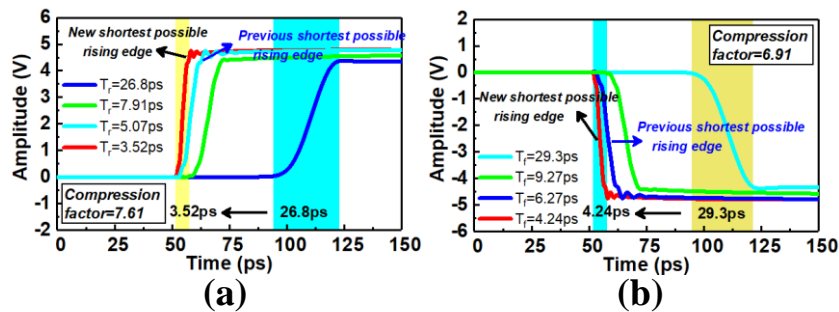


Figure 4.6 Response of corresponding rising and fall time compression circuits in six section stacked varactor diodes per NLTL cell. (a) Rise time compression factor; (b) Fall time compression factor

4.4 Design of pulse generators with results and discussions

This section is dedicated to the design of two different types of pulse generators based on the stacked varactor diode concept. Two different pulse generators are developed to show that the stacked varactor concept works for both rising and fall time-compression in practical circuits. In order to generate an efficient and compressed pulse, we integrate the mixed SRD topology [4] with

our proposed circuits and present the result in each scenario. The overall picture and development of these pulse generators can be easily visualized from the block diagram, as shown in Figure 4.7.

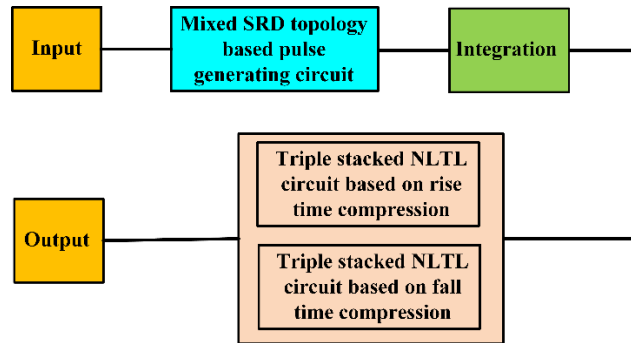


Figure 4.7 Block diagram of the overall scheme for developing pulse generators

4.4.1 Integrated triple-stacked NLTL pulse generator based on rising time-compression

Let's consider the circuit diagram of a six-section triple-stacked NLTL circuit for rising time-compression integrated with a mixed SRD combination, as presented in Figure 4.8. First, a mixed SRD topology is used to generate a Gaussian pulse with an input waveform represented by V_i , dc blocking capacitor represented by C_1 , inductor for pulse position adjustment represented by L_1 , dc source having a bypass capacitor (C_2), current-limiter (R_2), and RF-choke (L_2). R_3 is a fine-tuning resistor and is utilized for higher compression purposes. The optimized values of these parameters are: $L_1=20$ nH, $R_2=50$ Ω , $R_3=4.6$ K Ω , with a supply voltage of 5V and SRD diode models from the MAVR-0447 series. First, a varactor-diode-based model is utilized with non-commensurate parametric values, which are termed as triple-stacked arrangement having a single varactor diode per NLTL section and then followed by double and triple varactor diodes connected in series per NLTL section. So, by using a combination of single, double, and triple varactor diode cells, we utilize a greater portion of the non-linearity in comparison to the single varactor diode arrangement. This arrangement is more clearly shown in Figure 4.8, followed by coupling capacitance (C_D). L_1 - L_6 represents the fixed inductances utilized in the NLTL, while R_L is the terminal resistance and selected as 50 Ω .

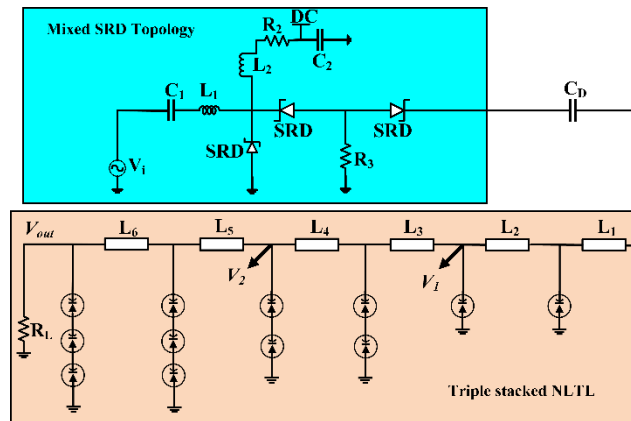


Figure 4.8 Six section triple stacked NLTL circuit for rising time compression integrated with mixed SRD topology

The pulse response of the circuit without a triple-stacked NLTL is given in Figure 4.9. It shows that we have an overall pulse duration of almost 80ps, FWHM of 40ps, and detailed ringing level of -9.61dB which is given as:

$$R_r = 20 \log \frac{\text{Ringing Amp}_{(\text{peak/peak})}}{\text{Pulse Amp}_{(\text{peak/peak})}} \quad (4.17)$$

Also, the waveform response is calculated at the intermediate nodes marked as V_1 and V_2 and are termed as node A and node B, respectively. The pulse response at node A is shown in Figure 4.10, where we have an overall pulse duration of almost 75ps, FWHM of 31ps, and detailed ringing level of -15.67dB. It is clear now that single varactor diodes per NLTL cell have improved the ringing level due to the soliton recombination process, but the compression is very limited in comparison to Figure 4.8. Similarly, the pulse response at node B is also shown in Figure 4.11, where we have an overall pulse duration of 68ps, FWHM of 26ps, and detailed ringing level of -14.70dB. It clearly shows that stacking the NLTL with two varactor diodes generates a higher compression in comparison to a single varactor diode per NLTL cell. Finally, we have a stacked triple varactor diodes per NLTL cell, and its output waveform is shown in Figure 4.12. The overall pulse duration, in this case, is almost 48ps, FWHM of 15.78ps, and detailed ringing level of -15.78dB. This further verifies the concept of stacked varactor diodes per NLTL cell. Although stacking varactor diodes in series would increase the circuit size, it is still highly pertinent as it is very advantageous in achieving compressed Gaussian pulses that can ultimately also be transformed to monocycle and

higher Gaussian derivatives. To highlight the novelty in much of stacked NLTL in a clearer way, we have plotted the response of the proposed circuit with and without stacked NLTL along with input voltage in Figure 4.13.

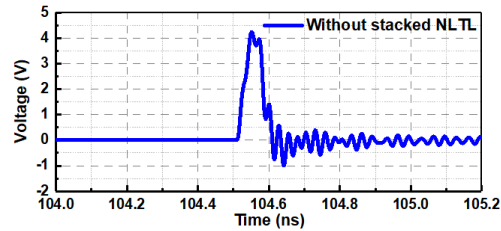


Figure 4.9 Response of the circuit without the integration of triple stacked NLTL

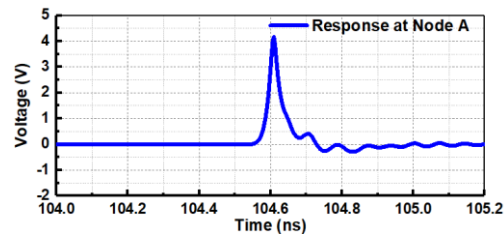


Figure 4.10 Response of the circuit at Node A

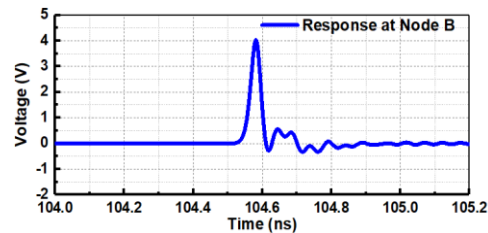


Figure 4.11 Response of the circuit at Node B

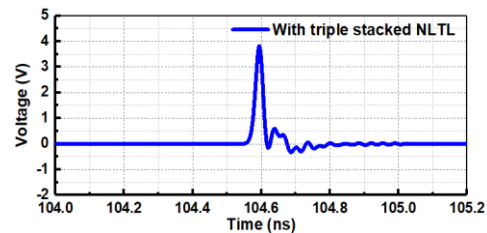


Figure 4.12 Response of the circuit with the integration of triple stacked NLTL for rise time compression

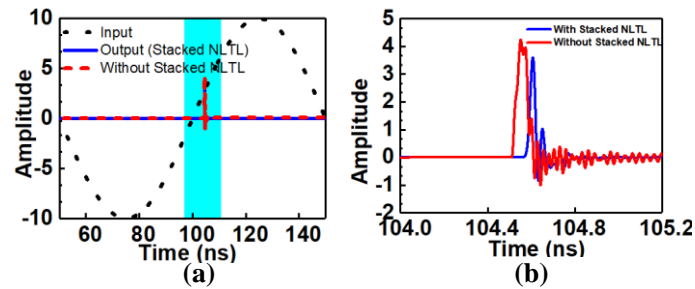


Figure 4.13 (a) Response of the proposed circuit with and without stacked NLTL along with input voltage. (b) Zoomed-in view output response with and without stacked NLTL

4.4.2 Prototype and measurement of the proposed pulse generator based on rising time-compression

The proposed ps pulse generator based on a triple-stacked NLTL integrated with a mixed SRD topology is also fabricated and measured. The fabricated prototype was built on a Roger R04350 substrate and described in Figure 4.14 with a block diagram of the experimental setup. As can be seen in Figure 4.14, the experimental setup comprises of the proposed pulse generator, a dc power supply, an arbitrary wave generator, an oscilloscope, and a universal testing fixture where the proposed fabricated circuit is placed. AWG Keysight M8190A is used for generating an input of 10-MHz PRF, and an oscilloscope is set for observing the output waveform. The dc biasing circuit is developed, which is controlled by a dc voltage source. The snapshot of the experimental setup during measurement is also indicated in Figure 4.15.

The corresponding response from simulation and measurement of the proposed pulse generator is also demonstrated in Figure 4.16. It is clear from the figure that the proposed pulse generator has a good performance with a slight variation in delay of almost 0.009ns. Also, the ringing level is degraded from -15.78dB to -11.29dB, but its overall pulse shape is well maintained. Also, the corresponding ringing level is within an acceptable level, which is appropriate for efficient UWB system applications. The variation in delay and ringing level in the measured result is due to the utilized RF cables, thermal behavior, and parasitic effects related to soldering.

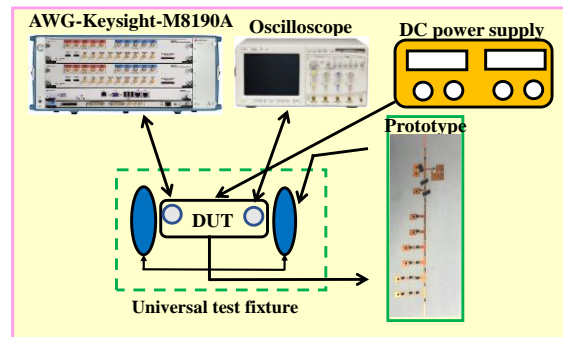


Figure 4.14 Block diagram of experimental setup of the proposed fabricated ps pulse generator based on rise time compression and triple stacked NLTL (The corresponding biasing wires are not indicated in the prototype)

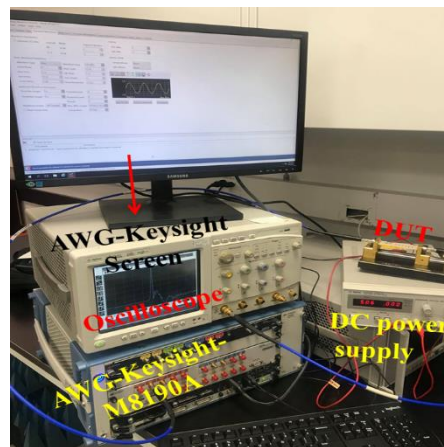


Figure 4.15 Snapshot of experimental setup during measurement

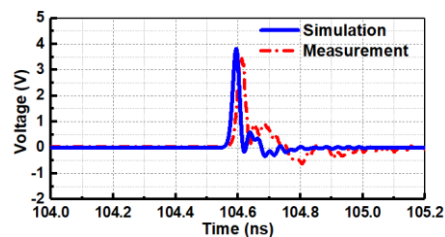


Figure 4.16 Response from simulation and measurement of the proposed pulse generator based on rise time compression and triple stacked NLTL

4.4.3 Simulation and measurement of integrated triple-stacked NLTL pulse generator based on fall time-compression

Let's consider the circuit diagram of a six-section triple-stacked NLTL circuit for fall time-compression integrated with a mixed SRD topology, as demonstrated in Figure 4.17. The parameters and values of this circuit are similar to Figure 4.8 with a modification in the polarities of the varactor diodes utilized in the triple-stacked NLTL block. The circuit in Figure 4.17 that is responsible for the fall time-compression-based NLTL edge sharpener is also fabricated, and the prototype is shown in Figure 4.18 (a), which is fabricated on Roger R04350 substrate. The PCB design is conducted using a Laser micromachining tool at the Poly-Grames Research Centre, and the corresponding SRD diodes, varactor diodes, fixed inductors, and load resistor are all soldered on the PCB as shown in Figure 4.18 (a). The experimental setup and measurements are the same as shown in Figure 4.14. The response from the simulation and measurement of the proposed pulse generator based on the fall time-compression and triple-stacked NLTL is also measured in reference to the setup in Figure 4.14. The final results are shown in Figure 4.18 (b). It is seen that the simulation and measurement agree well with a slight discrepancy in amplitude and ringing level having an undesirable delay of 0.015ns. The pulse width is almost 53ps with a pulse amplitude of 3.59V from simulation and 3.24V from measurement. The simulated detailed ringing level is almost -9.52dB and, in the measured results, has slightly degraded to -8.43dB.

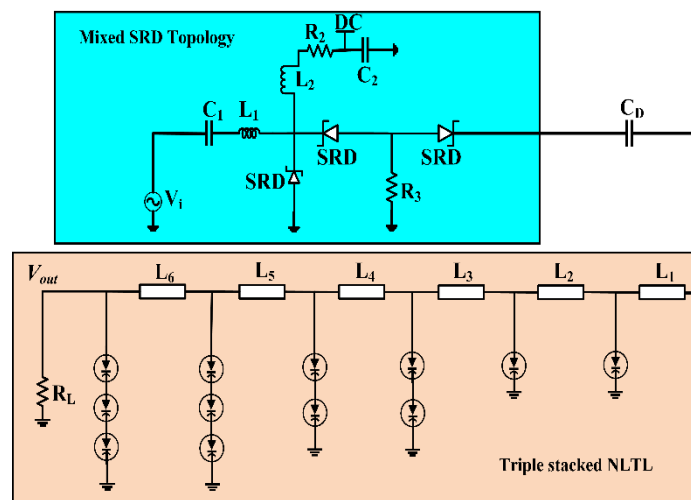


Figure 4.17 Six section triple stacked NLTL circuit for fall time compression integrated with mixed SRD topology

Among the parasitic elements, we identify the inductance in series and the capacitance in parallel with diodes as the critical parasitic elements, which lead to high-amplitude spikes and degradation of pulse duration. Consider the case where the simulation is carried out with ideal diodes and with parasitic elements. Its effect on FWHM is shown in Figure 4.19 versus R_3 that clarifies that how the optimization and selection of a specific parameter are performed.

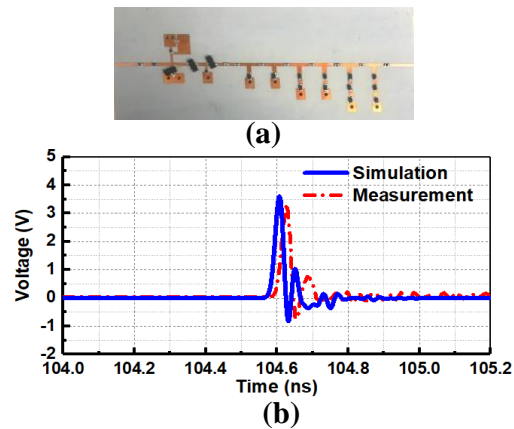


Figure 4.18 Prototype and measured response. (a) Prototype photo of the circuit for corresponding fall time compression. (b) Response from simulation and measurement of the proposed pulse generator based on fall time compression and triple stacked NLTL

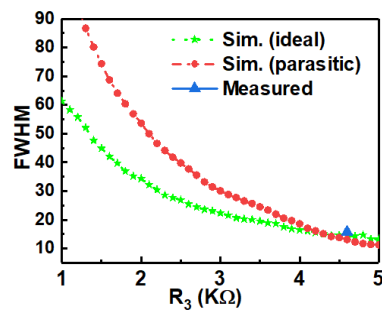


Figure 4.19 Computed and circuit simulated FWHM for parasitic and ideal cases

4.4.4 Frequency response of the proposed pulse generators

Figure 4.20 shows the frequency bandwidth of the generated pulse for the case of a fall time-compression, which is calculated using a fast Fourier transform. As it can be seen from the power spectrum plot, the proposed pulse generator fits into the well-defined spectrum masks for IR-UWB communication, according to US and European regulatory authorities [1,104].

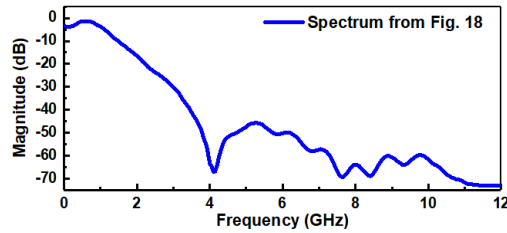


Figure 4.20 Power spectrum of the proposed pulse generator-based on fall time compression and triple stacked NLTL

4.4.5 Reconfiguring the proposed pulse generators to higher derivatives including monocycle and doublet pulses

The proposed pulse generators are also very flexible and can be easily reconfigured and transformed to higher-order Gaussian pulse shapes [105], including the monocycle pulse shape (1st order Gaussian derivative), doublet pulse shape, and so on. We will briefly discuss the modification to the monocycle pulse shape by integrating a simple pulse shape selector stage, as shown in Figure 4.21. This circuit is a modified form of Figure 4.8 by integrating a pulse shape selector stage where we have a coupling capacitance ($C_c=100$ nF), PIN diode, capacitance ($C_D=2.2$ pF), and load resistance ($R_L=50$ Ω). C_c is selected to be very larger compared to C_D in order to discard it through the differentiator calculation. The PIN diode inserted in parallel with C_D creates a reconfigurable capability between the Gaussian and corresponding monocycle pulse shapes. When the PIN diode is turned ON, a clean Gaussian pulse is generated while bypassing C_D . When the PIN diode is OFF, the overall capacitance of the differentiator becomes $C_{eff} = C_P + C_D$, and now a monocycle pulse is generated at the output.

Figure 4.22 shows the corresponding response of the reconfigurable pulse generator based on the triple-stacked NLTL in connection with the rise time-compression concept. It is seen that when the

PIN diode is ON, we have a Gaussian pulse shape similar to what is shown in Figure 4.12. When the PIN diode is OFF, we have a monocycle pulse shape. It is noteworthy that the triple-stacked NLTL based on the rise time-compression capability is modified for the monocycle pulse shape. However, this same technique may be adopted for the pulse generator based on the fall time-compression capability. The proposed pulse generators can also be easily modified to other innovative pulse shapes and will be useful for future arbitrary waveform generators.

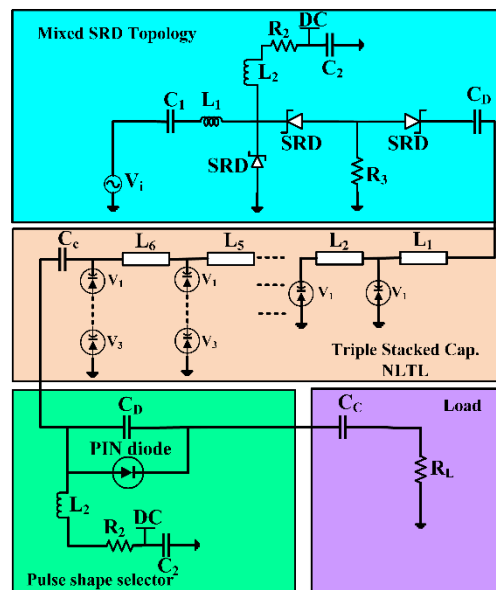


Figure 4.21 Reconfigurable behavior between monocycle and gaussian pulse shapes based on six sections triple stacked NLTL circuit for rise time compression integrated with mixed SRD topology

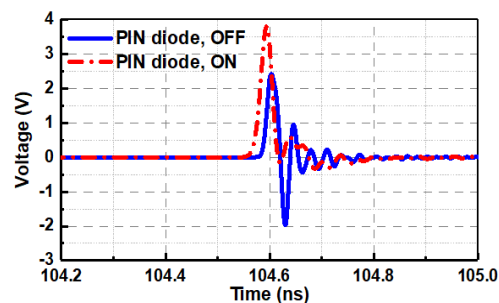


Figure 4.22 Output response of the reconfigurable pulse generator based on triple stacked NLTL.

(a) Gaussian pulse shape; (b) Monocycle pulse shape

4.5 Comparison with state-of-the-art pulse generators published in literature

The proposed NLTL-based pulse generators are compared with the literature's current state of the art. The important pulse parameters, including the FWHM, pulse width, pulse amplitude, and detailed ringing level, are tabulated in Table 4.1. The implemented techniques of all pulse generators are also mentioned briefly in Table 4.1 in order to differentiate them. It also shows that different techniques used for developing pulse generators have their own limitations. In addition, the table shows that our proposed concept is rather flexible and other important pulse shapes can be integrated easily by introducing pulse shaping networks. Table 4.1 shows the superiority of the proposed technique in comparison to the implemented techniques found in literature, specifically regarding overall pulse duration and compression capability. The detailed ringing level in Table 4.1 is calculated based on equation (4.17). The simplicity, flexibility, reconfigurable capability, cost-effectiveness, and good quality characteristics will make the proposed pulse generator one of the best candidates to be deployed in IR-UWB and ultrafast electronics applications.

Table 4.1 Comparison of the proposed pulse generators with current states of the arts. (N/A means not applicable and N/R means not reported)

Ref.	Technique implemented	Amp.	Pulse width	Ringin g	FWH M	Pulse shape	Compr ession
		(V)	(ps)	(dB)	(ps)		
[4]	Combination of FETs with four identical delay blocks	0.16	500	-6.11	N/R	7 th order Gaussian	N/A
[5]	Single SRD based pulse generator integrated with diode network	6.7	220	N/R	60	Gaussian Monocycle	N/A
[9]	Integrating Schottky diodes with pulse shaping filter	1.8-1.85	1000	-17.15	>300	Monocycle	Rise
[10]	Resonant tunnelling diodes (RTD)	0.31-0.93	100-120	N/R	35-40	Gaussian Monocycle	N/A
[11]	Combination of SRDs and tapered NLTL	3.95	80	-32.7	26	Gaussian	Rise
[12]	Delay circuits integrated with phase detector circuits	0.8	407.8	N/R	N/R	5 th order Gaussian	N/A
[18]	NLTL based shock wave pulse generator	0.1-0.3	800	-12.4	N/R	Gaussian	Fall

[19]	NLTL integrated with single SRD	3.3	130	-22.1	N/R	Gaussian	Rise
[20]	NLTL designed on standard 90nm CMOS technology	0.8-1.25	N/A	N/R	N/A	N/A	Only fall transients
[21]	Combination of rise time pulse train generator with pulse shaping circuit	1.67	(300-500)	-14.6	214	Gaussian Monocycle	Rise
[31]	Combination of pulse generating and pulse forming portions	1.4	150	-11	N/R	Monocycle	N/A
[32]	Integrating Schottky diodes with RC high pass filter	0.4	300	-17	120	Gaussian Monocycle	Rise
[33]	Gallium arsenide based NLTL circuit	-8	N/A	-6.02	N/A	N/A	Only fall transients
[34]	SRD in combination with wave-shaping circuit	1.88	307	-22.5	110	Gaussian	N/A
[35]	Pulsed oscillator integrated with pulse shaping filter	0.673	500	N/R	N/R	5 th order Gaussian	N/A
[36]	Single SRD based pulse generator	5	600	-7.32	175	Gaussian	N/A
[37]	Schottky diode connected in series with single SRD	0.6-0.8	170-400	-16	N/R	Gaussian	N/A
Prop. (1)	Six sections triple stacked NLTL integrated with mixed SRD topology for developing rise time compression-based pulse generator	3.82	48	-15.78	15.78	Gaussian Monocycle	Rise
Prop. (2)	Six sections triple stacked NLTL integrated with mixed SRD topology for developing fall time compression-based pulse generator	3.24	53	-9.52	17	Gaussian Monocycle	Fall

4.6 Conclusion

In this work, we have presented an NLTL-based scheme for maximizing the compression factor in pulse generation. A combination of single varactor diode cells and stacked varactor diode cells per NLTL section is utilized and a greater non-linearity portion of the varactor diodes is achieved. It is shown that this scheme generates a higher compression factor in both rising and fall time of NLTL circuits in comparison to single varactor diode per NLTL cell. Two pulse generators based on rising and fall time-compression respectively are simulated, fabricated, and measured. Important pulse parameters including the FWHM, pulse duration, and detailed ringing level are calculated and compared with the current state of the art reported in literature. The power spectrum of the proposed pulse generators is also presented, and it is demonstrated that they fit well within the IR-UWB spectrum set by regulatory agencies. It is also demonstrated that the proposed pulse generators have the capability to get reconfigured into monocycle pulse shape by integrating with a simple pulse shaping network. The proposed design has applications in IR-UWB systems and ultrafast electronics, including medical and sensing applications, and will pave the way for future picosecond technology development. Also, the proposed technique combined with pulse shaping network will also open a new horizon for the future development of ultrafast electronic instrumentation and measurements, interconnects, and system especially in connection with ultrashort pulse transmission.

CHAPTER 5 ARTICLE 3: THEORETICAL AND EXPERIMENTAL ANALYSIS OF PULSE COMPRESSION CAPABILITY IN NON- LINEAR MAGNETIC TRANSMISSION LINE

MuhibUr Rahman and Ke Wu

Published in the *Journal of Applied Physics*, vol. 131, no. 1, p.013901, 2022.

(Publication date: January 03, 2022)

This paper presents a theoretical and experimental analysis of non-linear magnetic transmission lines and demonstrates the phenomenon and capability of a simultaneous rise and fall time compression. A theoretical approach is formulated in which a new version of the modified Korteweg-de Vries Equation is developed utilizing the Gardner Morikawa transformation, continuum limit approximation, Toda-lattice approximation, and Mei theory of Maxwellian circuits. The proposed theoretical foundation work is validated through experimental demonstration. The pulse generation in a non-linear magnetic transmission line is then studied in detail, and the output pulse characteristics are explored under different magnetic field strengths and arbitrary magnetization directions. In particular, output waveforms are analyzed in terms of pulse amplitude, full width half maximum, detailed ringing level, and figure of merit. Magnetic losses that arise in the ferrite material are modeled. It is shown that these losses are responsible for originating dissipative effects, which in turn deteriorate pulse shaping and increase ringing level. The localized disturbance within ferrimagnetic materials is also studied, and its impact on the output waveforms is also discussed. This study can potentially open up a new and fruitful entry to explore magnetic materials and their impacts in the field of ultrafast electronics in parallel with nonlinear electrical transmission lines.

5.1 Introduction

Ferrimagnetic materials, such as yttrium iron garnet (YIG), have extensively been utilized in microwave electronics due to a number of attractive features for microwave and wireless systems. It is mainly attributed to these materials' high saturation magnetization and high resistivity. They become non-reciprocal and show anisotropic properties through magnetization using a static magnetic field H_{dc} . These characteristics make them into a great building platform to develop

microwave components and circuits as well as to realize the compression of short electromagnetic pulses.

Previously, YIG materials have widely been utilized in the design of ferrite delay lines, phase shifters, tunable filters, circulators, and variable attenuators [106-108]. Some of them have been used as a useful scheme for a discrete and continuous tuning range, which basically calls for four famous methods, namely the YIG-based magnetic tuning [109,110], varactor-based electric tuning [111-113], ferroelectric tuning such as Barium Strontium Titanate (BST) [114], and Micro-Electro-Mechanical-Systems or MEMS-based tuning [115-117]. All these techniques can achieve a limited tuning range due to a limited degree of freedom and thus cannot meet the optimal design requirements.

Also, a significant amount of interest has been invested in the investigation of nonlinear transmissions lines (NLTLs) for their well-established pulse sharpening and tuning capability. Regarding the classification of NLTLs, there exist nonlinear electrical transmission lines (NLETLS) which are usually composed of periodically loaded or distributed segments of lumped nonlinear inductors and capacitors.

The input pulse that is injected to the line will be subject to the dispersion and non-linear effects, which, finally, will be decomposed into a series of solitons. In this case, the non-linear components include both non-linear inductors, whose inductance changes nonlinearly with the corresponding current, and non-linear capacitors, whose capacitance is a nonlinear function of the applied biasing voltage [79,118,119]. Based on this configuration, we can establish three different types of NLTELS: capacitive, inductive, and hybrid NLETLS. An NLTL based on magnetic materials has yet been explored through theoretical considerations and experimental analysis. NLETLS with both capacitive and inductive non-linearity were explored [120,121]. Pulse compression capability was studied and validated theoretically, showing that a hybrid NLETLS possesses greater pulse compression as compared to the capacitive and inductive NLETLS structures per stage. In [122], such hybrid NLETLS structures were proposed, which can be utilized for RF generation as well. However, this study was only based on theory and simulations without experimental validations.

With the above discussion in mind, it is clear that NLETLS, including capacitive, inductive, and hybrid NLETLS structures, have been well explored theoretically and experimentally and its capability for pulse compression as well. However, in the present state of research, no attempt has

been made to explore the NLMTL and its capability for pulse generation and compression considering the difficulties and problems that arise in magnetic materials. Although gyromagnetic NLTLs (NLGTLs) were studied for high power microwave applications [122], they have a completely different state of operation and modeling foundation as their basic structure is entirely different from the NLMTL. These NLGTLs are designed in a way to be loaded with a nonlinear ferrite cores. Its corresponding wave Equation is easily transformed to a modified KdV-Burgers Equation that includes frequency dispersion, dissipation, and 3rd order non-linearity terms [123]. They are more advantageous than NLETLS due to their capability of stronger pulse oscillations and higher RF conversion efficiency. Also, it utilizes the stronger non-linearity of the ferrite-based inductance instead of the non-linearity caused by NLETLS.

Since the entire state of operation and geometrical topology of an NLMTL is different from a NLGTL, we need a special solution for the NLMTL; it cannot be completely visualized via the KdV or KdV-Burgers Equation because of localized disruptions in ferrimagnetic materials [124]. Moreover, it is well known that capacitive NLETLS are described by a non-linear lattice devised by Toda [76, 77]. The Toda lattice can be explained by a corresponding difference-differential Equation which was first used by Toda to model wave propagation. It was also previously explored that Toda Equations can be transformed into corresponding KdV Equations Under certain conditions. Additionally, the binary operator method was discovered [125]; it possesses the capability of formulating the exact solution of KdV or modified KdV Equations Hence, the strategy is developed so that we first utilize the K.K Mei theory of Maxwellian circuits [126] to obtain the basic difference-differential Equations of the unit section of an NLMTL. Then, it will be extended based on the continuum limit approximation and will be made equivalent to the Toda lattice form [78]. Next, using a specific scaling and transformation proposed by Gardner and Morikawa and modified by Karpman and Maslov we can transform our Equations into a modified KdV form [80,127]. Finally, with the binary operator technique, an exact solution can be derived for NLMTLS. In [128], they deployed the K. K. Mei theory to obtain the basic differential Equations of hybrid NLETLS, and then the perturbation and fixed point homotopy were further utilized to obtain a stable solution and improve its convergence. Inspired from this modeling strategy, NLMTLS were considered in this work; their corresponding soliton solutions were obtained and their pulse compression capability in arbitrary directions of magnetization were demonstrated. The classification of NLTL is well summarized in Figure 5.1.

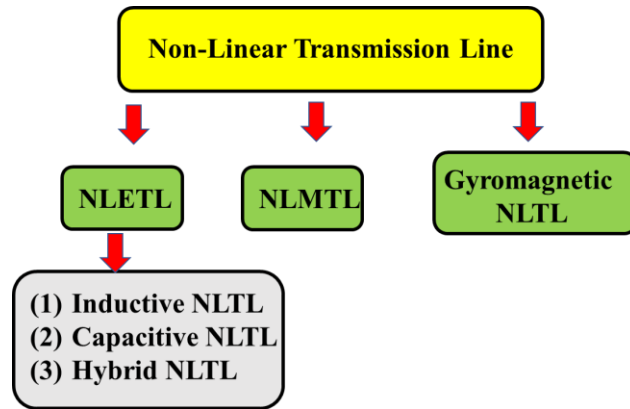


Figure 5.1 Classification of NLTLs

The objective of this paper is to develop a theoretical and experimental concept for the analysis of NLMTLs considering the localized disturbances that arise within ferrimagnetic materials. NLMTLs will be shown to present the capability of simultaneous rise and fall time compression due to its simultaneous control of magnetic field strength and applied biasing voltage. A theoretical background is proposed in this scenario by utilizing the K. K. Mei theory of Maxwellian circuits, various transformations and approximations, which lead to a new version of the modified KdV Equation. This Equation can easily be solved using the binary operator technique. Also, the arbitrary magnetization conditions of the magnetic materials are considered. An experimental setup is conceived and discussed. Measured results are provided to validate the pulse generation and compression under different magnetization conditions. This study will create an entry into the field of ultrafast electronics, which can benefit from the simultaneous non-linearity from magnetic materials and NLETLs for pulse compression features.

This paper is arranged as follows. Section II provides a detailed investigation of the theoretical developments of NLMTLs with an emphasis on magnetization conditions. Section III explains the step-by-step approach to the design and modeling concepts of non-linear transmission lines and their corresponding transformation to NLMTLs. Section IV presents the results with a detailed discussion based on the measurement setup, theoretical validation, output waveform response of NLMTLs at different magnetic fields, bias voltages, and arbitrary magnetization direction with fixed magnetic field strength. Section V provides comparison between NLMTL and NLGTL while Section VI concludes and summarizes the overall research work.

5.2 Theoretical development of NLMTLs

In this section, we begin with a detailed theoretical analysis of NLMTLs, which is used in this work. Here, we consider a unit section of an NLMTL shown in Figure 5.2, which comprises of a nonlinear magnetic flux induced in the corresponding n th section and represented by ϕ_n ; a nonlinear charge per unit section represented by Q_n ; a dissipative series impedance per unit section represented by Z_n ; and a leakage conductance represented by G_n .

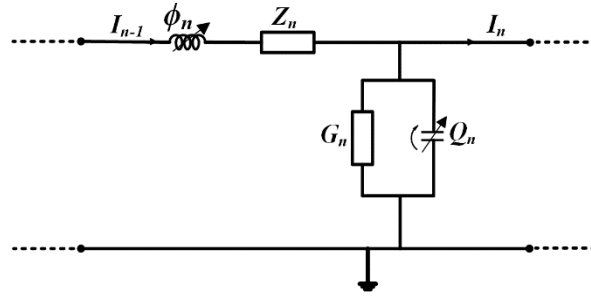


Figure 5.2 Unit Section of NLMTLs

The corresponding difference-differential Equations for a unit section of NLMTLs are given by:

$$I_{n-1}(t) - I_n(t) = G_n V_n + \frac{\delta}{\delta t} Q_n = G_n V_n + C \frac{d}{dt} V_n(t) \quad (5.1)$$

$$V_n(t) - V_{n+1}(t) = Z_n I_n + \frac{\delta}{\delta t} \phi_n \quad (5.2)$$

where $I_n(t)$ is the current passing through an n th nonlinear inductor with corresponding inductance $L[I_n(t)]$. Equations (5.1) and (5.2) can be transformed into the following simplified form:

$$I_{n+1} + I_{n-1} - 2I_n = K \frac{\delta^2}{\delta t^2} \phi_n \quad (5.3)$$

where K is a parameter used to simplify the analysis and is given as $K = -2C_d(V)/F(V_0)$ having $F(V_0)$ that is a function of the applied dc bias voltage V_0 , and $C_d(V)$ is determined from the measurement of differential capacitance calculated as $C_d(V) = dQ/dV$. Now, the term I_n must be changed into a continuous form. Thus, the McLaurin expansion [129] will be utilized as such:

$$I_{n+1} = [\exp(\partial/\partial n)] I_n \quad (5.4)$$

where n is now interpreted as a continuous variable, and the corresponding left-hand side of equation (5.3) will become:

$$I_{n+1} + I_{n-1} - 2I_n = \frac{\delta^2 I}{\delta x^2} + \frac{1}{12} \frac{\delta^4 I}{\delta x^4} + \frac{1}{6!} \frac{\delta^6 I}{\delta x^6} + \dots \quad (5.5)$$

$$K \frac{\delta^2}{\delta t^2} \phi_n = \frac{\delta^2 I}{\delta x^2} + \frac{1}{12} \frac{\delta^4 I}{\delta x^4} + \frac{1}{6!} \frac{\delta^6 I}{\delta x^6} + \dots \quad (5.6)$$

Next, the magnetic-flux induction as a function of frequencies and dc magnetic fields H_z must be evaluated. Since we know that there are three main dynamical Equations to model the nonlinearity of the magnetic materials, namely the Landau and Lifshitz Equation, the Gilbert Equation, and the Bloch-Bloembergen Equation based on phenomenological grounds. The latter one is selected for its capability to find the exact solution. The imaginary part of permeability in a transverse field is given by:

$$\mu = 1 - \frac{\gamma M_s (\omega - \gamma H_z)}{(\omega - \gamma H_z)^2 + (\gamma h_0)^2 T_1/T_2 + (1/T_2)^2} \quad (5.7)$$

where M_s signifies the saturation magnetization; γ stands for the gyromagnetic ratio; ω the angular frequency; H_z the applied static field; h_0 is RF magnetic field; while T_1 and T_2 represent the spin-lattice and transverse relaxation time, respectively.

When the geometry of NLMTLs is placed within the pole of a tunable magnet such that it can be magnetized in an arbitrary direction with arbitrary angles θ and φ as shown in Figure 5.3, the nonlinear permeability tensor and corresponding T_1 and T_2 , are now given as [130]

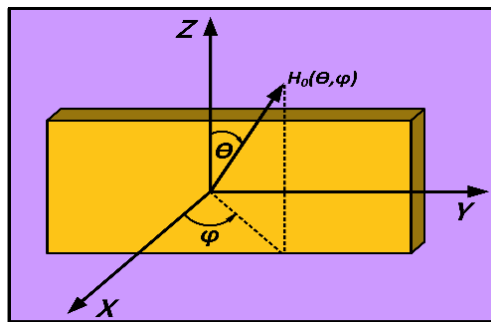


Figure 5.3 Geometry of NLMTLs magnetized in arbitrary angles H_θ and H_φ

$$|\tilde{\mu}| = \begin{vmatrix} \mu_{11} & \mu_{12} & \mu_{13} \\ \mu_{21}^* & \mu_{22} & \mu_{23} \\ \mu_{31}^* & \mu_{32}^* & \mu_{33} \end{vmatrix} \quad (5.8)$$

$$\mu_{11} = \mu' + (1 + \mu') \cos^2 \varphi \sin^2 \theta \quad (5.9)$$

$$\mu_{12} = \frac{1}{2}(1 - \mu') \sin 2\varphi \sin^2 \theta + j\kappa' \cos^2 \theta \quad (5.10)$$

$$\mu_{13} = \frac{1}{2}(1 - \mu') \cos \varphi \sin 2\theta - j\kappa' \sin \varphi \sin \theta \quad (5.11)$$

$$\mu_{22} = \mu' + (1 - \mu') \sin^2 \varphi \sin^2 \theta \quad (5.12)$$

$$\mu_{23} = \frac{1}{2}(1 - \mu') \sin \varphi \sin 2\theta + j\kappa' \cos \varphi \sin \theta \quad (5.13)$$

$$\mu_{33} = 1 - (1 - \mu') \sin^2 \theta \quad (5.14)$$

$$T_1 = \mu + (1 - \mu) \cos^2 \varphi \sin^2 \theta \quad (5.15)$$

$$T_2 = \frac{(1 - \mu)}{2} \sin 2\varphi \sin^2 \theta + j\kappa \cos \theta \quad (5.16)$$

Next, the magnetic flux is calculated while considering the permeability tensor from the above analysis. The general version of the magnetic flux is given by:

$$\phi_n = L_0 \int_0^I \mu(h_0) dh_0 = L_0 I + \frac{L_0 E}{\sqrt{F}} \frac{1}{\gamma \alpha} \tan^{-1} \left(\frac{\gamma \alpha I}{\sqrt{F}} \right) \quad (5.17)$$

where,

$$h_0 = \alpha I, \quad E = -(\omega - \gamma H_z) \gamma M_s, \quad F = (\omega - \gamma H_z)^2 \quad (5.18)$$

Now, by expanding ϕ_n we get:

$$\phi_n = L_0 \left(I + \frac{E}{\sqrt{F}} \right) \left(\frac{1}{\gamma \alpha} \right) \left(\frac{\gamma \alpha}{\sqrt{F}} \right) I - \frac{\left(\frac{\gamma \alpha}{\sqrt{F}} \right)^3}{3} I^3 + \frac{\left(\frac{\gamma \alpha}{\sqrt{F}} \right)^5}{5} I^5 - \dots \quad (5.19)$$

We can rewrite equation (5.19) more compactedly as:

$$\phi_n = L_0 \left(1 + \frac{E}{F} \right) I - \frac{L_0 E}{F^2} \left(\frac{\gamma \alpha}{3} \right)^2 I^3 + \frac{L_0 E}{F^4} \left[\frac{\gamma \alpha}{5} \right]^4 I^5 - \dots \quad (5.20)$$

By using the first and second terms from equation (5.20), then considering the approximation on the right-hand side of equation (5.3), and finally by applying the continuous approximation of equation (5.6) to the right-hand side of equation (5.3), the outcome yields the following form:

$$mI_n - n(I^3)_n = I_{xx} + \frac{2I_{xxxx}}{4!} + \frac{2I_{xxxxx}}{6!} + \dots \quad (5.21)$$

where,

$$m = L_0 K \left[1 + \frac{E}{F} \right], \quad n = L_0 K E \frac{(\gamma\alpha)^2}{F^2} \quad (5.22)$$

New space and time variables are used, based on the Gardner-Morikawa transformation [80] with specific scaling, as given in equation (5.23), to balance the time derivative, fourth derivative and nonlinear terms to the same order in I :

$$\xi = \varepsilon^{1/2}(x - t), \quad \tau = \varepsilon^{3/2}t \quad (5.23)$$

By expanding I , we get:

$$I = \varepsilon^{1/2}f^{(1)} + \varepsilon f^{(2)} + \varepsilon^{3/2}f^{(3)} + \dots \quad (5.24)$$

where ε is a parameter that makes the expansion more convenient. From Equation (5.23), the following identities can be verified.

$$\frac{\partial^2}{\partial t^2} = \varepsilon \frac{\partial^2}{\partial \xi^2} - \varepsilon^2 \frac{\partial^2}{\partial \xi \partial \tau} + \varepsilon^3 \frac{\partial^2}{\partial \tau^2} \quad (5.25)$$

$$\frac{\partial^2}{\partial x^2} = \frac{\partial^2}{\partial \xi^2} \quad (5.26)$$

Now by introducing these identities into equation (5.6) on different orders of ε such that $\varepsilon=3, 5/2$, and $7/2$, we obtain a set of Equations as follows.

$$-2m \frac{\partial^2 f(2)}{\partial \xi \partial \tau} + 4n \frac{\partial^2 f(1)^2 f(2)}{\partial \xi^2} - \frac{1}{12} \frac{\partial^4 f(2)}{\partial \xi^4} + (m-1) \frac{\partial^2 f(4)}{\partial \xi^2} = 0 \quad (5.27)$$

$$2m \frac{\partial^2 f(1)}{\partial \xi \partial \tau} + \frac{1}{3} n \frac{\partial^2 f(1)^3}{\partial \xi^2} - \frac{1}{12} \frac{\partial^4 f(1)}{\partial \xi^4} = 0 \quad (5.28)$$

$$-2m \frac{\partial^2 f(3)}{\partial \xi \partial \tau} + 2m \frac{\partial^2 f(1)}{\partial \tau^2} + 4n \frac{\partial^2 f(1)^3}{\partial \xi \partial \tau} - \frac{\partial^2 f(5)}{\partial \xi^2} - \frac{1}{12} \frac{\partial^4 f(3)}{\partial \xi^4} = 0 \quad (5.29)$$

As can be seen, equation (5.28) provides a balance between the fourth derivative and nonlinear terms. So now we can write it in the following general form:

$$\left(2mu_{\xi\tau} + \frac{nu_{\xi\xi}^3}{3} + \frac{u_{\xi\xi\xi\xi}}{12} \right) = 0 \quad (5.30)$$

Finally, by integrating equation (5.30) with respect to ξ we can generate the following new version of the modified KdV Equation as:

$$\left(2mu_{\tau} + \frac{nu_{\xi}^3}{3} + \frac{u_{\xi\xi\xi}}{12} \right) = 0 \quad (5.31)$$

This equation can also be written into other forms as well, such as the squared hyperbolic form which is achieved by using the binary operator method [125]. Equation (5.31) shows that NLMTLs possess a soliton solution with corresponding single soliton and multiple soliton solutions. We will use a single soliton solution and validate it via experimental analysis in different scenarios in the coming sections.

5.3 Design and modelling of NLMTLs

For the purpose of design, we have selected an NLMTL of six sections, as shown in Figure 5.4, which has a distributed model, as depicted in Figure 5.4 (a), and a corresponding equivalent circuit model, as described in Figure 5.4 (b). Here, the source pulse is characterized by V_s and R_s ; Z_0 represents the characteristics impedance of the transmission line utilized; and d denotes the physical length of unit section. This circuit is biased by a DC source, triggered by the input voltage (V_s) and has current limiter (R), RF choke (L_1), distributed capacitance of microstrip line (C_0), equivalent inductance (L), junction capacitance (C_m), and parasitic series resistance of the varactor diode (R_m).

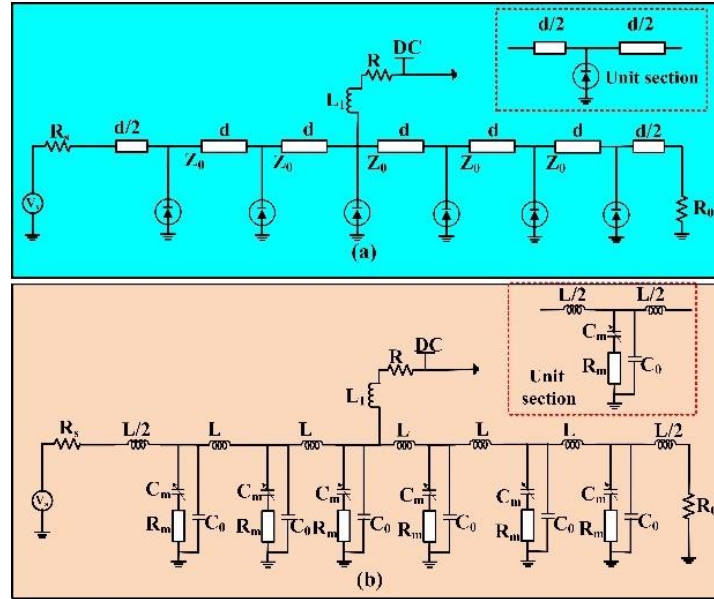


Figure 5.4 NLMTL with six sections. (a) Distributed model of NLMTL configuration; (b) Equivalent circuit model of NLMTL configuration

The cut-off frequency of this network in Figure 5.4 (b) can be given by:

$$\omega_{per} = \frac{2}{L[C_0 + C_m(V)]} \quad (5.32)$$

Considering $R_m=0$, the voltage of the next node is then written as:

$$V_0(t) = V_m[t - T(V)] \quad (5.33)$$

where, $T(V) = \sqrt{L_0(C_0 + C_m(V))}$. The junction capacitance of the varactor diode is responsible for the NLTL's delay, which is given by:

$$C_m(V) = \frac{C_{j0}}{\left(1 + \frac{V}{\phi}\right)^k} \quad (5.34)$$

where k represents the diode coefficient and is usually in the range of 1-3. The corresponding phase velocity, in this case, is given by:

$$v_p = \frac{1}{\sqrt{L(I)C(V)}} \quad (5.35)$$

The expression for the dispersion of the NLMTL can be extracted by considering a unit section, as shown in Figure 5.4. To simplify the derivation, we consider that $R_m=0$. The characteristic ABCD matrix for a single section is thus given by [106]:

$$\begin{bmatrix} A & B \\ C & D \end{bmatrix} = \begin{bmatrix} 1 & \frac{j\omega L}{2} \\ 0 & 1 \end{bmatrix} \begin{bmatrix} 1 & 0 \\ j\omega C & 1 \end{bmatrix} \begin{bmatrix} 1 & \frac{j\omega L}{2} \\ 0 & 1 \end{bmatrix} \quad (5.36)$$

$$C = C_0 + C_m = \frac{1}{V_h - V_l} \int_{V_l}^{V_h} C_m(V) dV \quad (5.37)$$

where, V is the applied bias voltage of the varactor, and V_h and V_l represent an upper and lower level of the voltage, respectively. The delay difference at each section of the NLMTL can be estimated as:

$$\Delta T = T(V_l) - T(V_h) = \sqrt{L[C_0 + C_m(V_l)]} - \sqrt{L[C_0 + C_m(V_h)]} \quad (5.38)$$

The propagation constant of the line is calculated by:

$$\cosh(\gamma d) = \frac{A+D}{2}, \quad \text{where } \gamma = \alpha + j\beta \text{ (m}^{-1}\text{)} \quad (5.39)$$

where α and β represent the attenuation and phase constants, respectively, and d stands for the physical length of the NLMTL. A lossless case is considered for simplicity in which $\cosh(\gamma d)$ is reduced to corresponding $\cos(\beta d)$. From Equation (5.36), the lossless dispersion relation can be extracted as:

$$\cos(\beta d) = 1 - \frac{\omega^2 LC}{2} \quad \text{or} \quad (\beta d) = \cos^{-1} \left[1 - \frac{\omega^2 LC}{2} \right] \quad (5.40)$$

The corresponding characteristic impedance of the line can be extracted from equation (5.36) as:

$$Z = \sqrt{\frac{B}{C}} = \sqrt{\frac{L}{C} - \frac{\omega^2 L^2}{4}} \quad (5.41)$$

Figure 5.5 shows the dispersion relation, while Figure 5.6 shows the characteristic impedance as a function of frequency for the corresponding unit cell configuration. It is obvious from the dispersion model that the NLMTL unit cell possesses a lowpass characteristic. The Bragg frequency is basically the low pass corner frequency at which βd (propagation factor or phase term)

becomes equal to π . The impedance becomes zero and is selected to be 12 GHz in our case. From equations (5.40) and (5.41), we have:

$$f_B = \frac{1}{\pi\sqrt{LC}} \quad (5.42)$$

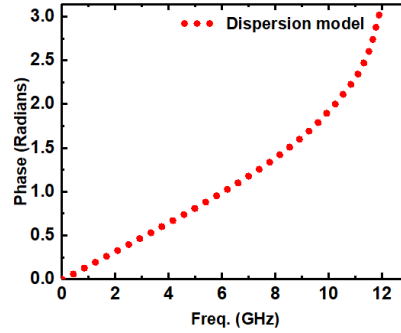


Figure 5.5 Dispersion diagram of lumped NLMTL unit cell configuration

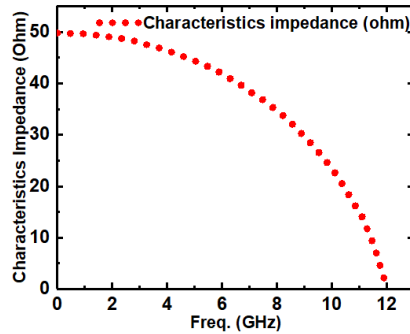


Figure 5.6 Characteristic impedance vs. frequency of lumped NLMTL unit cell configuration

5.4 Results and discussions

In this section, we will first develop and fabricate the NLMTL based on the analysis and modeling presented in Section III. Then, we will provide an experimental validation for our proposed NLMTL theory developed earlier in Section II. Finally, we will provide detailed results and discussions based on the NLMTL pulse compression principle, magnetization aspects, and corresponding NLMTL pulse generation characteristics in terms of amplitude, FWHM, ringing level, and overall figure of merit characteristics.

5.4.1 NLMTL circuits and measurement setup

The corresponding six- and ten-section NLMTL prototypes are developed and measured. The Bragg cutoff frequency is selected as 12 GHz based on the analysis discussed in Section III. Lumped components are soldered on the corresponding YIG material, as discussed in Figure 5.4 (a). SMV1231 varactor diodes are used here to perform the electrical tuning by varying the applied bias voltage from a DC source. It has been selected due to its high capacitance ratio and lowest series resistance.

Two different materials are investigated in this case. The YIG is selected for its low loss capability as compared to Nickel Ferrite (NF). A comparison between YIG and NF is shown in Table 5.1 detailing saturation magnetization, line width, and dielectric constant. The permeability components including dissipative and dispersive components at 12 GHz are also calculated [106]. It is plotted and the corresponding complex tensor dispersive permeability components of YIG and NF are shown in Figure 5.7 (a), while the complex tensor dissipative permeability components of both materials are shown in Figure 5.7 (b). It is obvious from Figure 5.7 that the ferromagnetic resonance (FMR) region begins nearly at 0.45T of applied magnetic biasing H_0 . The line width value of NF is much greater than the YIG's because the magnetic losses in NF begin to increase substantially even from 0.25T of the applied magnetic biasing, as can be seen in Figure 5.7. The FMR region in Figure 5.7 is highlighted in cyan color to be clearly indicated. Near the FMR region, both YIG and NF suffer from higher losses, though more pronounced in NF. The green region shows lower magnetic losses, and as such our device is operated below the FMR region. Hence, we have determined that, due to the incredibly low loss property of YIG, this material is more appropriate in the design and development of low loss NLMTL circuits. Similar characteristics can be seen for the dissipative permeability component as demonstrated in Figure 5.7 (b).

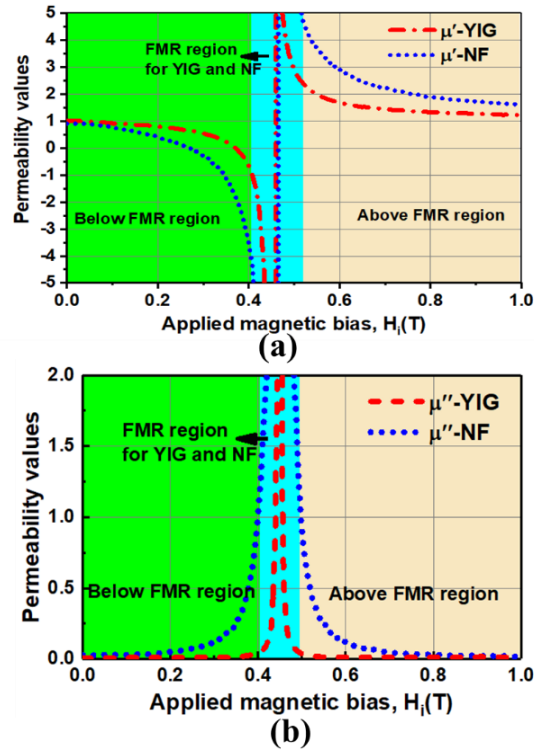


Figure 5.7 Calculated permeability components at 12 GHz. (a) Complex tensor dispersive permeability components of YIG and NF; (b) Complex tensor dissipative permeability components of YIG and NF

Table 5.1 Comparison between YIG and Nickel Ferrite

Ferrite material	Saturation Mag. ($4\pi Ms$)	Line Width (ΔH)	Dielectric constant (ϵ_r)	
			Mea.	Spec.
YIG	1780G	$\leq 170e$	14.81	$15.1 \pm 5\%$
NiFe ₂ O ₄	5000G	$\leq 1980e$	13.02	$13 \pm 5\%$

The experimental setup utilized for the measurement of NLMTL circuits comprises of a tunable magnet with the NLMTL placed between the poles of the tunable magnet. This tunable magnet is basically an electromagnet whose magnetic field induction may be changed by changing electric current of the electromagnet having two iron poles with very high μ_r . It is connected with the DTM-133 Digital Teslameter, which is used for changing the magnetic strength at different tensor aspects. The NLMTL is placed between poles of the tunable magnet and magnetized in the

transverse direction. The current source Sorenson DLM 60-10 is used to control the static magnetic field of the electromagnet. The corresponding DC magnetic field intensity within the poles of the electromagnet is measured using the probe. A DC power supply is used to change the capacitance of the varactors by changing the biasing voltage to perform electrical tuning. The input pulse is generated via an arbitrary wave generator (AWG-Keysight-M8190A-14Bit-12Ga/s) and the output is observed using an oscilloscope (Agilent infiumDSO81204B-12GHz-40Gsa/s). This setup delivers a maximum magnetic field of 1T within the poles of the electromagnet. The developed NLMTL circuits can also be magnetized at an arbitrary angle θ and φ by being rotated from a reference plane.

5.4.2 Experimental validation of NLMTL theory

This section demonstrates the validation of our theoretical approach based on the real-time circuits fabricated and measured as discussed in the previous sub-section. The corresponding output waveform is measured based on the setup discussed in previous section, with the selected six- and ten-section NLMTLs. First, an NLMTL with six sections is placed within the poles of the electromagnet and the corresponding output waveform is measured by generating a magnetic strength of 0.1T. The corresponding data extracted from the theoretical and experimental approaches are plotted and correlated in Figure 5.8. It can be seen that the measured results follow the theoretical trend with a very small deviation in amplitude and time. The error observed between amplitudes is less than 3% at the peak, which is quite appealing.

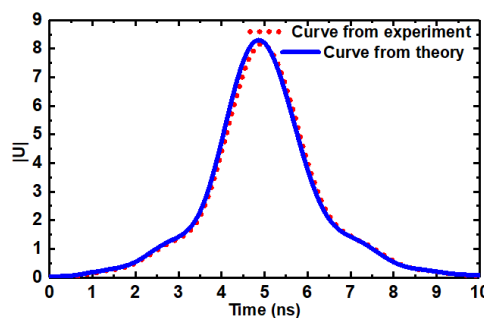


Figure 5.8 Output waveform of the implemented six-section NLMTL with $H_0=0.1T$ and data extracted from the theoretical approach (solid blue line), measurement result (dashed red line)

The ten-section NLMTL implemented and designed in this work is also measured with different magnetic field strengths and validated with the corresponding theoretical approach. The designed

ten-section NLMTL is placed within the poles of the electromagnet, and the corresponding output waveform is measured by generating a magnetic strength of 0.1T and 0.2T. The corresponding data obtained from the theoretical and experimental approaches are plotted and correlated in Figure 5.9 and Figure 5.10 for $H_0= 0.1\text{T}$ and 0.2T , respectively. It is clear from the plots that the theoretical approach formulated in Section II well matches at 0.1T. However, when the magnetic field strength is increased, there is an extensive ringing in measurements, which is due to the unexpected-localized disturbances in the ferrite materials. Though, we can clearly visualize the pulse duration and FWHM of the pulse for the developed theoretical study. The error observed between amplitude of the generated pulse is less than 7% of the peak when the magnetic field strength is 0.2T. A detailed ringing level of the pulse will also be visualized and investigated in the next sub-section.

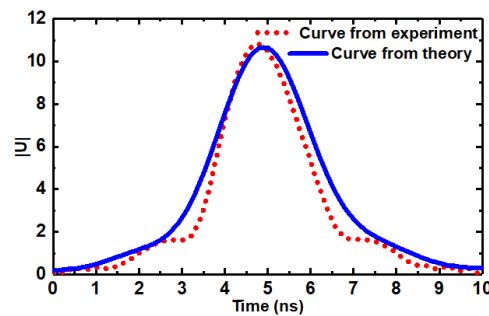


Figure 5.9 Output waveform of the implemented ten-section NLMTL with $H_0=0.1\text{T}$ and data extracted from the theoretical approach (solid blue line), measurement result (dashed red line)

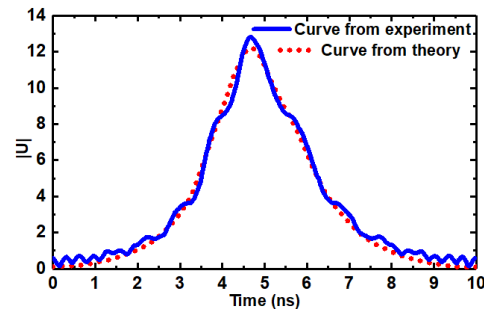


Figure 5.10 Output waveform of the implemented ten-section NLMTL with $H_0=0.2\text{T}$ and data extracted from the theoretical approach (dotted red line), measurement result (solid blue line)

5.4.3 NLMTL pulse compression capability

This section is dedicated to the investigation of the NLMTL pulse compression capability principle and its corresponding measured results in different scenarios. The pulse generation and compression characteristics of the designed NLMTL circuits are also discussed with corresponding responses. Output pulse waveforms are observed by simultaneously changing the magnetic field strength and biasing voltage of the varactors. We will first briefly explain the physical phenomena responsible for pulse compression in the ferrite materials. Then, we will show the corresponding measured results at different magnetic strength with different magnetization directions as well.

Consider a uniformly magnetized ferrite transmission line, as shown in Figure 5.11. Another transmission line having the impedance Z_0 is connected to the ferrite line as an input. An input pulse is injected on this line with a rise time T_R , as shown in Figure 5.11. The polarity of the present magnetic field of the pulse can be seen to be opposite to the polarity of the magnetization. Ultimately, spin reversal phenomena will start, and a large RF impedance will be seen by a pulse which is produced by a ferrite dissipation. However, the ferrite line will not appear as a large continuous impedance. Finally, the preliminary part of the ferrite line will be saturated. The large impedance will rapidly decrease having the saturated impedance Z_s , which is selected to be equal to input impedance Z_0 . As shown in Figure 5.11, this process will continue such that the spin saturation front propagates along the length of the line. When this front approach to the end of the ferrite line, the complete line will be oppositely magnetized to the original direction, and this occurs when $t=T_R$, as can be seen in Figure 5.11. It is also clear that when the pulse is injected at the initial part of the line, the spin reversal region will be large due to a small field within the ferrite. When the pulse amplitude increases, it will increase the spin saturation front velocity and eventually catch up to the field in the spin reversal region. This will ultimately sharpen the rise time, which can be further sharpened by increasing the magnetic bias.

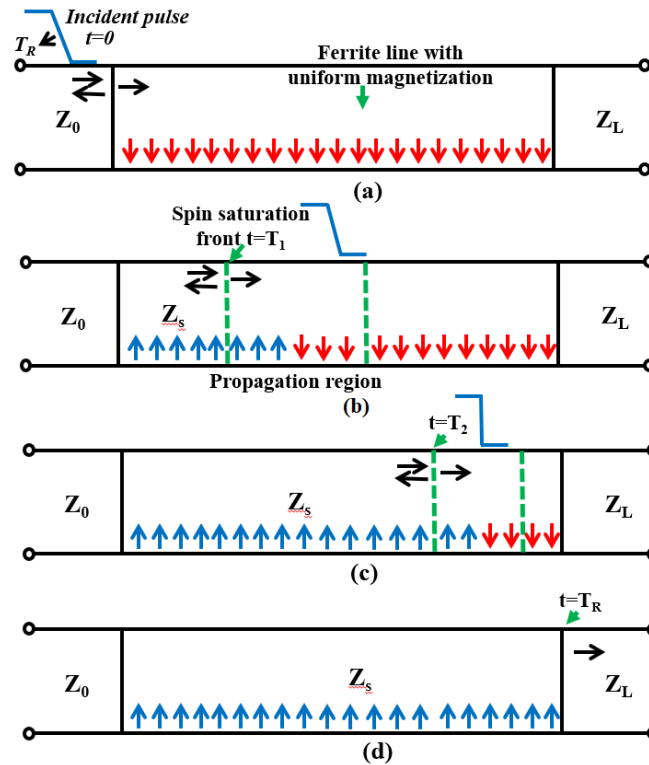


Figure 5.11 Principle of pulse sharpening behavior in ferrite material. (a) Spin saturation front at $t=0$; (b) Spin saturation front at $t=T_1$; (c) Spin saturation front at $t=T_2$; (d) Spin saturation front at $t=T_R$

A detailed measurement is performed to show the compression of the pulse passing through the NLMTL with varying magnetic field (H_0) and biasing voltage (V_b). Important pulse characteristics, which include amplitude, detailed ringing level, FWHM, and rise/fall time compression, are provided in each case. The detailed ringing level of the output pulse (R_l) in each case is also provided based on the following equation [14].

$$R_l = 20 \log \frac{\text{Ringing amplitude}_{\text{peak-to-peak}}}{\text{Pulse amplitude}_{\text{peak-to-peak}}} \quad (5.43)$$

The figure of merit (FOM) specifying and summarizing all these parameters is also provided based on the following equation:

$$FOM = \frac{\text{Pulse amplitude}}{FWHM \times \text{Ringing}(\%)} \quad (5.44)$$

The corresponding measured output waveforms of the ten-section NLMTL at different magnetic fields and biasing voltages, which have a fixed magnetization direction (θ, φ), are shown in Figure 5.12-5.15 along with the mentioned FWHM of the generated pulse. As can be seen from Figure 5.12 that when $H_0=0.1\text{T}$, we have a pulse with FWHM of almost 1.55ns, pulse amplitude of 10.5V, detailed ringing of almost -18.14dB (11.4%), and FOM of 0.59. When H_0 is increased from 0.1T to 0.2T, as shown in Figure 5.13, the pulse duration reduces and FWHM is improved from 1.55ns to 1.14ns. However, the corresponding peak to peak ringing level of the pulse also increases due to the local disturbances in the ferrite materials, which originates from losses and ultimately has a dissipative effect. The detailed ringing contribution, in this case, is almost -15.31dB (17.14%) which has been degraded. However, the overall FOM is improved from 0.59 to 0.62.

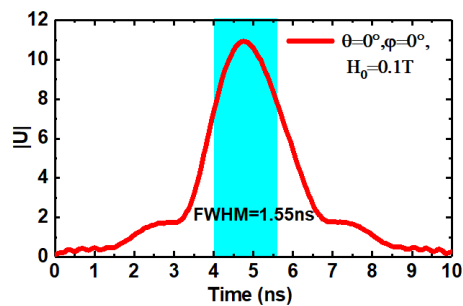


Figure 5.12 Measured output response of the ten-section NLMTL when $H_0=0.1\text{T}$

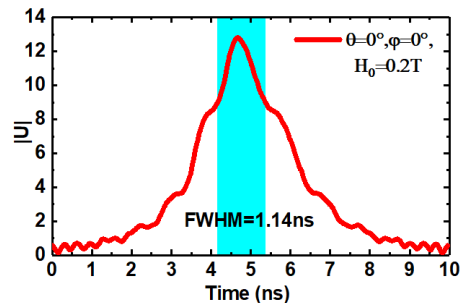


Figure 5.13 Measured output response of the ten-section NLMTL when $H_0=0.2\text{T}$

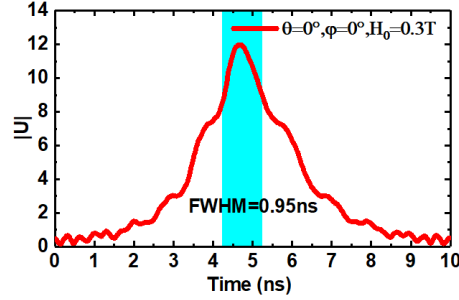


Figure 5.14 Measured output response of the ten-section NLMTL when $H_0=0.3T$

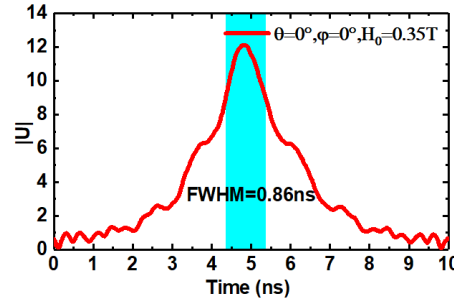


Figure 5.15 Measured output response of the ten-section NLMTL when $H_0=0.35T$

By changing the corresponding magnetic field and biasing voltage continuously, the FWHM is improved thanks to the corresponding rise/fall time compression effect. It also presents a degradation in ringing which arises from the originated losses, as judged and modeled in Figure 5.7. When $H_0=0.3T$, we have a pulse with FWHM of almost 0.95ns, pulse amplitude of 12.2V, detailed ringing level of almost -14.12dB (19.67%), and calculated FOM of 0.65, as shown in Figure 5.14. When H_0 is further increased from 0.3T to 0.35T as shown in Figure 5.15, the FWHM is improved from 0.95ns to 0.86ns. The detailed ringing contribution, in this case, is almost -13.63dB (20.8%) with the overall FOM improved from 0.65 to 0.68. So, clearly by increasing the magnetic field strength, we have a compression effect in the NLMTL with an increasing peak to peak ringing level. It must be noted that all the experiments here are performed below the FMR region as demonstrated in Figure 5.7. While dealing with ferrimagnetic materials, we need to be careful with the FMR region and need to operate either below or above that region. The overall performance in these scenarios in terms of pulse amplitude, FWHM, and ringing is summarized in Table 5.2.

Table 5.2 Summary of performance behaviors of NLMTL in terms of different important parameters

Magnetic field	Pulse amplitude (V)	FWHM (ns)	Ringing (dB)	FOM
0.1T	10.5	1.55	-18.14	0.59
0.2T	12.21	1.14	-15.31	0.62
0.3T	12.25	0.95	-14.12	0.65
0.4T	12.32	0.86	-13.63	0.68

The comparison between important metrics, which include compression factor, FWHM, and FOM, is plotted in Figure 5.16 and 5.17 for the six-section and ten-section NLMTLs, respectively. The compression factor is referenced as 2.37ns and 2.2ns for six- and ten-section NLMTLs, respectively, which are their corresponding FWHM in the non-magnetized case. Figure 5.16 and 5.17 both clearly reveal a reduction of FWHM and corresponding improvement in compression factor with increasing magnetic field. The overall FOM, which is defined in equation (5.44) and incorporates ringing behavior, is also improved with the increasing magnetic field strength in both cases. It is now evident that the ringing effect is increasing and become more dominant while approaching the FMR region, thus showing that this effect can be greatly mitigated by developing the extremely low loss magnetic materials.

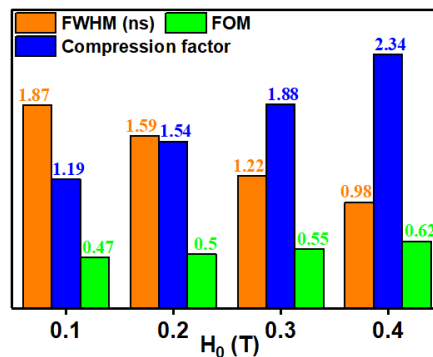


Figure 5.16 Comparison between important metrics of six-section NLMTL

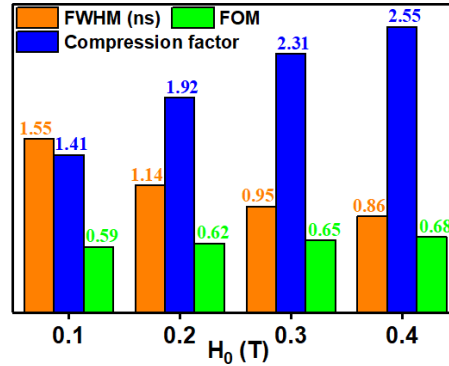


Figure 5.17 Comparison between important metrics of ten-section NLMTL

5.4.4 NLMTL pulse compression capability with arbitrary magnetization direction

The NLMTL is magnetized in different directions to visualize the pulse compression capability. It is seen that the NLMTL magnetized in $\theta=0^\circ$ and $\varphi=0^\circ$ has the highest pulse compression compared to other scenarios. This can be observed in Figure 5.18 and 5.19. First, an NLMTL is magnetized in such a way that φ is varied continuously with a fixed θ and $H_0=0.1\text{T}$. When $\theta=0^\circ$ and $\varphi=45^\circ$, we have a pulse with an amplitude of 8.85V, FWHM of 1.62ns, detailed ringing level of -17.72dB, and overall FOM of 0.42. When φ varies from 45° to 90° , we have a FOM degradation from 0.42 to 0.43 with a detailed ringing level of -18.72dB and an amplitude of 8.2V. This NLMTL behavior is shown in Figure 5.18 (a) and (b).

Figure 5.19 is also provided to show the behavior of the NLMTL by varying θ continuously with a fixed φ and a magnetic field strength of 0.1T. When $\theta=45^\circ$ and $\varphi=0^\circ$, we have a pulse with an amplitude of 8.3V, FWHM of 1.57ns, detailed ringing level of -16.73dB, and overall FOM of 0.36. When θ is varied from 45° to 90° , we have a FOM degradation from 0.36 to 0.22 with a detailed ringing level of -13.01dB and amplitude of 8.28V. As observed, when θ is changed from 0° to 90° , we have a switchable characteristic of bright to dark soliton based on the light-hill criteria [131]. Those solitons which satisfy the light-hill criterion are termed as bright solitons, while those which do not satisfy it are termed as dark solitons. This phenomenon can be further explored in the future, which is usually observed in the optical domain through very complicated techniques.

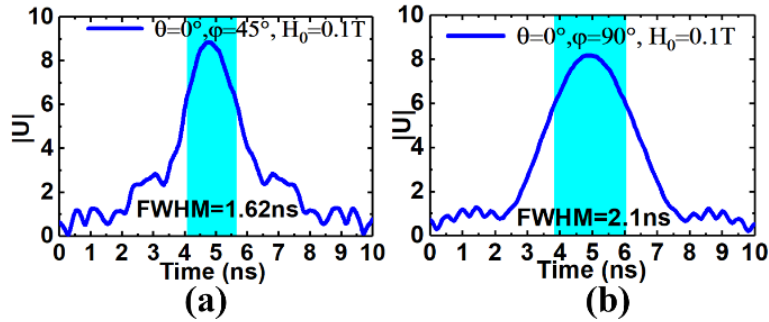


Figure 5.18 Measured output response of the ten-section NLMTL by varying ϕ with fixed θ . (a)

$\theta=0^\circ$ and $\phi=45^\circ$; (b) $\theta=0^\circ$ and $\phi=90^\circ$

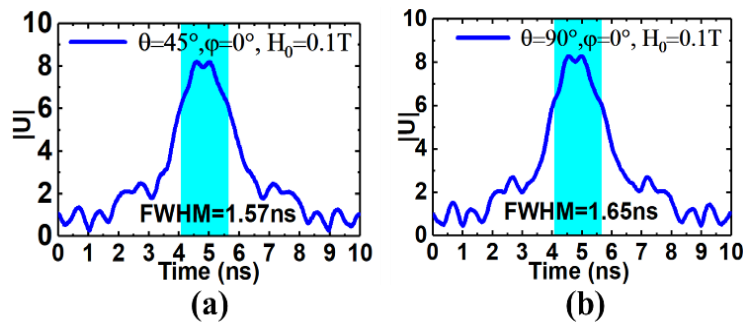


Figure 5.19 Measured output response of the ten-section NLMTL by varying θ with fixed ϕ . (a)

$\theta=45^\circ$ and $\phi=0^\circ$; (b) $\theta=90^\circ$ and $\phi=0^\circ$

5.5 Difference between NLGTL and NLMTL

The purpose of this section is to show the difference between the NLGTL presented in literature [39] and our proposed NLMLT. NLGTL is one of an NLTL type that has the capability to generate RF at high power [132,133]. Here, the medium that detaches the line conductor is built of magnetic materials. This type of NLTL is used as a compact, solid-state, RF source due to the magnetic moment in the ferromagnetic materials induced by damped gyromagnetic precession [37,134]. Externally applied biasing magnetic field and applied input pulse are set to control the amplitude and rise time of output generated pulses. The switching attributes of the ferrite which is basically the time it requires to switch from one state to the other on the material B-H curve, limit the corresponding rise time reduction [38].

Although NLGTLs were studied for high power microwave applications they have a completely different state of operation and modeling foundation as their basic structure is entirely different from the NLMTL. These NLGTLs are designed in a way to be loaded with a nonlinear ferrite core.

Its corresponding wave equation is easily transformed to a modified KdV-Burger's equation that includes frequency dispersion, dissipation, and 3rd order non-linearity terms [135]. They are more advantageous than NLETs due to their capability of stronger pulse oscillations and higher RF conversion efficiency. However, such a class of NLTL can only have the rise time compression capability and generate a tremendous amount of ringing during pulse generation and sharpening. They have high structural complexity and possess integration issues with other electronic circuitries as well.

To understand the difference in a much more compact way, we compared NLGTL and NLMTL based on their theoretical analysis, simulation, experiments, and observations. This is performed and summarized in Table 5.3 in terms of important parameters and the superiority of NLMTL can be seen in this connection.

Table 5.3 Summary of performance behaviors of NLMTL and NLGTL in terms of different important parameters

NLGTL	NLMTL
Continuous and nondispersive class of NLTLs, where the medium that separates line conductors is built from magnetic materials	Hybrid NLTL transformed to the magnetic regime, where NLTL circuitry is combined with microwave ferrite material.
Rise time compression is only possible	Both rise and fall time compression is possible due to variation of electric and magnetic field
A tremendous amount of ringing and cannot be controlled by any means	Ringing can be mitigated while taking care of magnetic field strength and biasing voltage
Can only use inductive non-linearity	Can use several variations due to tremendous flexibility (R, L, G, C)
Uniformity of bias magnetic field cannot be guaranteed within tunable magnet due to geometrical design	Uniformity of bias magnetic field is guaranteed within tunable magnet by placing iron plates to enclose bias fields
Stacking of the varactor diodes are not possible to increase non-linearity	Stacking of varactor diodes is possible which ultimately increases non-linearity

5.6 Conclusion

We presented a theoretical and experimental technique to analyze non-linear magnetic transmission lines (NLMTLs). A new version of the modified Korteweg-de Vries Equation is extracted, which uses different transformation and approximation schemes. The K. K. Mei's theory of Maxwellian circuits is effectively used to formulate the fundamental Equation of NLMTLs. It is shown that NLMTLs have the capability of simultaneous rise and fall time compression since magnetic field strength and biasing voltage can be varied at the same time. Also, the pulse generation capability of NLMTLs is studied in detail under different conditions for which the pertinent formulation is provided. The theoretical model agrees well with the experiments, and the measured results are shown in different possible scenarios. The losses generated within the ferrimagnetic material utilized—YIG in this case—create a dissipative effect and becomes more pronounced as we move towards the FMR region. This also increases the detailed ringing level. A metric termed as the FOM is set up to show the overall performance of pulses and is discussed in each case. The proposed analysis has provided a clear picture and deeper understanding of the NLMTLs, which were not previously investigated probably because of the sophisticated dissipative processes of ferrite materials. This study will pave the way for extremely low loss material investigations in ultrafast electronics in parallel with NLETL. As such, we will have the capability to simultaneously utilize the non-linearity of magnetic materials in addition with electrical non-linearity for pulse generation and compression characteristics.

CHAPTER 6 ARTICLE 4: THEORY AND PRACTICE OF PULSE COMPRESSION IN HYBRID AND GYROMAGNETIC NON-LINEAR TRANSMISSION LINES

MuhibUr Rahman and Ke Wu

Submitted in the *Journal of Applied Physics*, vol. 132, no. 12, p. 223902, 2022.

(Submission date: September 30, 2022)

This paper presents a comprehensive analysis of pulse compression capability in hybrid and gyromagnetic non-linear transmission lines (NLTLs). The corresponding theoretical analysis in the hybrid NLTLs is derived and discussed in detail with the generation and sharpening aspects of leading and trailing pulse edges. The parameters responsible for pulse sharpening are examined and their corresponding pulse compression capability is modelled by providing the output waveform while varying these parameters. A holistic overview and mathematical development of gyromagnetic NLTLs are also conducted, which are modeled and validated through an equivalent lumped element model. Important parameters such as saturation magnetization, gyromagnetic NLTL sections, and damping parameter are elaborated and their influences on pulse sharpening and compression capability are studied. Validation of the theoretical and parametric analysis is performed by an experimental demonstration. The results achieved from hybrid and gyromagnetic NLTLs are briefly summarized, and their corresponding advantages and disadvantages are highlighted. This research is set to provide a fresh and successful debut for investigating gyromagnetic and hybrid NLTLs and their inherent effects on pulse compression for future ultrafast electronic systems and interconnects.

6.1 Introduction

Non-linear transmission lines (NLTLs) inherently possess the capability to generate solitons having the ability to maintain their permanent pulse profile [78]. Since non-linearity is essential for the propagation of solitons, it cannot act in isolation. On the other hand, dispersion is a physical behavior that correspondingly counteracts the balance of non-linearity in NLTL [76]. Solitons that are usually generated in a lumped NLTL fall within the category of KdV solitons, which are

basically a single smooth hump [41]. The KdV solitons are usually based on the equation that approximately describes NLTL and often can be written in the following form [118]:

$$\frac{\partial u}{\partial t} + 6u \frac{\partial u}{\partial z} + \frac{\partial^3 u}{\partial z^3} = 0 \quad (6.1)$$

where the first term quantifies that it is a first-order evolution equation w.r.t t , and the second and third terms account for non-linearity and dispersion, respectively. The soliton solution for different cases was given in [120,128,136].

NLTLs are usually used for pulse generation and edges sharpening [4,137] and they are categorized into non-linear electrical transmission lines (NLETL) and non-linear magnetic transmission lines (NLMTL) [138]. NLETL further consists of three different types including non-linear capacitive transmission lines (NLCTL), non-linear inductive transmission lines (NLITL), and non-linear hybrid transmission lines (NLHTL) [132,133,138]. It was previously explored that NLETL and NLMTL have the ability of rising and fall time compression and the injected input pulse would be compressed after passing through NLTL. The minimum edge sharpening of a pulse is limited by the dispersive properties of the deployed NLTL [29]. A good approximation of rise and fall time reduction was given in different scenarios [79,127,139] of NLTL and it is usually determined by the difference among time delays of the corresponding sharpened edge of a pulse and peak of the waveform.

There exist another important class of NLTL that falls within the NLMTL category, and it is termed as gyromagnetic NLTL [134]. This type of NLTL comprises of continuous nondispersive NLTL, in which the inner conductor is lined with ferrite rings and the medium isolating the line conductors is constructed of a magnetic substance. Conceptually, the LC discrete line (hybrid NLTLs) and the non-dispersive continuous line are distinct. Gyromagnetic NLTLs are supposed to operate above 3.0 GHz [140] having an RF conversion efficiency of roughly 12%, which are essential for possible use in satellite communications. The gyromagnetic NLTL's operating concept is totally based on the compression of output pulse in relation to that of the applied input pulse since the permeability of a magnetic material depends on current. As the current pulse travels down the transmission line, the magnetic permeability drops along with the corresponding current amplitude. The peak of the pulse will move more quickly than its lower amplitude components due to the fact that the propagation velocity (v_p) in a corresponding nonlinear magnetic medium is $v_p = c/\sqrt{\epsilon_r \mu_r(I)}$, where

c represents the light speed in free space and ϵ_r , μ_r is the relative permittivity and permeability of the magnetic medium, respectively. Since the input leading edge of the pulse with a larger amplitude travel more quickly than the parts with smaller amplitudes, and so the pulse that appears on the output is sharper than the input pulse. In this scenario, the corresponding rise time of the output pulse can be estimated as [4], $\Delta T = \sqrt{L'C'} - \sqrt{L_{sat}C'}$, where L' and C' represents the inductance and capacitance of a coaxial line, respectively and L_{sat} is the coaxial line inductance at saturation.

The magnetic moment of ferrite M , which is originally aligned with external axial magnetic field H_{ext} , interacts with the corresponding azimuthal field produced by the current pulse around the inner conductor, causing M to create a damped precession motion about the longitudinal axis. As the pulse current travels along the line, the magnetic precession movement in the ferrite occurs, leading to high-frequency oscillations. These oscillations have a shape that is comparable to the input pulse but has a shorter rise time, and they are superimposed on the output pulse amplitude. Owing to the transition time from one state to the other on the material B-H curve (known as the spin reversal region), which is correlated with the relaxation frequency of the corresponding magnetic material [141], the rise time reduction in this case is limited by the switching properties of the ferrite.

Recently, gyromagnetic lines have been the subject of various research activities due to the reason that they have a better RF conversion efficiency and can produce stronger pulse oscillations at higher frequencies. Another advantage of the gyromagnetic NLTLs over the dielectric NLTL is the utilization of a higher inductance nonlinearity that ferrite can generate in comparison to the nonlinearity generation in a nonlinear ceramic capacitance. There also exist another class of NLTL known as dielectric NLTL where non-linear dielectric slabs are periodically loaded to a parallel brass plates [139]. All these NLTL types are briefly summarized in the form of Figure 6.1.

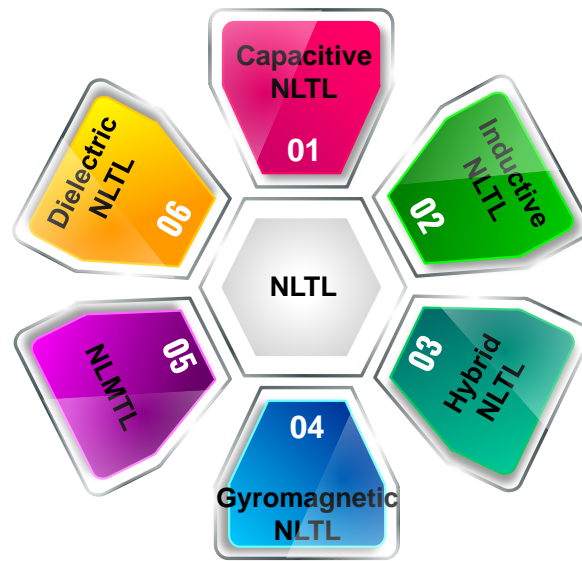


Figure 6.1 Different types of NLTL utilized in literature for pulse generation and compression

The objective of this work is to present a comprehensive analysis of the pulse generation and compression capability in hybrid and gyromagnetic NLTLs. The parameters principally responsible for pulse sharpening in the gyromagnetic and hybrid NLTLs are provided, and their corresponding pulse compression capability is modeled. The results achieved in case of hybrid and gyromagnetic NLTLs are briefly summarized and tabulated, and their corresponding advantages and disadvantages are discussed and highlighted.

This paper is organized as follows. Section II is dedicated to the theoretical and design aspect of hybrid NLTLs with a corresponding equivalent model. Section III provides the design and theoretical analysis of gyromagnetic NLTLs with corresponding transmission-line and lumped-element models. Section IV describes the compression capability of these NLTLs whereas section IV(A) is completely dedicated to hybrid NLTLs analysis and section IV(B) for gyromagnetic NLTLs. This section discusses all the pulse parameters responsible for pulse sharpening and its influence on output waveforms. Section V gives an experimental demonstration which is followed by section VI that compares hybrid NLTLs with gyromagnetic NLTLs. Finally, section VII concludes the overall research work.

6.2 Theory and design of hybrid NLTL

Consider a hybrid NLTL as shown in Figure 6.2 having nonlinear capacitors configuration represented in Figure 6.2 (a) while nonlinear inductors configuration represented in Figure 6.2 (b). To fully understand this nonlinear circuitry, we need to model its behavior mathematically and analyze its effect on pulse sharpening. The corresponding equations for the hybrid NLTL case is given as:

$$\frac{\delta I}{\delta x} = -\frac{\delta Q}{\delta t} \quad (6.2)$$

$$\frac{\delta V}{\delta x} = -L \frac{\delta I}{\delta t} \quad (6.3)$$

where,

$$V = T(Q) + R \frac{\delta Q}{\delta t} \quad (6.4)$$

where I , V , and Q represent the transmission line current, voltage, and charges, respectively, while the conductance per unit length is represented by R^{-1} . T signifies the voltage of the nonlinear capacitance, and is given as:

$$T(Q) = \frac{1}{C_0} (Q_0 + \eta Q^3) \quad (6.5)$$

where η represents the cubic nonlinearity strength and small-signal transmission line capacitance is shown by C_0 . To show the shock front's steady-state form, equation (6.2)-(6.5) can be solved as:

$$Q^2(n) = \frac{1}{2} Q_s^2 \left[1 - \frac{\tanh(n - x_0)}{w} \right] \quad (6.6)$$

where $n=x-vt$, v and Q_s represent the propagation velocity and charge amplitude of the shockwave, w represents the width of the corresponding shock front, and x_0 is a constant that describes the shock front's original position. As can be observed, the shock's velocity increases as the shock's amplitude and nonlinearity strength increase. Also, increasing non-linearity decreases the width of the shock wave which correspondingly decreases the pulse duration.

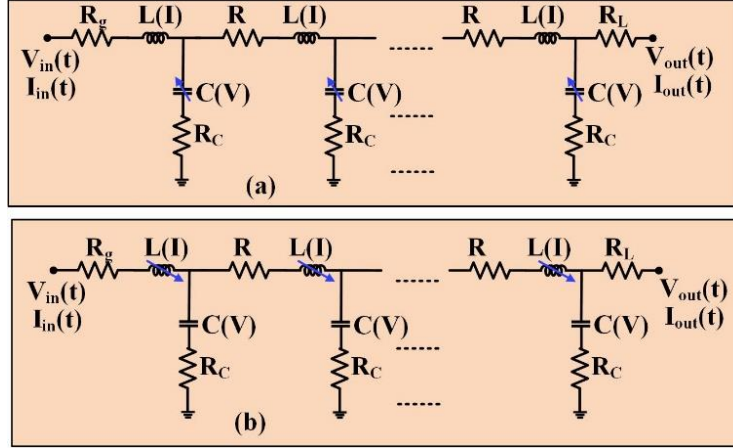


Figure 6.2 Hybrid NLTL having (a) nonlinear capacitors configuration; (b) nonlinear inductors configuration

Let's now take a look at the hybrid scenario depicted in Figure 6.2, where the series inductance is based on current and the shunt capacitance is dependent on voltage, resulting in a line with a constant characteristic impedance that can be terminated without a variable characteristic impedance. Considering the case of the square root non-linearity, we have:

$$C(V) = \frac{C_0}{(|V|)^{1/2}} \quad (6.7)$$

$$L(I) = \frac{L_0}{(|I|)^{1/2}} \quad (6.8)$$

The equations governed by the voltages and currents in the case of the LC ladder network as shown in Figure 6.2 can be given as [133]:

$$L \frac{dI_n}{dt} = V_n - V_{n+1} \quad (6.9)$$

$$C \frac{dV_n}{dt} = I_{n-1} - I_n \quad (6.10)$$

The forward traveling wave solution can be given as:

$$I(n, t) = I_0 e^{j(\omega t - kn)} \quad (6.11)$$

$$V(n, t) = V_0 e^{j(\omega t - kn)} \quad (6.12)$$

And the dispersion relation is obtained utilizing the technique in [106]

$$LC\omega^2 = 2(1 - \cos k) \quad (6.13)$$

The wavelength that corresponds to the cutoff frequency ω_c is given as:

$$\omega_c = \frac{2}{\sqrt{LC}} \quad (6.14)$$

Now equation (6.13) can also be re-written as:

$$\begin{aligned} (1 - \cos k) &= \frac{LC\omega^2}{2} \\ \cos k &= 1 - 2\left(\frac{\omega}{\omega_c}\right)^2 \end{aligned} \quad (6.15)$$

The line impedance can be determined from equation (6.8)-(6.11) as:

$$Z = Z_0 e^{j\phi} = \frac{V_0}{I_0} \quad (6.16)$$

where, $Z_0 = \sqrt{\frac{L}{C}}$, $\sin \phi = \frac{\omega}{\omega_c}$. In the case of a network constructed from T and pi sections [106], the matched terminating impedance can be given by equation (6.17) and (6.18), respectively:

$$Z_T = Z_0 \sqrt{\left(1 - \frac{\omega^2}{\omega_c^2}\right)} \quad (6.17)$$

$$Z_{\Pi} = \frac{Z_0}{\sqrt{\left(1 - \frac{\omega^2}{\omega_c^2}\right)}} \quad (6.18)$$

An approximate wave equation based on the combination of equation (6.9) and (6.10) is given as:

$$LC\left(\frac{d}{dt}\right)^2 V_n = V_{n+1} - 2V_n + V_{n-1} \quad (6.19)$$

Expressing V_{n+1} and V_{n-1} in terms of Taylor expansion, we get:

$$LC'\left(\frac{\partial}{\partial t}\right)^2 V - \left(\frac{\partial}{\partial x}\right)^2 V \approx \frac{\partial^2}{\partial x^2} \frac{\partial^4 V}{\partial x^4} \quad (6.20)$$

where, $L'\delta x = L$ and $C'\delta x = C$ and the equation can be modified as:

$$\frac{\partial^2 V}{\partial t^2} + \varepsilon \frac{\partial^2 f}{\partial t^2} \approx \frac{1}{L'C_0} \left(\frac{\partial^2 V}{\partial x^2} + \frac{\partial x^2}{12} \frac{\partial^4 V}{\partial x^4} \right) \quad (6.21)$$

Now using a small parameter ε to express V as a power series expansion:

$$V(x,t) = \varepsilon V^{(1)}(x,t) + \varepsilon^2 V^{(2)}(x,t) + \dots \quad (6.22)$$

where $V^{(1)}$ and $V^{(2)}$ are the first and second-order approximations. For convenience, let's change the coordinates as [4]:

$$\xi = \varepsilon^{1/2}(x - ct), \quad \tau = \varepsilon^{3/2}(ct) \quad (6.23)$$

where, $c = 1/\sqrt{L'_0 C'_0}$ and collecting terms of ε having the same power, we obtain an equation for $V^{(1)}$ as:

$$2 \frac{\partial^2 V^{(1)}}{\partial \xi \partial \tau} - \varepsilon \frac{\partial^2 f}{\partial \xi^2} + \frac{\partial x^2}{12} \frac{\partial^3 V^{(1)}}{\partial \xi^4} = 0 \quad (6.24)$$

Now integrating it w.r.t ξ and considering nonlinearity of the form such that $f(V) = -\alpha V^2$, we are able to finally get:

$$\frac{\partial V^{(1)}}{\partial \tau} + \alpha V^{(1)} \frac{\partial V^{(1)}}{\partial \xi} + \frac{\partial x^2}{24} \frac{\partial^3 V^{(1)}}{\partial \xi^3} = 0 \quad (6.25)$$

which shows the modified form of the well-known Korteweg-De Vries (KdV) equation. It is a significant finding that shows that an initial voltage waveform of any arbitrary value $v(\xi,0)$ will split into a number of solitons traveling in the right direction with $\xi \rightarrow +\infty$ and an oscillatory dispersive wave traveling to the left $\xi \rightarrow -\infty$. This result also shows that a shock front on a nonlinear hybrid network will divide into an array of solitons while propagating along a line and ultimately its edge sharpening will occur depending on the rise and fall time limit such that [4]:

$$T_{rise,min} = \frac{\pi}{4} \sqrt{L'C(V_{max})} \quad (6.26)$$

$$T_{f,min}(10\% - 90\%) = \frac{8.8}{\omega_a(0)} \frac{1}{\sqrt{1 - v/\phi} - 1} \quad (6.27)$$

where, $\phi = 0.4V$, $T_{f,min}$ represents the fall time limit, and $T_{rise,min}$ represents the rise time limit. By varying an input rise time with constant line length, we obtain 10 to 90 % data for output pulse. In order to validate the theoretical formulation, we compare the output response from theory and

simulation for ten section hybrid NLTL as shown in Figure 6.3. It shows that the simulation and theoretical response agrees very well. It must be noted that the designing of ten section NLTL is performed in Advanced Design System (ADS) and the simulation is extracted from it which will be explained in section IV(a).

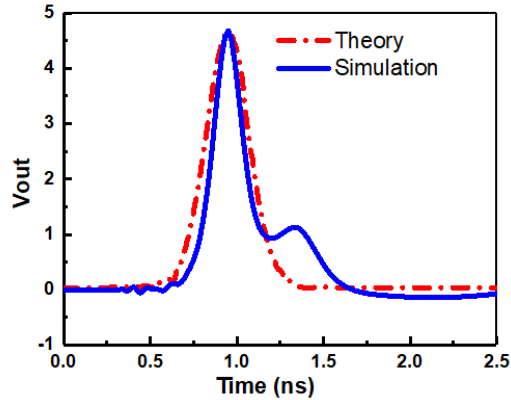


Figure 6.3 Response from theory and simulation for ten section hybrid NLTL

The results in equation (6.25) show that a shock front propagating along a nonlinear LC network will break into an array of solitons. This will ultimately produce the modulation of the delivered power to the load. Additionally, during this process, there will be an increasing fraction of the propagating power along the NLTL which will cause undesired oscillation. Because of instant variations of the matched values of the terminating impedance, any resistive termination will lead to the incident power reflection. This clarifies that there is a limit for rising or fall time where no further reduction exists and after that, the overall pulse shape will have deteriorated. For any resistive load, there exists an optimum point where peak power is maximum. This effect is well modeled for hybrid NLTL as shown in Figure 6.4 (a), where increasing RF load resistance increases pulse amplitude but at the cost of increased ringing. Increasing load resistance highly increases the oscillation amplitude. This eventually leads to a higher ringing, and it is modeled in Figure 6.4 (b), which shows the trend between RF load resistance versus the figure of merit (FOM). FOM is defined using equation 6.28 as:

$$FOM = \frac{\text{Pulse amplitude}}{FWHM \times \text{Ringing}(\%)} \quad (6.28)$$

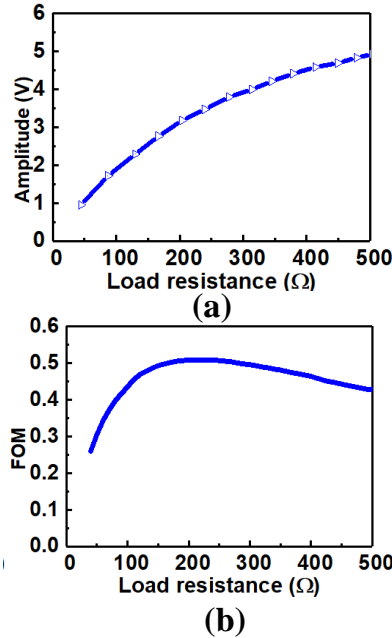


Figure 6.4 RF load resistance analysis. (a) load resistance analysis versus pulse amplitude in hybrid NLTL; (b) load resistance analysis versus FOM in hybrid NLTL

6.3 Theory and design of gyromagnetic NLTL

A continuous and nondispersive class of NLTL known as gyromagnetic NLTL uses magnetic materials as the medium separating the line conductors. The construction of the gyromagnetic line is detailed in Figure 6.5. As illustrated in Figure 6.5, the magnetic components that are possibly ferrite rings are positioned side by side along with the inner conductor.

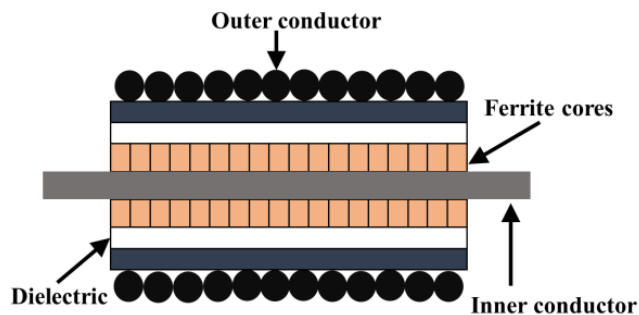


Figure 6.5 Gyromagnetic NLTL used for pulse compression

This kind of NLTL is advantageous over inductive NLTL due to the capability of generating stronger pulse oscillations at higher frequencies. Additionally, it may generate a wide frequency spectrum and use the stronger nonlinearity of the ferrite-based inductance. However, this type of NLTL can only support rise time compression.

We can derive the corresponding solitary wave solution and pulse width estimation of a gyromagnetic NLTL by analyzing its unit section. To this end, we consider a static axial bias in ferrite such that:

$$H_z = H_{bias} \quad (6.29)$$

The pulse current represented by i gives a mean value of the circumferential pulse field H_θ in the ferrite using the following relation:

$$H_\theta = i / \pi d_e \quad (6.30)$$

where effective diameter d_e of the ferrite is defined by

$$d_e = \frac{d_m - d_i}{\ln(d_m/d_i)} \quad (6.31)$$

where d_m represent the outer diameter and d_i represent the inner diameter of the utilized ferrite core. Now, the corresponding Landau-Lifshitz (LL) magnetization equation for a linear 1-D transmission line can be written as:

$$\frac{di}{dz} = -C_0 \frac{dv}{dt} \quad (6.32)$$

$$\frac{dv}{dz} = -\frac{d}{dt}(Li) \quad (6.33)$$

where i denotes the current, v specifies the voltage, L represents the inductance, and C_0 denotes the capacitance per unit length. Now equation (6.33) can be re-written in terms of flux as follows:

$$\frac{dv}{dz} = -\frac{d\phi}{dt} \quad (6.34)$$

where ϕ represents the circumferential flux per unit length. Then, separating the $d\phi/dt$ term into linear and magnetization-driven terms as:

$$\frac{d\phi}{dt} = L_0 \frac{di}{dt} + \mu_0 \frac{(d_m - d_i)}{2} \frac{dM_\theta}{dt} \quad (6.35)$$

where L_0 signifies the saturated inductance slope per unit length and dM_θ/dt shows the corresponding rate-change of the circumferential component of M . To obtain a numerical solution, the line is discretized into a series of axial elements having a length Δz . The corresponding equivalent circuit of the discretized model is shown in Figure 6.6. dM_θ/dt establishes the instantaneous magnitude of voltage sources $V_1 \dots V_m \dots V_n$ for each section, and can be given by

$$V_m = \mu_0 \frac{(d_m - d_i)}{2} \frac{dM_\theta}{dt} \Delta z \quad (6.36)$$

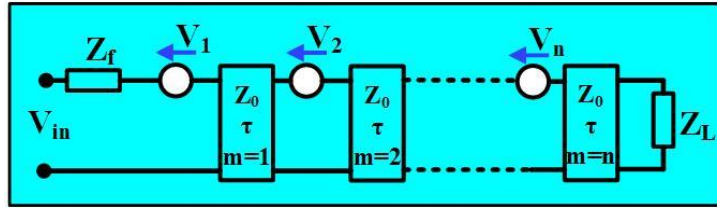


Figure 6.6 Transmission line element-based model of ferrite loaded gyromagnetic NLTL to be used for pulse compression

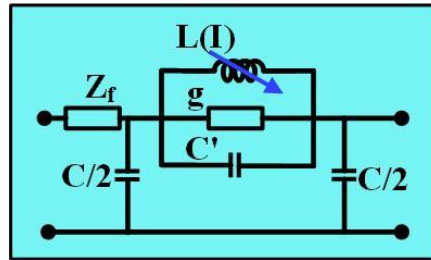


Figure 6.7 A typical unit section of a nonlinear gyromagnetic transmission line

Now, let's consider a typical unit section of the nonlinear gyromagnetic transmission line having a nonlinear inductor represented by $L(I)$, resistor g^{-1} , and pseudo-capacitor C' as shown in Figure 6.7. The resonance angular frequency of the ferrite can be formulated by

$$\omega_r = \mu_0 \gamma H_0 = \frac{1}{\sqrt{L_0 C'}} \quad (6.37)$$

Neglecting higher-order terms and deriving equation for change of current $I(t, z)$ lead to the following:

$$\frac{1}{L_0} \frac{\partial^2 \phi(I)}{\partial t^2} = \frac{1}{L_0 C} \frac{\partial^2 I}{\partial z^2} + \frac{g}{C} \frac{\partial^3 \phi(I)}{\partial z^2 \partial t} + \frac{1}{12 L_0 C} \frac{\partial^4 I}{\partial z^4} + \frac{C'}{C} \frac{\partial^4 \phi(I)}{\partial z^2 \partial t^2} \quad (6.38)$$

$$T = \varepsilon^{1/2} \left(t - \left[\sqrt{L_0 C} \right] z \right), \quad Z = \varepsilon^{3/2} \sqrt{L_0 C} z / 2, \quad G = \varepsilon^{1/2} G, \quad I = \varepsilon^{1/2} I \quad (6.39)$$

where ε is a small parameter and substituting equation (6.39) into equation (6.38), we get a modified KdV equation for the gyromagnetic NLTL case as:

$$u = I_s \operatorname{sech} \left[\sqrt{\left\{ \frac{\beta}{6 L_0 C} \left(\frac{1}{12} + \frac{C'}{C} \right) \right\}} |I_s| \left(t - \sqrt{L_0 C} \right) \times \left(1 + \frac{\beta}{6} I_s^2 \right)^{-1} z \right] \quad (6.40)$$

where the 1st order approximation of the flux is taken as:

$$\phi(I) \approx L_0 \left(1 - \frac{\beta}{3} I^2 \right) I \quad (6.41)$$

$$\beta = \frac{3n^2 (a^{-2} - b^{-2}) M}{16\pi^2 \ln(b/a) \left(1 + M/H_0 \right) H_0^3} \quad (6.42)$$

$$L_0 = \frac{\mu_0 n D \ln(b/a) \left(1 + M/H_0 \right)}{2\pi} \quad (6.43)$$

Finally, the half-power pulse width is calculated by

$$T_B = 1.76 \left[6 L_0 C \left(\frac{1}{12} + \frac{C'}{C} \right) / \beta \right]^{1/2} |I_s^{-1}| \text{ Seconds} \quad (6.44)$$

The corresponding results obtained from theory and simulation at a specific set of values are compared for pulse width in Figure 6.8. It can be seen from Figure 6.8 that there arises an unexpected inhomogeneity while increasing the magnetic strength. This model is able to judge the rise time compression in gyromagnetic NLTL for certain values of magnetic field strength.

It is also clear from equation (6.40) that the pulse width of a modified KdV soliton is inversely proportional to the amplitude of pulse represented by $|I_s|$. As a final observation, when g becomes zero and for a sufficient wide input pulse duration, the amplitude will become doubled with reference to that of an input pulse duration. This will ultimately lead to a rise time compression of the pulse.

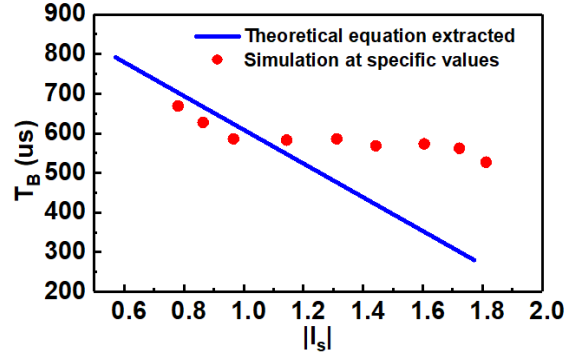


Figure 6.8 Comparison of pulse width from theory and simulations

6.4 Analysis of compression capability

In this section, we will first address the pulse compression capability issues of the hybrid NLTLs using a parametric study which is followed by those of the gyromagnetic NLTLs. Important pulse parameters including pulse amplitude, compression factor, and ringing behavior will be studied in this connection. Finally, our finding for both classes of NLTLs are summarized in the form of tables to understand and appreciate the behavior of specific parameters in a compact way.

6.4.1 Hybrid NLTL pulse compression capability and parametric analysis

A ten-section hybrid NLTL is developed based on the analysis provided in section II and it is shown in Figure 6.9. The modeling is performed in such a way that inductive and dissipative losses are all included. This model is designed so that it can easily incorporate the characteristics of the corresponding non-linear elements including current-dependent non-linear inductor $L(I)$ and voltage-dependent non-linear capacitor $C(V)$. The main components of this model include the user-defined input pulse, passive hybrid NLTL that further comprises of ten hybrid NLTL sections, input impedance R_g , load resistance R_L , R and R_C for characterizing losses in the inductors and capacitors, respectively.

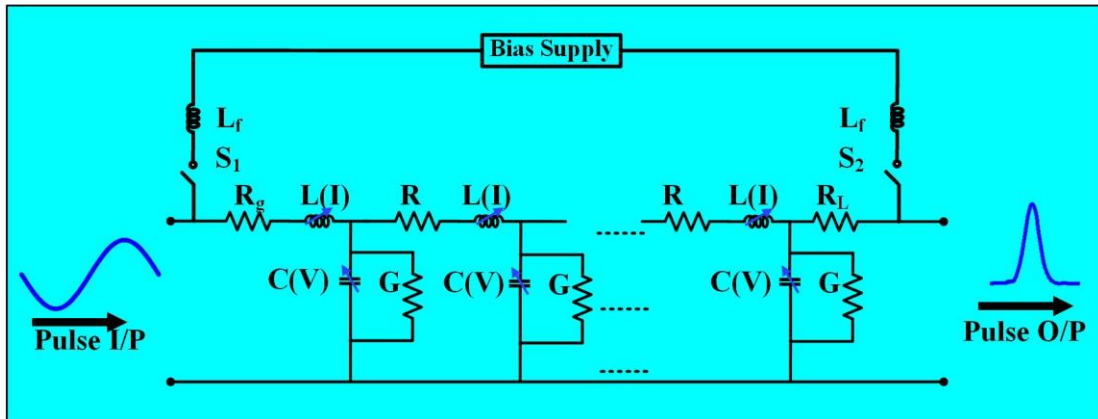


Figure 6.9 Circuit model of the designed hybrid NLTL

First, the effect on the output load voltage is depicted in Figure 6.10, where the number of LC sections (n) is changed from 4 to 10. Although it is noted that a small amount of oscillations occurs at roughly the same frequency in all the circumstances, there is a preferred number of the largest number of oscillating portions. As the number of the section is increased, the pulse is going to be sharpened and oscillation start to diminish at the cost of an increased circuit size.

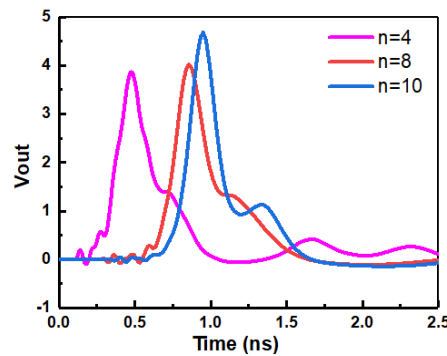


Figure 6.10 Varying the number of sections (n) of the designed hybrid NLTL and its corresponding effect on output pulse

The influence on the output load voltage is depicted in Figure 6.11, where the value of the resistive load R_L is changed from 50Ω to 500Ω . Ringing behavior and oscillation amplitudes are observed to grow as the load value goes up. However, it is interesting that there is an optimum point where the peak power is maximum as shown in Figure 6.11. It might be believed that the varying

impedance is matched well to the hybrid NLTL at such a particular value. As the load resistance rises, oscillations become more frequent until they reach the line's Bragg's frequency limit. Conclusively, we can say that the pulse distortion begins to occur for a high load resistance.

Here, the input pulse rise time is also varied to see its effect on the output voltage and it is assumed that the input pulse rise time and fall time are the same. The effect on the output load voltage is shown in Figure 6.12, where the rise time (T_R) is changed from 500 ps to 700 ps in steps of 100 ps. The frequency of oscillations is seen to remain constant as the rise time varies until the line is able to produce solitary waves. Although the pulse duration is constant, the section of the flat top decreases as the rise time increases, thus limiting the number of cycles for the same frequency. As a result, the number of oscillations falls as the rise time increases.

The overall summary of the parametric analysis of the hybrid NLTLs is tabulated in Table 6.1 to see the behavior of different effects on the output waveforms. These important parameters include input pulse variations, number of NLTL sections, resistive load, capacitive nonlinearity, and inductive nonlinearity.

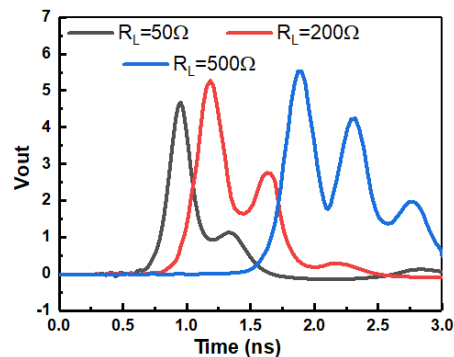


Figure 6.11 Varying load resistance (R_L) of the designed hybrid NLTL and its corresponding effect on output pulse

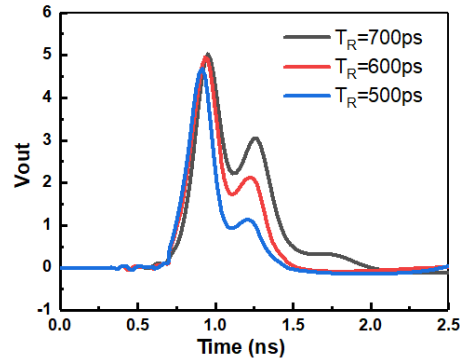


Figure 6.12 Effect of input pulse variation on output response of the designed hybrid NLTL

Table 6.1 Summary of a parametric study of hybrid NLTL

Parameters	Remarks
Rise time of rectangular input pulse, T_R	Increasing T_R is set to increase the number of oscillations as well as increase the output pulse duration.
Amplitude of rectangular input pulse	If amplitude is too high, oscillations will shift upward and produce distortions.
Number of NLTL sections, n	Increasing n , (a) Increases the amplitude of output peak voltage (b) Considerable reduction in ringing (c) Decrease pulse duration and so FWHM of the output pulse.
Resistive Load, R_L	Increasing R_L , (a) Increases the amplitude of oscillation in the output voltage (b) Increases the amplitude of ringing (c) Increases pulse duration (d) There exists R_L where the optimum power is maximum and thus has the best output performance.
Capacitive nonlinearity	Step capacitive nonlinearity: (a) Decreases oscillation amplitude (b) Decreases peak power
Inductive nonlinearity	Step Inductive nonlinearity: (a) Increases ringing in output voltage (b) Optimum point exists where peak power is maximum.

6.4.2 Gyromagnetic NLTL pulse compression capability

The gyromagnetic NLTLs work on a principle that the magnetic permeability of ferrite reduces swiftly with the current amplitude as the applied input pulse moves along the line, thereby speeding up the propagation velocity. The peak of the pulse can move more quickly than its base due to an

inverse relationship between magnetic permeability and propagation velocity, which is set to shorten the pulse rise time. This behavior is termed as the pulse sharpening effect which ultimately leads to a pulse compression in gyromagnetic NLTLs.

Different methods for simulating a continuous gyromagnetic line take Dolan's lumped-parameter network as a starting point [142,143]. It is possible to solve the shock front development process numerically thanks to the introduction of a time-stepping method introduced by Dolan's in [142]. Our proposed gyromagnetic model is developed in such a way that first a section of the network is designed and analyzed which involves a voltage source with shunt capacitance and series inductance that is powered by magnetization and is regulated by the rate of variation in magnetic flux through the ferrite rings. The created model is built on the work suggested by Dolan [142], in which the effects of magnetization of the ferrite are stated using the one-dimensional (1D) form of the LLG equation and represented by voltage sources as nonlinear elements. The proposed model's schematic is already shown and discussed in section III as Figure 6.6.

For the analysis of pulse edge sharpening and pulse compression behavior, we modeled a lossless gyromagnetic NLTL driven by a Gaussian-shaped pulse having an amplitude of 5V. The generator resistance and load in the circuit model are also 50Ω , matching the line characteristic impedance. The relative saturated permeability is 5, the relative permeability and permittivity of the dielectric are 2.1 and 1.0, respectively, the ferrite relative permittivity is 16, the ferrite outer diameter is 1.4mm, the diameter of the inner conductor is 0.8mm, the diameter of the outer dielectric is 2.5mm, having the optimum selected number of sections n is 12.

Figure 6.13 shows that the corresponding output pulse is sharpening by changing the number of sections (n) of the designed gyromagnetic NLTL. However, if we increase the number of sections, the simulation running time is also going to increase considerably. The impact of the damping parameter (α) on the rise time compression is demonstrated in Figure 6.14. The dimensionless damping parameter, whose corresponding value for this simulation is spanned between 0.01 and 1, is also investigated in detail. According to Figure 6.14, increasing the damping parameter results in a consistent decrease in the output pulse rise time. Additionally, we can see in Figure 6.14 that the output waveform variation is very small when the damping parameter is going beyond 0.5.

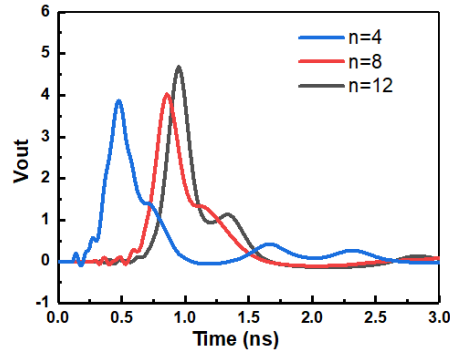


Figure 6.13 Varying the number of sections (n) of the designed gyromagnetic NLTL and its corresponding effect on output pulse

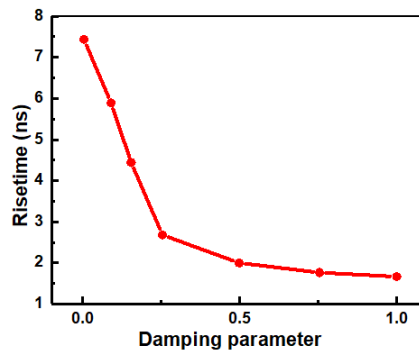


Figure 6.14 Variation of rise time with damping parameter of the gyromagnetic NLTL

The effect of input voltage on the corresponding output waveform is also investigated and it is shown in Figure 6.15. The amplitude of input voltage is varied from 3V to 8V, and it is seen that by increasing input voltage, we have a slight compression in rise time as predicted from Figure 6.15. Additionally, it is also noted in previous literature that a higher input voltage shortens the rise time. For instance, in [143] the 3D form of the LLG equation [144] was used while in [110,145] the 1D form of the respective LLG equation was used to replicate this effect. The variation of the rise time with saturation magnetization (M_s) of the designed gyromagnetic NLTL is demonstrated in Figure 6.16. The saturation magnetization is related to the saturated flux density by $B_s = \mu_0 M_s$ [39]. Additionally, we observe a minimum rise time at $B_s=0.30\text{T}$ and a steady decrease in output pulse amplitude with increasing M_s .

The overall summary of the parametric analysis of the gyromagnetic NLTL is tabulated in Table 6.2 to see the behavior of different parameters on the output waveform. These important parameters

include input pulse variations, number of NLTL sections, damping parameter, and saturation magnetization.

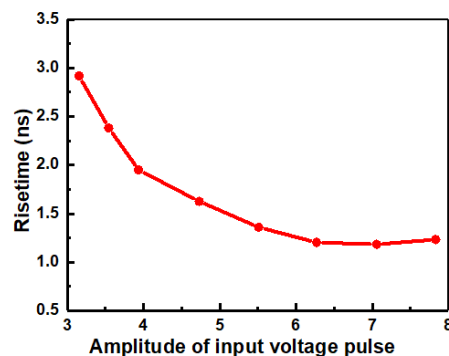


Figure 6.15 Variation of rise time with an input voltage amplitude of the designed gyromagnetic NLTL

Table 6.2 Summary of a parametric study of gyromagnetic NLTL

Parameters	Remarks
Number of NLTL sections, n	Increasing n , (a) Increases the amplitude of output peak voltage (b) Considerable reduction in ringing (c) Decrease pulse duration and so FWHM of the output pulse.
Damping parameter, α	Increasing the damping parameter decreases the rise time of the output pulse waveform, thus decreasing the corresponding pulse duration.
Input voltage amplitude	Increasing input voltage amplitude: (a) Increases oscillation amplitude (b) Decreases rise time of output voltage (c) Decreases output pulse duration
Saturation flux density, B_s	Increasing B_s is set to decrease pulse duration by reducing the rise time of output voltage, however, there exists B_s where the rise time starts to increase again and have different values for different magnetic materials.

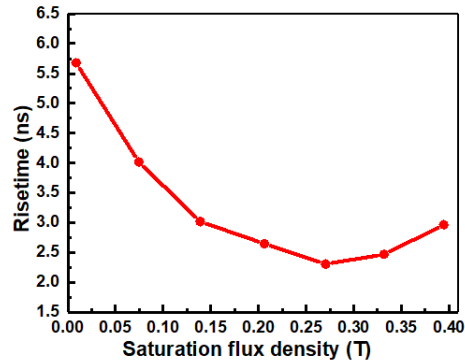


Figure 6.16 Variation of the rise time with saturation magnetization of the designed gyromagnetic NLTL

6.5 Experimental demonstration

Finally, an experimental demonstration is carried out for which a ten-section hybrid NLTL is designed, and its corresponding output response is measured to validate our theoretical analysis. Figure 6.17 provides the block diagram of our measurement setup. This experimental setup is composed of an arbitrary waveform generator used for generating an input waveform. The designed ten-section NLTL is placed between a universal test fixture whose one terminal is connected to an arbitrary waveform generator while the other terminal to an oscilloscope. DC power supply is used to change the biasing of hybrid NLTL, and it is connected via biasing wires. The output is observed on the oscilloscope and the corresponding prototype is also shown in Figure 6.17. The snapshot taken during the experimental demonstration is also given in Figure 6.18 and the corresponding simulated vs. measured response of the ten-section hybrid NLTL is displayed in Figure 6.19. It can be seen that the measured and simulated output responses are in a good agreement. To give a clear picture of the overall work, we have also compared the output response from theory, simulation, and measurements of ten section hybrid NLTL as shown in Figure 6.20. It must be noted that there is a slight increase in ringing behavior in the measured response due to parasitic elements.

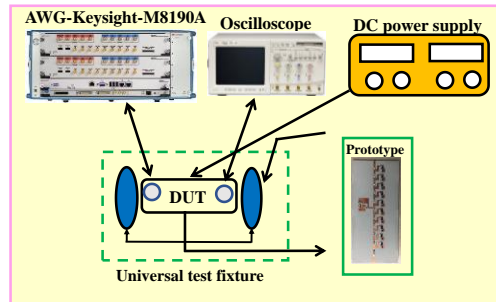


Figure 6.17 Block diagram of the measurement setup along with prototype

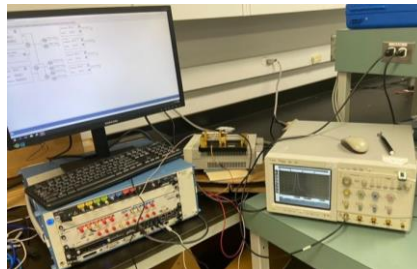


Figure 6.18 Snapshot of the experimental demonstration

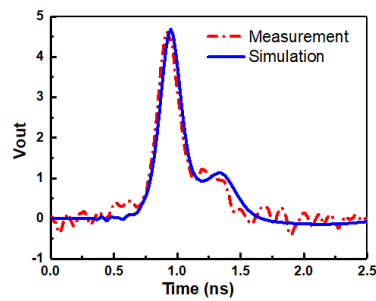


Figure 6.19 Simulated vs. measured responses of ten section hybrid NLTL

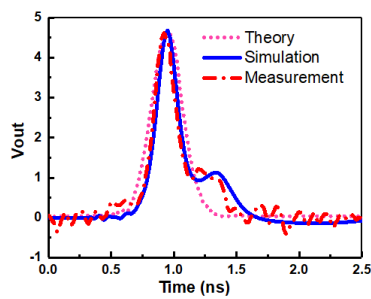


Figure 6.20 Comparison of output response from theory, simulation, and measurements of ten section hybrid NLTL

6.6 Difference between hybrid and gyromagnetic NLTLs

Now, we are in a position of comparatively examining the gyromagnetic NLTL and hybrid NLTL based on the analysis presented in the previous sections. Simulations and measurements are taken into account while making the observations to appreciate the difference in a much more concise manner. This is completely summarized in Table 6.3 in terms of critical parameters, and in this context, the advantages and disadvantages of both NLTLs can be remarked as well.

Table 6.3 Summary and performances of hybrid and gyromagnetic NLTLs

Hybrid NLTL	Gyromagnetic NLTL
Hybrid NLTL provides an opportunity for both rise and fall edge transients to be sharpened	Gyromagnetic NLTL provides an opportunity for rise edge to be sharpened
Hybrid NLTL utilizes both capacitive and inductive nonlinearity	Gyromagnetic NLTL utilizes inductive nonlinearity
Sharpening behavior is improved by increasing NLTL sections	Sharpening behavior is improved by increasing NLTL sections
Several parameter variations (R , L , G , C) can be used and so we have enough flexibility	Magnetic field strength can be varied to achieve a desired response
Compression is dependent on parameters including load resistance, input pulse duration and amplitude, number of sections, and nonlinearity of capacitors and inductors.	Compression is dependent on input pulse duration and amplitude, damping parameter, saturation flux density, number of sections, and magnetic field strength.
The pulse oscillations in comparison to gyromagnetic NLTL are quite low.	Can produce stronger pulse oscillations at higher frequencies.

6.7 Conclusion

A comprehensive pulse compression capability analysis of hybrid and gyromagnetic NLTLs is presented and discussed. Both classes of NLTLs are theoretically analyzed and their corresponding lumped-element models are developed. Parameters principally responsible for pulse sharpening in hybrid NLTLs include the number of NLTL sections, resistive load, input pulse variation, capacitive, and inductive nonlinearity. It is shown that there exists an optimum value for each parameter selection where the output power becomes maximum. Parameters concerned with pulse

sharpening in gyromagnetic NLTLs include the number of NLTL sections, input pulse variation, damping parameter, and saturation magnetization. All these parameters are modeled, and the selection of optimum value is provided. Finally, the advantages and disadvantages of both classes of NLTLs are highlighted and summarized. This work will provide an opportunity for the researchers to utilize simultaneous capacitive and inductive nonlinearity in hybrid NLTLs in the corresponding interconnection with magnetic materials and will pave the way toward ultrafast electronic systems and interconnects.

CHAPTER 7 ARTICLE 5: A RECONFIGURABLE PICOSECOND PULSE GENERATOR IN NON-LINEAR TRANSMISSION LINE FOR IMPULSE RADAR ULTRAWIDEBAND APPLICATIONS

MuhibUr Rahman and Ke Wu

Published in the *IEEE Microwave and Wireless Components Letters*, vol. 32, no. 5, pp. 448-451, 2022. (Publication date: January 07, 2022)

This paper presents a reconfigurable picosecond (ps) pulse generator having gaussian and monocycle pulse shapes for Impulse Radar Ultrawideband (IR-UWB) applications. A mixed step recovery diode (SRD) topology is used in combination with a non-linear transmission line (NLTL) and pulse shaping circuit to realize the pulse generator. The pulse shaping network comprises an RC differentiator embedded with a single PIN diode to provide two different switchable states. This pulse generator is capable of directly switching from a gaussian to a monocycle pulse without resorting to the increase in pulse width twice of the original gaussian pulse as deployed in the previous reconfigurable pulse generators. The pulse generator based on the proposed technique has a pulse duration of almost 70ps with a promising ringing level in both cases (gaussian and monocycle). Moreover, not only is the implementation of this technique easy, it can also modify the pulse into other important shapes such as the doublet and higher-order gaussian pulses. The proposed reconfigurable pulse generator is measured in both cases, and the results are presented in each case.

7.1 Introduction

The pulse generator is one of the most important components in any wideband and ultrafast system. The commonly realized pulses are the gaussian, monocycle, doublet, and polycycle pulses, each having their own advantages. However, the most popular shapes are monocycle and gaussian, owing to their simpler architecture realization and design as well as wide spectrum capability. Since the gaussian pulse spectrum holds very rich DC and corresponding low frequency components, it is generally a poor choice for wideband transmission and especially UWB radar applications. On the other hand, the monocycle pulse, which is the 1st derivative of the corresponding gaussian pulse, has no DC components and can be fed directly to a practical antenna setup. Better signal

characteristics along with minimum distortion and well-defined pulse shape can also be achieved on the receiver side using a monocycle pulse shape [13,146].

Various techniques are investigated and disseminated for electrical pulse generation, which include field effect transistors (FET), bipolar junction transistors (BJT), two-stage FET, CMOS, resonant tunnelling diodes (RTD), step recovery diodes (SRD), microstrip delay lines, AHCMOS and ECL logic gates, SRD integrated with pulse shaping network and NLTLs, and different combinations of PIN diodes and MESFETs [12,61,64,65,72,73,87,90]. Among them, the mixed SRD topology-based pulse generation technique is promising for realizing low-power picosecond pulse generators. Since it is well documented that SRD operates as a charge-controlling switch, its capability to quickly alter from a low impedance state to a corresponding high impedance state is utilized for sharpening waveform edges. However, the minority carrier lifetime (MCLT) and transition time (TT) are the main factors that limit SRD-based pulse compression. To overcome this limitation, in [4], NLTLs were integrated with mixed SRD topology to utilize a greater portion of non-linearity, thus considerably increasing pulse compression capability. However, such a technique can generate a single type of clean gaussian pulse. Also, state-of-the-art wideband architectures usually require transmitters to possess multiple pulse shape generation capability. To this end, we need a reconfigurable pulse generator that has the capability of generating multiple pulse shapes from a single circuit [87]. Also, a pulse sequence is considered to carry a burst of RF energy, where a single pulse holds one information per symbol. Consequently, multiple pulses are set to provide PSM, which is highly attractive for data encoding [93,147].

In this work, a reconfigurable picosecond (ps) pulse generator is proposed, which is inspired from the work reported in [4]. The developed pulse generator can switch from gaussian to monocycle pulse directly without increasing the pulse width to twice the size of the original gaussian pulse [148].

7.2 Design and configuration

The basic schematic of the proposed reconfigurable ps pulse generator based on the NLTL is shown in Figure 7.1. The proposed pulse generator comprises of a pulse generating circuit, NLTL circuit, pulse shape selector stage, and load. The pulse generation section involves a mixed SRD topology whose features are related to the MCLT and TT parameters. The MCLT affects the storage time in

the corresponding reverse bias state while the TT is responsible for minimum achievable pulse [75]. The SRD pulse generating circuit kicks off a sharp pulse from an input of 10 MHz PRF, and the SRDs are selected to have a TT of 120 ps and MCLT of 50 ns.

After passing through the pulse generating stage, there is a four-section NLTL block, which is used for the rising time pulse compression and ringing mitigation. This is because unavoidable pulse distortion and considerable ringing were generally anticipated after the pulse generating stage, which is tackled while utilizing an NLTL. The corresponding one soliton solution and minimum rise time limit in this topology is given as [4]:

$$V_n = F(V_0) \sinh^2 k \operatorname{sech}^2 \left\{ kn - \frac{1}{\sqrt{LC(V_0)}} (\sinh k)t \right\} \quad (7.1)$$

$$t_{rise,min} \approx \frac{\pi}{4} \sqrt{LC(V_{max})} \quad (7.2)$$

where, V_n represents the voltage at nth section, $T_{rise,min}$ stands for the minimum compressed rise time in both cases, $F(V_0)$ is the particular value having the dimension of voltage. In our case, we are able to obtain a clean gaussian pulse of almost 70ps after this stage. To generate a monocycle pulse from its gaussian counterpart, an RC differentiator stage is used as a pulse shape selector which avoids a pulse duration degradation of the original gaussian pulse [148]. The pulse shape selector stage and load constitute the capacitance C_D , load impedance R_L , coupling capacitance C_c , and a PIN diode for this task. C_c is selected to be larger in comparison to C_D , and hence it can be discarded through our differentiator calculation.

The gaussian pulse is described by equation (7.3) with its corresponding derivative, which is expressed in equation (7.4), thus representing a monocycle pulse shape:

$$V(A, t, f_c) = Ae^{-2(\pi f_c t)^2} \quad (7.3)$$

$$V(A, t, f_c) = 2A\sqrt{\pi} f_c e^{-2(\pi f_c t)^2} \quad (7.4)$$

where A corresponds to the amplitude of the pulse; t is the time; and f_c stands for the central frequency. Since, we can easily calculate C_D within a particular range by choosing a desirable frequency band and $R_L=50\Omega$. A PIN diode is inserted in parallel with C_D to produce a reconfigurable capability within the designed pulse generator. The PIN diode acts as a low

impedance during the ON state and cancels the differentiator effect through bypassing C_D , and so we have a clean gaussian pulse. During the OFF state, the PIN diode is considered as a small capacitance ($C_P < 1\text{pf}$) which is equivalent to a large impedance at corresponding higher frequencies. The overall effective capacitance (C_{eff}) of the differentiator in this case becomes ($C_{eff} = C_P + C_D$), and thus we have a corresponding monocycle pulse at the output. Therefore, this pulse generation is advantageous due to the reconfigurability behavior with PIN diode and tunability behavior with a single resistor RC. The corresponding biasing circuit shown in Figure 7.1 comprises a DC source with current limiter R_2 , bypass capacitor C_2 , and RF choke L . Other optimized values of the components utilized in this work are: $R_L = R_S = 50\Omega$, $L_1 = 20\text{nH}$, $R_c = 4.6\text{K}\Omega$, $C_c = 100\text{nF}$, $C_D = 2.2\text{pF}$, transmission line length of NLTL such that $L_1 = L_2 = L_3 = L_4$, forward resistance of the PIN diode $= 1\Omega$, and junction capacitance of the PIN diode $= 0.33\text{pF}$.

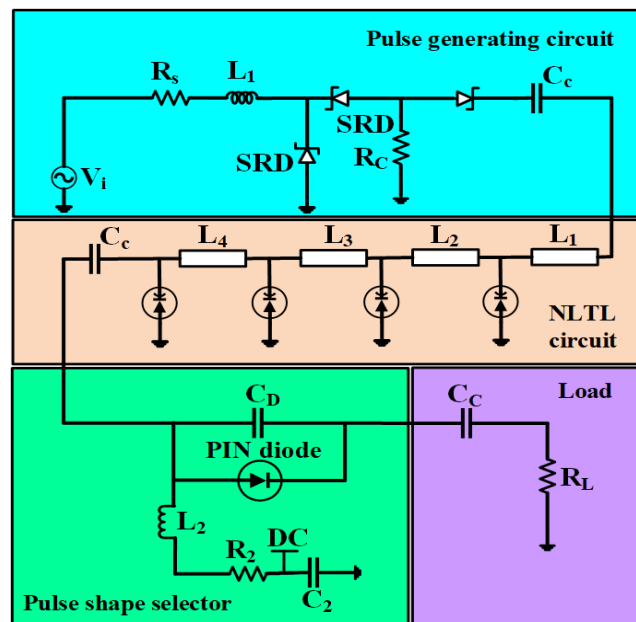


Figure 7.1 Schematic of reconfigurable picosecond pulse generator

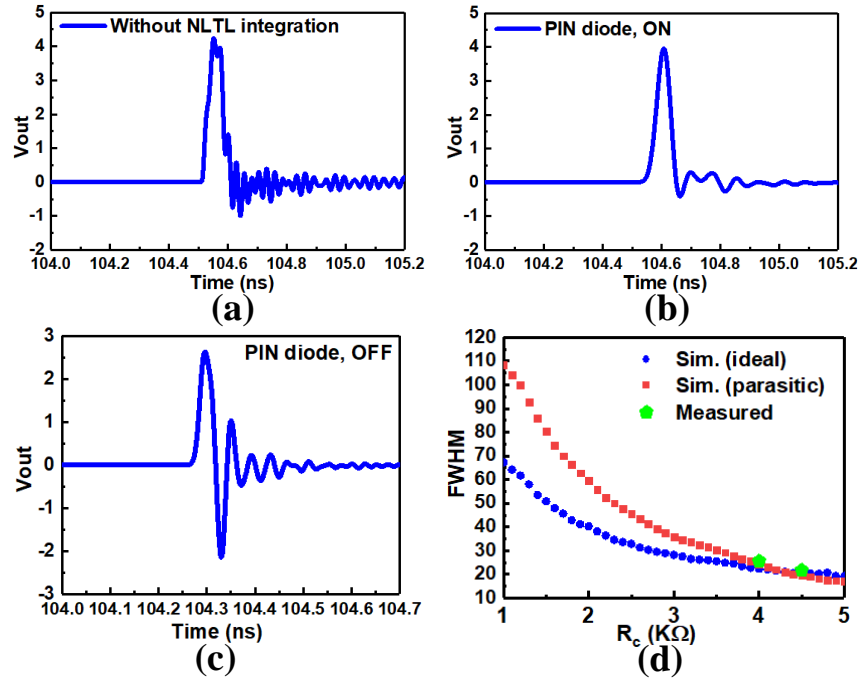


Figure 7.2 Simulation results of reconfigurable picosecond pulse generator based on NLTL. (a) Gaussian pulse shape without using NLTL in the circuit with PIN diode ON; (b) Gaussian pulse shape along with NLTL in the circuit with PIN diode ON; (c) Monocycle pulse shape with PIN diode OFF; (d) Controlled FWHM using fine-tuning resistor R_c

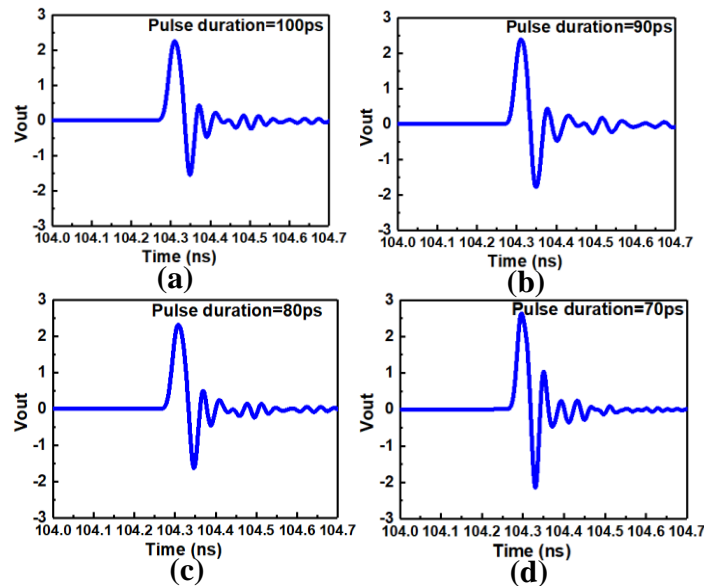


Figure 7.3 Controlled monocycle pulse duration using fine-tuning resistor R_c . (a) Pulse duration=100ps; (b) Pulse duration=90ps; (c) Pulse duration=80ps; (d) Pulse duration=70ps

7.3 Results and discussions

Various simulation studies are performed using Agilent ADS and different pulse shapes are shown in Figure 7.2. First, we show that without using an NLTL in the circuit, there is a considerable amount of ringing and pulse distortion, and the output waveform in case of a gaussian pulse shape is displayed in Figure 7.2 (a). The pulse amplitude, duration, detailed ringing level, and FWHM achieved in this case are almost 4.1V, 95ps, -17.9dB, and 34ps, respectively. The detailed ringing level is calculated based on equation in [149].

To compensate pulse distortions, edge sharpening, and ringing reduction, we add an NLTL stage to the circuit, and the resulting output waveform is presented in Figure 7.2 (b). The pulse amplitude, duration, detailed ringing level, and FWHM achieved is almost 3.95V, 70ps, -30.4dB, and 22ps, respectively. To reconfigure the pulse shape from gaussian to monocycle, the PIN diode is turned OFF, and we have a corresponding output waveform as shown in Figure 7.2 (c). The pulse amplitude observed is 2.7V with a pulse duration of almost 75ps and an FWHM of 24ps. It is also advantageous that a single fine-tuning resistor R_c is used to control the pulse duration, and this phenomenon is analyzed in the case of a gaussian pulse shape, as in Figure 7.2 (d). This plot demonstrates the variation in FWHM by varying R_c and compares it with the corresponding ideal and package inductances and capacitances of the SRDs. This phenomenon is also applicable in the case of a monocycle pulse shape, as displayed in Figure 7.3, in which the varying R_c , from 4.0 to 4.6 K Ω , reduces a pulse duration from 100 to 70ps. Still, during this compression process, we have an increase in the ringing level from -14.06dB to -12.35dB. However, the overall pulse shape is well preserved, and the ringing level is within an acceptable level, which is highly desirable in pulse shape modulation applications [150]. Figure 7.3 (a)-(d) also reveal that one can achieve an increase in amplitude of the monocycle pulse at the expense of an increase in ringing amplitude. It is also seen that the output pulse amplitude is dependent on the input excitation signal frequency and amplitude. The amplitude of the output pulse decreases by changing the excitation frequency, even though the pulse shape characteristics of the monocycle are well maintained. This behavior is also validated for varying input signal amplitudes from 2.5 to 10V. Figure 7.4 shows the corresponding bandwidth of the generated gaussian and monocycle pulse shapes, which are calculated by a fast Fourier transform. It is clear that the monocycle pulse that have no dc content is a good choice and can be fed directly via a practical antenna setup.

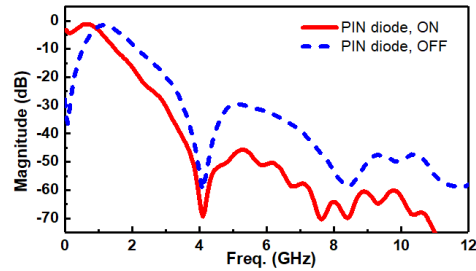


Figure 7.4 Power spectrum of generated monocycle and gaussian pulses

7.4 Prototype and measurements

The proposed reconfigurable ps pulse generator based on an NLTL is fabricated, and its measured results are shown in each case, as described in Figure 7.5. The experimental setup is shown in Figure 7.5 (c) which consists of the proposed pulse generator, a periodic signal generator, an oscilloscope, a DC power supply, and a universal test fixture where the proposed circuit is placed. The fabricated prototype is also shown in Figure 7.5 (c), which was built on a Roger R04350 substrate. Figure 7.5 (a) provides the measured results when the PIN diode is ON for the gaussian pulse, while Figure 7.5 (b) illustrates the results when the PIN diode is OFF for monocycle pulse.

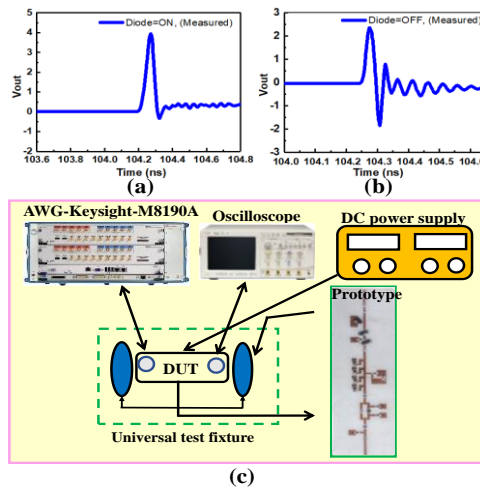


Figure 7.5 Experimental setup and measured results. (a) Gaussian pulse shape; (b) Monocycle pulse shape; (c) Experimental setup with fabricated pulse generators; the related biasing wires are not shown

7.5 Comparisons with the state of the art

Table 7.1 provides the comparison with related work in literature, which is based on important pulse metrics. A parameter termed as FOM (figure of merit) is defined as [90].

$$FOM = \frac{\text{Pulse amp. (V)}}{FWHM(ns) \times \text{Ringing}(\%)} \quad (7.5)$$

Table 7.1 Comparison of the proposed reconfigurable ps pulse generator based on NLTL with other reported works recently published in the literature.

Ref.	Pulse shape	Amp. (V)	Ringing (%)	FWHM (ps)	FOM
[13]	Monocycle	1.85	~5.5	300	1.1
[90]	Gaussian	1.67	~7	214	1.1
		0.83	~8	153	0.68
[93]	Gaussian	6.8	~5.8	220	5.3
		1	~11	60	1.5
[149]	Gaussian	13	14.5	250	3.58
[16]	Monocycle	1.4	~14	150	0.66
[151]	Monocycle	76	~6	3200	3.95
[252]	7 th order Gaussian	0.16	~5	140	0.22
This	Gaussian	3.95	~3	70	18.8
work	Monocycle	2.7	~11	75	3.27

7.6 Conclusion

A reconfigurable picosecond pulse generator based on the NLTL is designed, analyzed, fabricated, and measured for IR-UWB applications. The proposed pulse generator possesses switchable pulse shaping features between gaussian and monocycle pulse shapes. An SRD topology in combination with an NLTL is used as a pulse generating circuitry while a very simple RC differentiator with a single embedded PIN diode is used as a pulse shaping network. Due to circuit simplicity, it can be easily and effectively modified to consider other important pulse shapes including doublet and high-order gaussian pulses by introducing innovative pulse shaping networks. The simplicity, cost effectiveness, and good quality characteristics will make the proposed circuit useful in UWB systems and ultrafast techniques that require low-power and clean ps pulses.

CHAPTER 8 PICOSECOND PULSE GENERATION, SHAPING, TRANSMISSION, AND RECEPTION CHARACTERISTICS FOR WIRELESS SENSING APPLICATIONS

In this chapter, the wireless transmission and reception of picosecond pulses are discussed by estimating and incorporating antenna effects while considering the order of pulse, ringing distortion, and duration of the pulse. The impact on pulse order, system fidelity factor, pulse distortion, stretch ratio, detailed ringing level, and figure of merit are all analyzed on the receiver side with reference to various antennas of interest in different scenarios. A systematic analysis is performed in such a way that a Gaussian pulse is first generated which is then transformed to its derivative for transmission. For transmission and reception, some pertinent wideband antennas are explored and developed including Vivaldi, antipodal Vivaldi, slotted patch, bicone, and ridged horn antennas. An experimental demonstration is performed, and a complete system model is provided while presenting the radiated pulse characteristics in different scenarios. Finally, a combination of antennas are proposed to receive the desired radiated pulse on the receiver side. It can be seen that all the antennas differentiate the input pulse in time during the transmission and reception while bicone antenna in combination with any other antenna maintains the originally shaped pulse in the receiving mode. Important radiative pulse parameters including stretch ratio, ringing level, full width half maximum, and system fidelity factor are analyzed on the receiver side. This chapter will open up a new fruitful entry in the field of wireless sensing such as vital signs monitoring including heartbeat monitoring, tumors detection, touchless heartbeat and respiration detection of small conscious animals, and synthetic aperture radars by considering all system parameters.

8.1 Introduction

An effective use of antennas over a broad frequency range is required for numerous applications. One technology in this connection is ultrawideband (UWB), which has found many applications in wireless vital signs monitoring, ground penetrating radar (GPR), through wall respiration detection, geophysical exploration, and low probability radars [3,153,154,155,156]. Input excitation to the UWB antenna needs pulses that must have ultrashort duration. On the other hand, It has also been known that the input pulse having lower Full width half maximum (FWHM)

provides superior performances in comparison to that having a higher FWHM. So, it is crucial for the above-mentioned applications to have a pulse of shorter pulse duration along with a reduced ringing level. In this regard, UWB and even super wideband (SWB) antennas are explored in more detail along with the analysis and synthesis of accompanying radiated fields and received signals. However, very limited research has examined the radiative pulse characteristics and receiving waveforms [157-161].

UWB and SWB antennas become now more and more popular due to their many superior attributes. They can be modeled to achieve a great range resolution while focusing energy on a specific direction using short-pulse techniques. As a result, UWB signals enable precise position determination and object tracking. Furthermore, in multipath situations, UWB short-pulse systems perform better than narrowband systems because a UWB short pulse enables the differentiation of returns from different scatterers via time delay. It is preferred that UWB antennas emit the majority of their energy for short-pulse radiation in the direction where the pulse most closely resembles the stimulating waveform or a derivative of it. To achieve this objective, we need to mitigate the antenna dispersion and losses in transmission and reception [162,163].

The dipoles, monopoles, ridged horns, Vivaldi antennas, antipodal Vivaldi antennas, disc cones, and bicones are the most commonly utilized UWB antennas. For UWB signals with a 1 ns pulse width, the radiating properties of a large current radiator have been investigated in [164] and [165]. Additionally, [166] has examined the transmission and reception properties of the same antenna for Gaussian input pulse. Since the antenna's radiating aperture determines its radiation properties. An antenna for UWB short-pulse radiation has distinct transmitting and receiving properties than narrowband antennas. For system design purposes, many UWB applications require a prior knowledge of the received pulse shape, duration, and amplitude. This needs advanced pulse generation and shaping techniques to accurately analyze the pulse properties at the receiver sides. Also, all previous research deals with the input excitation of pulse and does not care about the pertinent pulse parameters at the receiver including stretch ratio, FWHM, system fidelity factor, and detailed ringing level.

It has been shown in [167] that an antenna's transmitting transient response is proportional to its receiving transient response in terms of time derivative. As a result, a UWB antenna's response in the receiving and transmitting modes differ. If we send the first-order derivative of a Gaussian

waveform, we will receive the second-order derivative of a Gaussian pulse at the receiver side. So, it is also important that we need some scenarios where we have the same pulse characteristics as those on the transmitter side. Also, it is well known that the Gaussian waveform has very rich dc spectral contents, so we need to modify it to its corresponding derivatives suitable for transmission [168-171]. In this regard, the pulse generator is needed that has the capability to reconfigure between Gaussian and monocycle pulse shapes.

From the above discussion, it is evident that a complete system model is needed by considering all the above parametric impacts in transmission and reception. Therefore, the first step is the design and modeling of a ultrashort reconfigurable pulse generator that has the capability of generating a Gaussian pulse with the corresponding transformation to higher orders counterparts while maintaining the signal integrity. Then, it is needed to accurately model wideband antennas that have the capability of pulse transmission. Finally, the response on the receiver side should be studied with different combinations in order to retrieve the originally generated pulse. The complete system model for radiative pulse characteristics having all modules is shown in the form of a block diagram in Figure 8.1.

This chapter will give a full model for transmitting and receiving picosecond pulses while accounting for antenna effects. The effects of several essential antenna combinations on pulse order, system fidelity factor, pulse distortion, stretch ratio, detailed ringing level, and figure of merit will be demonstrated on the receiver side. By building up a monocycle pulse generator, several wideband antennas, and their combinations, a comprehensive system model will be constructed, simulated, and tested. In each case, the experimental demonstration will be carried out by providing the radiative pulse characteristics. Finally, a combination of antennas will be proposed to receive the desired radiative pulse on the receiver side. This work will possibly pave the way for wireless sensing applications such as vital signs monitoring including heartbeat monitoring, tumors detection, touchless heartbeat, respiration detection of small conscious animals, and synthetic aperture radars.

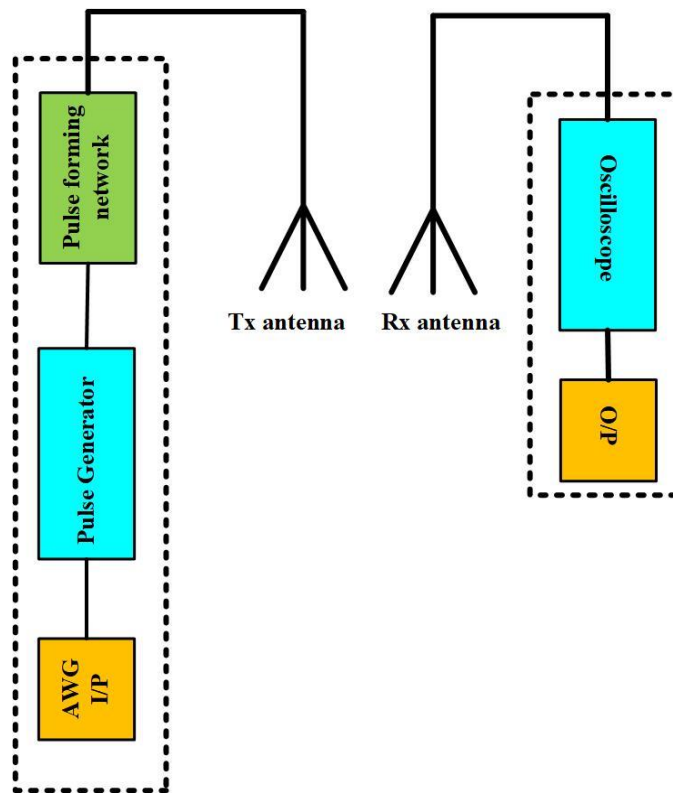


Figure 8.1 Complete system model for radiative pulse characteristics having all modules

8.2 Design and measurement of ultrashort reconfigurable pulse generator with multiple pulse shapes

Consider a pulse generator that has the capability of adopting Gaussian and monocycle pulse shape as shown in Figure 8.2, where Figure 8.2 (a) shows the detailed schematic of the pulse generator while Figure 8.2 (b) and (c) show the output response when the PIN diode is ON and OFF, respectively. This pulse generator is explained in [73,105] along with parameter optimization and critical parameter adjustment. Here, we will only utilize this pulse generator to excite the transmitter antenna in the case when the PIN diode is OFF (monocycle pulse shape). It is due to the reason that the Gaussian pulse spectrum contains very high dc and low-frequency components. Antennas are well recognized for neither transmitting nor receiving wireless signals that contain rich dc spectral contents. In light of this, UWB and other short-range radar applications should not use the Gaussian pulse. The antenna also alters the shape of the transmitted pulse by differentiating or integrating the input signal. Additionally, ringing on the transmitted pulse is caused by the antenna's constrained bandwidth and poor low-frequency impedance matching. As a result, the

antenna cannot receive the Gaussian pulse directly. The first-order derivative of Gaussian pulse known as the monocycle pulse contains no dc content in its frequency spectrum, and its pulse width can be used to modify the frequency spectrum and center frequency. Therefore, the monocycle pulse is considered as the perfect choice for pulse transmission, and we will utilize it during our complete system.

The amplitude of the monocycle pulse shape reported in [105] is 2.7 V, ringing is almost 11%, and FWHM is between 70 ps to 80 ps. The figure of merit is 3.27, which is calculated based on the following equation [105].

$$FOM = \frac{\text{Pulse amp. (V)}}{\text{FWHM (ns)} \times \text{Ringing (\%)}} \quad (8.1)$$

The experimental prototype of the circuit is shown in Figure 8.2 (d), which will connect with the transmitting antenna from one side and AWG from the other side along with the power supply for biasing input. The antennas of concern will be discussed in the next section briefly as well.

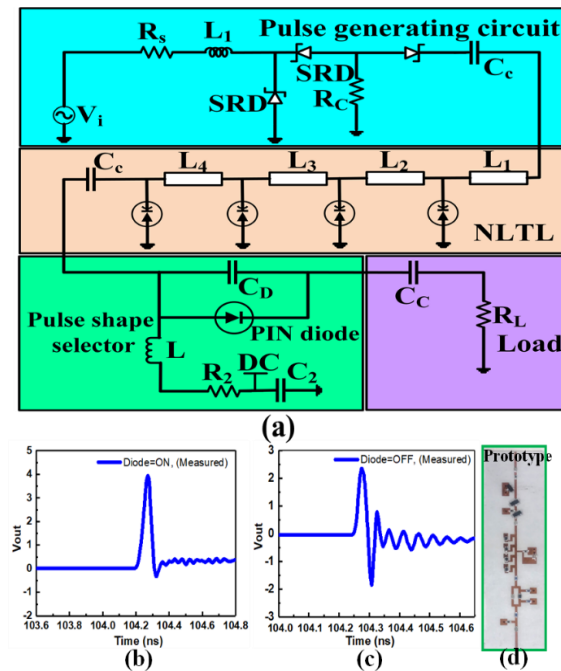


Figure 8.2 Ultrashort picosecond pulse generator switching between Gaussian and monocycle pulse shape. (a) Schematic of the pulse generator; (b) Gaussian pulse shape; (c) Monocycle pulse shape; (b) Prototype of the pulse generator

8.3 Various wideband antennas with simulations and measurements

This section is dedicated to the design of wideband antennas for the transmission and reception of ultrashort pulses. In this regard, we have selected different pertinent classes of wideband antennas including Vivaldi antenna, antipodal Vivaldi antenna, slotted patch monopole antenna, biconical antenna, and double ridged horn antenna. All these antennas will be discussed briefly here to see a step-by-step approach toward the final realization.

8.3.1 Vivaldi antenna

Gibson first proposed the Vivaldi antenna, a traveling-wave tapered slot antenna (TSA) for broadband applications in 1979 [172]. The reason it is referred to as a traveling-wave antenna is that when a wave is coupled from a microstrip line to a slot line, its energy is tightly bound to the opening width (W_{min}), and as it leaks from the transition moving toward the aperture width (W_{max}), its energy weakens and the wave is radiated to an empty space from the tapered antenna slot [173]. An exponentially tapered slot connected to the quarter wave slot with a specific length can be defined as [173]:

$$y(x) = \pm Ae^{rx} \quad (8.2)$$

where, A represents the minimum width of the tapered slot (W_{min}), x represents the position along the tapered slot length, and r is the magnification factor rate. It was observed that the performance of the antenna, particularly its bandwidth and gain, is significantly influenced by both r and L_T . From [173] we have:

$$L_T > \lambda_g \quad (8.3)$$

where, $\lambda_g = c/f_c \sqrt{\epsilon_{eff}}$ having c is the speed of light and f_c is the central frequency of the desired operating frequency band. The excitation of this antenna is happening from the coupling between the microstrip and slot lines in the transition. Based on this analysis, this antenna can be designed in such a way that it is operating between 1 GHz to 18 GHz. The optimized critical parameters chosen for the design are, $L_T=27\text{mm}$, $L_f=28\text{mm}$, $r_e=1.819\text{mm}$, and $W_{min}=0.28\text{mm}$ as shown in Figure 8.3 (a).

The prototype of the designed antenna with front and back is shown in Figure 8.3 (a) while the simulated vs. measured reflection coefficient response is shown in Figure 3(b). It is clear from Figure 8.3 (b) that this antenna is well matched within 1 GHz to 18 GHz as the value of the reflection coefficient is below -10 dB. Three different values are selected for measuring the radiation pattern of the designed antenna. These values fall within the lower, middle, and upper range of the operating frequency bands. The radiation patterns at these frequencies are shown in Figure 8.4 (a)-(c) while Figure 8.5 (a) shows the snapshot in an anechoic chamber in measurement.

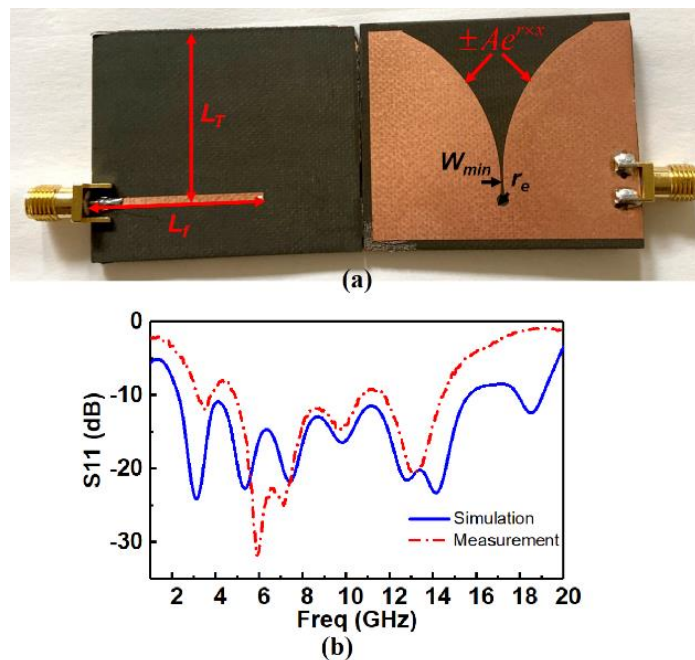


Figure 8.3 (a) Prototype of the designed wideband Vivaldi antenna; (b) Simulated vs. measured reflection coefficient response of the designed wideband monopole antenna

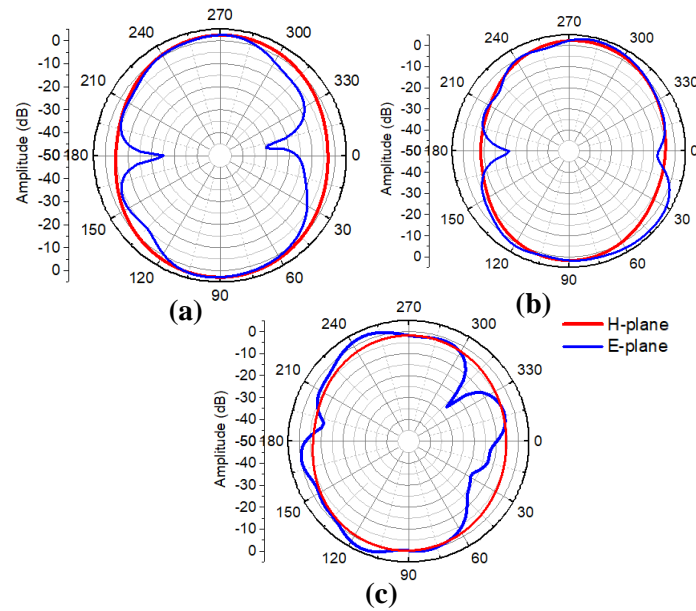


Figure 8.4 Measured radiation pattern of the designed wideband Vivaldi antenna. (a) 4.5 GHz; (b) 8 GHz; (c) 14 GHz

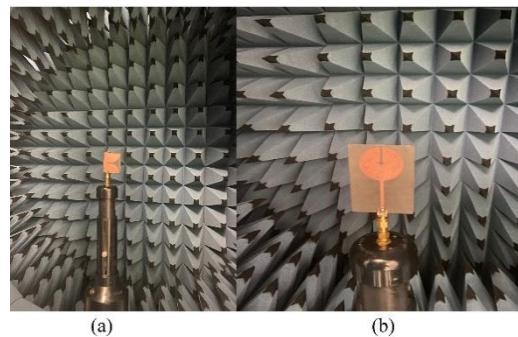


Figure 8.5 Snapshot during radiation pattern measurement. (a) Vivaldi antenna; (b) Slotted patch monopole antenna

8.3.2 Antipodal Vivaldi antenna

This section presents the brief design perspectives and results of a wideband antipodal Vivaldi antenna. The geometry of the designed antenna can be seen in Figure 8.6, where two symmetrical exponential patches are placed on the opposite side of the substrate. The substrate utilized is Rogers RT/Duroid 5880 having a dielectric constant of 2.20 and a thickness of 62 mil. Figure 8.6 displays the top and bottom views of the constructed antenna where the inner and outer edge tapers can be defined as [174].

$$x_i = \pm c_s \cdot e^{K_s y} \pm (c_s + 0.5 \cdot c_w) \quad (8.4)$$

$$x_o = \pm c_w \cdot e^{K_s y_{sf}} \pm (c_s + 0.5 \cdot c_w) \quad (8.5)$$

where, x_o and x_i represent the distances from the outer and inner edges, respectively. Based on the above equation and analysis presented in [174], the antenna is designed in such a way that it is operating between 1 GHz to 20 GHz. The prototype of the designed antipodal Vivaldi antenna with front and back is shown in Figure 8.6 while the simulated vs. measured reflection coefficient response is shown in Figure 8.7. The radiation patterns at 4.5 GHz, 8 GHz, and 14 GHz are shown in Figure 8.8 (a)-(c).



Figure 8.6 Prototype of the designed wideband antipodal Vivaldi antenna

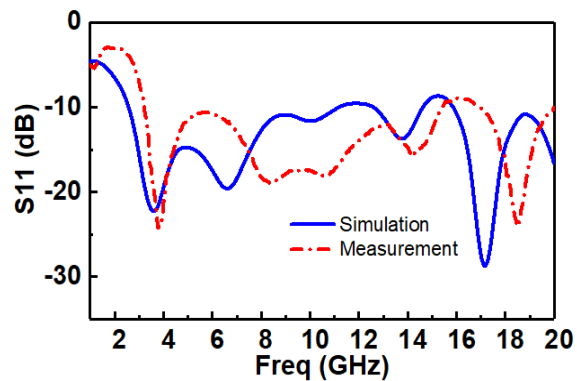


Figure 8.7 Simulated vs. measured reflection coefficient response of the designed wide band antipodal vivaldi antenna

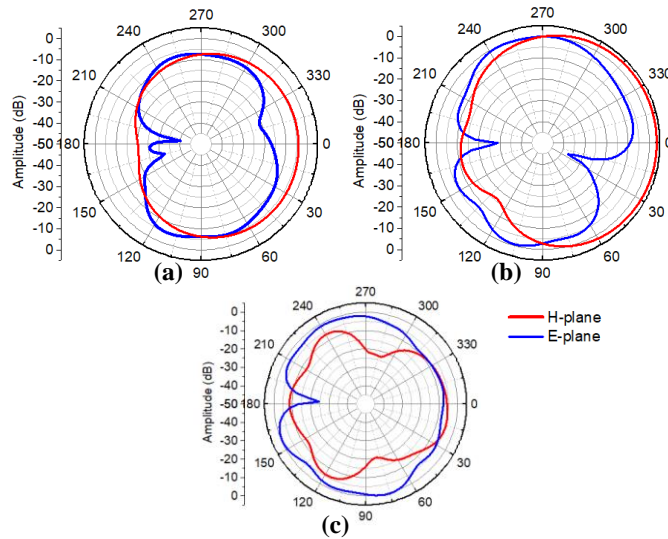


Figure 8.8 Measured radiation pattern of the designed antipodal Vivaldi antenna. (a) 4.5 GHz; (b) 8 GHz; (c) 14 GHz

8.3.3 Wideband slotted patch monopole antenna

In this section, the slotted patch monopole wideband antenna is investigated and designed for considering and estimating the order, ringing, and FWHM of the pulse in transmission and reception. The antenna is designed on Rogers RT/Duroid 5880 having a dielectric constant of 2.20 and a thickness of 62 mil. The analysis and design procedure of wideband antennas have been explained in [175,176]. Based on it, this antenna is designed in such a way that it is operating between 1 GHz to 20 GHz. The prototype of the designed antenna with front and back is shown in Figure 8.9 while the simulated vs. measured reflection coefficient response is shown in Figure 8.10. This antenna operates between 1 GHz to 20 GHz as its value of reflection coefficient is below -10 dB.

The radiation pattern of the designed antenna at three different frequencies are shown in Figure 8.11 while the snapshot taken during radiation pattern measurement is shown in Figure 8.5 (b). These values fall within the lower, middle, and upper range of the operating frequency bands.



Figure 8.9 Prototype of the designed wideband slotted patch monopole antenna

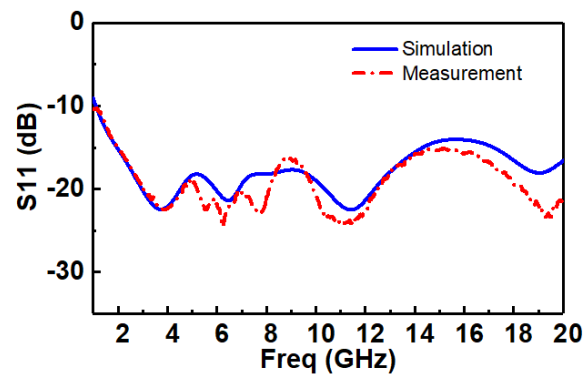


Figure 8.10 Simulated vs. measured reflection coefficient response of the designed wideband slotted patch monopole antenna

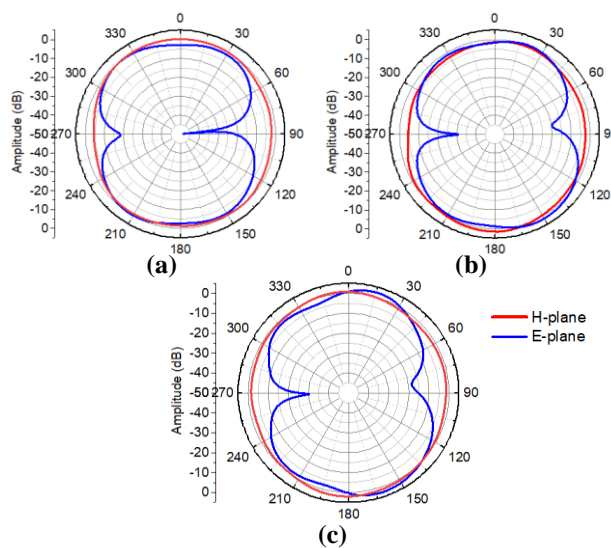


Figure 8.11 Measured radiation pattern of the designed wideband slotted patch monopole antenna. (a) 4.5 GHz; (b) 8 GHz; (c) 14 GHz

8.3.4 Biconical antenna

The biconical antenna also termed bicone antenna works in two modes based on its dimensions. If the length of aperture with $2L < 0.6\lambda$, it is considered as a conical dipole, and if $2L > 0.6\lambda$, it is considered as a horn. To design a wideband bicone antenna, the half-cone angle must be within the range of 30 degrees to 50 degrees as shown in Figure 8.12. In this case, the radiation pattern of the biconical antenna will be symmetrical around the bicone axis. The impulse response of the biconical antenna is approximated in [177] and can be given in compact form as:

$$\Gamma(R, t) = \frac{c\mu_0 \sin \theta}{4\pi R(1 - \cos \theta)} \left\{ \delta \left(t - \frac{R}{c} \right) \right\} \quad (8.6)$$

For observing the radiative pulse characteristics, the biconical wideband antenna is also simulated and the corresponding reflection coefficient response is shown in Figure 8.13.

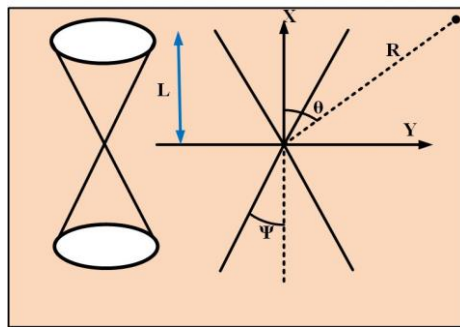


Figure 8.12 Design perspectives of bicone antenna

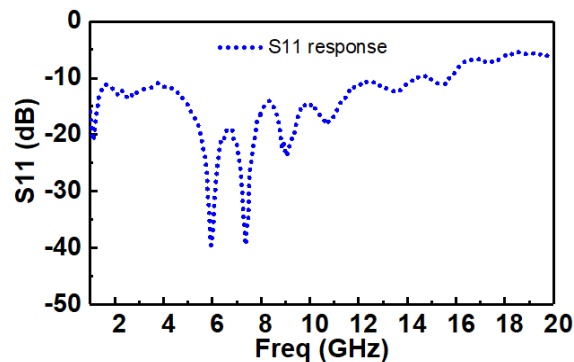


Figure 8.13 Simulated reflection coefficient of the designed bicone antenna

8.3.5 Ridged horn antenna

Waveguide-ridged horns radiate from an aperture with a fixed set of dimensions. Waveguide cut-off frequency on the lower frequency side and higher-order modes on the upper-frequency side are set to govern the antenna's bandwidth, respectively. The waveguide's monomode bandwidth is increased by the addition of two opposite ridges as shown in Figure 8.14 (a). On the other hand, the field distribution in the radiating aperture modifies the dimensions of the ridge. The normalized transfer function of the dual ridged horn antenna in transmitting and receiving mode is given by equations 8.7 and 8.8, respectively [167].

$$\Gamma(t) = \frac{-m\pi}{d \sin^2 \theta} \left\{ \cos^{m-1} \left[\frac{\pi c}{d \sin \theta} \left(t - \frac{d \sin \theta}{2c} \right) \right] \right. \\ \left. \times \sin \left[\frac{\pi c}{d \sin \theta} \left(t - \frac{d \sin \theta}{2c} \right) \right] \right\} \\ \times \left[u(t) - u \left(t - \frac{d \sin \theta}{c} \right) \right] \quad (8.7)$$

$$h(t) = \frac{1}{\sin \theta} \cos^m \left[\frac{\pi c}{d \sin \theta} \left(t - \frac{d \sin \theta}{2c} \right) \right] \\ \times \left[u(t) - u \left(t - \frac{d \sin \theta}{c} \right) \right] \quad (8.8)$$

We will also utilize a double ridged horn antenna in transmitting and receiving mode and will examine its output response. The simulated reflection coefficient of the double-ridged horn wave antenna is shown in Figure 8.14, which confirms that the antenna operates well within 1.5 GHz to 20 GHz.

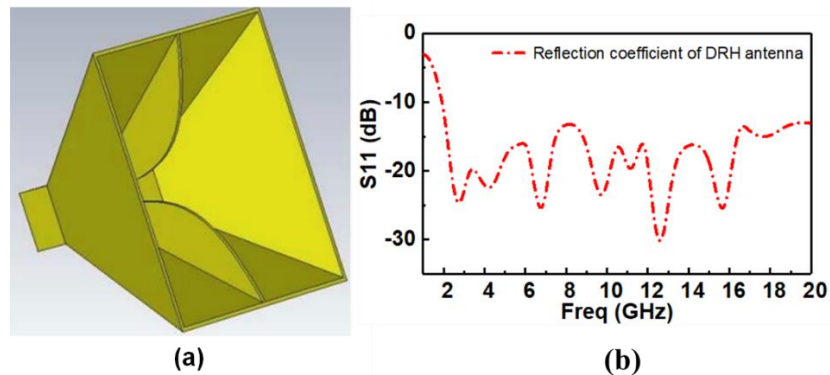


Figure 8.14 (a) Double ridged horn antenna; (b) S11 vs. frequency plot

8.4 Radiating pulse characteristics in different scenarios

In this section, we will discuss the input response of different sorts of antenna to see the output pulse response. For the case of experimental demonstration, we have selected Vivaldi, antipodal Vivaldi, and slotted patch monopole antenna, however, the analysis will be performed for different antennas to see the scenarios where a particular pulse shape is needed. It will include biconical antenna, ridged horn antenna, Vivaldi antenna, antipodal Vivaldi antenna, and slotted patch monopole antenna. All these antennas are properly analyzed and simulated to see the radiative pulse characteristics including pulse parameters of relevance.

First of all, we will discuss various fundamental pulse shapes that are considered in this work. The Gaussian function is in fact the zeroth order derivative. The derivative functions of even orders, including the zeroth order, are even functions (i.e., symmetric with respect to zero), and those of odd orders are odd functions (antisymmetric with respect to zero). The graphs of Gaussian derivative functions, from order 0 to order 2 are shown in Figure 8.15. In the time domain, it can be represented by equations (8.9)-(8.11) as follows:

$$y(t) = \frac{A}{\sqrt{2\pi}\sigma} \exp\left(-\frac{t^2}{2\sigma^2}\right) \quad (8.9)$$

$$y^{(1)}(t) = -\frac{At}{\sqrt{2\pi}\sigma^3} \exp\left(-\frac{t^2}{2\sigma^2}\right) \quad (8.10)$$

$$y^{(2)}(t) = A\left(\frac{t^2}{\sqrt{2\pi}\sigma^5} - \frac{1}{\sqrt{2\pi}\sigma^3}\right) \exp\left(-\frac{t^2}{2\sigma^2}\right) \quad (8.11)$$

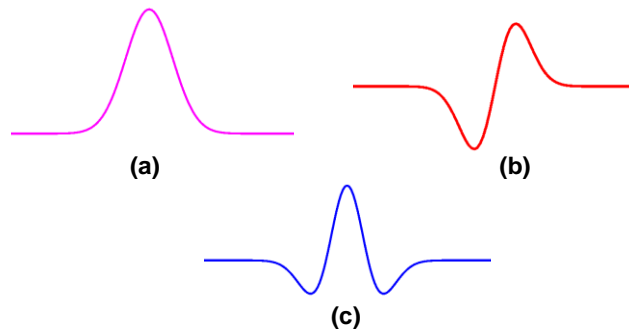


Figure 8.15 Various fundamental pulse shapes. (a) Gaussian pulse shape (zeroth order); (b) monocycle pulse shape (Order 1); (c) Doublet pulse shape (Order 2)

Now we will make use of the first-order Gaussian pulse as designed via a practical IR-UWB pulse generator to see the antenna effect on a pulse transmission and reception. As we know that the input pulse is dispersed by the band-limited gain of the antenna in the transmitter as well as on the receiver side. In this regard, various parameters are introduced to examine the performance of the pulse such as detailed ringing level, pulse stretch ratio, figure of merit (FOM), order of pulse, and system fidelity factor. The overall block diagram of the modules integrated is shown in Figure 8.16.

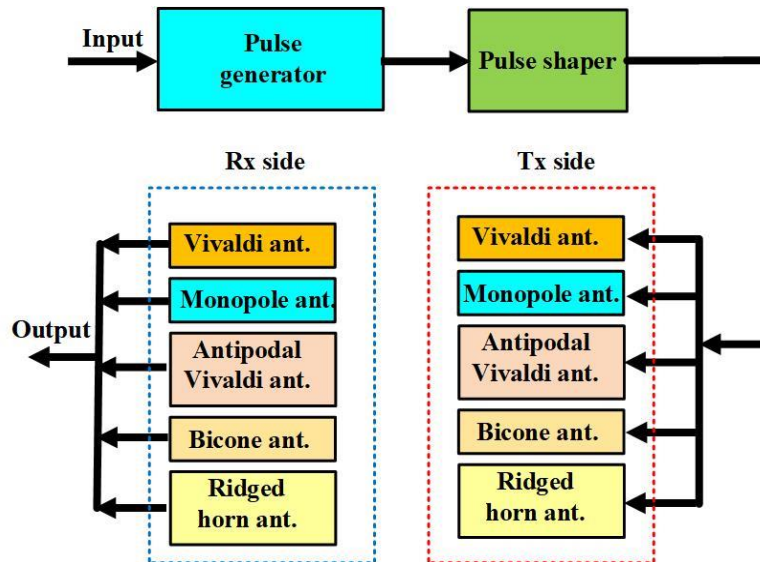


Figure 8.16 Block diagram of the overall system with all modules integrated

8.4.1 Vivaldi —Vivaldi combination

First, let's look into the case where the transmitting antenna is Vivaldi and the receiving antenna is also Vivaldi as designed, simulated, and measured in section III (a). Two similar Vivaldi antennas are separated by a distance d . These antennas are placed such that the distance between them is greater than $2D^2/\lambda$, where D represents the largest dimension of the Vivaldi antenna and λ is the wavelength at the central frequency of the antenna's operating frequency. The input pulse is taken from the pulse generator as designed in section II along with a pulse shaping network that is ultimately fed to the transmitting Vivaldi antenna. At the reception, a similar Vivaldi antenna is placed 100 cm away from the transmitting antenna to receive the transmitted pulse. It is seen that the transmitting Vivaldi antenna differentiates the transmitted pulse and a second order Gaussian pulse can be observed at the receiver side as shown in Figure 8.17.

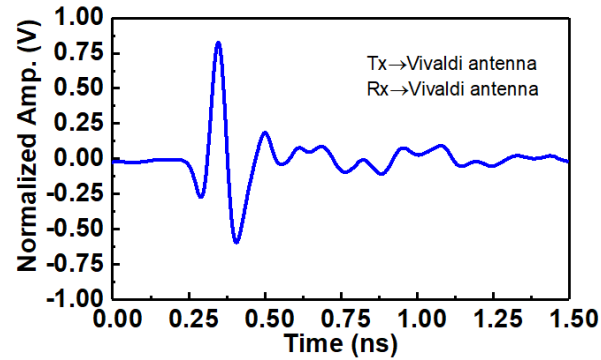


Figure 8.17 Received pulse at the output for the case where both Tx and Rx antennas are Vivaldi structure

8.4.2 Antipodal Vivaldi —Antipodal Vivaldi combination

Now let's examine the case where the transmitting antenna is antipodal Vivaldi and the receiving antenna is also antipodal Vivaldi as designed, simulated, and measured in section III(b). Two similar antipodal Vivaldi antennas are placed and separated by a distance of 50 cm. The input pulse is a first derivative Gaussian fed to the transmitting antipodal Vivaldi antenna and received by the receiving antenna. It is observed that the transmitting antipodal Vivaldi antenna differentiates the transmitted pulse and again we have a second-order Gaussian pulse at the receiver side as shown in Figure 8.18.

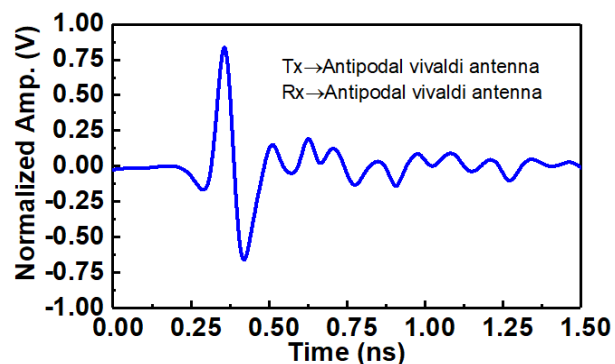


Figure 8.18 Received pulse at the output for the case where both Tx and Rx antennas are antipodal Vivaldi structure

8.4.3 Slotted monopole patch —Slotted monopole patch combination

Now, let's investigate the case where the transmitting antenna is a slotted monopole patch and the receiving antenna is also a slotted monopole patch as designed, simulated, and measured in section III(c). Two similar slotted patch radiators are placed by a distance of 100 cm. The input pulse is a first derivative Gaussian fed to the transmitting antenna and received by the receiving antenna. Again, the slotted patch radiators differentiate the transmitted pulse and a second order Gaussian pulse is obtained at the receiver side as shown in Figure 8.19.

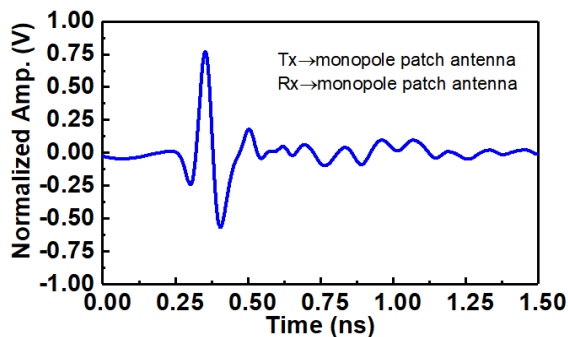


Figure 8.19 Received pulse at the output for the case where both Tx and Rx antennas are slotted patch structure

8.4.4 Double ridged horn —Double ridged horn combination

A scenario is studied where the transmitting antenna is a double-ridged horn, and the receiving antenna is also a double-ridged horn as designed and simulated in section III(e). Such a combination also differentiates the originally input signal with an increase in ringing level as shown in Figure 8.20.

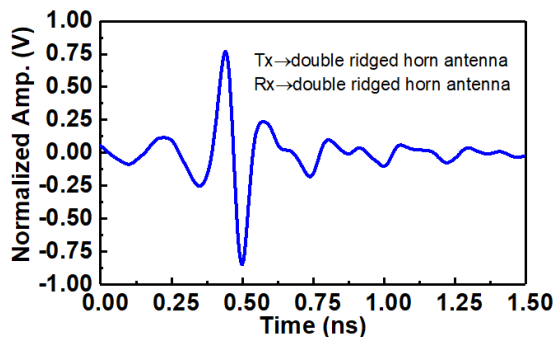


Figure 8.20 Received pulse at the output for the case where both Tx and Rx antennas are double ridged structure

8.4.5 Antipodal Vivaldi Antenna —Biconical Antenna combination

This time, a different combination scenario is studied where the transmitting antenna is an antipodal Vivaldi, and the receiving antenna is a bicone. The Vivaldi antenna is discussed in section III(a) while the bicone antenna is described in section III(d) along with frequency-dependent results. This combination gives the same pulse at the output without changing the order of the input pulse as shown in Figure 8.21. It is due to the reason why the biconical antenna (or bicone) operates in two modes. If the aperture length ($2L$) is less than 0.6λ , the bicone may be considered as a dipole with conical arms. If the aperture length is greater than 0.6λ , the bicone may be considered as a horn. The bicone has a radiation pattern that is rotationally symmetric around the axis of the bicone. For wideband bicones, the half cone angle (ψ) will be between 30° and 50° . The former one provides the same pulse order in comparison to the later one. This is a significant finding and will be much more helpful for some applications like wireless vital signs monitoring for breast tumor detection and the heartbeat and respiration of small conscious animals without touching [178].

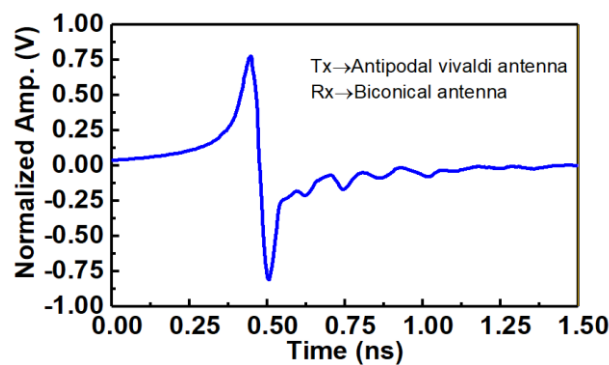


Figure 8.21 Received pulse at the output for the case where Tx antenna is antipodal Vivaldi and Rx antenna is bicone

So the overall above scenarios can be summarized in the form of a table as demonstrated in Table 8.1 by considering the order of the input and output pulses. It gives a clear relationship between various combination of transmitting and receiving antennas and the corresponding output pulses. This result will be helpful for various radar designers to select a proper scenario in their case while meeting the desired goals. It must be noted that we have represented Vivaldi antenna by VV, Antipodal Vivaldi antenna by AVV, Monopole patch antenna by MP, Double ridged horn antenna by DRH, and Bicone antenna by BC in this chapter. Also, in Table 8.1, the term Same mean that

transmitted and received pulses have same order, Diff. mean that transmitted pulse is differentiated, and Int. means that transmitted pulse is integrated on the output side.

Table 8.1 Summary and relationship of transmitting and receiving antennas for different antenna combinations

Transmitting Antennas	Receiving Antennas				
	VV	AVV	MP	DRH	BC
VV	Diff.	Diff.	Diff.	Diff.	Same
AVV	Diff.	Diff.	Diff.	Diff.	Same
MP	Diff.	Diff.	Diff.	Diff.	Same
DRH	Diff.	Diff.	Diff.	Diff.	Same
BC	Same	Same	Same	Same	Int.

8.5 Experimental demonstrations

An experimental demonstration is performed to show that the proposed setup operates properly and that the output received waveforms have the same order as simulations. In this regard, three different antennas are fabricated including Vivaldi, antipodal Vivaldi, and monopole patch radiators as discussed in section III along with the prototypes. The experimental setup is arranged in such a way that first calibration of the setup is carried out to eliminate different effects from cables and connector losses. Therefore, an arbitrarily generated pulse is fed to the transmitting antenna from an arbitrary waveform generator (AWG) and received via a receiving antenna, and finally displayed using an oscilloscope. It is clear from the test experiment that the calibration is excellent, and the delay is adjusted properly.

The block diagram of the complete measurement setup is shown in Figure 8.22. As can be seen that an input sinusoidal signal is generated by AWG Keysight M8190A which is fed as an input to the fabricated monocycle picosecond pulse generator. Also, a dc voltage source is employed to control the dc bias and modeled as a dc power supply. The other terminal of the pulse generator (PG) is connected to the transmitting antenna, which is basically the output of the pulse generator. The transmitting and receiving antennas are mounted by a turn-table stand specifically designed for these antennas. The receiver antenna is placed at a distance of greater than $2D^2/\lambda$ from the transmitting antenna. Finally, the receiving antenna is connected to an oscilloscope for monitoring the output pulse.

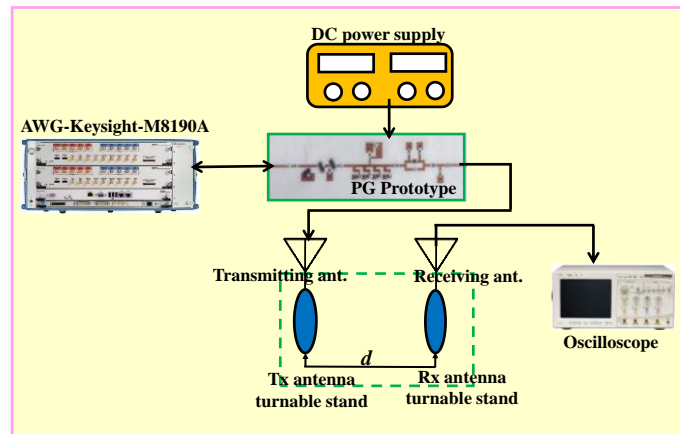


Figure 8.22 Complete measurement setup block diagram

First of all, we consider a case where the transmitting antenna is Vivaldi and the receiving antenna is also Vivaldi. The output response from the oscilloscope, in this case, is shown in Figure 8.23. It is clear from Figure 8.23 that compared to the simulated waveform, the same pulse shape is observed with the same pulse order and FWHM. However, there arises an undesired extra ringing level as seen in Figure 8.23. This is caused by the antenna impact on the radiated pulse. It is also noteworthy in each case that the amplitude of the measured output pulse is low, which can be bolstered easily by using a power amplifier with the antenna on the transmitter side.

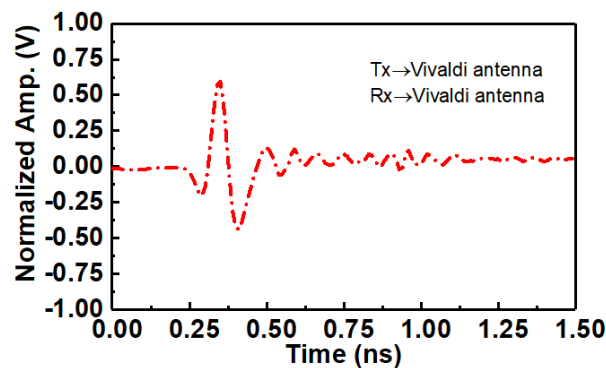


Figure 8.23 Measured received pulse at the output for the case where both Tx and Rx antennas are Vivaldi structure

Now, let's consider the scenario where the transmitting antenna is antipodal Vivaldi and the receiving antenna is also antipodal Vivaldi. The output response from the oscilloscope in this case is shown in Figure 8.24. It is clear from Figure 8.24 that with reference to the simulated waveform,

the same pulse shape is obtained with the same pulse order and FWHM, which means that the antipodal Vivaldi antenna differentiates the input signal. However, in this case, we have a considerable increase in ringing behavior as compared to the Vivaldi case, which shows the antipodal Vivaldi antenna's pronounced impact on the radiated pulse.

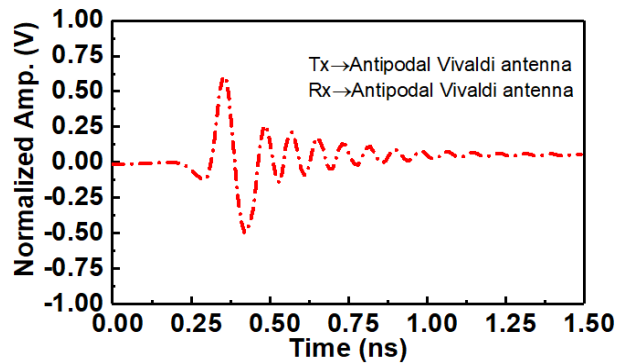


Figure 8.24 Measured received pulse at the output for the case where both Tx and Rx antennas are antipodal Vivaldi structure

The output response in the case when the transmitting antenna is a slotted patch monopole, and the receiving antenna is also a slotted patch monopole as shown in Figure 8.25. It is clear from Figure 8.25 that we have the same pulse order and pulse duration as the simulated counterparts, which suggests that the slotted patch monopole antenna differentiates the input signal. Also, in this case, we have a reduced level of ringing.

Finally, we consider the oblique incidence scenario in Figure 8.26 where we have a pulse distortion when the receiving antenna is arranged from the transmitting antenna at specific angles. As can be seen in Figure 8.26 that there is a pulse distortion along with a considerable dip in signal level when the antenna is moved from 10° to 40° in the azimuth plane. This scenario is modeled for the case where the transmitting antenna is a slotted patch monopole, and the receiving antenna is also a slotted patch monopole. It can also be modeled for other cases, depending on the desired applications and requirements.

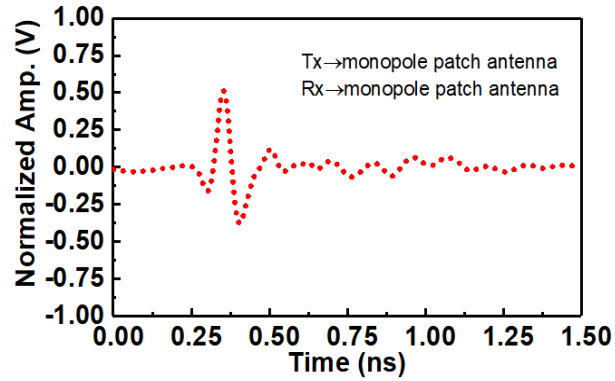


Figure 8.25 Measured received pulse at the output for the case where both Tx and Rx antennas are slotted patch structure

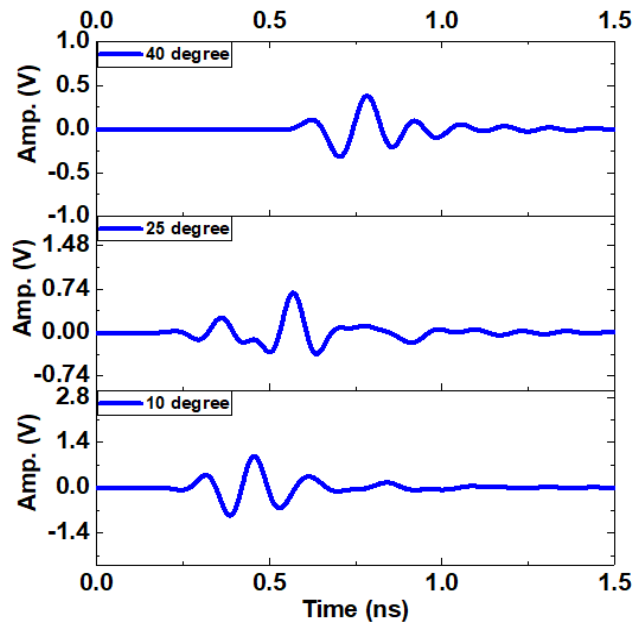


Figure 8.26 Measured received pulse distortion at various angles between the Tx and Rx antennas for the case where both Tx and Rx antennas are a slotted patch structure

8.6 Received pulse analysis in terms of important pulse parameters

Here some critical pulse parameters are modeled to show their corresponding values in different scenarios. It includes the pulse stretch ratio, system fidelity factor, ringing behavior, FWHM, and figure of merit (FOM).

8.6.1 Stretch ratio (SR)

The temporal width of the transmitted pulses can be a significant factor in the design of the UWB transceiver. For signal $x(t)$, the normalized cumulative energy function of the signal is given as [179]

$$E_s(t) = \frac{\int_{-\infty}^t |x(t')|^2 dt'}{\int_{-\infty}^{\infty} |x(t')|^2 dt'} \quad (8.12)$$

The corresponding pulse width for 90% of the captured energy is use to calculate the stretch ratio by removing 5% of the energy on either side of the pulse [179]. If $h(t)$ is the radiated electric field waveform and $G(t)$ is the input source, then the pulse stretch ratio (SR) can be defined as:

$$SR = \frac{E_h^{-1}(0.95) - E_h^{-1}(0.05)}{E_G^{-1}(0.95) - E_G^{-1}(0.05)} \quad (8.13)$$

In our analysis, we have calculated the stretch ratio at $\phi=0^\circ$ plane as the corresponding radiation pattern is almost omnidirectional. The ideal value of the stretch ratio is 1 and the stretch ratio for various received signals in various scenarios is modeled in Table 8.2.

Table 8.2 Stretch ratio for various angles at $\phi=0^\circ$ plane

Received Signal	σ (ps)	0°	40°
1 st order Gaussian (Tx:MP & Rx:BC)	200	1.2321	1.1545
2 nd order Gaussian (Tx:MP & Rx:MP)	150	1.3175	2.6784
2 nd order Gaussian (Tx:VV & Rx:VV)	150	1.2721	2.5602
2 nd order Gaussian (Tx:AVV & Rx:AVV)	150	1.2713	3.2985

8.6.2 System fidelity factor (SFF)

This parameter measures the strength of the correlation between the input signal voltage and the emitted electric field [179]. The SFF can be determined by multiplying the input impulse signal's frequency component by the system's frequency domain transfer function, which is then converted to the time component using an appropriate mathematical tool. The received signal pulse is completely identical to the transmitter's input signal pulse if the SFF value is 1, completely different

from the transmitter input if the SFF value is 0, and totally unrecognizable if the SFF value is less than 0.5. It can be given using the following relation:

$$SFF = \max_{\tau} \left[\frac{\int_{-\infty}^{\infty} G(t)S(t+\tau)dt}{\sqrt{\int_{-\infty}^{\infty} |G(t)|^2 dt} \sqrt{\int_{-\infty}^{\infty} |S(t+\tau)|^2 dt}} \right] \quad (8.14)$$

where the received signal is represented by $S(t)$ in equation (8.14). The calculated SFF values for various received pulses are given in Table 8.3.

Table 8.3 SFF is calculated from the corresponding measured transfer functions

Received Signal	σ (ps)	Side by Side	Face to Face
1 st order Gaussian (Tx:MP & Rx:BC)	200	0.7157	0.8934
2 nd order Gaussian (Tx:MP & Rx:MP)	150	0.7011	0.8872
2 nd order Gaussian (Tx:VV & Rx:VV)	150	0.6878	0.8718
2 nd order Gaussian (Tx:AVV & Rx:AVV)	150	0.6350	0.8557

8.6.3 Ringing behavior

Ringing is the undesired ripples found along with the radiated signals. The detailed ringing level of the output pulse (R_l) in each case is also provided based on the following equation [4]. The detailed ringing level of the received pulses in various scenarios is given in Table 8.4.

$$R_l = 20 \log \frac{\text{Ringing amplitude}_{\text{peak-to-peak}}}{\text{Pulse amplitude}_{\text{peak-to-peak}}} \quad (8.15)$$

When compared to the simulated result, the detailed ringing level is slightly lower. However, the ringing's peak is still eight times smaller than the pulse's peak amplitude, which is within acceptable limits.

Table 8.4 Detailed ringing level of received pulses in various scenarios

Received Signal	σ (ps)	R_L (dB)
1 st order Gaussian (Tx:MP & Rx:BC)	200	-19.36
2 nd order Gaussian (Tx:MP & Rx:MP)	150	-18.71
2 nd order Gaussian (Tx:VV & Rx:VV)	150	-17.93
2 nd order Gaussian (Tx:AVV & Rx:AVV)	150	-15.24

8.6.4 Figure of merit (FOM)

A novel parameter FOM is introduced as a criterion for comparison that involves critical pulse parameters including pulse width, amplitude, and ringing level as a unified single metric. It can be calculated by the following relation and mentioned for various scenarios in Table 8.5.

$$FOM = \frac{\text{Pulse amp. (V)}}{FWHM(ns) \times \text{Ringing amp.}} \quad (8.16)$$

Table 8.5 FOM of received pulses in various scenarios

Received Signal	σ (ps)	FOM
1 st order Gaussian (Tx:MP & Rx:BC)	200	1.53
2 nd order Gaussian (Tx:MP & Rx:MP)	150	1.32
2 nd order Gaussian (Tx:VV & Rx:VV)	150	1.29
2 nd order Gaussian (Tx:AVV & Rx:AVV)	150	1.10

8.7 Conclusion

In this chapter, a complete model for the transmission and reception of picosecond pulses is presented by estimating antenna effects. The impact on pulse order, system fidelity factor, pulse distortion, stretch ratio, detailed ringing level, and figure of merit are shown and evaluated on the receiver side from various fundamental antenna combinations. A complete system model is developed, simulated, and measured by deploying a monocycle pulse generator, various wideband antennas, and their combinations. The experimental demonstration is performed in each case by providing radiated pulse characteristics. Finally, a set of combinations of antennas are proposed to receive the desired radiated pulse on the receiver side. It is demonstrated that all other antennas differentiate the input pulse at the receiver side except the bicone antenna combination. This work will possibly pave the way for wireless vital signs monitoring including heartbeat monitoring, tumors detection, touchless heartbeat and respiration detection of small conscious animals, and synthetic aperture radars.

CHAPTER 9 GENERAL DISCUSSION

Ultra-broadband systems and ultrafast electronics, including such well-established and emerging applications as time domain reflectometer, arbitrary waveform generator, sampling oscilloscope, frequency synthesizer, through-wall radar imaging, indoor communication, radar surveillance, and medical radar detection, require the generation, transmission, and processing of high-quality ultrashort pulses ranging from nanosecond (ns) to picosecond (ps). Impulse radar advancements in industrial, scientific, and medical (ISM) domains are, for example, driven by ns-defined UWB technologies. Indeed, the generation of ultra-short ps pulses is highly desired for all these applications. On the other hand, due to the variety and applicability of different pulse generation and compression techniques, it is difficult for end users to select optimum or appropriate pulse generation and compression techniques. To this end, this thesis is set to develop and elaborate various ultra-short pulse electronic pulse generation and compression techniques along with the pulse transmission and reception characteristics. A technique is shown in Chapter 8 for the usage of these pulse generators in practical systems.

This thesis has shown the concept of soliton and shock waves with the corresponding transformation technique to the electrical domain, specifically microwave electronics. As it was discussed that different ultrashort pulse generators are made possible by the concept of soliton and shock waves having a higher FOM in comparison to the state of the art in the literature. When coming to the design of the ultrashort pulse generator, it is crucial that the output pulse has a reduced ringing level that is made possible by the good use of NLTLs to properly counteract the dispersion through the non-linearity.

It is also important that the developed pulse generators have the ability to transform to higher order pulse shapes and it is made possible by integrating innovative pulse shaping networks into the designed pulse generators. It was shown in Chapter 7 how the transformation is made possible between the Gaussian and monocycle pulse shapes while maintaining FWHM, pulse amplitude, and detailed ringing level.

It is also investigated that magnetic NLTLs including NLMTLs and NLGTLs are also worthy for pulse generation and compression. Since NLMTLs are proposed for the first time and it can be seen that this class of NLTL has the capability of simultaneous rise and fall time compression in comparison to traditional NLGTL, where we have only rise time compression. It was also shown

that the concept of soliton is applicable in the magnetic domain and NLMTLs follow the modified form of the KdV equation.

The parametric optimization of capacitive, inductive, hybrid, and gyromagnetic NLTLs is investigated and various important parameters are highlighted in detail. This will give a piece of critical information to the end user in the development and application of a specific class of NLTLs based on the desired goals. Finally, the radiated pulse characteristics of these pulse generators are explored and based on time domain analysis, the corresponding output response is shown in various scenarios of interest. Various antenna combinations are provided in this regard to appreciate the received pulse in each case. It was seen that majority of the antenna combination differentiates the transmitted pulse and the output pulse is the time derivative of the input pulse. However, in the case of the biconical antenna with any other antenna (Vivaldi, antipodal Vivaldi, slotted patch monopole, ridged horn) investigated in Chapter 8, it is seen that the received pulse is exactly the same shape as the input transmitted pulse.

It is also shown in Chapter 8 how the proposed pulse generators can be utilized in a practical setup. As we know there is a huge number of applications of ultrashort pulses in everyday life that come across us. Among them, some of the well-known are UWB radars, wireless vital signs monitoring, tumors detection, THz detection, medical imaging, and GPR applications.

One of them, UWB radar is widely used to detect and/or identify people at a close ranges through obstacles like walls and ruins. In contrast to magnetic induction, thermal imaging, X-ray, and some other success-restrictive methods, a human subject can be detected based on a subtle motion of his or her chest caused by breathing and heartbeat (micro-Doppler effects). This method is also unaffected by temperature, the composition of a non-metal wall, or target's clothing. The electromagnetic waves that UWB radar typically emits have a large bandwidth and nanosecond or picosecond pulse duration. Most notably, UWB radar can locate human individuals with greater accuracy when compared to continuous wave radar systems. Consequently, the UWB radar is thought to be ideal for localization and detection purposes, especially in the aftermath of natural disasters, where an important and critical part of the system is related to the development of a ultrashort pulse generation.

Similarly, breast tumors and cancer detection are another important potential medical and healthcare applications of ultrashort pulses. In this setup, Gaussian and monocycle pulses for breast cancer

detection are usually used. To guarantee the accuracy of detection, it is important to stabilize the pulse width and amplitude of the pulse generator. This technique is advantageous in comparison to conventional techniques as it is painless and more accurate.

The proposed solutions will pave the way toward the development of ultrafast electronics by resolving the major issues of compression limitation within electronic structures, which is a promising candidate for IR-UWB and high-speed interconnect networks. Breast cancer detection in early stages, geophysical exploration, irregular miniaturized tumor detection, etc. would be made possible by deploying our proposed pulse generation techniques in the system. The radiated pulse characteristic model provided in this work will be significant in GPR for antipersonnel landmine detection. The critical part of GPR in such applications is the utilization and selection of an appropriate antenna pair setup for transmission and reception that would ultimately help to show whether the transmitted pulse is integral, derivative, or the same on the receiver side. In short, this work offers a new horizon for the future development of ultrafast electronics especially in connection with ultrashort pulse transmission in free space.

CHAPTER 10 CONCLUSION AND RECOMMENDATIONS

10.1 Conclusion

This Ph.D. thesis explores, presents, and discusses two main streams of research where the former is based on investigating and developing new classes of NLTLs while the second is based on developing pulse generators based on these NLTLs and corresponding compression capability. The overall contents of this Ph.D. thesis can be summarized as:

- Theoretical foundations of NLETLS are developed from hydrodynamics perspectives by relating them with solitons and shock wave models. This multi-dimensional transformation approach has provided the most accurate model for NLETLS so far.
- Solitons in the electrical domain are studied via capacitive, inductive, and hybrid NLTL structures and the transformation of these structures for generating shock wave transients is provided and modeled.
- This work has for the first time provided techniques for the combination of rise and fall edge transients (less than 10ps) to achieve clean picosecond pulse generators.
- The concept of simultaneous rise and fall edge compression is made possible through NLETLS as well as NLMTLS.
- This work has demonstrated a theoretical and experimental concept for the analysis of NLMTLS considering the localized disturbances that arise within ferrimagnetic materials for the first time. NLMTLS are also validated so to present the capability of simultaneous rise and fall time compression due to their simultaneous control of magnetic field strength and applied biasing voltage.
- This work has also presented ultrashort pulses where the compression capability is maximized and a pulse of 10.1 ps is achieved with outstanding improvement in ringing behavior. The presented NLETL scheme stems from a unique combination of a single varactor diode and stacked varactor diode per NLETL cell, which was designed to exploit a significant effect of non-linearity in connection with the varactor diode. This technique generates a higher compression factor in both rise and fall time of NLETL circuits in

comparison to single varactor diodes per NLTL section. This scheme was validated to work well in a triple-stacked NLTL topology by maximizing the compression factor.

- Transformation of these ultrashort pulses into higher derivatives of the Gaussian pulse is provided in each scheme while maintaining the pulse compression integrity.
- The radiated pulse characteristics of these ultrashort pulses are investigated in detail. The transmission of these ultrashort electronic pulses in free space was explored for specific future applications.
- To transmit the ultrashort pulse in free space via a practical antenna setup, we need a higher derivatives of the Gaussian pulse. In this regard, various techniques are provided for 1st and second derivative of Gaussian pulses that would be ultimately used for UWB communication in breast cancer detection, vital signs monitoring in human beings, vital signs in small conscious animals for assessing their health and behavior, and ground penetrating radars.
- Different antennas are studied and designed for such transmission and reception including Bicone antenna, Vivaldi antenna, antipodal Vivaldi antenna, and super-wide band monopole antenna. The radiated pulse characteristics are studied by analyzing the transmission and reception in different combinations of antennas.

10.2 Recommendations

Efforts have been invested into this Ph.D. thesis to provide the most promising techniques for the generation, compression, shaping, and transmission of ultrashort pulses. However, more research work is still required, which can be summarized below:

- There is a huge gap in research on the transformation into the arena based on magnetic materials. Since it is seen that magnetic materials have the capability of compression, so it is much needed that new magnetic materials are explored for the possibility of pulse generation and compression. It is believed that NLMTLs will have higher compression capability than NLETs if properly explored. The localized disturbance within ferrimagnetic materials and sophisticated dissipative processes need to be explored in much more detail with different innovative magnetic materials. This research will possibly provide a fresh and successful avenue for investigating magnetic materials and their effects

on NLETs and ultrafast electronics by providing the direction to the researchers for the first time.

- Superconductors, photoconductive switches, and cryo-electronic research will probably continue to push for achieving shorter and shorter pulse widths and rise/fall time. Josephson junctions and memristors will be a possible key that the researcher will try to unlock this area further.
- Real-life applications were also reviewed from radiated pulse perspectives, where a huge gap for research still exists. It is seen that only sub-nanosecond pulses are used in these systems. The impact of picosecond-based pulses needs to be studied on these systems with new innovative super-wideband radiators for pulse radiation. Wireless vital signs monitoring will be one of the most focused research areas in the future, which will have a huge impact on the medical domain.
- Accurate breast tumor detection having irregular shape and size can be managed with such ultrashort pulses by utilizing into the future UWB radar transceivers.
- These extremely ultrashort rises and fall edge transients generated via this Ph.D. thesis research need to be used and explored in connection with high-speed and ultra-fast interconnects with all pass waveguide structures. The transmission of the ultrashort pulses via all pass waveguide structures will efficiently transmit picosecond electrical pulses for chip-to-chip interconnects in high-speed circuits while maintaining signal integrity.
- The radiated pulse characteristic model developed in this work can be used in GPR for antipersonnel landmine detection. The critical part of GPR in such applications is the utilization and selection of the correct antenna pair setup for transmission and reception that would ultimately help to show whether the transmitted pulse is integral, derivative, or the same on the receiver side.

REFERENCES

- [1] "Revision of Part 15 of the Commissions rules regarding ultra-wideband systems," *FCC, Washington, DC, FCC First Rep. and Order ET-Docket 98-153*, Apr. 2002.
- [2] D. Strickland, and G. Mourou, "Half of Nobel prize in physics honors the inventors of chirped pulse amplification," *Physics Today*, pp. 1-5, Dec. 2018.
- [3] D. Oloumi, J. -W. Ting and K. Rambabu, "Design of Pulse Characteristics for Near-Field UWB-SAR Imaging," *IEEE Transactions on Microwave Theory and Techniques*, vol. 64, no. 8, pp. 2684-2693, 2016.
- [4] M. Rahman and K. Wu, "A Nonlinear Transmission Approach to Compressing Rise and Fall Time in Picosecond Pulse Generation," *IEEE Transactions on Instrumentation and Measurement*, vol. 70, pp. 1-13, 2021, Art no. 2004013
- [5] Picosecond Pulse Labs, "A new breed of comb generators featuring low phase noise and low input power," *Microw. J.*, vol. 49, no. 5, pp. 278–280, May 2006.
- [6] J. F. Holzman, F. E. Vermeulen, and A. Y. Elezzabi, "Recombination-independent photogeneration of ultrashort electrical pulses," *Applied physics letters*, vol. 76, no. 2, pp. 134-136, 2000.
- [7] D. Oloumi, K. K. -M. Chan, P. Boulanger and K. Rambabu, "SAGD Process Monitoring in Heavy Oil Reservoir Using UWB Radar Techniques," *IEEE Transactions on Microwave Theory and Techniques*, vol. 64, no. 6, pp. 1884-1895, 2016.
- [8] E. C. Fear, J. Bourqui, C. Curtis, D. Mew, B. Docktor and C. Romano, "Microwave Breast Imaging With a Monostatic Radar-Based System: A Study of Application to Patients," *IEEE Transactions on Microwave Theory and Techniques*, vol. 61, no. 5, pp. 2119-2128, 2013.
- [9] K. Schab, D. Huang and J. J. Adams, "Pulse Characteristics of a Direct Antenna Modulation Transmitter," *IEEE Access*, vol. 7, pp. 30213-30219, 2019.
- [10] Jeongwoo Han and C. Nguyen, "On the development of a compact sub-nanosecond tunable monocycle pulse transmitter for UWB applications," *IEEE Transactions on Microwave Theory and Techniques*, vol. 54, no. 1, pp. 285-293, 2006.

- [11] S. Diamond et al., "Resonant tunneling diodes for switching applications," *Applied physics letters*, vol. 54, no. 2, pp. 153-155, 1989.
- [12] A. Matiss, A. Poloczek, A. Stohr, W. Brockerhoff, W. Prost, and F. J. Tegude, "Sub-nanosecond pulse generation using resonant tunneling diodes for impulse radio," *In 2007 IEEE International Conference on Ultra-Wideband*, pp. 354-359, Sep. 2007.
- [13] T. Xia, A. S. Venkatachalam, and H. Dryver, "A high-performance low-ringing ultrawideband monocycle pulse generator," *IEEE Trans. on Instrumentation and Meas.*, vol. 61, no. 1, pp. 261-266, Jul. 2012.
- [14] J. Zhou, X. Yang, Q. Lu, and F. Liu, "A novel low-ringing monocycle picosecond pulse generator based on step recovery diode," *PloS one.*, vol. 10, no. 8, pp. 1-9, Aug. 2015.
- [15] J. S. Lee, and C. Nguyen, "Uniplanar picosecond pulse generator using step-recovery diode," *Electronics letters*, vol.37, no. 8, pp. 504-506, 2001.
- [16] D. Lee, G. Shaker, and W. Melek, "Development of a compact monocycle pulse generator for UWB impulse radar applications," *Microwave and Optical Technology Letters*, vol. 62, no. 10, pp. 3119-3123, Oct. 2020.
- [17] C. Zhang and A. E. Fathy, "Reconfigurable Pico-Pulse Generator for UWB Applications," *2006 IEEE MTT-S International Microwave Symposium Digest*, pp. 407-410, 2006.
- [18] H. Hafdallah, A. Ouslimani, R. Adde, G. Vernet, and P. Crozat, "Feasibility of picosecond electrical sampling using GaAs FET," *IEEE Trans. on Instrumentation and Meas.*, vol. 49, no. 1, pp. 172-177, Feb. 2000.
- [19] J. Rao, W. Zhang, S. Jiang and Z. Li, "Nanosecond pulse generator based on cascaded avalanche transistors and Marx circuits," *IEEE Transactions on Dielectrics and Electrical Insulation*, vol. 26, no. 2, pp. 374-380, 2019.
- [20] S. Shen, J. Yan, G. Sun and W. Ding, "Improved Auxiliary Triggering Topology for High-Power Nanosecond Pulse Generators Based on Avalanche Transistors," *IEEE Transactions on Power Electronics*, vol. 36, no. 12, pp. 13634-13644, 2021.

- [21] J. Li et al., "Theoretical Analysis and Experimental Study on an Avalanche Transistor-Based Marx Generator," *IEEE Transactions on Plasma Science*, vol. 43, no. 10, pp. 3399-3405, 2015.
- [22] Q. Wang, X. Tian, Y. Liu, B. Li and B. Gao, "Design of an Ultra-Wideband Pulse Generator Based on Avalanche Transistor," *2008 4th International Conference on Wireless Communications, Networking and Mobile Computing*, pp. 1-4, 2008.
- [23] W. G. Magnuson, "Variable-Width Pulse Generation Using Avalanche Transistors," *IEEE Transactions on Instrumentation and Measurement*, vol. 12, no. 2, pp. 56-64, 1963.
- [24] D. Salameh and D. Linton, "Microstrip GaAs nonlinear transmission-line (NLTL) harmonic and pulse generators," *IEEE Transactions on Microwave Theory and Techniques*, vol. 47, no. 7, pp. 1118-1122, 1999.
- [25] D. Salamh and D. Linton, "Nonlinear transmission line (NLTL) design as a pulse generator," *IEEE MTT/ED/AP/LEO Societies Joint Chapter. United Kingdom and Republic of Ireland Section. 1996 2nd High Frequency Postgraduate Student Colloquium*, pp. 7-10, 1996.
- [26] P. Indirayanti, W. Volkaerts, P. Reynaert, and W. Dehaene, "Picosecond pulse generation with nonlinear transmission lines in 90-nm CMOS for mm-wave imaging applications," *19th IEEE International Conference on Electronics, Circuits, and Systems (ICECS 2012)*, pp. 885-888, 2012.
- [27] M. Samizadeh Nikoo, S. M. -A. Hashemi and F. Farzaneh, "Theory of RF Pulse Generation Through Nonlinear Transmission Lines," *IEEE Transactions on Microwave Theory and Techniques*, vol. 66, no. 7, pp. 3234-3244, 2018.
- [28] M. J. W. Rodwell, M. Kamegawa, R. Yu, M. Case, E. Carman and K. S. Giboney, "GaAs nonlinear transmission lines for picosecond pulse generation and millimeter-wave sampling," *IEEE Transactions on Microwave Theory and Techniques*, vol. 39, no. 7, pp. 1194-1204, July 1991.
- [29] E. Afshari, and A. Hajimiri, "Nonlinear transmission lines for pulse shaping in silicon," *IEEE Journal of Solid-State Circuits*, vol. 40, no. 3, pp. 744-752, Mar. 2005.
- [30] D. W. Van der Weide, "Delta-doped Schottky diode nonlinear transmission lines for 480-fs, 3.5-V transients," *Applied Physics Letters*, vol. 65, no. 7, pp. 881-883, 1994.

- [31] M. Falah and D. Linton, "High data rate pulse regeneration using non-linear transmission line technology (NLTL)," *6th IEEE High Frequency Postgraduate Colloquium (Cat. No.01TH8574)*, 2001, pp. 136-141, 2001.
- [32] M. Li, R. G. Harrison, R. E. Amaya, J. -M. Duchamp, P. Ferrari and N. G. Tarr, "CMOS varactors in NLTL pulse-compression applications," *2007 European Microwave Conference*, pp. 1405-1408, 2007.
- [33] J. O. Rossi and P. N. Rizzo, "Study of hybrid nonlinear transmission lines for high power RF generation," *2009 IEEE Pulsed Power Conference*, pp. 46-50, 2009.
- [34] F. S. Yamasaki, E. Schamiloglu, J. O. Rossi and J. J. Barroso, "Spice simulations of inductive Nonlinear Transmission Lines," *2015 SBMO/IEEE MTT-S International Microwave and Optoelectronics Conference (IMOC)*, pp. 1-5, 2015.
- [35] M. Rahman and K. Wu, "Hybrid Dissipative NLTL Soliton Solution Based on KdV Approach," *2020 IEEE International Symposium on Antennas and Propagation and North American Radio Science Meeting*, pp. 2041-2042, 2020.
- [36] F. S. Yamasaki, E. Schamiloglu, J. O. Rossi and J. J. Barroso, "Simulation Studies of Distributed Nonlinear Gyromagnetic Lines Based on LC Lumped Model," *IEEE Transactions on Plasma Science*, vol. 44, no. 10, pp. 2232-2239, Oct. 2016.
- [37] A. J. Fairbanks, A. M. Darr and A. L. Garner, "A Review of Nonlinear Transmission Line System Design," *IEEE Access*, vol. 8, pp. 148606-148621, 2020.
- [38] F. S. Yamasaki, J. O. Rossi, L. C. Silva, E. G. L. Rangel and E. Schamiloglu, "Operation of a Gyromagnetic Line with Magnetic Axial Bias," *2019 IEEE Pulsed Power & Plasma Science (PPPS)*, pp. 1-4, 2019.
- [39] J. W. Bragg, J.C. Dickens, and A. A. Neuber, "Material selection considerations for coaxial, ferrimagnetic-based nonlinear transmission lines," *Journal of Applied Physics*, vol. 113, no. 6, p.064904, 2013.
- [40] D. M. French, B. W. Hoff, S. Heidger and D. Shiffler, "Dielectric nonlinear transmission line," *2011 IEEE Pulsed Power Conference*, pp. 341-345, 2011.

- [41] M. Rahman and K. Wu, "Theory and Practice of Multidimensional Non-Linear Transmission Line," *2021 IEEE MTT-S International Wireless Symposium (IWS)*, pp. 1-3, 2021.
- [42] G. D. Cormack, and A. P. Sabharwal, "Picosecond pulse generator using delay lines," *IEEE Trans. on Instrumentation and Meas.*, vol. 42, no. 5, pp. 947-948, Oct. 1993.
- [43] J. Han, C. Huynh and C. Nguyen, "Tunable monocycle pulse generator using switch controlled delay line and tunable RC network for UWB systems," *2010 IEEE Antennas and Propagation Society International Symposium*, pp. 1-4, 2010.
- [44] F. Meyer, "Pulse measurements with resolution time of 18 ps," *Electronics Letters*, vol. 22, no. 6, pp. 703-704, 1970.
- [45] J. Andrews, "Picosecond pulse generators using microminiature mercury switches," *NBSIR 75-819, NBS, Boulder. CO.*, 1976.
- [46] A. Johnson and D. Auston, "Microwave switching by picosecond photoconductivity," *IEEE Journal of Quantum Electronics*, vol. 11, no. 6, pp. 283-287, June 1975.
- [47] S. J. Davis, "Fast, high-powered triode pulse amplifiers," *IEEE Conference Record of 1982 Fifteenth Power Modulator Symposium*, p.227, 1982.
- [48] D. F. McDonald, C. J. Benning, and S. J. Brient, "Subnanosecond risetime multikilovolt pulse generator," *Review of Scientific Instruments*, vol. 36, no. 4, pp. 504-506, 1965.
- [49] C. A. Hamilton, F. L. Lloyd, R. L. Peterson, and J. R. "A superconducting sampler for Josephson logic circuits," *Applied Physics Letters*, vol. 35, no. 9, pp. 718-719, 1979.
- [50] D. G. McDonald, R. L. Peterson, *U.S. Patent No. 4,168,441. Washington, DC: U.S. Patent and Trademark Office.* 1979.
- [51] C. J. Madden, M. J. W. Rodwell, R. A. Marsland, D. M. Bloom, and Y. C. Pao, "Generation of 3.5 ps fall-time shock waves on a monolithic nonlinear transmission line," *IEEE Electron Device Lett.*, vol. EDL-9, no. 6, pp. 303-305, Jun. 1988.
- [52] R. Boudot, S. Guérandel, S., and E. De Clercq, "Simple-design low-noise NLTL-based frequency synthesizers for a CPT Cs clock," *IEEE Trans. on Instrumentation and Meas.*, vol. 58, no. 10, pp. 3659-3665, Jul. 2009.

- [53] M. Case, M. Kamegawa, R. Yu, M. J. W. Rodwell, and J. Franklin, "Impulse compression using soliton effects in a monolithic GaAs circuit," *Appl. Phys. Lett.*, vol. 58, no. 2, pp. 173–175, Jan. 14, 1991.
- [54] M. Tan, C. Y. Su, and W. J. Anklam, "7 electrical pulse compression on an inhomogeneous nonlinear transmission line," *Electron. Lett.*, vol. 24, no. 4, pp. 213–214, 1988.
- [55] R. A. Marsland, V. Valdivia, C. J. Madden, M. J. W. Rodwell, and D. M. Bloom, "130 GHz GaAs monolithic integrated circuit sampling head," *Appl. Phys. Lett.*, vol. 55, no. 6, pp. 592–594, Aug. 7, 1989.
- [56] R. Hirota and K. Suzuki, "Theoretical and experimental studies of lattice solitons in nonlinear lumped networks," *Proc. IEEE*, vol. 61, no. 10, pp. 1483–1491, Oct. 1973.
- [57] T. E. McEwan and G. E. Dallum, "Soliton Quenching NLTL Impulse Circuit With a Pulse Forming Network at the Output," *U.S. Patent 5 804 921*, Sep. 8, 1998.
- [58] S. Ibuka, K. Abe, T. Miyazawa, A. Ishii, and S. Ishii, "Fast high-voltage pulse generator with nonlinear transmission line for high repetition rate operation," *IEEE Trans. Plasma Sci.*, vol. 25, no. 2, pp. 266–271, Apr. 1997.
- [59] O. Wohlgenuth, M. J. W. Rodwell, R. Reuter, J. Braunstein, and M. Schlechtweg, "Active probes for network analysis within 70–230 GHz," *IEEE Trans. Microw. Theory Tech.*, vol. 47, no. 12, pp. 2591–2597, Dec. 1999.
- [60] D. W. van der Weide, "Delta-doped Schottky diode nonlinear transmission lines for 480-fs, 3.5-V transients," *Appl. Phys. Lett.*, vol. 65, no. 7, pp. 881–883, Aug. 15, 1994.
- [61] F. Zito, D. Pepe, and D. Zito, "UWB CMOS Monocycle Pulse Generator," *IEEE Trans. on Circuits and Sys. I.*, vol. 57, no. 10, pp. 2654–2664, May. 2010.
- [62] Y. Y. Ruai, Y. Konishi, S. T. Allen, M. Reddy, and J. W. Rodwell, "A traveling-wave resonant tunnel diode pulse generator," *IEEE Microw. Guided Wave Lett.*, vol. 4, no. 7, pp. 220–222, Jul. 1994.
- [63] J. F. Holzman, F. E. Vermeulen, and A. Y. Elezzabi, "Recombination-independent photogeneration of ultrashort electrical pulses," *Appl. Phys. Lett.*, vol. 76, no. 2, pp. 134–136, Jan. 2000.

- [64] M. Gerding, T. Much, and B. Schiek, "Generation of short electrical pulses based on bipolar transistors," *Adv. in Radio Science.*, vol. 2, no. A.1, pp. 7-12, May. 2004.
- [65] A. Ouslimani, G. Vernet, H. Hafdallah, and R. Adde, "Large amplitude picosecond step generation with FETs," *Elec. Lett.*, vol. 26, no. 19, pp. 1563-1564, Sep. 1990.
- [66] Y. Zhu, J. Zuegel, J. R. Marciante, and H. Wu, "Distributed waveform generator: A new circuit technique for ultra-wideband pulse generation, shaping and modulation," *IEEE J. Solid-State Circuits.*, vol. 44, no. 3, pp. 808–823, Mar. 2009.
- [67] S. Bagga, A. V. Vorobyov, S. A. P. Haddad, A. G. Yarovoy, W. A. Serdijn, and J. R. Long, "Codesign of an impulse generator and miniaturized antennas for IR-UWB," *IEEE Trans. Microw. Theory Tech.*, vol. 54, no. 4, pp. 1656–1666, Apr. 2006.
- [68] L. Stoica, A. Rabbachin, and I. Oppermann, "A low-complexity noncoherent IR-UWB transceiver architecture with toa estimation," *IEEE Trans. Microw. Theory Tech.*, vol. 54, no. 4, pp. 1637–1646, Jun. 2006.
- [69] T. Kikkawa, P. K. Saha, N. Sasaki, and K. Kimoto, "Gaussian monocycle pulse transmitter using 0.18 μm CMOS technology with on-chip integrated antennas for inter-chip UWB communication," *IEEE J. Solid-State Circuits.*, vol. 43, no. 5, pp. 1303–1312, May 2008.
- [70] L. Giaccone, D. Giordano, and G. Crotti, "Identification and correction of artifact in the measurement of pulsed magnetic fields," *IEEE Trans. on Instrumentation and Meas.*, vol. 66, no.6, pp. 1260-1266, Feb. 2017.
- [71] A. De Angelis, M. Dionigi, A. Moschitta, and P. Carbone, "A low-cost ultra-wideband indoor ranging system," *IEEE Trans. on Instrumentation and Meas.*, vol. 58, no. 12, pp. 3935-3942, Nov. 2009.
- [72] A. De Angelis, M. Dionigi, R. Giglietti, R., and P. Carbone, "Experimental comparison of low-cost sub-nanosecond pulse generators," *IEEE Trans. on Instrumentation and Meas.*, vol. 60, no. 1, pp. 310-318, May 2010.
- [73] M. Rahman and K. Wu, "A Fine Picosecond Pulse Generator Based on Novel SRD Topology and Tapered NLTL," 2020 IEEE/MTT-S International Microwave Symposium (IMS), Los Angeles, CA, USA, 2020, pp. 301-304.

- [74] K. L. Kotzebue, "A circuit model of the step-recovery diode," *Proceedings of the IEEE*, vol. 53, no. 12, pp. 2119-2120, 1965.
- [75] J. Zhang, and A. Raisanen, "A new model of step recovery diode for CAD," *IEEE International Microwave symposium (IMS) 1995.*, pp. 1459-1462, May. 1995.
- [76] M. Toda, "Nonlinear lattice and soliton theory," *IEEE Transactions on Circuits and Systems.*, vol. 30, no. 8, pp. 542-554, 1983.
- [77] D. J. Korteweg, and G. De Vries, "XLI. On the change of form of long waves advancing in a rectangular canal, and on a new type of long stationary waves," *The London, Edinburgh, and Dublin Philosophical Magazine and Journal of Science.*, vol. 39, no. 240, pp. 422-443, 1985.
- [78] F. Martín, and X. Oriols, "Simple model to study soliton wave propagation in periodic-loaded nonlinear transmission lines," *Applied Physics Letters.*, vol. 78, no. 18, pp. 2802-2804, 2001.
- [79] X. Oriols, and F. Martín, "Analytical solitons in nonlinear transmission lines loaded with heterostructure barrier varactors," *Journal of Applied Physics.*, vol. 90, no. 5, pp. 2595-2600, 2001.
- [80] V. I. Karpman and E. M. Maslov, "Perturbation theory for solitons," *Sov. Phys. JETP.*, vol. 46, pp. 281, 1977.
- [81] J. S. Lee, C. Nguyen, and T. Scullion, "New uniplanar sub-nanosecond monocycle pulse generator and transformer for time-domain microwave applications," *IEEE Trans. on Microw. Theory and Tech.*, vol. 49, no. 6, pp. 1126-1129, Jun. 2001.
- [82] J. Han, and C. Nguyen, "A new ultra-wideband, ultra-short monocycle pulse generator with reduced ringing," *IEEE Microw. Wire. Comps. Lett.*, vol. 12, no. 6, pp. 206-208, Aug. 2002.
- [83] J. Han, and C. Nguyen, "Coupled-slotline-hybrid sampling mixer integrated with step-recovery-diode pulse generator for UWB applications," *IEEE Trans. on Microw. Theory and Tech.*, vol. 53, no. 6, pp. 1875-1882, Jun. 2005.
- [84] J. Han and C. Nguyen, "On the development of a compact subnanosecond tunable monocycle pulse transmitter for UWB applications," *IEEE Trans. Microw. Theory Techn.*, vol. 54, no. 1, pp. 285-293, Jan. 2006.

- [85] J. Zhou, Q. Lu, F. Liu, and Y. Li, "A novel picosecond pulse generation circuit based on SRD and NLTL," *PloS one*, vol. 11, no. 2, pp. 1-10, Aug. 2016.
- [86] A. Kamal, A. Bhattacharya, M. Tamrakar, and C. Roy, "Low-ringing and reduced-cost step recovery diode based UWB pulse generators for GPR applications," *Microwave and Optical Technology Letters.*, vol. 56, no. 10, pp. 2289-2294, Oct. 2014.
- [87] J. Han, and C. Nguyen, "Ultra-wideband electronically tunable pulse generators," *IEEE Microw. Wireless Compon. Lett.*, vol. 14, no. 3, pp. 112-114, Mar. 2004.
- [88] K.G. Lyon, and E. C. Kan, "Microwave pulse generation using the Bragg cutoff of a nonlinear transmission line," *In IEEE MTT-S International Microwave Symposium Digest*, pp. 1461-1464, Jun. 2008.
- [89] M. Dwyer, H. Kim, L. Mawst and D. van der Weide, "Double-uniform Schottky diode nonlinear transmission line generating sub-picosecond transients," *2018 IEEE Radio and Wireless Symposium (RWS), Anaheim, CA, USA*, pp. 287-289, 2018.
- [90] R. Fegghi, D. Oloumi, and K. Rambabu, "Design and development of an inexpensive subnanosecond Gaussian pulse transmitter," *IEEE Trans. Microw. Theory Techn.*, vol. 67, no. 9, pp. 3773-3782, Sep. 2019.
- [91] L. Han and K. Wu, "Multifunctional Transceiver for Future Intelligent Transportation Systems," *IEEE Transactions on Microwave Theory and Techniques*, vol. 59, no. 7, pp. 1879-1892, July 2011.
- [92] J. Moghaddasi and K. Wu, "Millimeter-Wave Multifunction Multiport Interferometric Receiver for Future Wireless Systems," *IEEE Transactions on Microwave Theory and Techniques*, vol. 66, no. 3, pp. 1452-1466, March 2018.
- [93] R. Fegghi, D. Oloumi and K. Rambabu, "Tunable Subnanosecond Gaussian Pulse Radar Transmitter: Theory and Analysis," *IEEE Transactions on Microwave Theory and Techniques*, vol. 68, no. 9, pp. 3823-3833, Sept. 2020.
- [94] A. M. Nicolson, H. M. Cronson, P. G. Mitchell, "Subnanosecond risetime pulse generators," *IEEE Trans. on Instrumentation and Meas.*, no. 2, pp. 104-107, jun. 1976.

- [95] Y. Song, J. Hu, Y. Dai, T. Jin and Z. Zhou, "Estimation and Mitigation of Time-Variant RFI in Low-Frequency Ultra-Wideband Radar," *IEEE Geoscience and Remote Sensing Letters*, vol. 15, no. 3, pp. 409-413, March 2018.
- [96] X. Wang, S. Zhang, M. Liu, K. Jin, X. Zhu and M. Lu, "Generating Narrow Pulses with Programmable Waveform, Amplitude, and Position Based on Spectrum Stitching," *IEEE Trans. on Instrumentation and Meas.*, vol. 70, pp. 1-9, 2021.
- [97] T. Song et al., "Low-power technique for SRAM-based on-chip arbitrary-waveform generator," *IEEE Trans. Instrum. Meas.*, vol. 60, no. 4, pp. 1187-1196, Apr. 2011.
- [98] S. Shen, G. Sun, W. Ding and L. Li, "Design and Application of Repetitive Nanosecond Pulse Generator Based on Avalanche Transistors," *2021 International Conference on Electrical, Communication, and Computer Engineering (ICECCE)*, pp. 1-4, 2021.
- [99] R. He, Y. Li, Z. Liu, J. Jin and Z. Sun, "Development of a High Peak Voltage Picoseconds Avalanche Transistor Based Marx Bank Circuit," *IEEE Access*, vol. 9, pp. 64844-64851, 2021.
- [100] W.J. Anklam, and W.E. Kunz, "Nonlinear transmission lines having noncommensurate varactor cells," *Hewlett Packard Co*, U.S. Patent: 5,023,574, June 1991.
- [101] F. S. Yamasaki, L. P. S. Neto, J. O. Rossi and J. J. Barroso, "Soliton Generation Using Nonlinear Transmission Lines," *IEEE Transactions on Plasma Science*, vol. 42, no. 11, pp. 3471-3477, Nov. 2014.
- [102] S. Sim, D. Kim and S. Hong, "A CMOS UWB Pulse Generator for 6-10 GHz Applications," *IEEE Microwave and Wireless Components Letters*, vol. 19, no. 2, pp. 83-85, Feb. 2009.
- [103] A. Zhu, F. Sheng and A. Zhang, "An implementation of step recovery diode-based UWB pulse generator," *2010 IEEE International Conference on Ultra-Wideband*, pp. 1-4, 2010.
- [104] "The protection requirements of radiocommunications systems below 10.6 GHz from generic UWB applications," *Electron. Commun. Committee (ECC), Helsinki, Finland*, ECC Rep. 64, Feb. 2005.

- [105] M. Rahman and K. Wu, "A Reconfigurable Picosecond Pulse Generator in Non-linear Transmission Line for Impulse Radar Ultrawideband Applications," *IEEE Microw. Wireless Compon. Lett.*, Feb. 2022.
- [106] D. M. Pozar, "Microwave engineering.," *John Wiley & Sons*, 2009.
- [107] L. F. Chen, C. K. Ong, C. P. Neo, et al., "Microwave Electronics: Measurement and Materials Characterization.," *John Wiley & Sons, West Sussex, England*, 2004.
- [108] Y. Huang, G. Wen, W. Zhu, J. Li, L. M. Si, and M. Premaratne, "Experimental demonstration of a magnetically tunable ferrite-based metamaterial absorber.," *Optics express*, vol. 22, no. 13 16408-16417, 2014.
- [109] He G, Wu R-x, Poo Y, et al. "Magnetically tunable double-negative material composed of ferrite-dielectric and metallic mesh," *J Appl Phys.*, 107, 093522, 2010.
- [110] M. Weiner, and L. Silber, "Pulse sharpening effects in ferrites," *IEEE Transactions on Magnetics.*, vol. 17, no. 4, pp. 1472-1477, 1981.
- [111] F. F. He, K. Wu, W. Hong, L. Han, and X. Chen, "A low phase-noise VCO using an electronically tunable substrate integrated waveguide resonator," *IEEE Trans. Microw. Theory Tech.*, vol. 58, no. 12, pp. 3452–3458, Oct. 2010.
- [112] P. Rundqvist, A. Vorobiev, E. Kollberg, et al. "Large signal circuit model of parallel-plate ferroelectric varactors," *J. Appl. Phys.*, 100, 074101, 2006.
- [113] B. W. Kim and S. W. Yun, "Varactor-tuned combine bandpass filter using step-impedance microstrip lines," *IEEE Trans. Microw. Theory Techn.*, vol. 52, no. 4, pp. 1279–1283, Apr. 2004.
- [114] I. B. Vendik, P. A. Turalchuk, G. Orest et al. "Modeling tunable bulk acoustic resonators based on induced piezoelectric effect in BaTiO₃ and Ba_{0.25}Sr_{0.75}TiO₃ films," *J. Appl. Phys.*, vol. 103, p.014107, 2008.
- [115] M. Abadi, S. Amin, John H. Booske and N. Behdad "MAcro-Electro-Mechanical Systems (MÆMS) based concept for microwave beam steering in reflectarray antennas," *J. Appl. Phys.*, 120, 054901, 2016.

- [116] I. C. Reines, C. L. Goldsmith, C. D. Nordquist, C. W. Dyck, G. M. Kraus, T. A. Plut, P. S. Finnegan, F. Austin, IV, and C. T. Sullivan, "A low loss RF MEMS -band integrated switched filter bank," *IEEE Microw. Wireless Compon. Lett.*, vol. 15, no. 2, pp. 74–76, Feb. 2005.
- [117] K. Entesari and G. M. Rebeiz, "A 12–18 GHz three-pole RF MEMS tunable filter," *IEEE Trans. Microw. Theory Techn.*, vol. 53, no. 8, pp. 2566–2571, Aug. 2005.
- [118] E. Afshari, H. S. Bhat, A. Hajimiri, et al. "Extremely wideband signal shaping using one- and two-dimensional nonuniform nonlinear transmission lines," *J. Appl. Phys.*, 99, 054901, 2006.
- [119] A. C. Scott, F. Y. Chu, and D. W. McLaughlin, "The soliton: a new concept in applied science," *Proc. IEEE*, vol. 61, no. 10, pp. 1443-1483, Oct. 1973.
- [120] N. S. Kuek, A. C. Liew, E. Schamiloglu, and J. O. Rossi, "Circuit modeling of nonlinear lumped element transmission lines including hybrid lines," *IEEE Trans. Plasma Sci.*, vol. 40, no. 10, pp. 2523–2534, Oct. 2012.
- [121] O. S. F. Zucker and W. H. Bostick, "Theoretical and practical aspects of energy storage and compression," *Energy Storage, Compression and Switching, New York, NY, USA: Plenum*, pp. 71-93, 1976.
- [122] J. Gaudet, E. Schamiloglu, J. O. Rossi, C. J. Buchenauer, and C. Frost, "Nonlinear transmission lines for high power microwave applications-A survey," *28th IEEE Int. Power Modulators High Voltage Conf., Las Vegas, NV, USA*, pp. 131-138, May 2008.
- [123] T. Yagi, H. Watanabe, and A. Noguchi, "Growth and damping of solitons in a nonlinear transmission line with moving parameters," *Proc. IEEE*, vol. 66, no. 6, pp. 702-703, 1978.
- [124] M. Sparks, "Ferromagnetic-relaxation theory," *McGraw-Hill*, 1964.
- [125] R. Hirota and K. Suzuki, "Theoretical and experimental studies of lattice solitons in nonlinear lumped networks," *Proc. IEEE*, vol. 61, no. 10, pp. 1483–1491, Oct. 1973.
- [126] K. K. Mei, K. "Theory of Maxwellian circuits," *URSI Radio Science Bulletin.*, no. 306, pp. 6-13, Sep. 2003.

- [127] C. S. Gardner, J. M. Greene, M. D. Kruskal, and R. M. Miura, "Method for solving the Korteweg-de-Vries Equation," *Phys. Rev. Lett.*, vol. 19, no. 19, pp. 1095-1097, 1967.
- [128] M. Rahman, and K. Wu, "Hybrid Non-Linear Transmission Shock-Wave Solution by Combined Approach of Perturbation and Fixed Point Homotopy," *2020 IEEE MTT-S International Wireless Symposium (IWS), Shanghai*, 20th Sept. pp. 1-3, 2020.
- [129] C. Canuto, and A. Tabacco, "Mathematical Analysis I and II," vol. 85, *Springer*, 2015.
- [130] G. Tyras, "The permeability matrix for a ferrite medium magnetized at an arbitrary direction and its eigenvalues," *IRE Trans. Microw. Theory Techn.*, vol. 7, no. 1, pp. 176-177, 1959.
- [131] A. N. Slavin and I. V. Rojdestvenski, "'Bright" and "dark" spin wave envelope solitons in magnetic films," *IEEE Trans. on Magnetics.*, vol. 30, no. 1, pp. 37-45, Jan. 1994.
- [132] W. B. Hatfield and B. A. Auld, "Electromagnetic Shock Waves in Gyromagnetic Media," *J. Appl. Phys.*, 34, 2941, 1963.
- [133] I. V. Romanchenko, V. V. Rostov, A. V. Gunin, et al. "High power microwave beam steering based on gyromagnetic nonlinear transmission lines," *J. Appl. Phys.*, 117, 214907, 2015.
- [134] I. V. Romanchenko, V. V. Rostov, A. V. Gunin and V. Yu. Konev "Gyromagnetic RF source for interdisciplinary research," *Rev. Sci. Instrum.*, 88, 024703, 2017.
- [135] T. Yagi, H. Watanabe, and A. Noguchi, "Growth and damping of solitons in a nonlinear transmission line with moving parameters," *Proc. IEEE*, vol. 66, no. 6, pp. 702-703, 1978.
- [136] M. Rahman and K. Wu, "Capacitive NLTL Solitary Wave Equation with Mutual Inductance," *2020 IEEE International Symposium on Antennas and Propagation and North American Radio Science Meeting*, pp. 2073-2074, 2020.
- [137] A. M. Bobreshov, A. S. Zhabin, A. D. Ryazantsev, V. A. Stepkin, and G. K. Uskov, "Application of Nonlinear Transmission Lines for Picosecond Pulse Sharpening," *IEEE Microw. Wireless Compon. Lett.*, vol. 32, no. 5, pp. 460-462, 2022.
- [138] M. Rahman, and K. Wu, "Theoretical and experimental analysis of pulse compression capability in non-linear magnetic transmission line," *J. Appl. Phys.*, vol. 131, no. 1, 013901, 2022.

- [139] T. Yagi, and A. Noguchi, "Gyromagnetic nonlinear element and its application as a pulse-shaping transmission line," *Electron. Lett.*, vol. 22, no. 13, pp. 683-685, 1977.
- [140] D. V. Reale et al., "Bias-field controlled phasing and power combination of gyromagnetic nonlinear transmission lines," *Rev. Sci. Instrum.*, 88, 024703, 2017.
- [141] C. R. Spikings, N. Seddon, R. A. Ibbotson, and J. E. Dolan, "HPM systems based on NLTL technologies," *Proc. IET Conf. High Power RF Technol., London, U.K.*, pp. 1-3, 2009.
- [142] J. E. Dolan, "Simulation of ferrite-loaded coaxial lines," *Electron. Lett.*, 29, pp. 762-763, 1993.
- [143] J. E. Dolan "Simulation of shock waves in ferrite-loaded coaxial transmission lines with axial bias," *J. Phys. D: Appl. Phys.*, 32, 1826, 1999.
- [144] L. Huang, J. Meng, D. Zhu, and Y. Yuan, "Field-line coupling method for the simulation of gyromagnetic nonlinear transmission line based on the Maxwell LLG system," 48, 3847–3853 (2020). *IEEE Trans. Plasma Sci.*, 48, 3847-3853, 2020.
- [145] S. Furuya, H. Matsumoto, H. Fukuda et al., "Simulation of nonlinear coaxial line using ferrite beads," *Jpn. J. Appl. Phys.*, 41, 6536, 2002.
- [146] E. Maxwell, T. Weller and E. Odu, "Design and Analysis of a Multiport Circuit for Shaping Sub-Nanosecond Pulses," *IEEE Trans. Microw. Theory Techn.*, vol. 56, no. 12, pp. 2764-2770, Dec. 2008.
- [147] M. Mirshafiei, M. Abtahi, and L. A. Rusch, "Ultra-wideband pulse shaping: bypassing the inherent limitations of the Gaussian monocycle," *IET communications*, vol. 6, no. 9, pp. 1068-1074, Jun. 2012.
- [148] K. M. Chan, K. Rambabu, A. C. Tan, and M. W. Chia, "Efficient passive low-rate pulse generator for ultra-wideband radar," *IET Microw. Antennas Propag.*, vol. 4, no. 12, pp. 2196-2199, Dec. 2010.
- [149] W. Xu, J. Chen, Z. Shi and A. Zhang, "A Novel Picosecond-Pulse Circuit Based on Marx Structure and SRD," *2021 IEEE 4th International Conference on Electronic Information and Communication Technology (ICEICT)*, 2021.

- [150] M. Ghavami, L. B. Michael, S. Haruyama, and R. Kohno, "A novel UWB pulse shape modulation system," *Wireless Pers. Commun.*, vol. 23, no. 1, pp. 105-120, Oct. 2002.
- [151] X. Xia, L. Liu, S. Ye, H. Guan and G. Fang, "A novel subnanosecond monocycle pulse generator for UWB radar applications," *Journal of Sensors*, Jan. 2014.
- [152] X. An, J. Wagner and F. Ellinger, "A 7th Derivative Gaussian Pulse Generator for IR-UWB Radar Applications in Pedestrian Detection," *25th IEEE International Conference on Electronics, Circuits and Systems (ICECS)*, pp. 317-320, 2018.
- [153] D. J. Daniels, "The impact of antenna design on short range radar performance," *Proc. IEEE Conf. Antenna Meas. Appl. (CAMA), Antibes, France*, pp. 1-4, Nov. 2014.
- [154] D. Ganguly, D. Guha, S. Das and A. Rojatkhar, "Systematic Approach to Estimating Monocycle Pulse for Time-Domain Studies of UWB Antennas Using Numerical Computations and Simulation Tools," *IEEE Antennas Propag. Mag.*, vol. 56, no. 4, pp. 73-87, Aug. 2014.
- [155] C. L. Bennet and G. F. Ross, "Time-domain electromagnetics and its applications," *Proc. IEEE*, vol. 66, no. 3, pp. 299-318, Mar. 1978.
- [156] J. D. Taylor, "Introduction to Ultra-Wideband (UWB) Radar Systems," *Boca Raton, FL: CRC*, 1995.
- [157] V. Venkatasubramanian, H. Leung, and X. Liu, "Chaos UWB radar for through-the-wall imaging," *IEEE Trans. Image Process.*, vol. 18, no. 6, pp. 1255-1265, Jun. 2009.
- [158] D. Oloumi, P. Mousavi, M. I. Pettersson, and D. G. Elliott, "A modified TEM horn antenna customized for oil well monitoring applications," *IEEE Trans. Antennas Propag.*, vol. 61, no. 12, pp. 5902-5909, Dec. 2013.
- [159] A. D. Pitcher, C. W. Baard and N. K. Nikolova, "Design and Performance Analysis of a Picosecond Pulse Generator," *IEEE Transactions on Instrumentation and Measurement*, Early access, 2022.
- [160] K. -R. Chen, Y. -L. Lin and M. -C. Yang, "Medical communication device with compact planar antenna and heterogeneous wireless resource for ubiquitous real-time healthcare

- monitoring," *2013 ICME International Conference on Complex Medical Engineering*, 2013, pp. 224-227.
- [161] G. R. Wang, H. G. Han, S. Y. Kim and T. W. Kim, "Wireless Vital Sign Monitoring Using Penetrating Impulses," *IEEE Microwave and Wireless Components Letters*, vol. 27, no. 1, pp. 94-96, Jan. 2017.
- [162] K. Yan, Z. Xia, S. Wu, X. Liu and G. Fang, "Through-Floor Vital Sign Imaging for Trapped Persons Based on Optimized 2-D UWB Life-Detection Radar Deployment," *IEEE Antennas and Wireless Propagation Letters*, vol. 21, no. 1, pp. 39-43, Jan. 2022.
- [163] X. Shang, J. Liu and J. Li, "Multiple Object Localization and Vital Sign Monitoring Using IR-UWB MIMO Radar," *IEEE Transactions on Aerospace and Electronic Systems*, vol. 56, no. 6, pp. 4437-4450, Dec. 2020.
- [164] H. F. Harmuth and D.-R. Shao, "Antennas for nonsinusoidal waves. I-Radiators," *IEEE Trans. Electromagn. Compat.*, vol. EMC-25, no. 1, pp. 13-24, Feb. 1983.
- [165] H. F. Harmuth, "Radiation of nonsinusoidal waves by a large-current radiator," *IEEE Trans. Electromagn. Compat.*, vol. EMC-27, no. 2, pp. 77-87, May 1985.
- [166] M. G. M. Hussain, "Antenna pattern of nonsinusoidal waves with the time variation of a Gaussian pulse-Part II," *IEEE Trans. Electromagn. Compat.*, vol. 30, no. 4, pp. 513-522, Nov. 1988.
- [167] M. Kanda, "Time-domain sensors and radiators," *Time-Domain Measurements in Electromagnetics*, E. K. Miller and V. N. Reinhold, Eds. New York: Kluwer, 1986, ch. 5.
- [168] K. Rambabu, A. E.-C. Tan, K. K.-M. Chan, and M. Y.-W. Chia, "Estimation of antenna effect on ultra-wideband pulse shape in transmission and reception," *IEEE Trans. Electromagn. Compat.*, vol. 51, no. 3, pp. 604-610, Aug. 2009.
- [169] A. E.-C. Tan, K. Jhamb, and K. Rambabu, "Design of transverse electromagnetic horn for concrete penetrating ultrawideband radar," *IEEE Trans. Antennas Propag.*, vol. 60, no. 4, pp. 1736-1743, Apr. 2012.

- [170] H. Öztürk, K. Yeğin and H. Nazlı, "High Fidelity Gaussian Monocycle Generation Using Microstrip Lines," *IEEE Microwave and Wireless Components Letters*, vol. 24, no. 10, pp. 722-724, Oct. 2014.
- [171] C. -L. Yang, Y. -L. Yang and C. -C. Lo, "Subnanosecond Pulse Generators for Impulsive Wireless Power Transmission and Reception," *IEEE Transactions on Circuits and Systems II: Express Briefs*, vol. 58, no. 12, pp. 817-821, Dec. 2011.
- [172] P.J. Gibson, "The Vivaldi aerial," *IEEE 9th Eur. Microw. Conf.*, pp. 101-105, 1979.
- [173] C.A. Balanis, "Antenna Theory: Analysis and Design," *John wiley & sons*, 2016.
- [174] M. C. Greenberg and K. L. Virga, "Characterization and design methodology for the dual exponentially tapered slot antenna," *IEEE Antennas and Propag. Soc. Int. Symp., Orlando, FL*, Jul. 1999, vol. 1, pp. 88-91.
- [175] J. Liu, K. P. Esselle, S. Hay, and S. S. Zhong, "Compact super-wideband asymmetric monopole antenna with dual-branch feed for bandwidth enhancement," *Electronics Letters*, vol. 49, no. 8, pp. 515-516, 2013.
- [176] K. R. Chen, and J. S. Row, "A compact monopole antenna for super wideband applications," *IEEE Antennas and Wireless Propagation Letters*, vol. 10, pp. 488-491, 2011.
- [177] G. S. Smith, "Teaching antenna radiation from a time-domain perspective," *Amer. J. Phys.*, vol. 69, no. 3, pp. 288-300, Mar. 2001.
- [178] X. Hui, and E. C. Kan, "No-touch measurements of vital signs in small conscious animals," *Science advances*, vol. 5, no. 2, eaau0169, 2019.
- [179] D. H. Kwon, "Effect of Antenna Gain and Group Delay Variations on Pulse-Preserving Capabilities of Ultrawideband Antennas," *IEEE Trans. Antennas Propag.*, vol. 54, no. 8, pp. 2208-2215, Aug. 2006.

APPENDIX A LIST OF PUBLICATIONS & AWARDS

1. Peer-reviewed journal papers:

1.1 Published papers:

(J1) **M. Rahman** and K. Wu, "A Nonlinear Transmission Line Technique for Generating Efficient and Low-Ringing Picosecond Pulses for Ultrabroadband and Ultrafast Systems," *IEEE Transactions on Instrumentation and Measurement*, vol. 71, pp. 1-11, 2022, Art no. 2005511.

(J2) **M. Rahman** and K. Wu, "A Reconfigurable Picosecond Pulse Generator in Non-linear Transmission Line for Impulse Radar Ultrawideband Applications," *IEEE Microwave and Wireless Components Letters*, vol. 32, no. 5, pp. 448-451, May 2022

(J3) **M. Rahman** and K. Wu, "A Nonlinear Transmission Approach to Compressing Rise and Fall Time in Picosecond Pulse Generation," *IEEE Transactions on Instrumentation and Measurement*, vol. 70, pp. 1-13, 2021, Art no. 2004013.

(J4) **M. Rahman** and K. Wu, "Theoretical and experimental analysis of pulse compression capability in non-linear magnetic transmission line," *Journal of Applied Physics*, vol. 131, no. 1, p. 013901, 2022.

(J5) **M. Rahman** and K. Wu, "Theory and Practice of Pulse Compression in Hybrid and Gyromagnetic Non-Linear Transmission Lines," *Journal of Applied Physics*, vol. 132, no. 12, p. 223902, 2022.

1.2 Submitted papers:

(J6) **M. Rahman** and K. Wu, "A Comprehensive Review on Pulse Generation and Compression Techniques in Microwave Electronics," *Electromagnetic Science*, Under review, (Invited Review).

(J7) **M. Rahman** and K. Wu, "Picosecond Pulse Generation, Shaping, Transmission, and Reception Characteristics for Wireless Sensing Applications," *IEEE Transactions on Microwave Theory and Technique*, To be Submitted.

2. Conference papers:

(C1) **M. Rahman** and K. Wu, "A Picosecond Ultrafast Pulse Generation Featuring Switchable Operation Between Monocycle and Doublet Pulses," *2022 IEEE/MTT-S International Microwave Symposium - IMS 2022*, 2022, pp. 56-59.

(C2) **M. Rahman** and K. Wu, "Simultaneous Electric and Magnetic Two-Dimensional Tuning in Nonlinear Magnetic Transmission Line," *2021 51st European Microwave Conference (EuMC)*, 2022, pp. 30-33.

(C3) **M. Rahman** and K. Wu, "Theory and Practice of Multidimensional Non-Linear Transmission Line," *2021 IEEE MTT-S International Wireless Symposium (IWS)*, 2021, pp. 1-3.

(C4) **M. Rahman** and K. Wu, "Hybrid Non-Linear Transmission Shock-Wave Solution by Combined Approach of Perturbation and Fixed Point Homotopy," *2020 IEEE MTT-S International Wireless Symposium (IWS)*, 2020, pp. 1-3.

(C5) **M. Rahman** and K. Wu, "Technique for Eliminating Resonant Artifacts in Low Loss Material Measurement," *2020 50th European Microwave Conference (EuMC)*, 2021, pp. 264-267.

(C6) **M. Rahman** and K. Wu, "Capacitive NLTL Solitary Wave Equation with Mutual Inductance," *2020 IEEE International Symposium on Antennas and Propagation and North American Radio Science Meeting*, 2020, pp. 2073-2074.

(C7) **M. Rahman** and K. Wu, "Hybrid Dissipative NLTL Soliton Solution Based on KdV Approach," *2020 IEEE International Symposium on Antennas and Propagation and North American Radio Science Meeting*, 2020, pp. 2041-2042.

(C8) **M. Rahman** and K. Wu, "A Fine Picosecond Pulse Generator Based on Novel SRD Topology and Tapered NLTL," *2020 IEEE/MTT-S International Microwave Symposium (IMS)*, 2020, pp. 301-304.

(C9) **M. Rahman** and K. Wu, "A Picosecond Pulse Transmission and Reception System for Wireless Sensing and Imaging Applications," *2023 IEEE/MTT-S International Microwave Symposium (IMS)*, (Submitted).

3. Patent filed:

(P1) **M. Rahman** and K. Wu, "Gaussian Doublet Electronic Pulse Generator," (Huawei Ref: 92021447PCT01).

4. Awards:

(A1) IEEE MTT-S Graduate Fellowship Award, 2022.

(A2) Travel Grant Award (IEEE IMS, Denver), June. 2022.